MATHEMATICAL MODELLING OF CANCER INVASION AND METASTATIC SPREAD

Linnea Christin Franssen

A Thesis Submitted for the Degree of PhD
at the
University of St Andrews

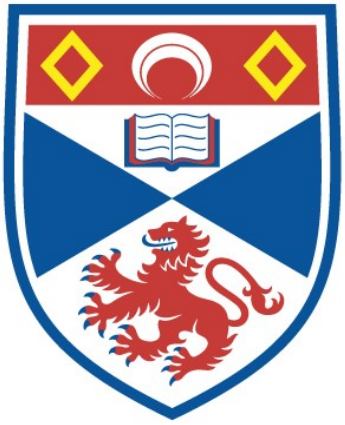

2019

University of
St Andrews

Mathematical Modelling of Cancer Invasion and Metastatic Spread

A thesis submitted for the degree of
Doctor of Philosophy

by

Linnea Christin Franssen

August 2019

In memory of Opa Gustav Nachtigahl Franßen.

Abstract

Metastatic spread—the dissemination of cancer cells from a primary tumour with subsequent re-colonisation at secondary sites in the body—causes around 90% of cancer-related deaths. Mathematical modelling may provide a complementary approach to help understand the complex mechanisms underlying metastasis. In particular, the spatiotemporal evolution of individual cancer cells during the so-called *invasion-metastasis cascade*—i.e. during cancer cell invasion, intravasation, vascular travel, extravasation and metastatic growth—is an aspect not yet explored through existing mathematical models.

In this thesis, such a spatially explicit hybrid multi-organ metastasis modelling framework is developed. It describes the invasive growth dynamics of individual cancer cells both at a primary site and at potential secondary metastatic sites in the body, as well as their transport from the primary to the secondary sites. Throughout, the interactions between the cancer cells, *matrix-degrading enzymes* (MDEs) and the *extracellular matrix* (ECM) are accounted for. Furthermore, the individual-based framework models phenotypic variation by distinguishing between cancer cells of an epithelial-like, a mesenchymal-like and a mixed phenotype. It also describes permanent and transient mutations between these cell phenotypes in the form of *epithelial-mesenchymal transition* (EMT) and its reverse process *mesenchymal-epithelial transition* (MET). Both of these mechanisms are implemented at the biologically appropriate locations of the invasion-metastasis cascade. Finally, cancer cell dormancy and death at the metastatic sites are considered to model the frequently observed maladaptation of metastasised cancer cells to their new microenvironments.

To investigate the EMT-process further, an additional three-dimensional discrete-continuum model of EMT- and MET-dependent cancer cell invasion is developed. It consists of a hybrid system of partial and stochastic differential equations that describe the evolution of epithelial-like and mesenchymal-like cancer cells, again under the consideration of MDE concentrations and the ECM density. Using inverse parameter estimation and sensitivity analysis, this model is calibrated to an *in vitro* organotypic assay experiment that examines the invasion of HSC-3 cancer cells.

Candidate's declaration

I, Linnea Christin Franssen, do hereby certify that this thesis, submitted for the degree of PhD, which is approximately 50,000 words in length, has been written by me, and that it is the record of work carried out by me, or principally by myself in collaboration with others as acknowledged, and that it has not been submitted in any previous application for any degree.

I was admitted as a research student at the University of St Andrews in February 2016.

I received funding from an organisation or institution and have acknowledged the funder(s) in the full text of my thesis.

Date: Signature of candidate:

Supervisor's declaration

I hereby certify that the candidate has fulfilled the conditions of the Resolution and Regulations appropriate for the degree of PhD in the University of St Andrews and that the candidate is qualified to submit this thesis in application for that degree.

Date: Signature of supervisor:

Permission for publication

In submitting this thesis to the University of St Andrews we understand that we are giving permission for it to be made available for use in accordance with the regulations of the University Library for the time being in force, subject to any copyright vested in the work not being affected thereby. We also understand, unless exempt by an award of an embargo as requested below, that the title and the abstract will be published, and that a copy of the work may be made and supplied to any bona fide library or research worker, that this thesis will be electronically accessible for personal or research use and that the library has the right to migrate this thesis into new electronic forms as required to ensure continued access to the thesis.

I, Linnea Christin Franssen, have obtained, or am in the process of obtaining, third-party copyright permissions that are required or have requested the appropriate embargo below.

The following is an agreed request by candidate and supervisor regarding the publication of this thesis:

Printed copy

No embargo on print copy.

Electronic copy

No embargo on electronic copy.

Date: Signature of candidate:

Date: Signature of supervisor:

Underpinning Research Data or Digital Outputs

Candidate's declaration

I, Linnea Christin Franssen, hereby certify that no requirements to deposit original research data or digital outputs apply to this thesis and that, where appropriate, secondary data used have been referenced in the full text of my thesis.

Date: Signature of candidate:

Acknowledgements

Throughout the writing of this thesis, I have gratefully received the support, assistance, and friendship of many.

Firstly, I would like to thank my supervisors Prof Mark Chaplain and Dr Tommaso Lorenzi for their academic and personal support. Thank you also for so generously sharing your knowledge of mathematical biology and having so many laughs with me. Mark, your refreshing positivity and enthusiasm are contagious! Thank you for always enabling and encouraging me to follow my interests. As a result of your open-minded leadership approach, I look back on an exciting, joy-filled and well-rounded PhD journey. Tommaso, I have learned so much from you! I will carry the benefits from your detailed advice on academic writing as well as the opportunity to witness your approach to critical thinking and your kindness with me through the rest of my life.

As my collaborator, whose contributions to my PhD experience far exceed our work in Chapter 6, I would also like to thank Dr Nikolaos Sfakianakis. Thank you for your insightful comments about this work, our many in-depth (non-)scientific discussions, sharing your immense knowledge of numerical analysis and your genuine encouragement.

Moreover, I would like to thank the StAMBio group for being such friendly and supportive colleagues—my gratitude extends to all the staff in the School of Mathematics and Statistics. In particular, I would like to thank you, Dr Fiona Macfarlane, for being the inspiringly warm-hearted, easy-going and considerate office mate and friend that you are. Thank you also for the many giggles and journeys to the office that we have shared.

Jack Nichols, your support in chasing—seemingly invincible—bugs, your patient answers to my C++ questions and your encouragement to further develop my programming skills have been an inspiration to me. I owe my enthusiasm for programming to you.

Also, thank you, Prof Tuula Salo and Dr Ahmed Al-Samadi, for the discussions about your experiments, as well as to my examiners Prof Kevin Painter and Dr Giorgos Minas.

I owe Averill, Patrick, Norman and Carina a special thank-you for welcoming me to their homes. Living with you during my time in St Andrews has been a privilege as each one of you has touched and inspired me with your endless kindness, generosity and friendship.

I count myself lucky to be blessed with family and friends all over Europe, North America, and Africa. You have all been so supportive that I never felt the distance between us and I am thankful to have each one of you in my life. My mother Silke and sister Jule have been the proudest and most excited remote support team imaginable. I am further blessed to have my grandma Christa and late grandpa Gustav in my life, who have always been there for me. The letters from my grandparents Deike and Christoph have brightened up many rainy days. I would like to express my special gratitude towards Tina for enriching my life every day through our virtual dialogue, and for her support and encouragement. Besides, learning from her trained eye for graphic visualisation has enhanced the UX of my work. Moreover, I feel blessed to be writing these acknowledgements from the sunshine of the Canary Islands—thank you for having me to my father Sven.

Finally, thank you, Craig, for being the most supportive, loving, inspiring and patient partner I could ask for, and for your perpetual encouragement to follow my dreams. Meeting you has been the true gift of my PhD journey.

Funding

This work was supported by the Engineering and Physical Sciences Research Council (EPSRC).

Contents

List of abbreviations

ABM	Agent-based model
ADME	Absorption, distribution, metabolism and excretion
ARD	Advection-reaction-diffusion
CAF	Cancer-associated fibroblast
CBM	Centre-based model
CPM	Cellular Potts model
CSC	Cancer stem cell
CT	Computer tomography
CUP	Cancer of unknown primary site
DTC	Disseminated tumour cell
ECC	Epithelial-like cancer cell
ECM	Extracellular matrix
EGT	Evolutionary game theory
EMT	Epithelial-mesenchymal transition
FTCS	Forward-time central-space
FV	Finite volume
HIF-1	Hypoxia-inducible factor-1
IMEX-RK	Implicit-explicit Runge-Kutta
LGCA	Lattice gas cellular automata
MC	Markov Chain
MCC	Mesenchymal-like cancer cell
MDE	Matrix-degrading enzyme
MET	Mesenchymal-epithelial transition
MMP	Matrix metalloproteinase
MMP-1	Matrix metalloproteinase-1
MMP-2	Matrix metalloproteinase-2
MSG	Metastasis suppressor gene
MT1-MMP	Membrane-type-1 matrix metalloproteinase
myc	Myelocytomatosis viral oncogene homolog
NET	Neutrophil extracellular trap
NK	Natural killer

ODE	Ordinary differential equation
PAI-1	Plasminogen activator inhibitor-1
PCC	Partial-EMT cancer cell
PCR	Polymerase chain reaction
PDE	Partial differential equation
ras	Rat sarcoma virus homolog
RMS	Root mean square
SCC	Squamous cell carcinoma
SDE	Stochastic differential equation
TAF	Tumour angiogenic factor
TEM	Transendothelial migration
TGF-β	Transforming growth factor-β
TIMP2	Tissue inhibitor of metalloproteinase-2
TMEM	Tumour microenvironment of metastasis
uPA	Urokinase-type plasminogen activator
VEGF	Vascular endothelial growth factor
VIM	Vimentin

Chapter 1

Introduction

According to statistics published by the World Health Organization (Ferlay et al., 2015), it is highly unlikely for any person's life to—directly or indirectly—stay untouched by cancer. In 2012, there were 32.6 million people worldwide living with the disease (within five years of diagnosis), 14.1 million new cases of cancer, and 8.2 million cancer deaths. These figures show that there is an urgent need to improve our understanding of this complex disease and to enhance the effectiveness of cancer treatment.

In recent years, new technologies have allowed us to gather vast amounts of data on cancer and to gain insight into its mechanisms of evolution. This has resulted in great advances in the treatment of some of the over 200 cancer types. However, the mechanisms underlying secondary—so-called *metastatic*—tumour spread are still poorly understood. Yet, metastatic spread causes around 90% of all cancer-related deaths (Hanahan and Weinberg, 2000; Gupta and Massagué, 2006). Therefore, to improve patient survival, we must further our understanding of metastatic spread and its driving forces.

Hanahan and Weinberg (2000) attempted to systematise the immense complexity involved in the disease of cancer in their seminal paper *Hallmarks of cancer* by giving an overview of the acquired features of cancer cells that are common across all forms of cancer. Its follow-up paper *Hallmarks of cancer: the next generation* (Hanahan and Weinberg, 2011)—at the time of writing this—led the list of the most cited articles in the journal *Cell* (Elsevier B.V., 2006), indicating how influential the hallmarks of cancer are, and how well-perceived by the scientific community. One hallmark of cancer, *tissue invasion and metastasis*, is at the centre of the mathematical models proposed in this thesis.

Developing a mathematical modelling framework can enhance the understanding of the processes underpinning cancer invasion and metastatic spread. Mathematical models, in combination with biomarker diagnostics and imaging data, could then be used to individualise cancer treatment. They can aid the prediction of the disease evolution as well as the search for an optimal treatment approach for a particular patient. This approach of patient-specific therapy is described schematically in Figure 1.1.

The history of weather forecasting provides an analogy that explains how the difference between traditional and patient-specific cancer treatment emerges, *cf.* Franssen (2018). Traditionally, the only possible way to predict the future weather was to closely examine data from the past. While this is certainly preferable to spending no thought on weather prediction at all, current forecasting techniques are a lot more useful. Much of the

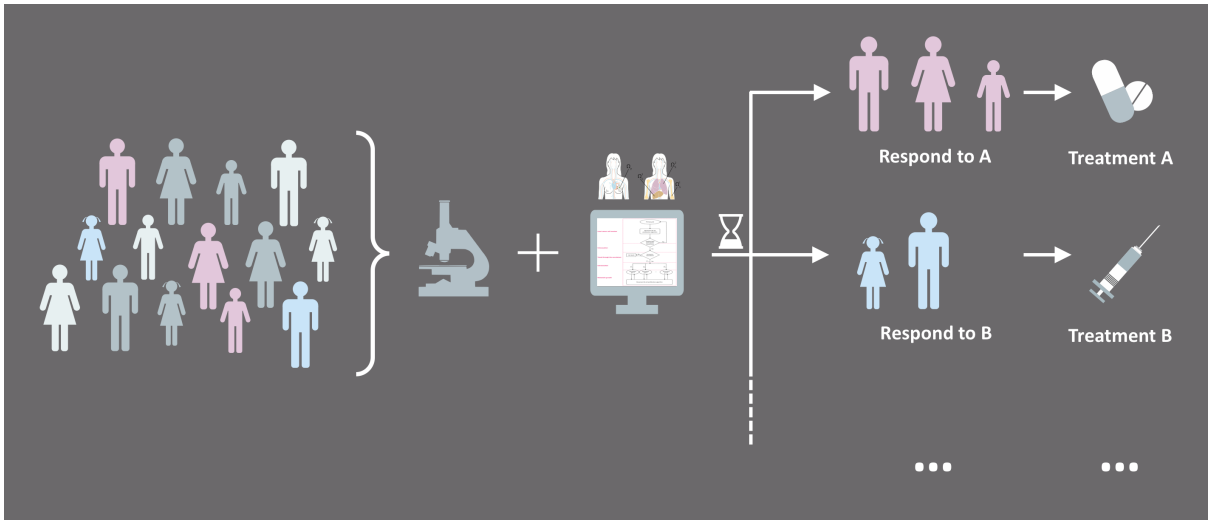

Figure 1.1: ***Personalising cancer treatment through computational modelling.*** *In a diverse cohort of cancer patients, different patients respond to different treatment approaches. Modern imaging technologies, methods image analysis and staining techniques combined with spatial, cell-based computational models like the one proposed in this paper can in the future be used to help identify the best available treatment for each cancer patient.*

accuracy of today's weather forecasting results is owed to complex computational models. These use algorithms to 'crunch' large data sets—in stark contrast to traditional weather forecasting. Similarly, clinicians traditionally have treated cancer patients by examining and classifying their type of cancer to then choose a treatment according to what has worked for patients with similar disease states in the past. This proves fruitful in a subset of patients but others either do not respond to the treatment at all, experience overall adverse effects or unexpectedly relapse after they seem to have been cured. The reason for the mixed occurrence of wanted and unwanted outcomes is that each cancer patient and each tumour has a unique genetic make-up, implying a unique response to any treatment applied.

This thesis gives examples of modelling techniques that could be further developed in order to advance cancer treatment to one where modern diagnostic techniques together with computational models are used in a clinical setting, as shown in Figure 1.1. As in the case of weather forecasting, computational models are indispensable when it comes to making future predictions from large amounts of data on a patient's disease outcome. Firstly, they give us insight into how a tumour is likely to develop. Secondly, accurate models also allow us to theoretically try out treatments in a non-invasive manner and within a short time frame. The simulation outcomes of individually parametrised relevant mathematical models for a particular patient can then inform clinicians. This enables them to choose the best possible modes of treatment, the optimal order of application, their best timing and the optimal dosage to be used.

Collaborations between clinical oncologists and mathematicians are already in place in an effort to, for instance:

- predict the response of solid tumour growth to radiotherapy, while taking into

account the effects of hypoxia and the cell cycle, as well as optimise the scheduling for combined radiotherapy-chemotherapy treatment (Powathil et al., 2013);

- optimise the efficacy of potential targeted therapies on bone metastatic prostate cancer (Cook et al., 2016);
- simulate glioma growth and invasion in an anatomically accurate brain domain (Massey et al., 2018);
- predict the optimal dosing regimen through a mathematical model of tumour uptake for cancer immunotherapy (Ribba et al., 2018).

These are only three examples of how mathematical modelling can be used to aid in a clinical setting. Because cancer is such a complex disease, the aspects that could be incorporated in physiologically accurate predictive models are vast. Focussing on separate aspects of cancer growth to subsequently build multiscale models to predict growth outcomes in particular scenarios is thus the most feasible approach.

This thesis will thoroughly examine the mathematical modelling of the ability of cancer cells to invade tissue and to spread to secondary sites in the body. To obtain physiologically realistic modelling outcomes, space is taken into account explicitly throughout.

In Chapter 2, we provide the biological foundation knowledge required to understand the invasion of cancer cells into the surrounding tissue and their metastatic spread through the body. We include a detailed description of healthy tissue dynamics and describe how its homeostasis is disturbed during cancerous growth by considering the *hallmarks of cancer*, *cf.* Hanahan and Weinberg (2000, 2011). We continue by explaining invasion and metastatic spread—the hallmark of cancer the models in this thesis are concerned with—in detail. In particular, we highlight the role of *epithelial-mesenchymal transition* (EMT) and its reverse process *mesenchymal-epithelial transition* (MET) in the invasion-metastasis cascade. Finally, we describe an *in vitro* invasion study that we later simulate using the model developed in Chapter 6.

In Chapter 3, we review existing models of cancer invasion and metastasis. The former includes both spatially local and non-local models and the latter models that describe the acquisition of a metastatic phenotype in cancer cells as well as those that investigate metastatic growth dynamics.

In Chapter 4, we present a mathematical modelling framework that captures for the first time the interconnected processes of invasion and metastatic spread of individual cancer cells in a spatially explicit manner—a multi-grid, hybrid, individual-based approach. This framework accounts for the spatiotemporal evolution of mesenchymal- and epithelial-like cancer cells, *membrane-type-1 matrix metalloproteinase* (MT1-MMP) and the diffusible *matrix metalloproteinase-2* (MMP-2), and for their interactions with the extracellular matrix. Using computational simulations, we demonstrate that our model captures all the key steps of the invasion-metastasis cascade, i.e. invasion by both heterogeneous cancer cell clusters and by single mesenchymal-like cancer cells; intravasation of these clusters and single cells both via active mechanisms mediated by *matrix-degrading enzymes* (MDEs) and via passive shedding; circulation of cancer cell clusters and single cancer cells in the vasculature with the associated risk of cell death and disaggregation of clusters; extravasation of clusters and single cells; and metastatic growth at distant

secondary sites in the body. By faithfully reproducing experimental results, our simulations support the evidence-based hypothesis that the membrane-bound MT1-MMP is the main driver of invasive spread rather than diffusible MDEs like MMP-2.

In Chapter 5, we extend the metastasis model introduced in Chapter 4 to account for the roles of EMT and MET in the invasion-metastasis cascade. In addition to cancer cells of epithelial and of mesenchymal phenotype, we now also include those of an intermediate partial-EMT phenotype. Furthermore, we allow for the switching between these phenotypic states via EMT and MET at the biologically appropriate steps of the invasion-metastasis cascade. Finally, we account for the adaptivity of cancer cells to the tissue microenvironment in an organ-specific manner and differentiate between the tissues of the organs involved in the simulations. This way, we create a first multi-organ mathematical model that explicitly accounts for EMT processes in individual cancer cells in the context of the invasion-metastasis cascade.

In Chapter 6, we introduce a three-dimensional mathematical model to describe the transition from collective to individual cancer invasion strategies by formulating a coupled hybrid system consisting of partial and stochastic differential equations that describeas the evolution of epithelial-like and mesenchymal-like cancer cells.

In Chapter 7, we provide perspectives on how the models introduced in this thesis could be developed further. The extensions of the metastasis modelling framework introduced in Chapters 4 and 5 are discussed jointly. As a particular extension to this modelling framework, an *evolutionary game-theory* (EGT) approach to capturing interactions of cancer cells of different phenotypes in various tumour-microenvironments is introduced in the form of an initial model. Samples of the dynamics of interactions between cancer cells of various phenotypes in different microenvironments are presented through simulation results. Finally, ideas for extensions to the three-dimensional hybrid-continuum model of EMT-/MET-dependent cancer cell invasion from Chapter 6 are outlined.

Chapter 2

Cancer invasion and metastasis: Biological background

Throughout this thesis, we will focus on *solid tumours*—and, in particular, *carcinomas* as a subcategory of solid tumours. Solid tumours are all tumours that usually do not contain liquid areas or cysts. Differing by the tissue they have arisen from, carcinomas, lymphomas, and sarcomas are examples of solid tumours, whereas leukemias generally are not (Urs et al., 2008; National Cancer Institute, 2017). Carcinomas are the subclass of solid tumours that arise from epithelial tissue, as we further explain in Section 2.1.1. They constitute between 80% and 90% of all cancer cases (Institute, 2017) and they account for over 80% of cancer-related deaths in the Western world.

We will start by outlining the composition of healthy tissue and explain how homeostasis is maintained in Section 2.1. We proceed by describing how tumours are classified and which capabilities their cells have acquired that allow them to proliferate and thrive. In Section 2.2, we take a closer look at the ten *hallmarks of cancer*. Tissue invasion and metastasis are two of these acquired capabilities by cancer cells, which are so closely linked that they are summarised as one hallmark of cancer. This hallmark is central to the mathematical models reviewed in Chapter 3. Moreover, it is the centrepiece of our mathematical models proposed in Chapters 4, 5 and 6. Accordingly, in Section 2.3, we will explain the underlying biology of the so-called *invasion-metastasis cascade* in more detail. In Section 2.4, we explore the roles of EMT and MET in cancer invasion and metastatic spread. This provides further biological background information for the models introduced in Chapters 5 and 6. Finally, in Section 2.5, we explore an *in vitro* invasion study by Nurmenniemi et al. (2009). This builds the foundation for the three-dimensional hybrid discrete-continuum model of EMT-/MET-dependent cancer cell invasion presented in Chapter 6—there we use this hybrid model to predict the organotypic invasion assay results from these experiments.

The content of this section draws its information primarily from Hanahan and Weinberg (2000, 2011) as well as from Chapters 5, 8 and 13 of the textbook *The biology of cancer* by Weinberg (2013).

2.1 Healthy tissue

Traditionally, research biologists have considered the entities which tissue consists of separately or in smaller functional units when studying them. This approach has advanced science greatly but, by the end of the twentieth century, it had become increasingly clear that healthy and cancerous tissue is more than the sum of disconnected functional units. Today, it is broadly accepted that, in order to understand tissue, we need to study it as an ecosystem that accounts for the interaction of different cell types and the stroma.

2.1.1 Epithelial and connective tissue

There are four types of tissue arising in all vertebrates (McGuire and Beerman, 2012; Starr et al., 2010):

- *epithelial tissue*, which covers and lines organs, cavities and body surfaces such as the intestines or the skin;
- *connective tissue*, which connects body parts and grants stability;
- *muscle tissue*, which is essential for movement; and
- *nervous tissue*, which can detect stimuli and transfer information.

Epithelial tissue and connective tissue typically grow adjacent to one another, separated by a thin, tough layer *called basal lamina*, as Figure 2.1 demonstrates. Following Chapter 20 of *Essential Cell Biology* by Alberts et al. (2013), we now consider the architecture of these tissues more closely.

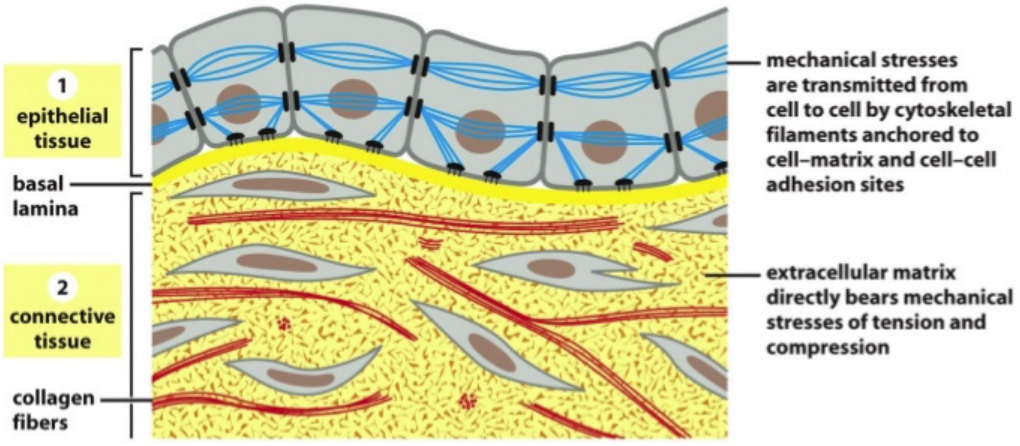

Figure 2.1: ***Schematic cross-section through the epithelium and adjacent connective tissue.*** *The top-most epithelial tissue consists of epithelial cells (grey) connected by cadherins (black). These cells bind to the underlying connective tissue via integrins (black). The connective tissue consists of ECM (yellow), collagen fibres (red) and fibroblasts (brown) (Alberts et al., 2013). Reproduced with permission from Garland Science/ Taylor & Francis LLC.*

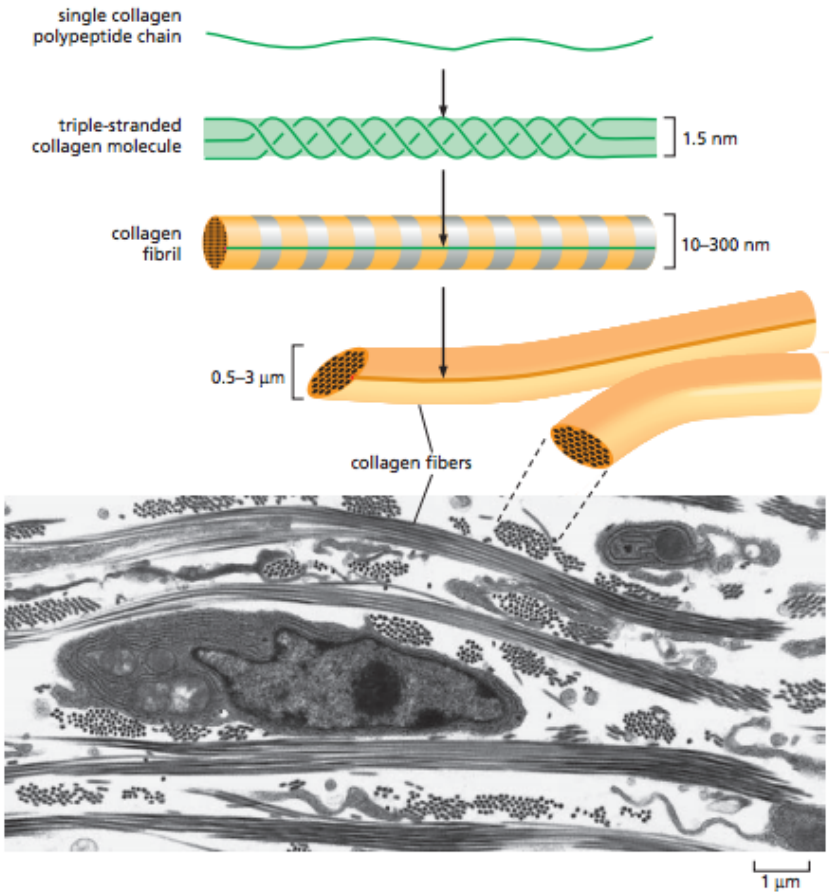

Figure 2.2: ***Collagen fibre composition.*** *The top shows a schematic description of collagen fibre composition. The electron micrograph of embryonic chick skin tissue at the bottom, originally published in Ploetz et al. (1991), corresponds to the schematic description of connective tissue in Figure 2.1. Collagen fibres run through the connective tissue with an angle of approximately* 90° *between them. The fibroblast cell in the centre secretes collagen and other ECM macromolecules (Alberts et al., 2013). Reproduced with permission from Garland Science/Taylor & Francis LLC.*

As illustrated in Figure 2.1, cells in the *epithelial tissue*, which lines all internal cavities in the body and covers external surfaces such as the skin, are tightly linked to one another by junctions since they function as a barrier. Epithelial tissue sheets can be *simple*, i.e. only one cell layer thick—as the one depicted in the schematic representation in Figure 2.1—or *stratified*, meaning that they are many cell layers thick, as in the epidermis. They are only selectively permeable, which allows them to export waste and uptake nutrients; to keep some molecules out while letting others in; to prevent fluid loss and the invasion of microorganisms; and to detect environmental signals with their receptors.

Epithelial cell junctions have a variety of functions such as providing strong mechanical attachment of the epithelial cells, ensuring leakproofness, and enabling chemical communication. They can be classified according to the binding proteins involved:

- *Adherens junctions* and *desmosomes* bind epithelial cells to one another. Their corresponding transmembrane proteins belong to the family of *cadherins* and bind

to identical cadherin molecules of their neighbouring cells. In Figure 2.1, these cadherins are shown in black between the epithelial cells.

- *Hemidesmosomes* bind epithelial cells to the basal lamina by proteins called *integrins*. In Figure 2.1, integrins are represented in black where the epithelial tissue meets the basal lamina.

The ability of cells to adhere to one another via hetero- and homophilic bonds together with their ability to adhere to the ECM gives healthy tissue its stability and shape.

The *basal lamina*—a thin, tough layer consisting of ECM—is attached to the epithelial tissue by integrins. It is mainly composed of a protein called *laminin*, to which the integrins of epithelial cells can adhere, as well as of type-IV collagen.

While epithelial tissue consists mainly of cells, the basal lamina and connective tissue predominantly consist of ECM. The ECM is a mesh of secreted proteins and other molecules that surrounds most cells in tissues and provides structure for the spaces between cells. This matrix constantly undergoes remodelling according to the environment's demand. This ensures that, for example, in a wound or during development the rate of remodelling is comparatively high.

Connective tissue, as depicted in Figure 2.1, consists predominantly of ECM. Scattered into the ECM of connective tissue are cells called *fibroblasts* (or *osteoblasts* in the bone). They produce ECM macromolecules and collagen. This strength varies depending on which type and quantity of collagen a tissue contains as well as on which other molecules coexist. Depending on the connective tissue composition, it can be dense and hard like in bone, flexible like in cartilage, or soft like the jelly inside of the human eye.

Throughout connective tissue, *collagen*—a fibrous protein that provides strength for the tissue—is found. It the most prominent type of protein in the human body—over a quarter of our body's protein mass is collagen. The collagen molecules themselves are typically of a long, stiff, triple-stranded helical structure as Figure 2.2 shows. Certain types of collagen further pack together into ordered polymers, *collagen fibrils*, which may or may not assemble into even thicker *collagen fibres* as in the case of our connective tissue cross-section in Figure 2.1.

2.1.2 Ensuring tissue homeostasis

To assure adequate tissue composition, or *homeostasis*, appropriate proportions of cell types within the tissue need to be maintained, superfluous and damaged cells discarded, and missing cells replaced. To describe how this is achieved in healthy tissue, we will first explain how growth signals are transmitted to cells and then examine proliferation—the balance between cell loss from cell differentiation or cell death and cell divisions—itself more closely.

Highly effective regulatory circuits control proliferation, and thus ensure homeostasis, in healthy tissue environments. The quantity and quality at which growth-promoting *mitogenic factors* are produced in the tissue and released is tightly regulated by feedback mechanisms—as a result of intercellular communication of neighbouring cells of various types. Once released, these growth-promoting signals initiate and steer the *cell growth-and-division cycle* (or *cell cycle*), which is depicted schematically in Figure 2.3. In the absence of these mitogenic growth signals, the vast majority of normal cells will not

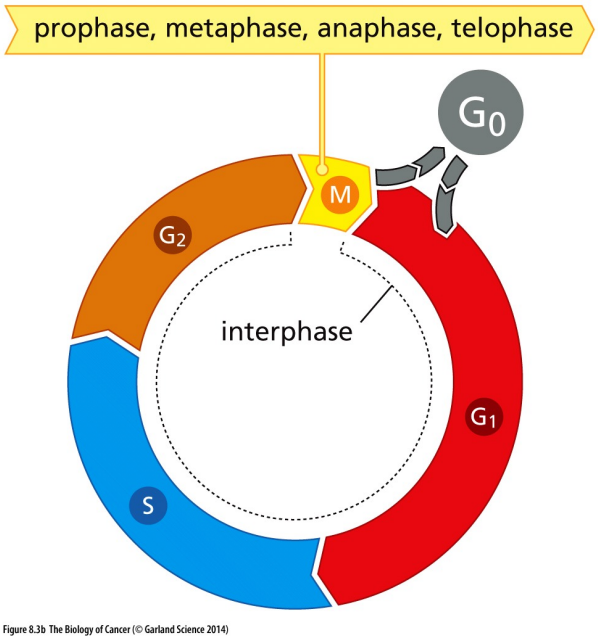

Figure 2.3: ***The cell cycle.*** *Schematic representation of the sequence of stages a cell passes through in preparation for cell division (Weinberg, 2013). Reproduced with permission from Garland Science/Taylor & Francis LLC.*

proliferate. However, the safety net to prevent uncontrolled proliferation in normal cells extends beyond this: Even if growth factors surround a cell, signalling proteins such as *transforming growth factor-β* (TGF-β) can inhibit proliferation by overruling mitogenic signalling. Finally, there are further extra-cellular signals that can force a cell into a post-mitotic state, implying that it will never be able to replicate again.

All these signals surrounding a cell are received by receptors on its surface—Figure 2.4 provides an impression of the complexity of this process. Figure 2.5 shows schematically how the so-called *cell cycle clock*, the master governor of decisions located in the cell's nucleus, processes these extracellular signals together with intracellular signals to decide about the cell's fate.

If—after receiving the corresponding stimulating signals—a cell is due to divide, the *cell cycle*, shown in Figure 2.3, is initiated. This cycle is divided into four phases: In the first growth phase (G_1), the size of the cell increases. The cell then copies its DNA during the synthesis (S) phase. It prepares for division in the second growth phase (G_2) to subsequently divide in the mitotic (M) phase. The G_1, S and G_2 phase together make up the so-called *interphase*. The M phase is further divided into four stages (*prophase*, *metaphase*, *anaphase* and *telophase*) to describe phases within cell division, as shown on top of Figure 2.3. In addition to these four active phases of the cell cycle, cells can exist in an aforementioned fifth state—the quiescent (G_0) state.

Furthermore, there are highly regulated mechanisms in healthy tissue to induce the controlled cell death, so-called *apoptosis*. This process is, again, coordinated by signals, which either stem from within a cell or are delivered to its surface receptors externally.

The controlled growth dynamics described above have developed over millions of years and ensure proper tissue architecture and function. Interestingly, it remains largely obscure which mitogenic signals exactly operate in healthy tissue. The same applies to the question where their precise origins lie and by which mechanisms their release is controlled. However, it is evident that the processes involved are highly specific and regulated with regards to space and time (Hanahan and Weinberg, 2011).

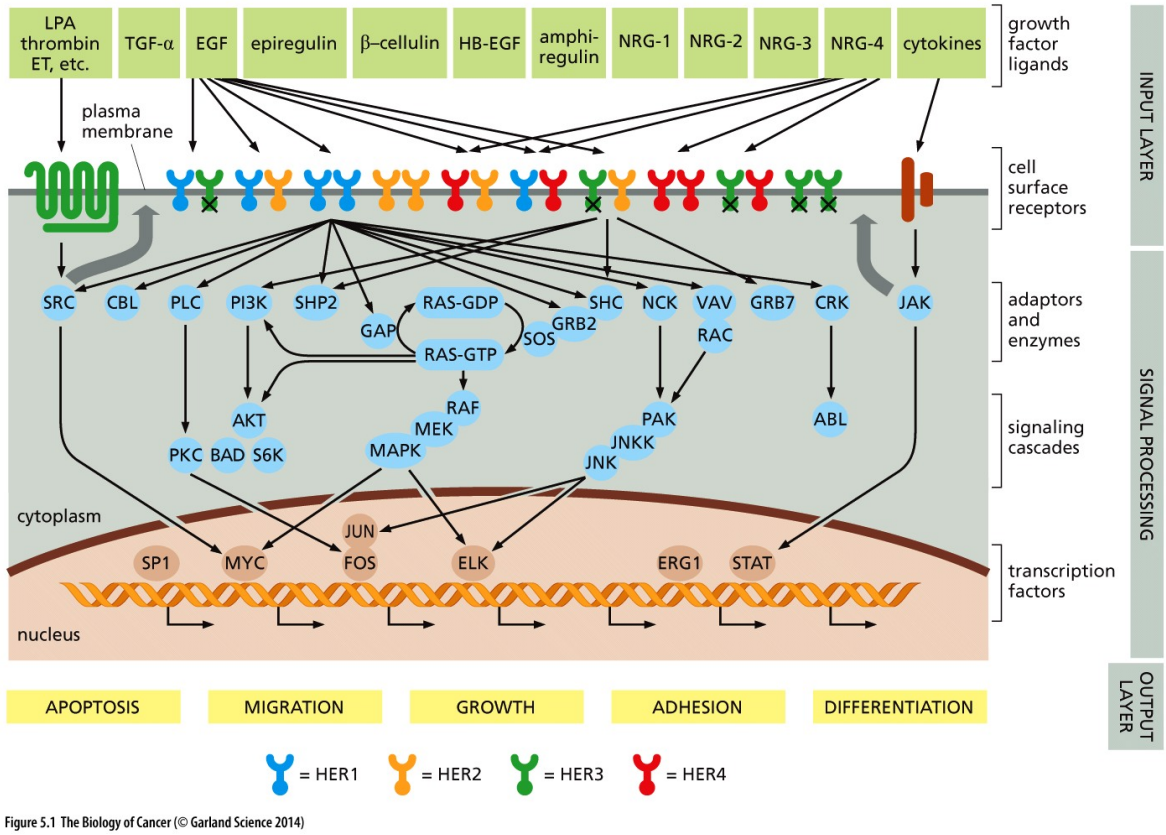

Figure 2.4: ***A schematic representation of how cells communicate with their surrounding.*** *Growth factor ligands surrounding the cell bind to receptors in the cell's surface. These deliver signals through the plasma membrane into the cytoplasm, where a complex cascade of signal-transducing proteins passes on the signals further into the nucleus. Here, the cell cycle clock shown in Figure 2.5 decides which of the responses shown in yellow at the bottom of the figure is currently required. Published in Weinberg (2013) and reproduced with permission from Garland Science/Taylor & Francis LLC.*

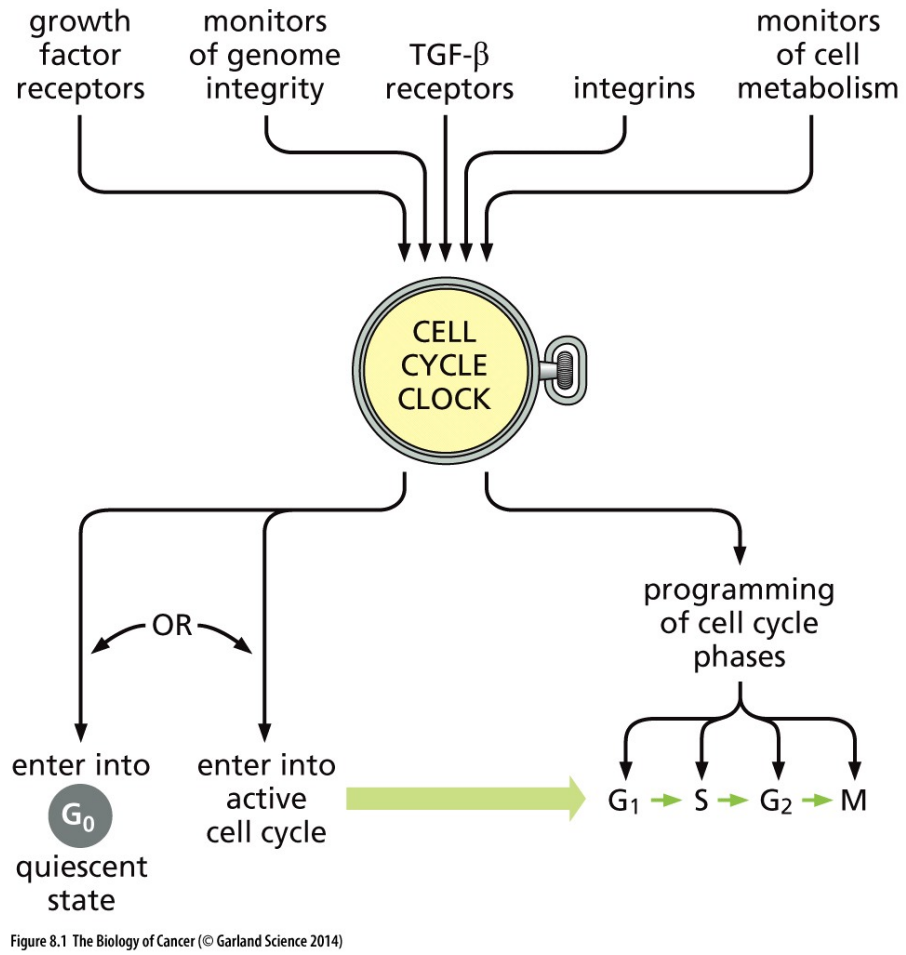

Figure 2.5: ***The cell cycle clock.*** *The master governor of decisions located in the cell's nucleus processes intra- and extracellular signals to decide whether the cell will proliferate, become quiescent or post-mitotic (Weinberg, 2013). Reproduced with permission from Garland Science/Taylor & Francis LLC.*

2.2 Cancerous tissue and the hallmarks of cancer

Most solid tumours start with mutations of key genes either in one or in a small group of the more than 10^{13} healthy cells in the human body (Bianconi et al., 2013). In carcinomas, these mutations first occur in cells of the epithelium. The resulting acquired features of these mutated cells cause an imbalance in the formerly homeostatic tissue.

Hanahan and Weinberg (2000, 2011) postulate that tumourigenesis is a multistep process, during which formerly normal cells acquire several common capabilities, the hallmarks of cancer, which make them increasingly malignant. Further, they suggest that this process is subject to Darwinian evolution in the sense that, over time, the fittest cells survive in a given tissue environment. It is hypothesised that the hallmarks acquired by successfully mutated cells grant them a competitive edge over the healthy cells in their microenvironment in this selective process.

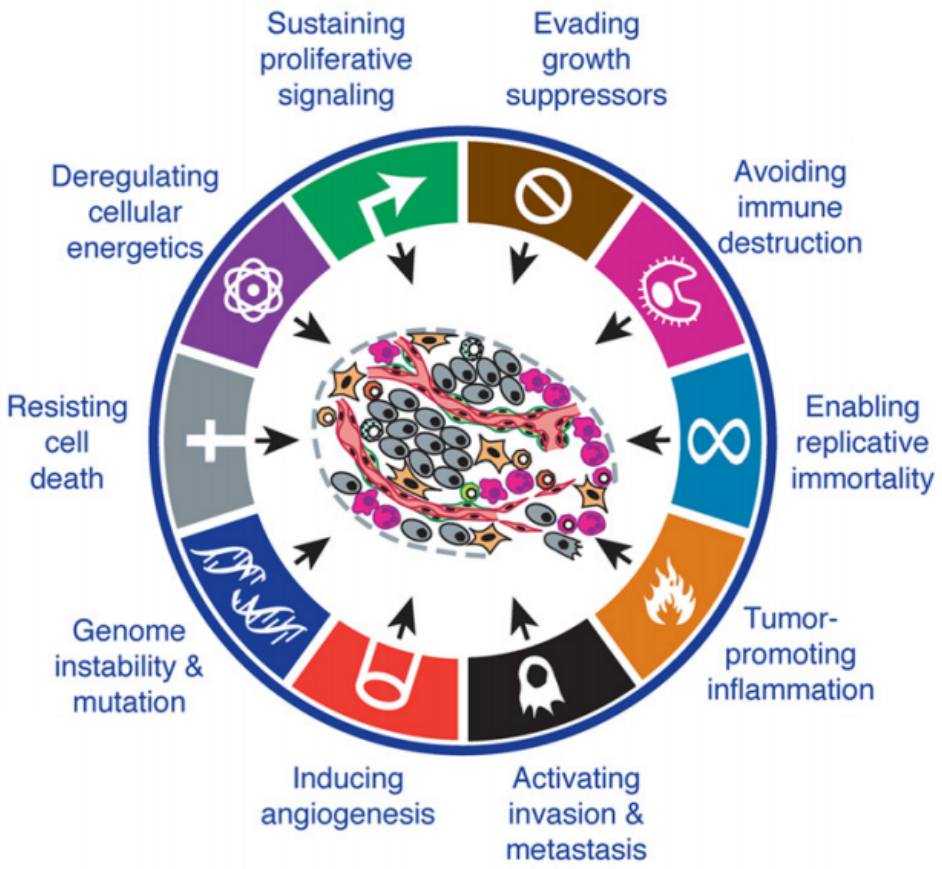

Figure 2.6: ***The eight hallmarks of cancer together with their two enabling characteristics.*** *As suggested by Hanahan and Weinberg (2000, 2011). Modified and reproduced with permission from Elsevier.*

The eight hallmarks of cancer together with two enabling characteristics suggested by Hanahan and Weinberg to date are shown in Figure 2.6. These are:

- sustaining proliferative signalling,
- evading growth suppressors,

- activating invasion and metastasis,
- enabling replicative immortality,
- inducing angiogenesis,
- resisting cell death,
- deregulating cellular energetics, and
- avoiding immune destruction.

Furthermore, two characteristics that enable the acquisition of the hallmarks in the first place are:

- genome instability and mutation, and
- tumour-promoting inflammation.

The mathematical models in this thesis examine the third hallmark in the list above, *cancer cell invasion and metastasis*. The remainder of this chapter is dedicated to explaining the involved processes in more detail.

It remains undisputed that cancer cells with a more aggressive phenotype—i.e. a phenotype with a larger number of mutation-acquired hallmarks—have a better chance at successfully invading, as suggested in Hanahan and Weinberg (2000, 2011); Weinberg (2013). Yet, the hypothesis that successful cancer cells will need to have acquired *all* hallmarks of cancer prior to their invasion and metastatic spread has recently become a subject undergoing discussion in the scientific community. Two suggested models of metastatic dissemination have been proposed—the 'traditional' linear progression model and the more recently suggested parallel progression model.

The latter model arose due to findings in carcinomas, e.g. in the breast (Hüsemann et al., 2008; Harper et al., 2016), the lung (Podsypanina et al., 2008) and the pancreas (Rhim et al., 2012), which indicated that so-called *disseminated tumour cells* (DTCs) that have spread to secondary sites in the body can be found in previously unexpectedly early stages of neoplastic transformation rather than only once the later stages of the multi-step progression of primary tumours are reached. Yet, it is currently unclear whether, as assumed by the parallel progression model, these detected early DTCs ever become potent enough to develop into full-blown malignant metastatic tumours.

The linear progression model denies that this is possible. It proposes that, since successfully metastasising cancer cells disseminate at late stages of the primary tumour formation, the degree of genetic divergence between successful DTCs and the tumour at the metastatic site is small.

While there are arguments and evidence for and against either theory, *cf.* Lambert et al. (2017) and the references therein) neither hypothesis can be proven to hold exclusively at present. Indeed, a current review of comparative genomic studies between primary and secondary tumours by Turajlic and Swanton (2016) concluded that, even within the same patient, *'the two models are not mutually exclusive and are part of a biological continuum'*.

2.3 Cancer cell invasion and metastatic spread

Abnormally rapid cell proliferation is one of the most notable results of the acquired hallmarks of cancer, which can lead to the formation of a small nodule of cancer cells. Over time, this nodule can expand, while acquiring increasingly aggressive mutations, into a full avascular tumour with a diameter of up to approximately 0.1–0.2 cm (Folkman, 1990). Further growth is limited by the diffusion of nutrients (e.g. oxygen). To expand beyond this size, cancer cells provoke the formation of new blood vessels by secreting chemicals—collectively known as *tumour angiogenic factors* (TAFs) (Folkman and Klagsbrun, 1987). This neovascularisation process is called *(tumour-induced) angiogenesis*. The resulting vasculature serves the tumour's increased metabolic needs by transporting the required nutrients. The newly formed blood vessels additionally benefit the tumour in the subsequent *vascular growth phase*, when the cancer cells become invasive so that gradients in nutrients, oxygen and ECM drive cancer cells away from the primary tumour mass. If cancer cells successfully intravasate into the newly grown blood vessels *and* survive in the vessel environment (where they are exposed to risks such as attacks by the immune system and shear stress in the blood flow), they can extravasate and relocate at distant sites in the body. At these new sites, nutrients and space are less of a limiting factor to growth. The described sequence of steps of the successful redistribution of cancer cells from a primary location to a secondary location is known as *metastatic spread*. It can lead to the formation of secondary tumours, called *metastases*, at sites in the body away from the primary tumour. In the first instance, however, the successfully extravasated cancer cells occur either as single DTCs or as small clusters of cancer cells, called *micrometastases*. These DTCs and micrometastases may remain dormant but have the potential to proliferate into vascularised metastases at the secondary sites at some later point in time. The full process described here, which is shown schematically in Figure 2.7, is also known as the *invasion-metastasis cascade* (Fidler, 2003; Talmadge and Fidler, 2010).

In what follows, we will describe the significance of the invasion-metastasis cascade and then continue by describing the steps that can enable a small primary nodule of cancer cells to spread to distant sites throughout the body and colonise there. The information is largely based on Chapter 14 of Weinberg (2013), unless stated otherwise.

2.3.1 Why invasion and metastasis matter

Expanding and deepening our understanding of the invasion-metastasis cascade is of vital importance in order to e.g. increase cancer patient survival. Approximately 10% of cancer-related deaths are caused by often asymptomatic primary tumours alone that, for example, have grown to a size at which they affect organ function by exerting physical pressure. Locations where obstructions by primary tumours typically turn problematic are the lungs, the liver, the pancreas and the colon. If detected early, many localised primary tumours can be treated successfully, e.g. by resection or chemotherapy. An incentive for modelling local tumour invasion is, for example, that to prevent a relapse after excision of a detected tumour, as little as possible healthy tissue but all cancerous tissue should be removed. At the time of writing this, the gold-standard histopathology techniques consist of post-operatively processing and staining tissue samples to then embed them in wax blocks before cutting them into slim slices to be able to mount

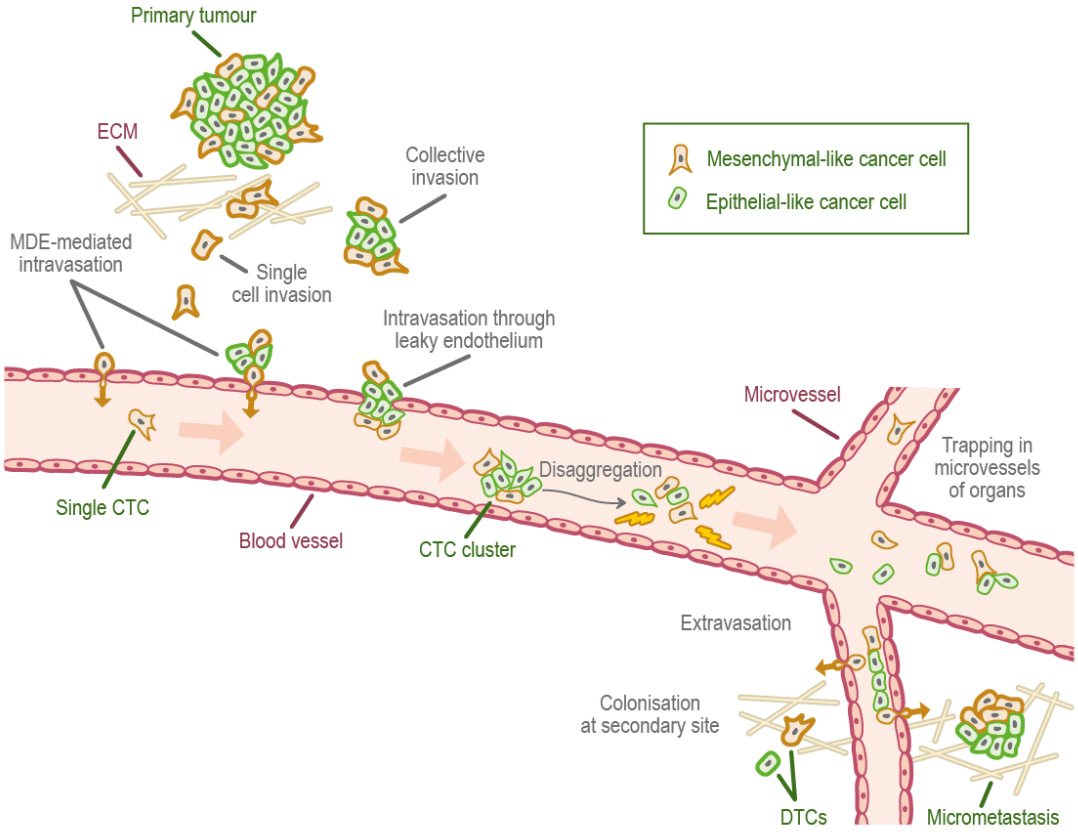

Figure 2.7: ***A schematic overview of the invasion-metastasis cascade.*** *Single mesenchymal-like cancer cells and heterogeneous clusters of mesenchymal- and epithelial-like cancer cells break free from the primary tumour and invade the surrounding tissue (top left). They can intravasate via active MDE-mediated and passive mechanisms (upper left, epithelium of vessel). Once in the vasculature,* circulating tumour cell *(CTC) clusters may disaggregate (centre) and CTCs may die. Surviving cells may extravasate via the walls of the microvasculature to various secondary sites in the body. Successful colonisation there is rare but can result in either DTCs or micrometastases (bottom right), which have the potential to develop into full-blown metastases.*

them on slides. These stained two-dimensional slices are then viewed using traditional microscopes. This process typically takes days. Hence, the surgery team will only post-operatively have a better idea of whether they have excised sufficient tissue. Mathematical models of local cancer invasion may, for instance, aid the estimation of the tissue to be resected—see e.g. Anderson et al. (2000).

Although this alone is an incentive to model cancer growth, it is to be noted that the other 90% of cancer-related deaths arise due to metastases growing at distant sites away from the primary tumour (Hanahan and Weinberg, 2000; Gupta and Massagué, 2006). This is because once cancer cells have begun to spread throughout the body, it becomes increasingly difficult to detect them. DTCs and secondary (micro-)metastases also typically consist of more aggressive phenotypes, making it increasingly difficult to treat a patient at this stage. Hence prognosis is often very poor. Besides, metastasis *'remains the most poorly understood component of cancer pathogenesis'* according to Chaffer and

Weinberg (2011).

Mathematical modelling can be a useful tool to capture and unravel the complexity of the invasion-metastasis cascade by enhancing our insight into details that are currently not fully understood. Ultimately, resulting predictive models may also help to advance treatment success through personalised medicine directly if they are used in a clinical setting to inform oncologists.

2.3.2 Local cancer cell invasion

When the cancer cells are invading the tissue surrounding the primary tumour, they have to overcome structural obstacles. The cells need to make their way through the fairly rigid ECM, which mainly consists of various tissue-bound macromolecules such as structure-providing collagens (mainly of type-I), as well as of fibronectin, vitronectin and laminin, which influence the spreading, motility and adhesion of cancers cells. Often, the cancer cells additionally have to penetrate the even more rigid basal laminae of blood vessels and potentially of the primary sites they originate from.

The two main mechanisms used by cancer cells to overcome these hurdles, which have been discussed in detail by, for example, Friedl and Wolf (2003), are *protease-dependent* and *protease-independent* invasion.

Protease-dependent invasion earns its name from collagen-cleaving proteinases, and more specifically MDEs. MDEs are involved in the non-pathogenic remodelling of healthy tissue but are overexpressed by some cancer cell types. The cleaving of collagen allows all types of cancer cells to subsequently invade along the paths created. Hundreds of proteolytic enzymes have been identified in the human genome to date. Two types of such proteolytic enzymes over-expressed in cancer cells are *urokinase-type plasminogen activator* (uPA) and *matrix metalloproteinases* (MMPs), a family of zinc-dependent endopeptidases MDEs (Egeblad and Werb, 2002). MMPs consist of 23 proteolytic enzymes (Jackson et al., 2010) and are able to degrade the vast majority of surrounding tissue in humans (Kleiner and Stetler-Stevenson, 1999). While some members of the MMP family paradoxically have been shown to prevent tumour invasion in animal models (Noël, 2012), we will focus on those which definitely aid cancer cell invasion. Amongst these, we further distinguish between *soluble* MMPs, like MMP-2 or MMP-9, which the cancer cells secrete into the surrounding ECM, and six *membrane-bound* MMPs (MT-MMPs) MT1-/MT2-/MT3-/MT4-/MT5-/MT6-MMP, which remain attached to the cell membrane. Amongst the latter, MT1-MMP (also known as MMP-14) has, to our knowledge, been investigated most to date (Itoh, 2015). It has been shown that this membrane-bound MMP plays a key role in both cancer cell invasion through interstitial type-I collagen tissues and the breaching of cancer cells through basement membranes, which mainly consist of type IV collagen (Mook et al., 2004; Poincloux et al., 2009). MMP-2 and MMP-9 are well-investigated soluble MMPs with the ability to degrade the similar types of tissue, except for type IV collagen (Itoh, 2015). Apart from in their active form, both exist in their inactive forms *pro-MMP-2* and *pro-MMP-9*. For the activation of MMP-2—the soluble MMP we will focus on throughout the rest of the thesis—two MT1-MMP monomers and *tissue inhibitor of metalloproteinase 2* (TIMP2), which belongs to a family of four protease inhibitors that can collectively inhibit all known MMPs, is needed. The formation of a complex of a MT1-MMP dimer, TIMP2 and pro-MMP-2 allows for MMP-2 activation,

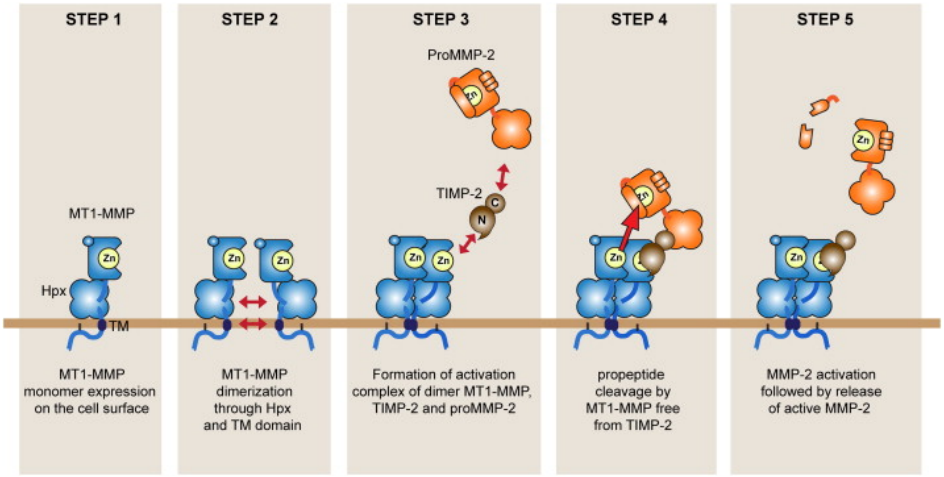

Figure 2.8: ***MMP-2 activation by MT1-MMP.*** *A complex of a MT1-MMP dimer, TIMP2 and pro-MMP-2 is required to activate MMP-2. Reproduced from Itoh (2015) under Creative Commons License.*

as Figure 2.8 shows in more detail.

Protease-independent invasion relies on cancer cells changing from a mesenchymal-like to an amoeboid-like shape—a process called *mesenchymal-amoeboid transition*. This increases the morphological plasticity of the cells and enables them to squeeze through the collagen-like pores, rather than needing to solely rely on ECM degradation.

It has been shown by Sabeh et al. (2009) that cancer cells cannot migrate unless the proteinases have cleared the collagen prevalent in normal tissue of its covalent cross-links, and that protease-dependent invasion on its own is a sufficient invasion mechanism. In their experiments, multicellular spheroids of HT-1080 fibrosarcoma cells were embedded in three-dimensional gels of native type-I collagen in order to create conditions reflecting those found in interstitium of the human body. As can be seen in the panels in the left column of Figure 2.9, the HT-1080 cancer cells successfully invaded the surrounding ECM within three days by using soluble MMP-1 and MMP-2, as well as membrane-bound MT1-MMP to cleave the type-I collagen. Silencing MMP-1 and MMP-2 simultaneously still resulted in cancer cell infiltration in a 'starburst' fashion, as shown in the second column of panels in Figure 2.9. Silencing MT1-MMP, however, resulted in the failure of ECM invasion over the three days, as shown in the third column. Only by electroporating MT1-MMP-silenced cancer cells with an expression vector for *mouse* MT1-MMP, which is resistant to the silencing mechanism of human HT-1080 cells, the cancer cells became invasive again. These results were further found to extend to experiments where actual human mammary gland explants were used instead of reconstituted cross-linked collagen gels. Again, both MDA-MB-231 and SUM-159 breast cancer cells invaded into the stromal microenvironment of the initial tumour extensively within three days in the cases of no silencing and of simultaneous MMP-1- and MMP-2-silencing but not in the case of MT1-MMP-silencing (unless counteracted by mouse MT1-MMP). Invasion distances of breast cancer cells into the surrounding tissue in each case are shown in Figure 2.10.

In the context of the study, it was found that protease-dependent invasion is necessary and sufficient for cancer cell invasion. Hence, we focus solely on this mechanism throughout the rest of this thesis.

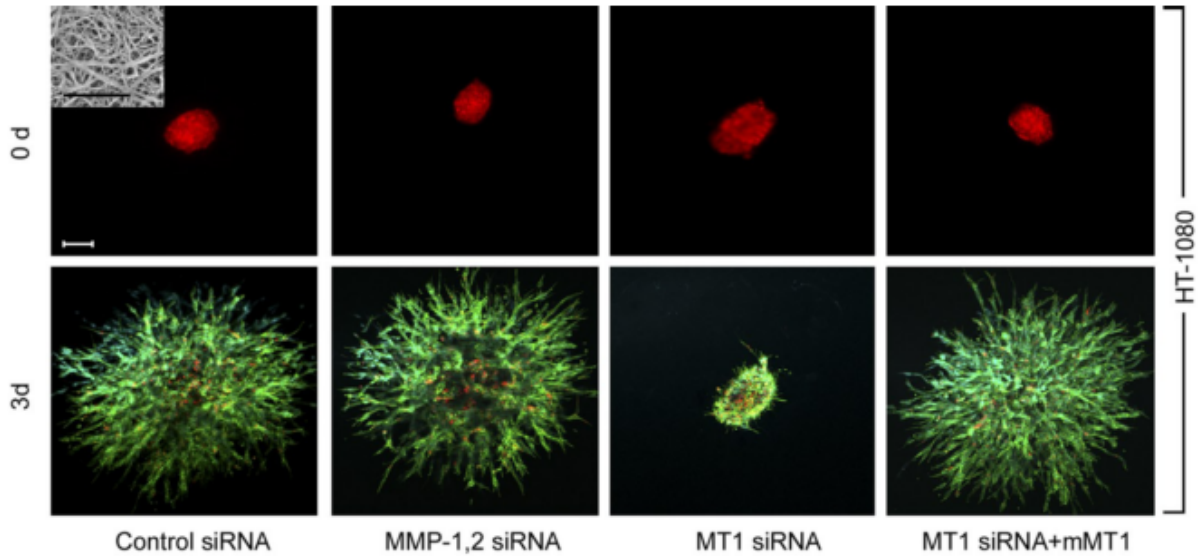

Figure 2.9: ***Invasion of multicellular spheroids of HT-1080 fibrosarcoma cells into 3D gels of native type-I collagen.*** *Over a three day period, the HT-1080 cells successfully infiltrated the ECM without silencing of MMPs but also when MMP-1 and MMP-2 are silenced simultaneously, as the first two columns show, respectively. When MT1-MMP is silenced, cancer cells cannot invade (third column) unless this silencing is counteracted by mouse MT1-MMP, which escapes the human-specific MT1-MMP siRNA introduced in the third column. Modified and reproduced from Sabeh et al. (2009) with permission from Rockefeller University Press.*

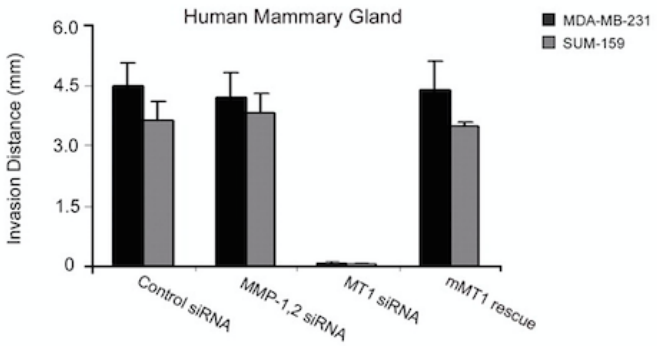

Figure 2.10: ***Invasion of MDA-MB-231 and SUM-159 breast cancer cells into human mammary gland explants.*** *In real human breast tissue, the pattern regarding invasion distance of two types of cancer cells into the ECM is the same as that of HT-1080 cells invading into reconstituted gels in Figure 2.9. Modified and reproduced from Sabeh et al. (2009) with permission from Rockefeller University Press.*

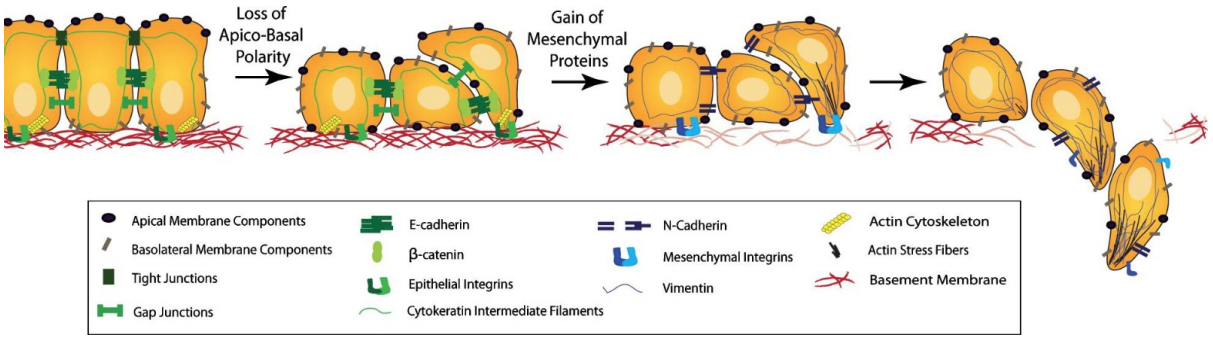

Figure 2.11: ***Schematic representation of EMT (left to right).*** *As an outcome of EMT, the cell-cell adhesion, which is predominantly enforced via E-cadherin, gap junctions and tight junctions between formerly epithelial-like cancer cells, is reduced together with their expression of epithelial integrins. These are replaced by the expression of cell-matrix adhesion-enhancing molecules like N-cadherin and integrins that are specific to extracellular components on the cell membrane. Moreover, the actin cytoskeleton remodels into stress fibres that accumulate at the areas of cell protrusions. Also, epithelial cytokeratin intermediate filaments are increasingly replaced by vimentin. This combination of changes enhances invasiveness. Further, cancer cells become more potent at degrading the basement membranes of organs and vessels, as shown towards the right of the figure, as well as the ECM in general. This allows the mesenchymal-like cancer cells to invade the surrounding stroma. During MET, which is explained graphically by reading the figure from right to left, these phenotypic changes are reversed. Reproduced from Micalizzi et al. (2010) with permission from Springer.*

Cancer cells of two phenotypes are often distinguished—epithelial-like cancer cells and mesenchymal-like cancer cells. These cancer cell types arise due to an observed tradeoff between a cell's invasiveness and its ability to proliferate, also known as the *go-or-grow dichotomy*, which was observed in the context of astrocytomas, a type of brain cancer originating in a particular kind of glial cell called *astrocyte* (Giese et al., 1996; Tamaki et al., 1997; Khoshyomn et al., 1999). The mesenchymal-like cancer cells resemble mobile cells in embryo development and are therefore more motile. These cancer cells can invade and intravasate individually. Due to their loss of cell-cell adhesion as well as their expression of MDEs. Epithelial-like cancer cells, on the other hand, cannot invade effectively without the coexistence of MDE-secreting mesenchymal-like cancer cells. This is because cancer cells with an epithelial-like phenotype do not express MDEs. They are also comparatively less motile. However, the epithelial-like cell type is more proliferative and its role should not be ignored in the invasion-metastasis cascade. Also, mesenchymal-like cancer cells have been suggested to be able to develop from epithelial-like cancer cells via a process termed the *epithelial-mesenchymal transition* (EMT) (Kalluri and Weinberg, 2009), which is shown schematically in Figure 2.11 and explained in detail in Carragher et al. (2006); Friedl and Wolf (2003); Gadea et al. (2008); Wolf et al. (2003a,b, 2007). The reverse process, *mesenchymal-epithelial transition* (MET), is additionally hypothesised to be involved in metastatic spread, for instance by contributing to the colonisation of DTCs at secondary sites (Gunasinghe et al., 2012). Section 2.4 elucidates the role of EMT and MET, and of the resulting cell phenotypes, in each of the steps of the invasion-metastasis

cascade in further detail.

Mesenchymal-like and epithelial-like cancer cells have been observed to invade most effectively in a setting where both cancer cell types are present. This gives rise to the hypothesis of a second protease-dependent invasion mechanism in addition to mesenchymal-like cancer cells invading individually. Friedl et al. (2012), amongst others, have shown that *collective migration* of cohesive cell cohorts is an important invasion mechanism for cancer cells. The theory is that clusters consisting of cancer cells of heterogeneous phenotypes may invade the ECM together. Figure 2.7 shows the invasion of single mesenchymal-like cells versus collective groups of cells.

2.3.3 Intravasation

Once suitably mutated single cancer cells and oligoclonal clusters derived from the same primary tumour (Aceto et al., 2014) have invaded the tissue far enough to find themselves adjacent to a lymph or blood vessel (whether in the form of or individually), they can potentially intravasate into the blood system through the basal laminae of blood vessels. The exact mechanism of intravasation into the vasculature is still unclear, mainly because it shows to be difficult to establish tumour models in which intravasation and cancer cell shedding can be observed (Bockhorn et al., 2007). While there is experimental evidence suggesting that a subset of cancer cell lines may only be able to access the blood vessels indirectly via prior intravasation into the lymph vessels, the spread to distant sites in the body ultimately happens by dissemination through the blood vessels (Wong and Hynes, 2006; Lambert et al., 2017). Also, two main intravasation modes —*active* versus *passive* intravasation—are proposed in the biological literature. These are likely not mutually exclusive (Cavallaro and Christofori, 2001; Bockhorn et al., 2007; Jie et al., 2017). The *active* intravasation hypothesis postulates that cancer cells crawl towards and into vessels actively with the help of MDEs while being led by chemokine and nutrient gradients. *Passive* intravasation, on the other hand, implies a more accidental shedding of cancer cells via newly formed immature vessels, which are fragile and may collapse due to trauma or under the physical pressure caused by rapid tumour expansion.

The following overview of evidence for active and passive mechanisms in cancer cell intravasation was collected by Bockhorn et al. (2007). It highlights that there exists evidence for both the active and passive intravasation hypothesis. In Bockhorn et al. (2007), each of the bullet points below is supported by up to five studies.

Evidence for active intravasation:

- cytoskeletal activity associated with metastasis;
- integrin upregulation involved in metastasis;
- accumulation of mutations needed for metastasis;
- transient, microenvironment-induced changes in gene profile;
- MMPs produced by metastatic cells;
- tumour microenvironment can induce migration-related pathways via hypoxia and other stresses.

Evidence for passive intravasation:

- most shed cells are non-viable;
- shed cells are not clonogenic;
- blood vessels have fragile walls;
- solid stress collapses vessels;
- loss of cell-cell and cell-matrix adhesion associated with shedding and metastasis;
- tumour microenvironment confers survival advantages to random cells via hypoxia and other stresses.

A particular focus of this thesis is the role of mesenchymal-like cancer cell phenotypes in contrast to epithelial-like phenotypes—Can cells of one phenotype intravasate without the presence of the other?

A study by Tsuji et al. (2009), the results of which are visually explained in Figure 2.12, sheds some light on this question. Using a mouse model, the study examined cancer cells that had undergone EMT—and were thus of mesenchymal phenotype—and cancer cells of epithelial phenotype with regards to their intravasation success. Successful intravasation was measured as the cells' ability to penetrate blood vessels once they had been transplanted into the mice subcutaneously. While tumours consisting of mesenchymal-like cancer cells only were able to intravasate (top row of Figure 2.12), those consisting of epithelial-like cancer cells only were not (third row of Figure 2.12). Simultaneous subcutaneous injection of the two cell types resulted in successful intravasation of both cell types (fifth row of Figure 2.12).

The difference between mesenchymal-like and epithelial-like cancer cells, as described in Section 2.3.2 together with the above-explained differentiation between active and passive intravasation gives rise to three entry modes of cancer cells into the vasculature. These are further explained in Francart et al. (2018):

- Single MDE-expressing mesenchymal-like cancer cells actively enter the blood vessels and thereafter disseminate as single *circulating tumour cells* (CTCs).
- Cancer cells of epithelial and of mesenchymal phenotype cooperate in the sense that mesenchymal-like cancer cells allow epithelial-like cancer cells to enter the vasculature together with or shortly after them. Mesenchymal-like cells express the MDEs required to degrade the vessels' basal laminae. This allows for co-invasion of the epithelial-like cancer cells in the vicinity. Thus, both mesenchymal-like and epithelial-like cancer cells enter the blood system jointly as a cluster.
- Any single cancer cell or cancer cell clusters near a ruptured blood vessel intravasate via the passive entry mode.

These entry mechanisms are depicted—left to right—in Figure 2.7 along the upper left blood vessel wall.

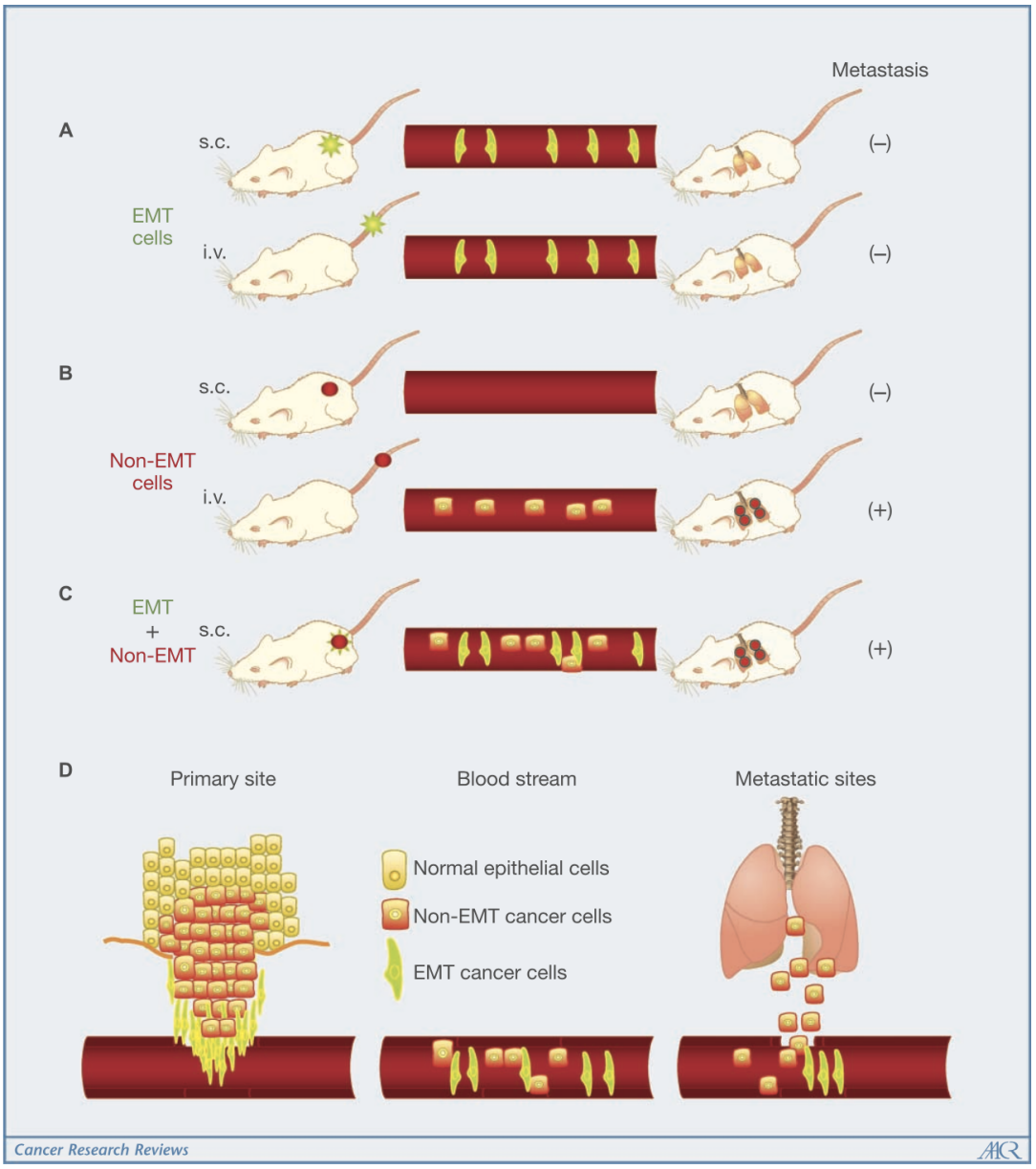

Figure 2.12: ***Visual representation of results from mouse model by Tsuji et al. (2009) suggesting synergetic effects of cells of mesenchymal and epithelial phenotypes in metastatic spreading.*** *(A) Mesenchymal-type cells alone did intravasate into the bloodstream but did not form lung metastases; (B) Epithelial-type cells alone were unable to intravasate but, if injected directly into the bloodstream, could extravasate and metastasise; (C) Jointly subcutaneously injected epithelial-like and mesenchymal-like cells invaded the tissue locally, intravasated, extravasated and successfully colonised as metastases; (D) Proposed synergetic model of cancer cell metastasis: Mesenchymal-like cells invade into surrounding tissue clearing the path for cells of epithelial phenotype to invade and intravasate. Cell types jointly enter the circulation but only the epithelial-like cancer cells can successfully colonise at distant organs. Reproduced from Tsuji et al. (2009) with permission from the American Association for Cancer Research.*

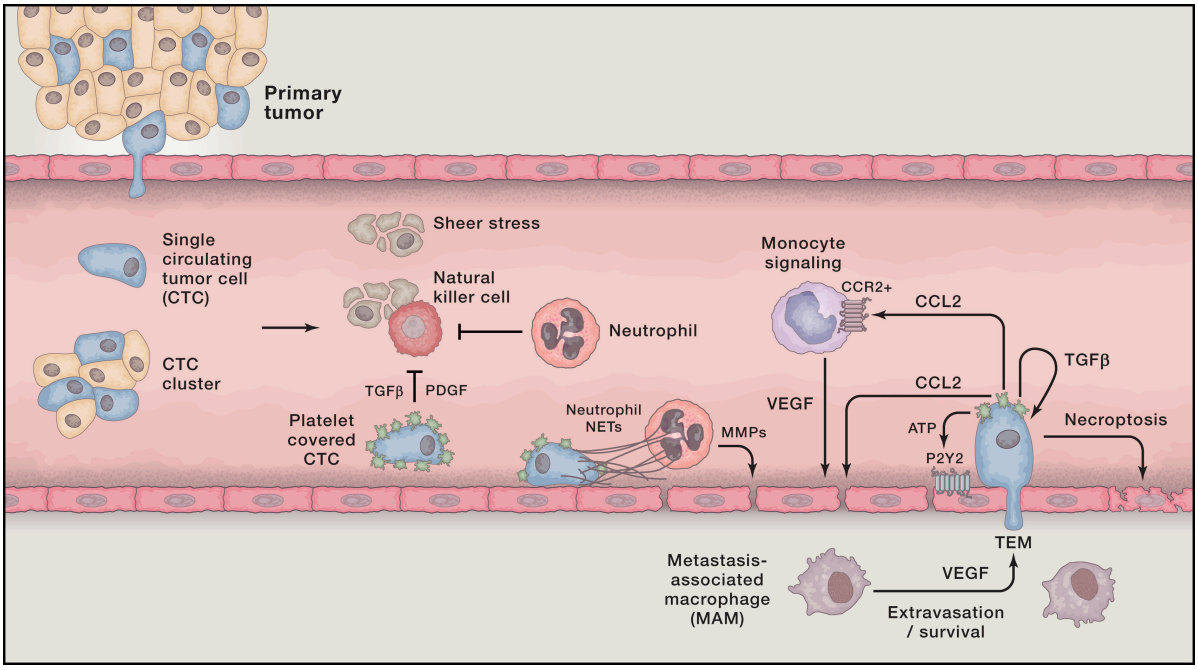

Figure 2.13: ***Cancer cells in the blood system.*** *Once single cancer cells or cancer cell clusters have intravasated, several mechanisms—both to aid the cancer cells (e.g. platelets covering cell surface, neutrophils that enhance extravasation through NET expression, and MMP secretion) and to destroy them (e.g. physical stresses; attacks by NK cells)—come into action. Reproduced from Lambert et al. (2017) with permission from Elsevier Inc.*

2.3.4 Travel through the vasculature and extravasation

Successful intravasation into the vasculature by no means implies that the respective cancer cells will succeed in metastasising. Cancer cells encounter further obstacles in the bloodstream. In fact, as Figure 2.13 shows, single CTCs and CTC clusters are exposed to physical stresses, which include hydrodynamic flow, loss of attachment to a substrate and shear stress. Other obstacles involve the human immune system—in particular, *natural killer* (NK) *cells*, which kill some of the cancer cells in the bloodstream—as well as *anoikis*, programmed cell death induced by lack of appropriate attachment anchorage-dependent cells to the ECM (Gilmore, 2005). These factors lead to a significant decrease in the number of cancer cells that reach the metastatic site from the primary tumour. Further, these factors frequently cause cancer cell clusters to disaggregate during the travel through the vasculature, as shown in the centre of Figure 2.7. This generally leads to smaller CTC clusters and an increased number of single CTCs. Other cells in the bloodstream assist the cancer cells. Platelets coat the surfaces of cancer cells, which prevents NK cells from recognising and destroying them. Neutrophils have a similar effect and additionally support the extravasation of cancer cells. As depicted in the middle of the lower vessel wall shown in Figure 2.13, neutrophils can express *neutrophil extracellular traps* (NETs), which entangle cancer cells. This is suggested to enhance the cancer cells' survival potential, as well as the probability that they will adhere to endothelial cells and extravasate. Neutrophils also secret various MMPs upon arrest, which aid the extravasation of the cancer cells by cleaving the vessel wall. *Transendothelial migration* (TEM) is further pro-

voked by bioactive factors (e.g. *vascular endothelial growth factor* (VEGF), MMPs and ADAM12), which are secreted by activated platelets and by cancer cells. These factors can act on cancer cells themselves, on monocytes and on endothelial cells. Inflammatory monocytes promote TEM by differentiating into *metastasis-associated macrophages* (MAMs) that reside in the parenchyma of the potential secondary sites. Finally, it has recently been found by Strilic et al. (2016) that cancer cells can induce necroptosis of healthy endothelial cells, as shown on the bottom right of Figure 2.13, which allows the cancer cells to extravasate without TEM. More in-depth information on the biological background of extravasation can be found in Lambert et al. (2017).

Whether a certain cancer cell phenotype is required for successful extravasation at secondary sites is unclear. As a result of the aforementioned mouse study by Tsuji et al. (2009) shown on the bottom left of Figure 2.12, it was proposed that mesenchymal-like cancer cells may fail to adhere to the target organ endothelium due to their reduced adhesive properties. Diepenbruck and Christofori (2016) argue instead that mesenchymal-like cancer cells can arrive at metastatic sites but that MET is required for them to outgrow as macrometastases. Upon closer examination, it becomes evident that this would not necessarily contradict the findings of the mouse model by Tsuji et al. (2009), which checked for *metastasis*—rather than newly arrived DTCs and/or micrometastases—when the primary tumour had reached 20% of the bodyweight of the mice. Further, NETs may entangle cells of both phenotypes and the mesenchymal phenotype may have the advantage of MMP-expression upon extravasation.

2.3.5 Metastatic growth

A successfully extravasated single cancer cell or cluster of cancer cells can either contribute to *self-seeding* to an existing metastasis or to the primary tumour, or it can settle as a potential initial seed of a new metastasis (Pantel and Speicher, 2016). However, even if cancer cells have extravasated successfully into the parenchyma of a potential new metastatic site, success in growing into a full-blown secondary tumour is not guaranteed. As illustrated in Figure 2.14, extravasated cancer cells can be grouped into the three stages—single DTCs, small avascular micrometastases and (macro-)metastases. While newly extravasated single cancer cells and cancer cell clusters may progress through all of these stages, it is much more likely for them to die or to remain dormant during one of the first two phases. Here, for single cancer cells, remaining dormant means that the cell neither proliferates nor dies and for micrometastases, dormancy implies that there is an actively controlled balance between apoptosis and proliferation (Chambers et al., 2002). While some dormant DTCs and micrometastases may never cause a problem in a patient's life and while it is difficult to deliver a formal proof that a detected metastasis has developed directly from a dormant DTC or micrometastases, a correlation between existing micrometastases in the bone marrow at the time of breast cancer diagnosis and relapse due to metastatic spread has e.g. been identified by Braun et al. (2005). However, by far most of all cancer cells arriving in the tissue of the new metastatic site never become metastases but die in the process. To give a rough idea of the probability that a cancer cell, which has already intravasated successfully, will ultimately develop into a micro- or macrometastasis, we can quote the result of an experimental study by Luzzi et al. (1998). The authors investigated the proportions of melanoma cells that formed micro-

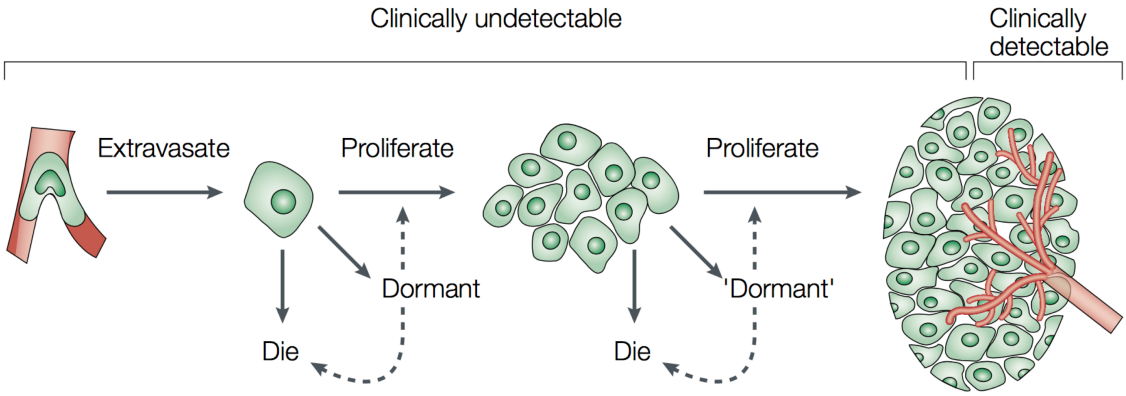

Figure 2.14: ***Possible fates of extravasated cancer cells.*** *Once single CTCs arrive at secondary sites and extravasate (left), they can continue to exist as single DTCs (mid-left), grow into small avascular micrometastases (mid-right) or even into vascularised (macro-)metastases (right). At the two pre-vascularised stages, only a small subset of cells will proceed to the respective next stage. The remaining DTCs or micrometastases die or remain dormant, where 'dormancy' refers to cells that neither die nor proliferate in the case of single cells and to zero net growth under active proliferation and apoptosis in the case of micrometastases. DTCs and micrometastases are not clinically detectable and some macrometastases are not either. Reproduced from Chambers et al. (2002) with permission from Nature Publishing.*

and macrometastases after the melanoma cells were injected intraportally to target mouse livers. It was found that 2.04% of the injected single cancer cells formed micrometastases after 3 days but after 13 days only 0.07% of the initially injected cancer cells were still present as micrometastases. Additionally, it was observed that $0.018\% \pm 0.017\%$ of initially injected cancer cells had formed macrometastases after 13 days. These survival probabilities for single CTCs may, according to Valastyan and Weinberg (2011), even be an overestimation. CTC clusters were described to have between 23 and 50 times the metastatic potential of single CTCs (Aceto et al., 2014). Note, however, that this is only a rough estimate and will depend on other factors such as the particular cancer cell lines and the secondary sites involved, as explained in detail below.

There are many unsolved questions regarding the exact mechanisms that determine the sites of successful metastatic colonisation. At the time of writing, no recurrent genetic mutations that allow for successful colonisation have been found. However, three central requirements that could be important for successful metastatic colonisation were proposed in Lambert et al. (2017):

- the development of a supportive microenvironmental niche;
- the capacity to fabricate adaptive colonisation programmes, which are often specialised to the organs;
- the ability to seed and to sustain a population of tumour-initiating cells.

The first point was addressed as far back as 1889, when the British surgeon Stephen Paget noted, after having treated many breast cancer patients, that the location of metastatic

spread is by no means random. He laid the groundwork for the *seed and soil hypothesis* by postulating that cross-talk between selected cancer cells (the 'seeds') and specific organ microenvironments (the 'soil') drives metastatic spread:

> When a plant goes to seed, its seeds are carried in all directions; but they can only live and grow if they fall on congenial soil. While many researchers have been studying 'the seeds', the properties of 'the soils' may reveal valuable insights into the metastatic peculiarities of cancer cases (Paget, 1889).

This seed and soil hypothesis still stands over 100 years later, emphasising the dependence of secondary tumour survival on the local microenvironment in the secondary site's stroma. Additionally, in the current state of research it is suggested that, while tumours actively recruit this stroma once they are local, it may also be the case that so-called *pre-metastatic niches* establish prior to DTC arrival. A primary tumour itself may even play an important role in niche establishment by secretion of signalling factors with systemic effects on pre-metastatic niche formation, as well as on the primary tumour's own expansion and on growth activation in previously latent micrometastases (McAllister and Weinberg, 2014).

Regarding the second point suggested by Lambert et al. (2017), some organ-specific metastatic programs have been discovered to date (Nguyen et al., 2009; Sethi and Kang, 2011; Obenauf and Massagué, 2015). These organ-specific programs explain how cancer cells spread into organs such as the lungs (Chen et al., 2011), the brain (Valiente et al., 2014), the bones (Weilbaecher et al., 2011), or the liver (Loo et al., 2015). However, the programmes discussed in these publications likely only explain a small proportion of survival mechanisms of cancer cells in their new microenvironment. The majority of mechanisms remain undiscovered to date.

The final pre-requisite suggested by Lambert et al. (2017) for successful colonisation at the metastatic site involves cells, whose defining trait is the ability to initiate tumour growth. Several types of cancer cells—such as those involved in breast, ovarian, colorectal, renal and pancreatic cancer—are suggested to acquire this distinguishing trait after the activation of EMT programmes have been initiated (Lambert et al., 2017).

Other factors such as the adaptability of the cancer cell 'seed' and anatomical factors have been found to play a role in determining recurrent metastatic spread patterns as well. An example for the latter is the propensity of advanced gastrointestinal malignancies to metastasise into the liver as a result of the portal vein emptying directly into the liver (Gupta and Massagué, 2006). Yet, the distribution of clinically observed metastatic spread suggests that the anatomy of the circulatory system only plays a role in a small subset of seeding routes and thus cannot explain general patterns of metastatic spread.

While the specific mechanisms of and the reasons for cancerous spread to specific metastatic sites remain largely unknown, some studies can provide insight into typical patterns of metastatic tumour spread of a certain primary cancer type. To tie in with Stephen Paget's 19th century observation that breast cancer spread does not occur randomly, we can, for example, consult data on the metastatic spread of primary breast cancer. These were collected from 4181 breast cancer patients (3735 early-stage breast cancer patients diagnosed at MD Anderson Cancer Center and 446 breast cancer patients at Memorial Sloan Kettering Cancer Center, who had no detectable metastases upon diagnosis but all developed some eventually). They were then visualised through

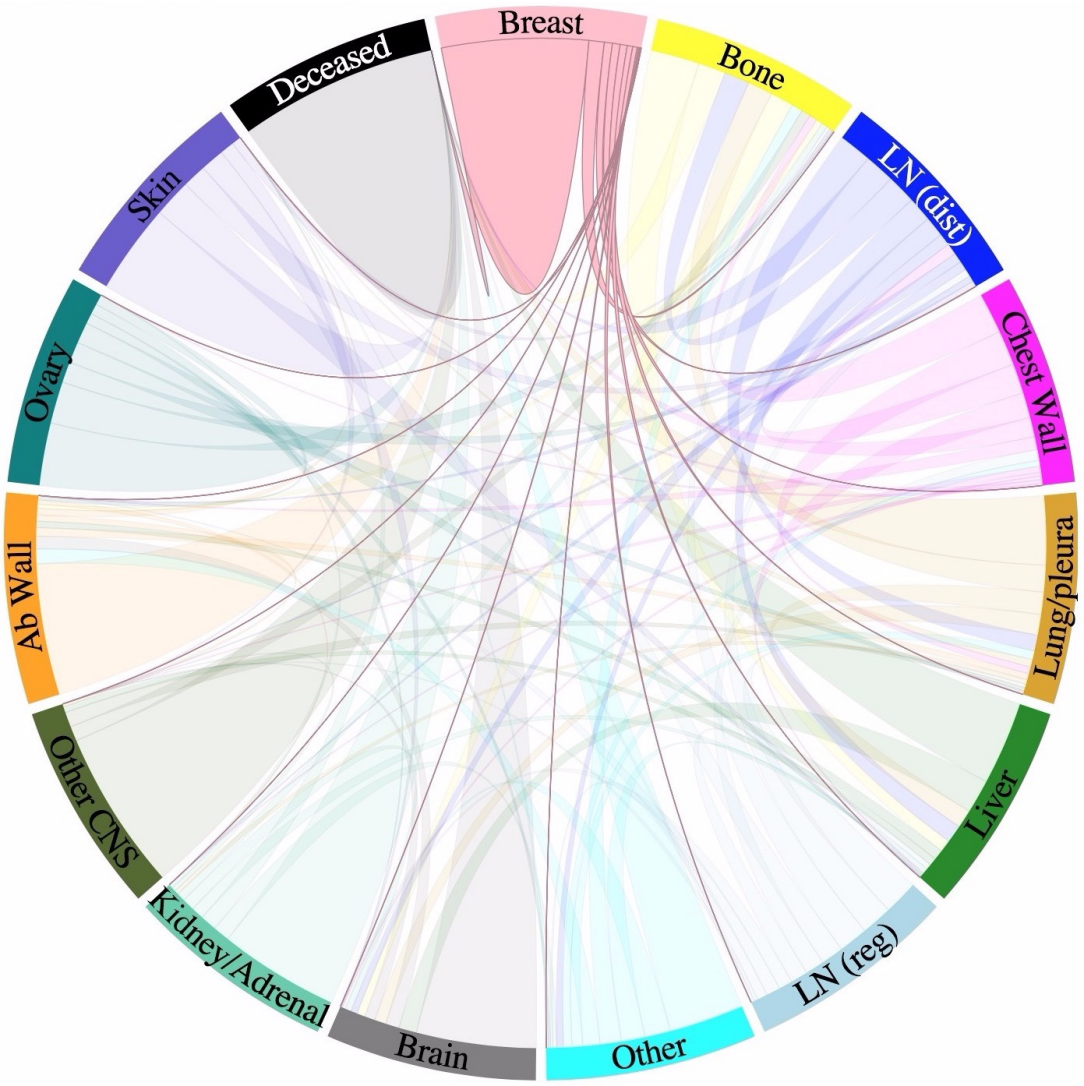

Figure 2.15: ***Metastatic progression of breast cancer.*** *Circular chord diagram showing MC network of data on metastatic spread from 4181 breast cancer patients over a 10-year period. Primary breast cancer is located on top. Metastatic sites—including the bones, lungs and brain—are ordered clockwise in decreasing order of transition probability from the primary breast tumour. Chord widths starting from the 'breast' represent one-step transition probabilities between two sites. Further information on the exact data origin and patient criteria can be found at* `http://kuhn.usc.edu/breast_cancer/`*. Courtesy of Dr Jeremy Mason, University of Southern California using the interactive tool published at* `http://kuhn.usc.edu/forecasting` *—the corresponding publication is Newton et al. (2013).*

interactive graphs by the Kuhn Laboratory (2017). Figure 2.15 shows typical metastatic spread patterns of a primary breast tumour 10 years after diagnosis from such an interactive figure.

2.4 The role of EMT and MET in the invasion-metastasis cascade

As briefly explained in Section 2.3, cancer cells adapt to the environmental requirements of the various steps of the invasion-metastasis cascade via changes in phenotype (Jolly et al., 2017). EMT and MET are a canonical group of—at least transiently—observed phenotypic changes that are assumed to be crucial for metastatic spread (Guo et al., 2012; Ye et al., 2015; Krebs et al., 2017). Various combinations of so-called *EMT-inducing transcription factors* (EMT-TFs) together with a number of extracellular molecules in the tumour microenvironment and related pathways are thought to trigger EMT (Jie et al., 2017). As an outcome of EMT, the cell-cell adhesion, which is predominantly enforced via E-cadherin, gap junctions and tight junctions between formerly epithelial-like cancer cells, is reduced together with their expression of epithelial integrins. These are replaced by the expression of cell-matrix adhesion-enhancing molecules like N-cadherin, as well as of integrins that are specific to extracellular components on the cell membrane. Moreover, the actin cytoskeleton remodels into stress fibres that accumulate at the areas of cell protrusions and epithelial cytokeratin intermediate filaments are increasingly replaced by vimentin (Micalizzi et al., 2010). As part of this combination of changes, the characteristic polygonal cobblestone-like cell shape of epithelial cells is progressively replaced by a spindle-shaped morphology. Figure 2.11 schematically shows the changes cells undergo when switching from an epithelial-like (left) to a mesenchymal-like (right) phenotype. Moreover, the motility and invasiveness of the cancer cells are enhanced (Jie et al., 2017; Dongre and Weinberg, 2019). As another result of EMT, the cells become increasingly potent at degrading the underlying basement membranes of organs and vessels as well as the ECM via the expression of *metalloproteases* (MMPs) (Dongre and Weinberg, 2019). Additionally, in the case of glioma cells a trade-off has been observed between proliferation and motility (Giese et al., 1996). MET can reverse the phenotypic changes induced by EMT. Thus—generally speaking—MET causes the cells to become less motile and invasive while enhancing their proliferative potential. Traditionally, the EMT-process has been viewed to result in cells of epithelial and of mesenchymal phenotype in a binary sense (Pastushenko and Blanpain, 2018; Dongre and Weinberg, 2019). Yet, more recently, intermediate states—commonly referred to as *hybrid*, *incomplete* or *partial-EMT* states—on the spectrum between the fully epithelial and fully mesenchymal state have been shown to exist in various cell lines of patient xenografts and of human primary cancers, such as breast, head and neck, and pancreatic cancer (Pastushenko and Blanpain, 2018). Cancer cells in these intermediate phenotypic states are assumed to show a variety of combinations of the above-mentioned phenotypic traits. The full transition from an epithelial to a mesenchymal state, which had formerly been assumed to be the only possible outcome of EMT, has recently been shown to actually be rare during carcinogenesis (Dongre and Weinberg, 2019). Furthermore, cell cycle arrest may occur in these fully mesenchymal cancer cells (Vega et al., 2004; Lovisa et al., 2015), while partial-EMT cancer cells continue to be able to proliferate (Handler et al., 2018).

In what follows, the roles of EMT and MET as well as of epithelial, partial-EMT and mesenchymal cancer cells during the various steps of the invasion-metastasis cascade are elucidated in more detail. Sections 2.3.2 to 2.3.5 introduced the five steps of the invasion-metastasis cascade in detail. Therefore, we will only focus on the respective EMT-related

features, as well as those related to the partial-EMT phenotype, in Sections 2.4.1 to 2.4.4.

2.4.1 Local cancer cell invasion

In Section 2 we established that carcinomas are tumours that arise from epithelial tissue. However, during local cancer invasion, cancer cells have been found to either invade as single cells of partial-EMT or of mesenchymal phenotype or as clusters, which often consist of cancer cells of heterogeneous phenotypes (Friedl and Wolf, 2003). Hence, EMT of some degree at least in a subset of the cancer cells at the primary site is a prerequisite for this first step of the invasion-metastasis cascade (Francart et al., 2018; Pastushenko and Blanpain, 2018). Migrating cells usually employ their acquired mesenchymal traits, i.e. the decrease or loss in cell-cell adhesion and increase in cell-ECM adhesion and in MDE-expression, to invade (Friedl and Wolf, 2003; Bill and Christofori, 2015). This hypothesis is, for example, supported by reports suggesting that invading cancer cell clusters contain cells that have undergone partial EMT *in vivo* (Tsai et al., 2012; Ocaña et al., 2012). Moreover, the occurrence of *clusters* highlights that partial EMT allows for the cancer cells to maintain at least some aspects of their epithelial cell-cell adhesion (Cheung and Ewald, 2016). Furthermore, the spatial location of cancer cells of partial-EMT and of epithelial phenotype was investigated by Puram et al. (2017) *in situ* in oral

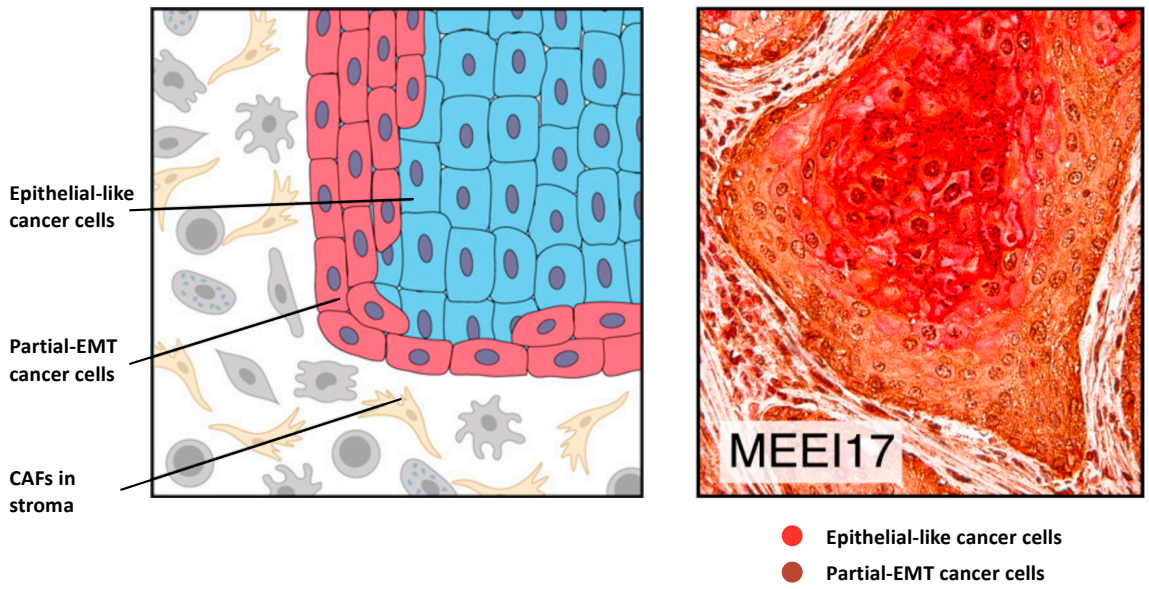

Figure 2.16: ***Partial EMT occurs at the leading edge in HNSCC.*** *In situ spatial location of cancer cells expressing a partial EMT programme versus those expressing an epithelial phenotype within HNSCC tumours schematically (left) and in human tissue (right). On the right, immunohistochemistry was used to stain the tumour for PDPN, one of the top genes in the partial-EMT programme, as well as SPRR1B, an epithelial differentiation marker. Partial-EMT cancer cells were located at the leading edge of tumours in proximity to the surrounding stroma, epithelial-like cancer cells at the core of tumours. Reproduced from Puram et al. (2017) with permission from Elsevier.*

cavity *head and neck squamous cell carcinomas* (HNSCCs). Using immunohistochemistry to stain a collection of tumours, they found that, while the core of the tumours contained malignant cells of epithelial phenotype, partial EMT had occurred in the cancer cells at the leading tumour edge in the proximity of *cancer-associated fibroblasts* (CAFs) in the tumour microenvironment. A corresponding stained tissue sample and an explanation in the form of a diagram are shown in Figure 2.16.

2.4.2 Intravasation

As explained in detail in Section 2.3.3, only MDE-expressing cancer cells may intravasate into intact vessels. Therefore, partial-EMT cancer cells are—like mesenchymal-like cancer cells—able to intravasate undamaged vessels (Jolly et al., 2018). Similarly, cancer cell clusters that consist at least partially of partial-EMT and mesenchymal-like cancer cells can enter undamaged vessels using MDEs.

2.4.3 Travel through the vasculature and extravasation

The bulk of CTCs and CTC clusters that travel through the vasculature were found to be of partial-EMT phenotype (Jolly et al., 2018). In terms of experimental evidence of typical CTC phenotypes, Armstrong et al. (2011) found that in women with metastatic breast cancer and men with castration-resistant prostate cancer more than 75% and 80% of CTCs, respectively, coexpressed epithelial and mesenchymal markers. Similarly, studies by Thiery and Lim (2013) and by Yu et al. (2013) reported that a significant proportion of CTCs were of partial-EMT or mesenchymal-like phenotype in patients with metastatic breast cancer. CTCs of partial-EMT phenotypes have further been observed in the blood of patients with cancer of the liver, prostate and lungs as well as in patients with colorectal, nasopharyngeal and gastric cancer. In these types of cancer, the partial-EMT phenotype correlates with poor clinical prognosis when compared to the occurrence of cancer cells of pure epithelial or pure mesenchymal phenotype (Pastushenko and Blanpain, 2018). The prominence of cells of partial-EMT phenotype at the tumour edge as well as their ability to intravasate into the vasculature using MDEs offer potential explanations of these findings. An additional explanation is that at least a subset of partial-EMT CTCs is more resistant to anoikis, i.e. to apoptosis induced by lack of correct cell-ECM attachment (Huang et al., 2013).

2.4.4 Metastatic growth

Cancer cell phenotypes are, once again, of crucial importance when it comes to the colonisation and metastatic growth of cancer cells at the secondary sites. Also, EMT alone fails to explain this last step of the invasion-metastasis cascade given that macrometastases in humans often present similar histopathological traits to the primary tumours they typically originate from. These include a mainly epithelial-like morphology (Pastushenko and Blanpain, 2018) with a relatively small subset of cancer cells with phenotypes further along the EMT spectrum (Dongre and Weinberg, 2019). This is despite the above-described evidence of the abundance of partial-EMT CTCs in the vasculature. Consequently, this suggests that some degree of MET is needed for macrometastatic growth.

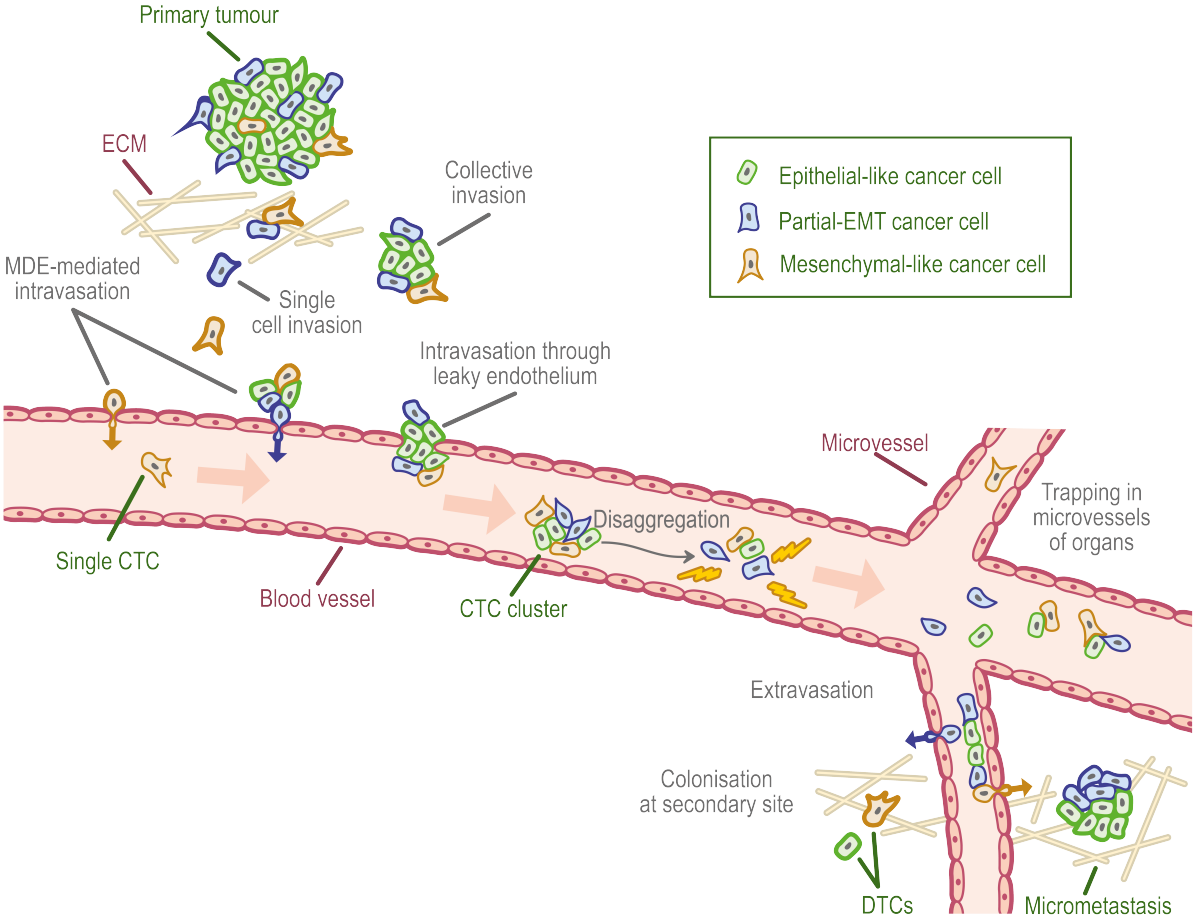

Figure 2.17: ***Schematic overview of the invasion-metastasis cascade with—as opposed to Figure 2.7—additional detail regarding the role of the EMT-process and partial-EMT cancer cells.*** *Single mesenchymal-like and partial-EMT cancer cells as well as heterogeneous clusters consisting of mesenchymal-like, partial-EMT and epithelial-like cancer cells break free from the primary tumour and invade the surrounding tissue (top left). They can intravasate via active matrix-degrading enzyme (MDE)-mediated and passive mechanisms (mid-left, along epithelium of the vessel). Once in the vasculature, circulating tumour cell (CTC) clusters may disaggregate (centre) and CTCs may die. Surviving cells may extravasate through the walls of the microvasculature to various secondary sites in the body (bottom right). Successful colonisation there can result in either disseminated tumour cells (DTCs) or in micrometastases, which have the potential to develop into full-blown metastases.*

A murine prostate cancer model by Ruscetti et al. (2015) delivers further insight. Cancer cells in macrometastases that had spread to the lungs were found to have mainly epithelial markers and few mesenchymal markers; the inverse constitution was found in dormant micrometastatic lesions. Coherently, in a study by Ocaña et al. (2012), it was proposed that the constant overexpression of the EMT-inducer PRRX1 in human breast tumour cell lines, which were injected intravenously into chick embryos, may lock cancer cells in a mesenchymal-like phenotypic state. This was suggested to inhibit the cells from performing MET, which, in turn, failed to give rise to lung metastases. Similarly, Kröger et al. (2019) concluded from a number of studies that a stable mesenchymal-like phenotype without any MET potential cannot succeed in metastatic re-seeding.

2.5 An example of an *in vitro* invasion study

In this section, we explore how experimentalists study invasion *in vitro* and quantify their results. As an example, we introduce an organotypic assay experiment by Nurmenniemi et al. (2009) that we subsequently use to demonstrate that our mathematical model for cancer invasion of the ECM in Chapter 6 provides biologically accurate predictive results. The experiment by Nurmenniemi et al. (2009) uses human tongue squamous cell carcinoma cells of cell line HSC-3 that invade uterine leiomyoma tissue. Since this mimics the *in vivo* invasion of the tumour microenvironment in oral squamous cell carcinoma (OSCC), we first explain OSCC and the composition of its tumour microenvironment *in vivo*. With reference to experimental evidence, the suitability of uterine leiomyoma tissue to represent the tumour microenvironment of OSCC is demonstrated. We proceed by describing the experimental setup of the invasion organotypic assays in Nurmenniemi et al. (2009), their experimental results and the methods applied to quantify these results.

2.5.1 Oral squamous cell carcinoma (OSCC)

Head and neck cancer is one of the 10 most common types of cancer worldwide, afflicting more than 5×10^5 individuals each year. OSCC represents 95% of all forms of head and neck cancer, and over the last decade, its overall incidence has increased by 50%. OSCC is a malignant neoplasm derived from the stratified squamous epithelium of the oral mucosa as Figure 2.18 shows. The neoplasm can occur at various sites, the most frequent being the lip, lateral edges of the tongue and floor of the oral cavity.

Oral carcinogenesis is a multistage process, which simultaneously involves precancerous lesions, invasion and metastasis. Oral cancer is considered to be a preventable condition, due to the possibility of early detection and treatment. However, the majority of OSCC are diagnosed at a late phase which markedly decreases the chances of survival and leads to a significant deterioration in patient quality of life. Despite the currently available therapeutic strategies, which include the excision of malignant tissue and combination of radiotherapy and chemotherapy, the five-year survival rate is only 53%. A high percentage of patients have a poor response to therapy and high recurrence rates (Rivera and Venegas, 2014).

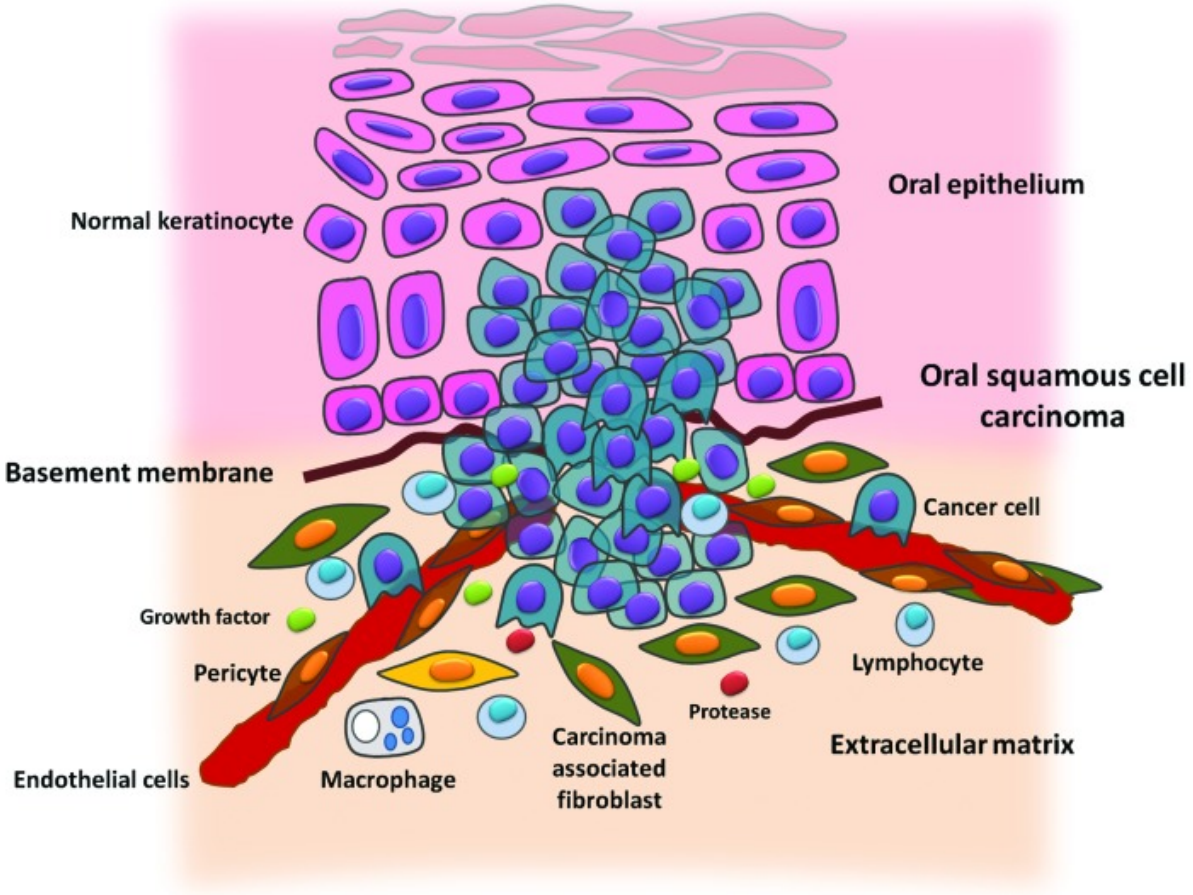

Figure 2.18: ***OSCC and its tumour microenvironment.*** *In the tumour microenvironment, different stromal cells—including vascular and lymphatic endothelial cells, and pericyte support fibroblast innate and adaptive immune cells—as well as tumour cells are observed. Furthermore, the tumour microenvironment contains non-cellular components, including the ECM, growth factors, proteases, protease inhibitors or other signalling molecules that are significant in the reactions of the stroma in the tumour microenvironment (Koontongkaew, 2013). From Rivera and Venegas (2014) under Creative Commons License.*

2.5.2 The OSCC tumoural microenvironment

Traditionally, organotypic assays to study carcinoma cell invasion in three dimensions consist of type I collagen, e.g. Nyström et al. (2005); Nurmenniemi et al. (2009); Sabeh et al. (2009), a combination of type I collagen and Matrigel, e.g. Gaggioli et al. (2007), or fibroblasts embedded in collagen e.g. Fusenig et al. (1983); Mackenzie (2004). However, as Figure 2.18 suggests, the *in vivo* tumour microenvironment is far more complex than the organotypic assays used in any of the cited experimental setups. Indeed, the tumour microenvironment contains numerous types of cells, including smooth muscle cells, endothelial cells and their precursors, pericytes, fibroblasts, cancer-associated fibroblasts, myofibroblasts, neutrophils, mast cells, basophils, eosinophils, T and B cells, natural killer cells and antigen-presenting cells, such as dendritic cells and macrophages (Lorusso and Rüegg, 2008) (see Figure 2.18). Further, the tumour microenvironment consists of other

non-cellular components, such as the ECM, proteases, protease inhibitors, growth factors and other signalling molecules (Koontongkaew, 2013). After cancer invasion was, for a long time, considered to be dependent solely on the mutated cancer cells with abnormal proliferative capacities, it has recently become evident that the tumour microenvironment and its interaction with the cancer cells considerably affects the invasive outcome (Kenny et al., 2007).

To mimic the tumour microenvironment of OSCCs *in vivo*, Nurmenniemi et al. (2009) recommended the use of real human uterine leiomyoma tissue, rather than of more traditional organotypic assays such as type I collagen, for three-dimensional invasion experiments. Using immunostaining for various cell markers and proteins, it was confirmed that the *in vivo* tumour microenvironment of OSCCs compares to uterine leiomyoma tissue—compare Figure 3 in Nurmenniemi et al. (2009). The study found that the myoma tissue consists of abundant quantities of ECM proteins, such as collagen type I and III and laminins. Further, they found basement membrane proteins like collagen type IV and fibronectin, smooth muscle actin-positive cells. Other cell types like smooth muscle cells, endothelial cells, lymphocytes, macrophages and fibroblasts were also observed. Finally, to compare invasion outcomes, Nurmenniemi et al. (2009) constructed invasion experiments that were equal apart from uterine leiomyoma tissue being used in some and collagen I in others. It was observed that using myoma enhanced the invasion depth of cancer cells as well as possibly promoted EMT. Overall, the conclusion was reached that myoma provided a biologically relevant human matrix for squamous cell carcinoma.

2.5.3 Experimental method for the HSC-3 organotypic invasion assay culture

In this thesis, we provide a summary of those details of the experimental setup in Nurmenniemi et al. (2009) that are relevant to our modelling approach and simulations in Chapter 6. Further details can be found in the publication itself.

For the organotypic culture, only non-degraded human uterine leiomyoma tissue was selected and any areas with macroscopically heterogeneous tissue were omitted. The suitable tissue was cut into 3 mm thick slices. From these, discs of 8 mm diameter were punched. 7×10^5 human tongue squamous cell carcinoma cells (HSC-3) were allowed to attach to the top of each myoma disc overnight. Subsequently, the myoma discs were transferred onto uncoated nylon discs that rested on curved steel grids in 12-well plates with sufficient volume of media. This arrangement is shown on the top left of Figure 2.19, which presents the steps of the experimental procedure elaborated in what follows.

At days 2, 8 and 14, the organotypic cultures, which all stemmed from the same myoma to minimise differences in tissue, were formalin-fixed. Then they were dehydrated, bisected and embedded in paraffin to reach the state shown in the centre of Figure 2.19. Next, they were sectioned into slices of 6 µm thickness and immunostained according to the question the authors sought to address. For the main invasion experiment, which our model focusses on, pancytokeratin AE1/AE3 was used, which stains epithelial-derived HSC-3 cells brown, as shown on the bottom of Figure 2.19.

The same staining was used in an experiment to investigate EMT, as depicted in the middle panel of Figure 2.20. In this experiment, Nurmenniemi et al. (2009) further stained the sections with the mesenchymal marker *vimentin* (VIM), which stains cells

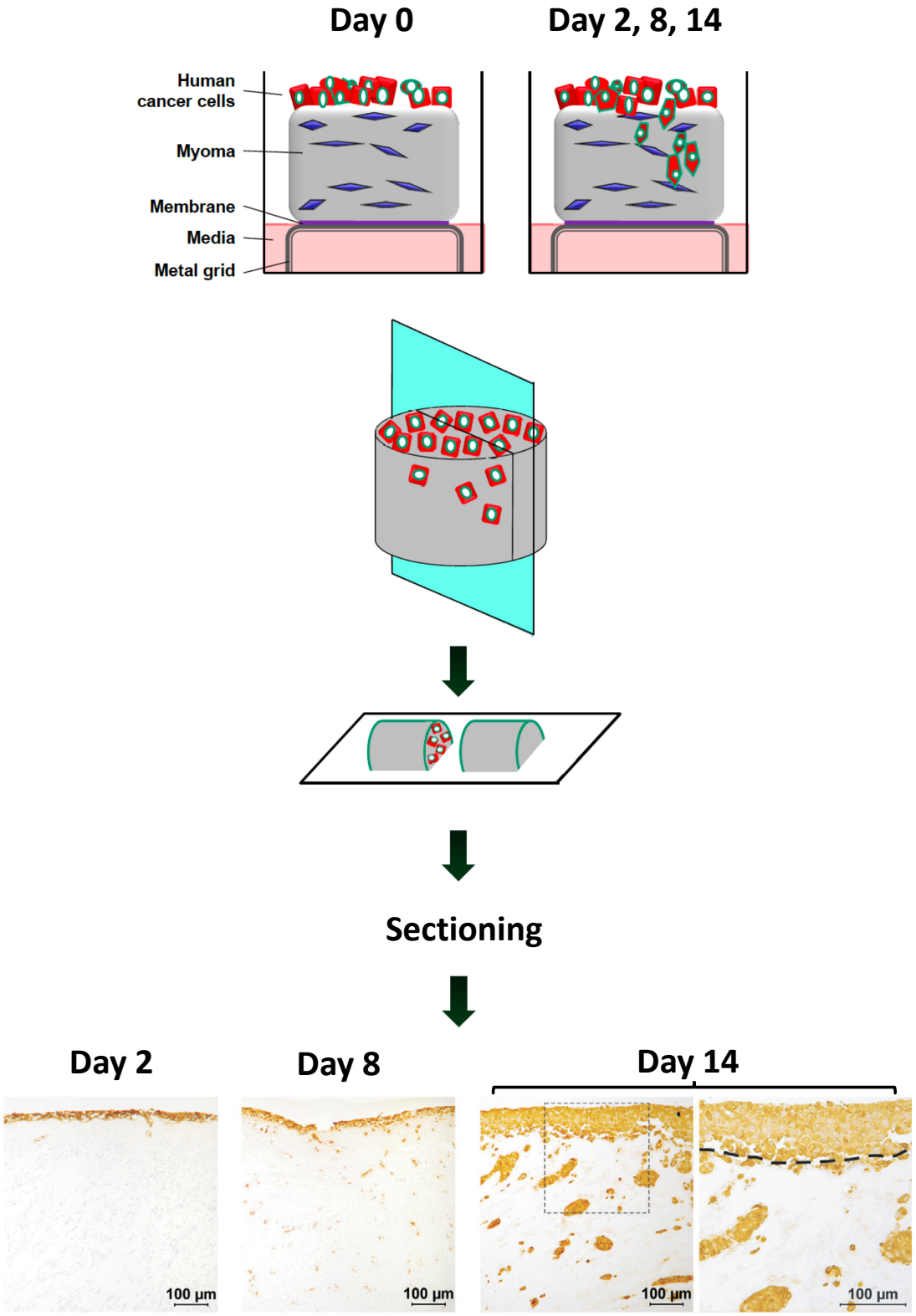

Figure 2.19: ***Graphical representation of HSC-3 myoma assay experimental procedure.*** *See text for details on the experimental procedure by Nurmenniemi et al. (2009). Reproduced from Nurmenniemi et al. (2009) with permission from Elsevier (bottom) and from Rissanen et al. (2013) (top).*

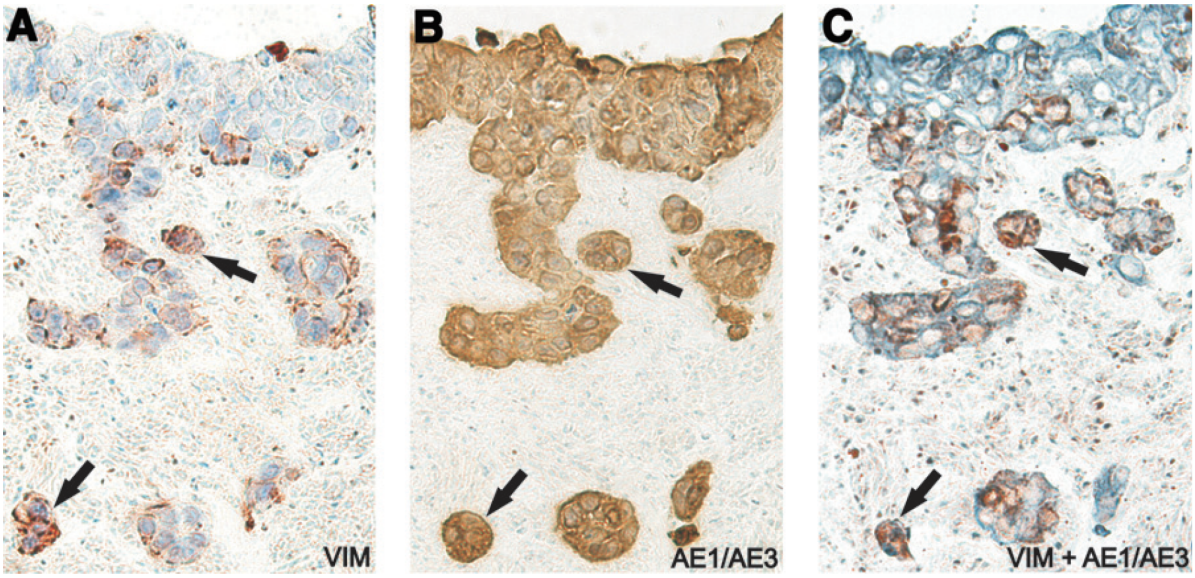

Figure 2.20: ***Immunostaining for mesenchymal and epithelial markers.*** *Immunostained sections with (A) VIM, which stains cells of mesenchymal phenotype red; (B) pancytokeratin AE1/AE3, which stains epithelial-derived cells brown; (C) both VIM (red) and pancytokeratin (blue) simultaneously. Reproduced from Nurmenniemi et al. (2009) with permission from Elsevier.*

of mesenchymal phenotype red, as the left panel of Figure 2.20 demonstrates. Finally, simultaneous staining was carried out as well—the right panel of the same figure shows VIM in red and pancytokeratin in blue.

2.5.4 Quantification of the HSC-3 myoma assay results

The bottom of Figure 2.19 shows microscopic fields with pancytokeratin AE1-/AE3-stained organotypic assays that initially consisted of a single HSC-3 cell layer on top of visually homogeneous myoma tissue at day 2, 8 and 14 (left to right).

Qualitatively, it can be observed that at day 2, the single-cell layer on top of the myoma assay had increased in thickness. Myoma invasion in the form of subtle protrusive strands that continued to be attached to the upper non-invasive cell layer as well as in the form of two small invading cancer cell clusters were visually detectable. By day 8, however, the myoma tissue area studied was infiltrated by many single cancer cells and small clusters of cancer cells. At day 14, the top-most non-invasive cell layer had notably extended further to a thickness of approximately 36–43 µm. Furthermore, the depicted myoma tissue was infiltrated by large cancer cell clusters throughout, with the 'islands' nearer the non-invasive cell layer generally tending to present a larger surface area.

Quantitatively, invasion results were measured via the *maximal invasion depth*, the *invasion area* and the *invasion index*, as shown in Figure 2.21 (left to right). To determine the maximum invasion depth for each slice, the distances of the three HSC-3 cells that had invaded furthest from the myoma surface—measured perpendicularly to the top edge of the microscopic field—were measured using Fiji software, as shown in Figure 2.22, and the mean of the distances was calculated, as described in Åström et al. (2018). This

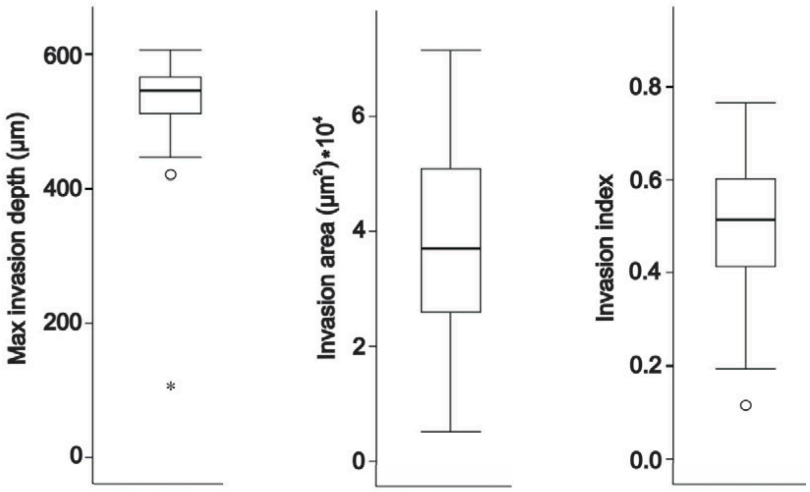

Figure 2.21: ***Quantification of invasion results.*** *Invasion results on day 14 were measured via the maximal invasion depth, the invasion area and the invasion index, which are presented in the form of box plots (left to right). The central rectangles span the first quartile to the third quartile. The segment inside the rectangle shows the median. The 'whiskers' above and below the box show the locations of the respective minimum and maximum. Suspected outliers are indicated by a circle and outliers by a star. The results for the maximal invasion depth consist of at least three measurements, cf. Figure 2.22, of two to eight slices from two to four independent assays. For the invasion area and index, one measurement per representative area was taken from each of the two to eight slices from the two to four independent assays. Modified from Nurmenniemi et al. (2009) with permission from Elsevier.*

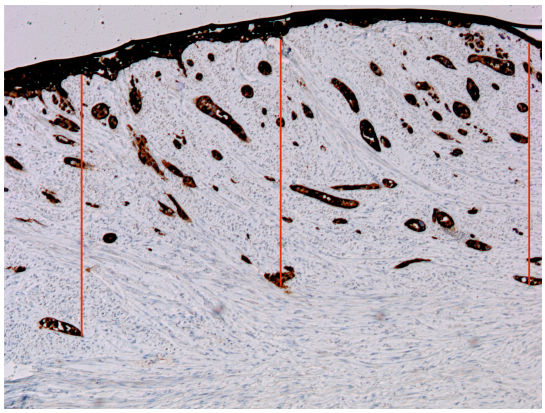

Figure 2.22: ***Maximal invasion depth.*** *The invasion distances of the three epithelial-like HSC-3 cells that invaded furthest into the myoma—measured perpendicularly to the top edge of the microscopic field—were measured as indicated by the red line. Then, their mean was calculated as described in Åström et al. (2018).*

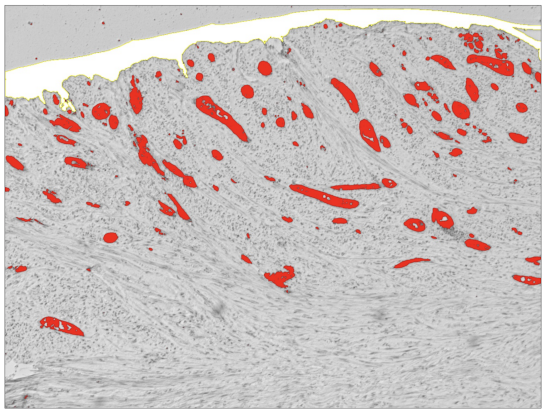

Figure 2.23: ***Invading vs. non-invading cell area.*** *The area of the upper non-invading epithelial-like HSC-3 cell layer is shown in white; the area that is occupied by invading epithelial-like HSC-3 cells is shown in red. Cells of mesenchymal-like phenotype were not accounted for in the determination of the respective areas.*

was repeated for 3 to 8 slices from the same myoma disc and then averaged. Using this method, the maximal invasion depth was found to be 547 µm, with interquartile range 61 µm, in this experiment. The invasion index used was introduced in Nyström et al. (2005). To calculate the index, Nurmenniemi et al. (2009) first quantified the area of the upper non-invading cell layer, which corresponds to the respective area coloured in white in Figure 2.23 in each microscopic field, as well as the area occupied by the sum of the remaining invading epithelial-like HSC-3 cells, which is highlighted in red in the same figure. These measurements were, again, taken from 3 to 8 slices of the same myoma to determine the mean area of the upper non-invading cell layer (A_{inv^-}) and the mean invading cell area (A_{inv^+}). The invasion index (I) was then calculated as

$$I = \frac{A_{\mathsf{inv}^-}}{A_{\mathsf{inv}^+} + A_{\mathsf{inv}^-}}, \tag{2.5.1}$$

which gave $I = 0.51\ [0.41, 0.60]$ in this particular experiment.

Chapter 3

Mathematical models of cancer invasion and metastasis

In this chapter, we review existing models of cancer invasion and metastasis. We consider both spatially local and non-local invasion models. The metastasis models reviewed either describe the acquisition of a metastatic phenotype in cancer cells or investigate metastatic growth dynamics. The models proposed in Chapters 4–6 are motivated by this literature review—they focus on aspects previously unexplored through mathematical models, such as the spatiotemporal evolution of individual cancer cells in the invasion-metastasis cascade and the role of EMT-processes therein.

3.1 Mathematical models of cancer invasion

Arguably, the roots of solid tumour growth models lie in modelling work by Hill (1928) on general, non-cancer-specific diffusion of oxygen and lactic acid through tissue. Other cancer-specific spatiotemporal models of non-invasive tumour growth by diffusion, such as Burton (1966); Greenspan (1972, 1976); Deakin (1975), started developing around half a century ago. While Burton (1966); Greenspan (1972); Deakin (1975) considered solid tumour growth by diffusion only, the later biomechanical model of solid tumour growth (Greenspan, 1976) introduced the effects of cell movement and pressure on tumour growth. Models focusing on cancer cell *invasion*, in particular, began to be developed in the early nineties. We give an overview of the development of these models in this section. Throughout, we distinguish models which include only *local* interactions between cancer cells and their environment and those that additionally capture interactions that are *non-local* in space through integral terms. This includes a review of existing mathematical models that account for, in the wider sense, EMT-related features in the context of spatially explicit cancer invasion.

The information in this chapter is based on the review sections in Enderling and Chaplain (2014); Araujo and McElwain (2004); Byrne (2010); Gerisch and Chaplain (2008); Deakin (2015); Knutson (2011); Peng et al. (2017); Metzcar et al. (2019) as well as on the results of a personal literature search.

3.1.1 Local invasion models

Early models of cancer invasion used *ordinary differential equations* (ODEs) in a continuum approach. Nowadays, local continuum models also exist in the form of e.g. systems of advection-reaction-diffusion *partial differential equations* (PDEs). This allows accounting for space in the invasive process. Furthermore, both hybrid and discrete approaches to modelling cancer invasion are also well-established in the literature.

Continuous local invasion models

Gatenby (1991) proposed a first ODE model describing cancer cell invasion by applying mathematical modelling techniques from population ecology to cancer growth. Healthy mesenchymal or epithelial cells, which initially were assumed to be in an equilibrium state under the given resources entering through blood vessels or reach them by diffusion, took on the role of the host in population biology. Cancer cells were treated as the initially rare invading population. The outcome of studying cancer invasion using this first non-spatial model was either coexistence of both cell types or the extinction of either cancer cells or healthy cells. Two further ODE models by Gatenby (1995a, 1996) also examined invasion from a population ecology perspective.

During the same time, Gatenby (1995b) started developing ODE models to test whether the so-called *acid-mediated invasion hypothesis* as further explained in Gatenby et al. (2006) could be verified using mathematical models. This hypothesis claims that cancer outcompetes healthy resident cells by changing the tissue environment to give cancer cells a competitive advantage over normal cells. Cancer cells have been shown to have an altered glucose metabolism—their glucose uptake exceeds that of normal cells. The resulting increase in H^+ ions in the local environment of the cancer cells diffuses into adjacent healthy tissue along the H^+ ion concentration gradient. This causes the pH, which is defined as $\mathrm{pH} = -\log_{10} H^+$, where H^+ is the hydrogen ion activity, in the adjacent normal tissue to decrease i.e. the tissue becomes more acidic. According to the acid-mediated invasion hypothesis, this change in pH causes healthy cells to release more proteolytic enzymes, which degrade the ECM. Another effect is the induction of death of healthy cells. As the tumour cells are resistant to the acidic environment, the space created through cell death and ECM degradation allows them to continue to proliferate and to invade the normal adjacent tissue.

However, due to their ODE nature, the models in Gatenby (1991, 1995a, 1996) could approximate the evolution of the total number of cells over time but could not account for their spatial evolution. Yet, as described in Chapter 2, cancer invasion as a biological phenomenon is an inherently spatial process. The ODE invasion models' limitation with regards to accounting for space was first overcome in the PDE model developed in Gatenby and Gawlinski (1996). More specifically, this was an early paper of a group of so-called *reaction-diffusion(-taxis) models*. These models, which the remainder of this review subsection deals with, are granted their name by the directed movement of cancer cells in response to the ECM gradient, known as *haptotaxis*, and cell movement responding to chemical gradients in the tissue, *chemotaxis*. This paper also described acid-mediated invasion but this time the phenomenon was modelled using a system of reaction-diffusion PDEs rather than ODEs. It follows a brief overview of the model presented in the seminal

paper. To allow a better comparison to other modelling work in this thesis, we adjust the original notation. The PDE model tracks the spatiotemporal evolution of

$c(t, \mathbf{x})$ density of neoplastic (i.e. cancerous) tissue,

$m(t, \mathbf{x})$ excess concentration of H^+ ions,

$w(t, \mathbf{x})$ density of normal tissue,

where $\mathbf{x} \in \mathbb{R}$.

The dimensional model describing the spatiotemporal evolution of the density of cancerous tissue c, H^+ ion concentration m and normal tissue density w is given by:

$$\frac{\partial c}{\partial t} = \overbrace{\nabla \cdot (D_c[w] \nabla c)}^{\text{diffusion}} + \overbrace{r_c c \left(1 - \frac{c}{K_c} - \alpha_{cw} \frac{w}{K_w}\right)}^{\text{growth}}, \tag{3.1.1}$$

$$\frac{\partial m}{\partial t} = \overbrace{D_m \nabla^2 m}^{\text{diffusion}} + \overbrace{r_m c}^{\text{production}} + \overbrace{d_m m}^{\text{reabsorption}}, \tag{3.1.2}$$

$$\frac{\partial w}{\partial t} = \overbrace{r_w w \left(1 - \frac{w}{K_w} - \alpha_{wc} \frac{c}{K_c}\right)}^{\text{growth}} - \overbrace{d_m m w}^{\text{tissue death}} + \overbrace{\nabla \cdot (D_w[c] \nabla w)}^{\text{diffusion}}. \tag{3.1.3}$$

Here, the constants are:

$D_c[w]$ normal tissue-dependent cancer cell diffusion coefficient,

r_c growth rate of cancerous tissue,

K_c carrying capacity of cancerous tissue,

α_{cw} parameter characterising tumour tissue growth reduction due to competition with normal tissue,

K_w carrying capacity of normal tissue,

D_m H^+ ion diffusion coefficient,

r_m H^+ ion production rate,

d_m H^+ ion reabsorption rate,

r_w growth rate of healthy tissue,

α_{wc} parameter characterising normal tissue growth reduction due to competition with tumour tissue,

$D_w[c]$ cancerous tissue-dependent normal tissue diffusion coefficient.

As equation (3.1.1) shows, in Gatenby and Gawlinski (1996) cancer cells underwent non-linear diffusion. The rate of diffusion was assumed to depend on the density of the normal tissue, w—the higher the density of the normal tissue, the lower the diffusion of the logistically growing cancerous tissue. The cancerous tissue produced H^+ ions at rate r_m, as equation (3.1.2) shows. These H^+ ions also diffused with coefficient D_m and they underwent linear decay at rate d_m. The decay rate took into account the effects of mechanisms that increase the local tissue pH via reabsorption of H^+ ions, such as large scale vascular evacuation and buffering. The H^+ ion production and reabsorption rates were taken to be equal for simplicity. Furthermore, H^+ ions were assumed to degrade the logistically growing normal tissue, as shown in equation (3.1.3).

The model was non-dimensionalised and studied using both travelling wave analysis and computer simulations. Using data from *in vivo* measurements of interstitial pH gradients in healthy and in cancerous tissue, which had recently become available through experiments by Martin and Jain (1994), Gatenby and Gawlinski (1996) predicted the existence of a pH gradient as well as the gradient's range correctly and found growth rates of malignant and benign tumours to *'reasonably approximate clinical observations'*.

Truly groundbreaking about the seminal work by Gatenby and Gawlinski (1996) was the prediction of a biological phenomenon that had not yet been observed experimentally. They closely examined the effect of the tissue degradation rate. The crucial corresponding non-dimensional parameter they examined in this regard was $\gamma = \frac{d_w}{d_m} \times \frac{r_m}{r_w} \times K_c$. For a tumour to be invasive, they found that $\gamma > 1$ was required. Different values of $\gamma > 1$ corresponded to different invasive tumour-host tissue-interfaces. Arguably the most interesting case was $\gamma >> 4$, when a hypocellular gap between the invading tumour and the reclining normal tissue edges was predicted. This is a fascinating case in the short history of mathematical oncology as the examination of tissue samples in response to the outcome of their mathematical model did indeed confirm the existence of this hypocellular gap, which previously had not been discovered by the medical community. The simulations and corresponding experimental results are shown in Figure 3.1.

Clinical research at the time had recently brought the attention of the scientific community to the role of MDEs in cancer invasion. The MDEs themselves and their effect on the ECM density were included in a number of reaction-diffusion-taxis PDE models following (Gatenby and Gawlinski, 1996). These models accounted for the effect of directed cell migration—as a response to gradients in ECM density or in adhesive molecules located in the ECM—on cancer invasion. The gradients in ECM occur naturally in the body but are especially relevant in cancer invasion as the cancer cells secret MDEs that degrade the ECM locally, as described in Section 2.3.2.

A first model of several that considered random motility, haptotaxis and/or chemotaxis in the context of invasive cancer cells interacting with MDEs, ECM proteins, normal cells and non-invasive cancer cells was published by Perumpanani et al. (1996). Like Gatenby and Gawlinski (1996), they analysed their one-dimensional model using a combination of travelling wave analysis and computer simulations. This way, they examined how deeply and at what speed cancer cells invade the ECM when led by hapto- and chemotactic cues. They found the invasion speed and the invasion wave profile to be determined by the profile of local chemoattractants as well as by the phenotypic composition of the tumour and the ECM.

A renowned model focussing on haptotaxis is the continuum PDE model by Anderson

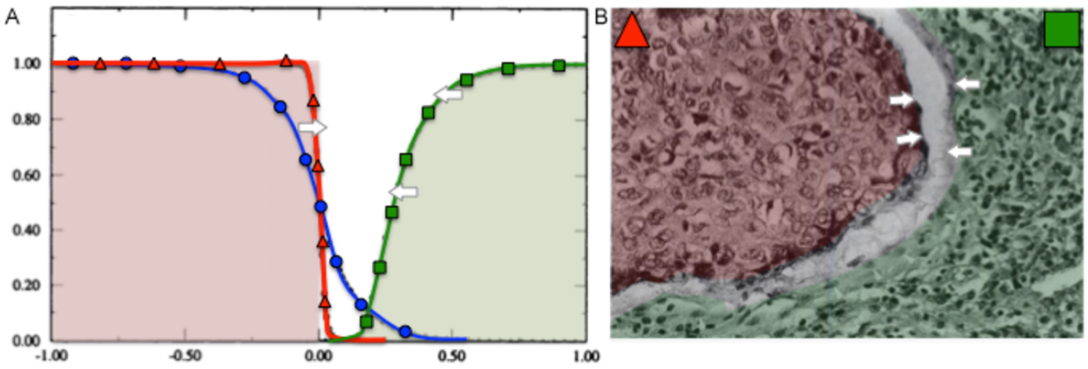

Figure 3.1: ***Hypocellular interstitial gap discovered through PDE model.*** *(A) Computer simulations with a degradation rate of healthy tissue $\gamma = 12.5$ resulted in a significant hypocellular gap (pointed at by the white arrows) between advancing cancer tissue front (red) and retracting normal tissue (green). The blue circles represent H^+ ions, which are secreted by the cancer cells, diffuse into the healthy tissue and degrade it. (B) Subsequently initiated hematoxylin-eosin (H & E) stained micrograph of the tumour-host interface confirms the existence of the previously unrecognised hypocellular interstitial gap. Originally published in Gatenby and Gawlinski (1996); depicted modified version taken from Enderling and Chaplain (2014) with permission from Bentham Science Publishers Ltd.*

et al. (2000), which—to our knowledge—was the first of its kind that extended PDE modelling to a second dimension. The full system of PDEs is described in equations (4.1.1), (4.1.9) and (4.1.10). Like other authors have done in the past (e.g. Gerisch and Chaplain (2008), *cf.* Section 3.1.2), we will base our model of local cancer cell invasion model on Anderson et al. (2000). Unlike many previous models, including Gatenby and Gawlinski (1996), the system of PDEs proposed in Anderson et al. (2000) neither included a cancer cell population growth nor ECM remodelling term. Instead, they suggest accounting for cell growth after discretising the model with a central difference scheme (*cf.* hybrid models in Section 3.1.1).

Subsequently, several continuum reaction-diffusion-taxis PDE models that focussed on MDEs in the form of uPAs and MMPs were proposed. The role of uPA, one type of proteolytic enzyme over-expressed in invading cancer cells, has, for instance, been studied by Chaplain and Lolas (2005, 2006) using different systems of reaction-diffusion-taxis PDEs and—building on the former and latter, respectively—by Kolbe et al. (2016) and Andasari et al. (2011). In all these papers, spatiotemporally heterogeneous invasion patterns were observed in the model-based simulations.

Chaplain and Lolas (2006) approached modelling cancer invasion by a system of three PDEs to account for the spatiotemporal interaction between cancer cells, uPA and ECM. Contrary to the model proposed by Anderson et al. (2000), cancer cell proliferation, as well as ECM remodelling, were both included in this two-dimensional model. In the absence of the ECM, cancer cells were assumed to follow logistic growth. However, competition for space between cancer cells and the ECM was included via a crowding term. Further, cell movement due to random diffusion, haptotaxis and chemotaxis was accounted for. The following dimensional PDE system was suggested in Chaplain and Lolas (2006):

$$\frac{\partial c}{\partial t} = \overbrace{\nabla \cdot (D_c \nabla c)}^{\text{diffusion}} - \overbrace{\nabla \cdot (\chi c \nabla m)}^{\text{chemotaxis}} - \overbrace{\nabla \cdot (\phi c \nabla w)}^{\text{haptotaxis}} + \overbrace{\rho c(1 - \frac{c}{c_0} - \frac{w}{w_0})}^{\text{proliferation}}, \tag{3.1.4}$$

$$\frac{\partial m}{\partial t} = \overbrace{D_m \nabla^2 m}^{\text{diffusion}} + \overbrace{\alpha c}^{\text{production}} - \overbrace{\nu m}^{\text{decay}}, \tag{3.1.5}$$

$$\frac{\partial w}{\partial t} = \overbrace{\mu c(1 - \frac{c}{c_0} - \frac{w}{w_0})}^{\text{re-establishment}} - \overbrace{\gamma m w}^{\text{degradation}}. \tag{3.1.6}$$

Similarly to before, for $\mathbf{x} \in \mathbb{R}^2$,

$c(t, \mathbf{x})$ cancer cell density,

$w(t, \mathbf{x})$ ECM density,

and, slightly different to the section above as we are now considering uPAs rather H^+ ions,

$m(t, \mathbf{x})$ uPA concentration.

Additionally, we have the following:

D_c (linear or non-linear) cancer cell diffusion coefficient,

χ chemotactic function,

ϕ haptotactic function,

ρ cancer cell proliferation rate,

c_0 maximum sustainable tumour cell density,

w_0 maximum sustainable ECM density,

D_m constant uPA diffusion coefficient,

α rate of uPA production by cancer cells,

ν uPA decay rate,

μ constant ECM production rate,

γ ECM degradation rate.

In their preceding paper, Chaplain and Lolas (2005) proposed a system of five equations, which described the interactions between cancer cells, uPA, uPA inhibitors of type *plasminogen activator inhibitor-1* (PAI-1), the ECM-cleaving and MMP-activating enzyme plasmin, and the ECM component vitronectin. Cancer cells diffused and moved in response to both chemo- and haptotactic cues. While uPA and its inhibitor PAI-1 triggered chemotactic movement, the ECM component vitronectin induced haptotactic movement. Spatiotemporally heterogeneous patterns were observed in simulations of the cell movement.

The model by Andasari et al. (2011) extended and analysed the system of equations initially proposed in Chaplain and Lolas (2005). Moreover, it allowed for cancer cells to mutate into a phenotype which diffuses, migrates and proliferates more rapidly, which was modelled using a Heaviside function. While the current biological evidence on EMT-related phenotypic changes somewhat contradicts the notion of such a 'go-*and*-grow' mutation, the proposed model was an important step towards modelling mutations in cell phenotype in spatial cancer invasion models. Andasari et al. (2011) further showed by linear stability analysis that the observed spatiotemporally heterogeneous patterns were caused by a taxis-driven instability of the spatially homogeneous steady state.

The analytical and numerical study of a system of equations as proposed in Chaplain and Lolas (2005) constitutes challenges since exploring it using classical numerical methods requires very fine discretisation of the grids to accurately resolve the dynamics. To this end, Kolbe et al. (2016) applied adaptive mesh refinement techniques to the model with the aim of resolving the dynamics of the system's solution accurately with reasonable computational cost. As a result, a higher-order, stable, and robust numerical method for the system of equations originally established in Chaplain and Lolas (2005) was proposed.

Hellmann et al. (2016) proposed a model, in which cancer cell haptotaxis, ECM degradation by MMPs, and production of MMPs by cancer cells were taken into account based on the work in Anderson et al. (2000). Yet, they extended the model by considering additional features. The spatiotemporal evolution of differentiated cancer cells and of *cancer stem cells* (CSCs), which have biological properties comparable to the epithelial-like and the mesenchymal-like cancer cells in our model, respectively, was included in the model. Also, EMT as well as logistic proliferation and MMP production of the cancer cells were considered. In particular, in Hellmann et al. (2016) EMT was triggered by *epidermal growth factors* (EGFs) in the ECM. This way, physiological mechanisms that lead to EMT from differentiated cancer cells to CSCs were accounted for in the model. To study the invasion of both types of cancer cells into the ECM, an advection-reaction-diffusion system of Keller-Segel taxis type was used. Numerical simulations were proposed as a proof of concept to show that combining the two systems can account for EMT in a biologically accurate manner.

Sfakianakis et al. (2017) developed this model of EGF-driven EMT further by also accounting for transdifferentiation of the CSCs to *cancer-associated fibroblasts* (CAFs) as well as fibroblast-driven remodelling of the extracellular matrix. The extended model was then analysed in a component-wise manner. In the corresponding simulations, the detachment of CSCs from the main tumour body of differentiated cancer cells—due to the ability of CSCs to invade the tissue comparatively more rapidly—was reproduced qualitatively.

By building on a multiscale moving boundary method introduced by Trucu et al. (2013), a multiscale model of cancer invasion was suggested by Peng et al. (2017). In this work, the above-mentioned models by Chaplain and Lolas (2005); Andasari et al. (2011) were used to govern the macroscale (i.e. tissue scale) dynamics of cancer invasion. The microscale (i.e. cell-level) dynamics were expressed using a system of three coupled PDEs, which described the local dynamics of the spatiotemporal interaction of uPA, PAI-1 and plasmin. Together, these equations at two scales described not only the evolution of the invasive edge of the tumour in time and space but also how the macroscopic movement on the tissue scale was induced by dynamics at the cell level. Simulations based on this model presented heterogeneous invasion patterns, which qualitatively resembled those found in tissues of many cancer types. Insights gained through this continuum model concerned the depth of finger-like protrusions at the tumour boundary into the tissue as well as the existence of heterogeneous patterns inside the tumour. For instance, heterogeneous initial ECM conditions, which are representative of the ECM in the human body, led to a more finger-like tumour spread than homogeneous ones. Further, heterogeneous patterns inside the tumour region revealed that chemotaxis dominated the invasive cancer cell movement. Quantitative predictions were not possible as the model was not (yet) calibrated or dimensionalised.

Karagiannis and Popel (2004) presented an ODE model that accounts for the role of MDEs of type MMP, rather than of uPAs like in previous models. Here, the role of pro-MMP-2-activation by MT1-MMP together with TIMP2 in cancer invasion was studied. It was suggested to use the model as a means of quantifying the activation of pro-MMP-2 as a function of TIMP2 and MT1-MMP concentrations in a well-mixed scenario.

Furthermore, Deakin and Chaplain (2013) developed a spatial approach to investigating the roles of membrane-bound MMPs like MT1-MMP and soluble MMPs like MMP-2. This approach also accounted for the effects of ECM density, which affects how effectively each the two MMPs invade the ECM. Their modelling approach consisted of a system of seven PDEs describing the spatiotemporal interaction of cancer cell density, ECM density, the *matrix suitability modifier*[1], and the concentrations of MMP-2, MT1-MMP, TIMP2 and of MT1-MMP:TIMP2 complex. The results of this model produced matrix heterogeneity using ECM degradation only, which allowed separating the effects that result from ECM degradation by MMPs as opposed to those arising from pre-existing heterogeneity in matrix density. In particular, they found that ECM environments that force invasion to rely on MT1-MMP only resulted in a slower invasion—as did TIMP2 overproduction.

Local discrete and hybrid invasion models

While the above-mentioned continuum models have been used to make great advances in producing qualitative insights into cancer invasion, all of them described cancer invasion using cancer cell *density*. Consequently, these continuum models cannot follow the movement of individual cells as they invade the ECM. However, it appears that the minority of cancer cells that invade further into the ECM than others while carrying crucial mutations are typically exactly those cells that ultimately cause life-threatening metastases.

[1]This was a PDE describing the degree of difficulty the cells experience when invading the ECM. It further accounted for the amount of ECM that was still degradable.

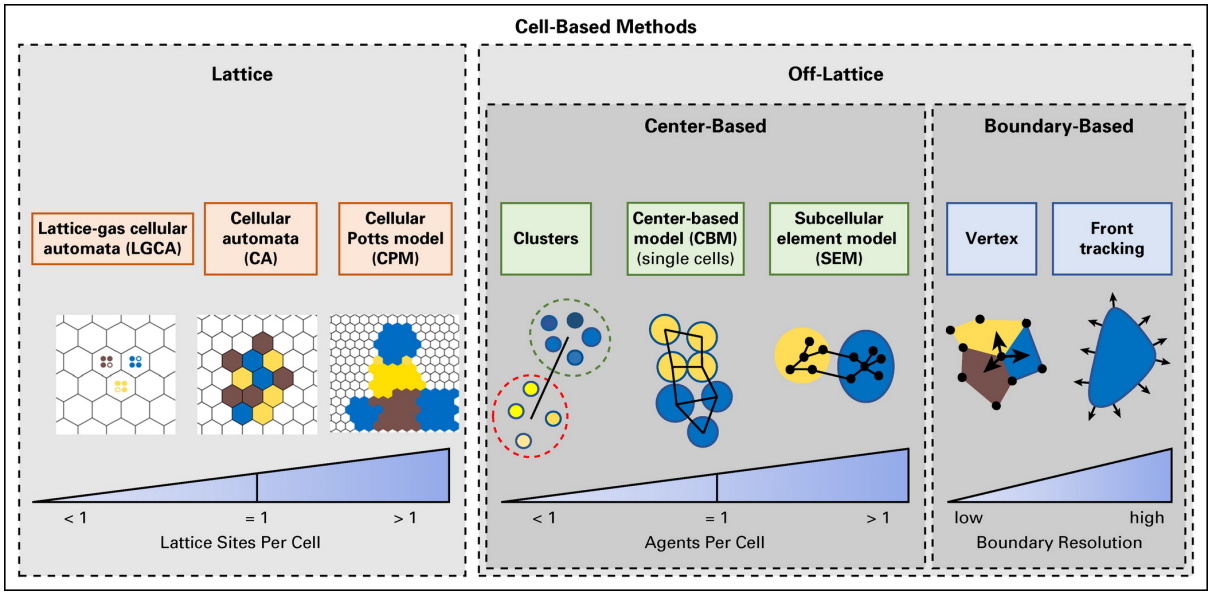

Figure 3.2: ***Schematic overview of discrete cell-based modelling methods.*** *Discrete cell-based methods can be classified into lattice-based models (left) and off-lattice models (right). The latter can be distinguished further into centre-based versus boundary-based methods. Specific examples of each of these types of models are explained schematically. More detailed explanations and examples from the literature regarding applications of the modelling techniques to cancer invasion are given in the text. Reproduced from Metzcar et al. (2019) with permission from the American Society of Clinical Oncology.*

Moreover, phenotypic properties—such as mutations, cell size or cell shape—which are intrinsically important to cancer growth, also can best be captured when modelling at the level of the individual cell. To this end, advances in computational speed have increased the popularity of discrete and hybrid modelling approaches, which are, on average, computationally more costly than their continuum counterparts.

Discrete, or *cell-based*, methods for modelling of cancer invasion can be broadly classified into *lattice-based* and *off-lattice* models (see Figure 3.2). Modelling techniques falling into the former category include IBMs, which are also known as *agent-based models* (ABMs), as were presented for instance in Anderson and Chaplain (1998); Anderson et al. (2000); Zhang et al. (2009), *cellular automata models* (CAMs) like Kansal et al. (2000); Patel et al. (2001); Deutsch and Dormann (2005); Hatzikirou and Deutsch (2008); Enderling et al. (2009), extensions of CAMs— namely, *lattice gas cellular automata* (LGCA) models as proposed in Dormann and Deutsch (2002); Wurzel et al. (2005); Hatzikirou et al. (2010, 2015), *cellular Potts models* (CPMs) approaches as used in Turner and Sherratt (2002); Popławski et al. (2009); Kabla (2012); Scianna et al. (2013); Hallou et al. (2017), and *hybrid discrete-continuum models* as found in Anderson (2005); Rejniak and Anderson (2011); Sfakianakis et al. (2018a). Off-lattice models like Ramis-Conde et al. (2008a,b), on the contrary, do not require agents to stay on lattices but are *force-based* instead. These include *centre-based models* (CBMs) such as Kim and Othmer (2013) and boundary tracking models, e.g. Rejniak (2007); Fletcher et al. (2014). This list of discrete modelling approaches does not claim completeness—a wide range of such approaches has been used to study cancer invasion. To give an overview, we will give a short explanation

of the above-mentioned model types in what follows. The review sections of the papers we give as examples for the respective model type contain further information.

CAMs consist of a finite-dimensional—typically regular—grid of cells, each in one of a finite number of states. A basic scenario would be a 'grid' in the form of a one-dimensional line with two states, which e.g. represent *on* and *off*. However, Cartesian grids of an arbitrary number of dimensions may be considered. The most common and historically earliest CAMs are two-dimensional. These could, for instance, take the shape of squares, triangles and hexagons. The initial cell constellation evolves through a number of discrete time steps based on the states of the cells in the neighbourhood of a particular cell. The change in state typically occurs according to typically one but sometimes multiple set rules, which can generally be expressed as mathematical functions. The rules are applied iteratively for the desired number of steps (Toffoli and Margolus, 1987; Schiff, 2011). The concept of the cellular automaton was discovered by John von Neumann in the 1940s in the context the development of a self-replicating machine, the so-called *universal constructor*. His work was published posthumously in Von Neumann and Burks (1966). CAMs in tumour growth have been reviewed in Moreira and Deutsch (2002).

An extension to CAMs, so-called LGCA models, allow for multiple cells per lattice site (Wolf-Gladrow, 2004; Deutsch and Dormann, 2005). Instead of tracking the movement of individual cells, they account for the number of cells that move through channels between the lattice sites. As a result, LGCAs can simulate large numbers of cells over long periods (Metzcar et al., 2019).

Potts models are another extension to CAMs: Different to standard CAMs, Potts models identify individual cells by indexing them with a *spin number* Q. The CPM is a modification of a Potts model with a large spin number Q that was introduced by Graner and Glazier (1992) to examine the sorting behaviour of two cells differing in adhesivity. CPMs applied to cancer have for example been reviewed in Szabó and Merks (2013). The stochastic multiparticle CPMs use probabilistic rules to update lattice sites one after the other. The models typically have two or three dimensions. Different to CAMs, CPMs can express cell types and shapes as cells can extend over more than one grid point, as shown in Figure 3.3. Assuming that we are looking at a model that captures cells moving on a two-dimensional grid, for a population of N cells, each cell is assigned one of the N spins $Q(x_i, y_j) = 1, ..., N$, where (x_i, y_j) is a generic grid point occupied by a cell. So if two or more grid points have the same spin Q, this implies that the same cell resides on them. Moreover, different types can be assigned to (groups of) cells. Graner and Glazier (1992), for instance, distinguished between three types $T(Q) = l, d$, or M. While l and d represented cells of low and high adhesivity, respectively, M modelled the ECM. At each time step, the spin number Q of a grid point changed with a certain probability, allowing cell sizes and shapes to evolve over time. How the spin numbers changed in Graner and Glazier (1992) depended on whether the potential new configuration had lower, higher or equal surface tension, which reflected the adhesive forces between the cells. Two neighbouring cells with high adhesivity, for example, would have low surface energy—those with low adhesivity, on the contrary, high surface energy.

To integrate the effect of locally varying gradients of chemoattractants on cell movement into invasion models, Anderson and Chaplain (1998) developed a technique in their discrete quasi-stochastic model of tumour-induced angiogenesis. In this model, individual endothelial cells moved up TAF and fibronectin gradient concentrations in addition

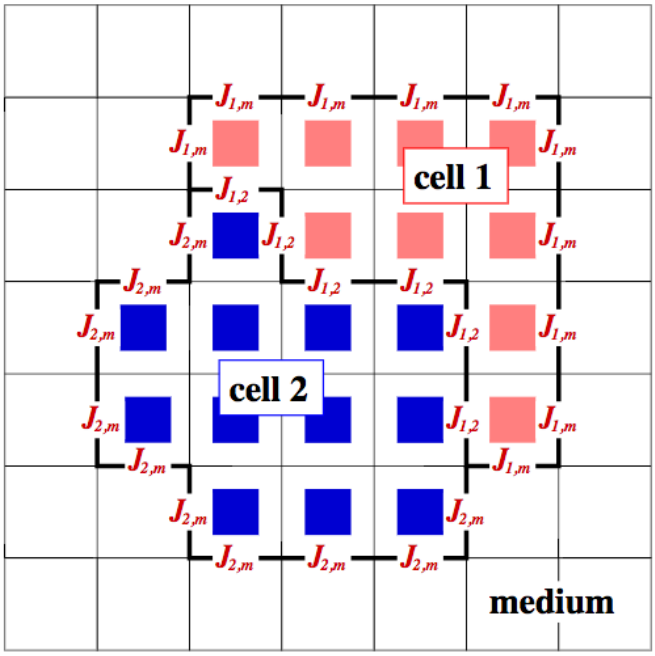

Figure 3.3: ***Example of two cells of different shape in the CPM.*** Cell 1 *and* cell 2 *are depicted in some medium. Their boundaries contain information about the local adhesion coefficient* $J_{i,j}$ *between* cell 1 *and* cell 2*, or between one of them and the medium. High adhesivity tends to increase the contact surface between the two entities involved. Reproduced from Le Guillou et al. (2009) with permission from AMSI & Collegium Basilea.*

to permanently moving by random diffusion. Hence, they performed a *biased* random walk. By using an IBM that is derived from the continuum model using a *Forward-Time Central-Space* (FTCS) finite-difference scheme, Anderson and Chaplain were not only able to recover the qualitatively realistic large-scale results of their continuum PDE model, but also to track the paths of single endothelial cells, which led the tip of a vessel sprout. This enabled them to simulate the growth path of vessel sprouts. Thus, their simulation results reproduced a capillary network of qualitatively realistic morphology and structure.

In Anderson et al. (2000), the same technique was applied to the problem of cancer invasion, laying a foundation for discrete quantitative invasion modelling. Anderson et al. (2000) obtained their IBM by discretising the system equations (4.1.1), (4.1.9) and (4.1.10), using the same FTCS scheme as described in Chapter 4. This yielded the discretised model in equations (4.1.3), (4.1.4) and (4.1.5).

Both the continuum and the discrete model showed that haptotaxis and ECM structure were important for cancer invasion. While the continuum model in equations (4.1.1), (4.1.9) and (4.1.10) did not include proliferation, this was considered in the discrete model via proliferation rules that were added to the discretised model. These allowed for mitosis once a parent cell had reached maturity as long as there was enough space for two daughter cells in the immediate neighbourhood of the parent cell. Furthermore, the discrete model emphasised that the ECM structure may aid individual cancer cells to escape from the main tumour via haptotaxis. This is a crucial feature in modelling metastasis, yet

these cells could not be observed when considering continuous cancer cell densities rather than the evolution of individual cancer cells. The authors argued that this phenomenon potentially had important consequences in a clinical setting as the model predicted that single cancer cells moved further into the tissue than surgeons can predict by visual inspection.

The above-mentioned IBMs (Anderson and Chaplain, 1998; Anderson et al., 2000) contained more information than a basic CAM on each grid point: Rather than solely incorporating Boolean-type information about the occupancy of a grid point, they assigned additional phenotypic features to it. Anderson (2005) also used the FTCS scheme to discretise a model consisting of the continuum model in equations (4.1.1), (4.1.9) and (4.1.10) with an additional fourth equation describing the oxygen concentration on the grid. However, the crucial difference in this model was that only the movement of the cancer cells and their cell-specific processes—such as proliferation, death, mutation, cell-cell adhesion, MDE production, and oxygen uptake—were modelled by discretisation of the continuum equations and thus simulated by imposing cellular automata-like rules. The spatiotemporal evolution of oxygen concentration, ECM density and MDE concentration was still modelled using a continuum approach, in accordance with their physically near-continuous nature. Due to this combination, the authors named their approach a *hybrid* model. The results and insights obtained using this hybrid approach could not be recovered by using the continuum model alone. They included the observation that, while cell-cell interaction was important in the early developmental stages of a tumour, cancer cell-matrix interactions master the geometry of the tumour later on due to mutations occurring during tumour growth. These mutations caused those cancer cells that survive the process of natural selection to lose cell-cell adhesion and to, in general, become increasingly aggressive. Aggressive features in the framework of the model included: a large haptotactic coefficient, a low proliferation age, a large oxygen uptake, high MDE production as well as expressing low to no cell-cell adhesion. The results in Anderson (2005) suggested that cancer cells of aggressive phenotypes, which had been introduced into the cell population through random mutations, would ultimately dominate in the tumour.

More recently, Sfakianakis et al. (2018a) introduced a coupled two-dimensional hybrid system that governed the spatiotemporal evolution of individual mesenchymal cancer cells by a system of *stochastic differential equations* (SDEs), while the collectively moving epithelial cancer cells, the ECM and the MMPs evolved according to PDEs. This novel modelling technique considered the effects of EMT and MET—so of the transition of cancer cells between the epithelial and the mesenchymal phenotypic state—on cancer invasion using phase transition operators. As a result, the *in silico* invasion assays simulated using the Sfakianakis et al. (2018a) approach presented 'islands' of invading cancer cells ahead of the expanding initial main cancer cell mass, which had arisen from EMT and subsequent MET. A sample simulation is shown in Figure 3.4. These 'islands' at some distance from the tumour mass are frequently observed *in vivo* but do not typically present themselves in solely macroscopic or atomistic cancer invasion models.

Lattice free, force-based models (see left and middle panel of Figure 3.2) can be grouped into models that track the cells' centre of mass, so-called *centre-based models* (CBMs), and those focussing on cell boundaries. A brief explanation, largely based on the review in Metzcar et al. (2019), follows.

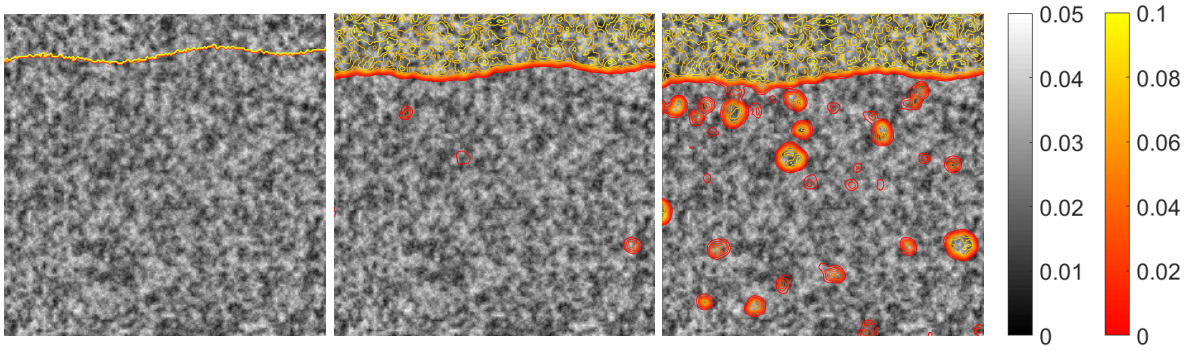

Figure 3.4: ***Simulation results from hybrid multiscale model of cancer invasion by Sfakianakis et al. (2018a).*** *The spatiotemporal evolution of an initially uniformly dense epithelial-like cancer cell population placed on top of the two-dimensional representation of an invasion organotypic assay consisting of ECM of heterogeneous density is depicted at times $t = 1$, $t = 150$ and $t = 200$ (left to right). The density of the epithelial-like cancer cells is represented via yellow and red isosurfaces corresponding to the outer colour bar; the heterogeneous ECM density (grey) corresponds to the inner colour bar. EMT spawns mesenchymal-like cancer cells (not depicted here), which can invade the ECM via haptotaxis and thus much more rapidly than the slowly diffusing epithelial-like cancer cells at the cost of their proliferative potential. The reverse process, MET, creates the 'islands' of epithelial-like cancer cells observed in the middle and right panel, which eventually reconnect with the invading tumour mass (right panel). Authorised use of authors' copy of the figure.*

CBMs represent cells as points or volumes of spheres or more realistic shapes. Their positions are updated according to locomotive, drag-like, adhesive and repulsive forces. Using this approach, multiple cells can be modelled as functional units where biologically appropriate (e.g. when modelling mammary glands). Also, at additional computational cost, single cells can be broken down into their subcellular units, which are modelled to interact via mechanical forces, to better represent cell morphology.

Boundary-tracking models make use of vertex-based, level set and front-tracking methods. To apply the former method, cells are represented as polygons and polyhedra, in two and three dimensions, respectively. Then, the forces acting on their vertices are computed. This vertex-based method is especially useful when modelling surfaces that are completely covered in cells. Front-tracking methods compute fluid flow inside and between cells by solving PDEs and then advect boundary points along cell membranes in this flow. Finally, level set methods implicitly track all boundary movement but are computationally highly costly.

3.1.2 Non-local invasion models

Many of the local reaction-diffusion(-taxis) models mentioned in the section above assume that cells move in response to hapto- or chemotactic gradients in the tissue. As explained in Section 2.1.1, this involves the binding and loosening of cell-matrix and cell-cell adhesions. Depicted in Figure 2.1 are the proteins involved in cell-cell binding (*cadherins*) and in cell-matrix attachment (*integrins*). Signals in the microenvironment

of a cell influence how often these attachments are unbound and rebound as well as how strong the adhesive forces are, which affects cancer cell movement.

To this end, *non-local* PDE models in the form of integro-differential equations, which incorporate cell-cell adhesion using integral terms, have been developed. A first non-local model for adhesion was proposed in Sekimura et al. (1999) in the context of pattern formation of scale cells in the wings of butterflies and moths. Differential adhesion was first explored in a continuum model of adhesion forces and their influence on cell movement proposed by Armstrong et al. (2006). They accounted for adhesion by an integral term, which modelled non-local interactions in the PDE model. Their model was the first of its kind to include cell-cell adhesion in a continuum model of interacting cell populations. Applications to both single-cell and multi-cell populations were presented. While not considering cancer invasion explicitly, it was found that when studying the cell sorting behaviour in a cell population consisting of multiple cell types, the resulting behaviour resembled that observed in experiments. While this had previously been achieved using discrete approaches, the technique in Armstrong et al. (2006) pioneered in the inclusion of cell-cell adhesion in a continuum model of interacting cell populations.

Two years later, Gerisch and Chaplain (2008) based their first non-local cancer invasion PDE model on Armstrong et al. (2006). They represented one or more cancer cell populations by a PDE each and additionally considered a PDE to represent the ECM, which was modelled to be fixed in space. They extended the continuous local haptotaxis-based PDE model in Anderson et al. (2000) to include cell proliferation and ECM remodelling. Also, by adding non-local terms, cell-matrix and cell-cell adhesion were considered explicitly. To incorporate this non-local phenomenon, the haptotactic flux term, which had been assumed to be local in previous models, was replaced by the non-local flux term $-cA\mathbf{u}$ (explained below). In notation coherent with previously mentioned models wherever possible, the dimensional system of equations became:

$$\frac{\partial c}{\partial t} = \overbrace{\nabla \cdot (D_c \nabla c - cA\mathbf{u})}^{\text{diffusion/adhesion}} + \overbrace{\rho c(1 - \theta_c c - \theta_w w)}^{\text{proliferation}}, \tag{3.1.7}$$

$$\frac{\partial m}{\partial t} = \overbrace{\nabla \cdot (D_m \nabla m)}^{\text{diffusion}} + \overbrace{\alpha c}^{\text{production}} - \overbrace{\nu m}^{\text{decay}}, \tag{3.1.8}$$

$$\frac{\partial w}{\partial t} = \overbrace{\mu(1 - \theta_c c - \theta_w w)}^{\text{remodelling}} - \overbrace{\gamma m w}^{\text{degradation}}, \tag{3.1.9}$$

where, like in equations (3.1.4)–(3.1.6) but with $\mathbf{x} \in \Omega$, where Ω is the respective spatial domain:

$c(t, \mathbf{x})$ cancer cell density,

$w(t, \mathbf{x})$ ECM density,

and, slightly differently than in the above section as now generic MDEs were considered rather uPAs specifically,

$m(t, \mathbf{x})$ MDE concentration.

Furthermore, the following constants were defined:

D_c cancer cell diffusion coefficient,

ρ cancer cell proliferation rate,

θ_c fraction of 1 unit volume of physical space occupied by cancer cells at unit density,

θ_w fraction of 1 unit volume of physical space occupied by ECM at unit density,

D_m MDE diffusion coefficient,

α rate of MDE released by cancer cells,

ν MDE decay rate,

μ ECM remodelling rate,

γ ECM degradation rate.

The most crucial difference, however, was the non-local $A\mathbf{u}$-term, where $\mathbf{u} = (c, w, m)$, which the authors referred to as the *adhesion velocity*. On a one-dimensional domain Ω—again building on previous work by Armstrong et al. (2006)—this was defined to be a function of $\mathbf{x} \in \Omega$ and of time t:

$$A\mathbf{u} := \frac{1}{R} \int_0^R \sum_{k=0}^{1} \mathbf{n}(k) \cdot \Omega(r) g(\mathbf{u}(t, \mathbf{x} + r\mathbf{n}(k))) dr, \tag{3.1.10}$$

where the right and left unit outer normal vectors were $\mathbf{n}(k) = -1^k$, $k = 0, 1$. On a two-dimensional domain Ω, the adhesion velocity became

$$A\mathbf{u} := \frac{1}{R} \int_0^R r \int_0^{2\pi} \mathbf{n}(\theta) \cdot \Omega(r) g(\mathbf{u}(t, \mathbf{x} + r\mathbf{n}(\theta))) d\theta dr, \tag{3.1.11}$$

with the unit outer normal vector corresponding to angle θ given by $\mathbf{n}(\theta) = (\cos\theta, \sin\theta)^\top$. $R > 0$ was the *sensing radius* of a cell located at $\mathbf{x}$; $\Omega(r)$ was the *radial dependency function*, which depended on the distance $r \geq 0$ from $\mathbf{x}$; and $g(\mathbf{u})$ was the vector of concentrations $\mathbf{u}$, which in the case of Gerisch and Chaplain (2008) were the cancer cell density c and the ECM density w at time t and location $\mathbf{x} + r\mathbf{n}$:

$$g(c, w) = (S_{cc}c + S_{cw}w) \cdot (1 - \theta_c c - \theta_w w)^+,$$

where $(\cdot)^+ := max\{0, \cdot\}$, and S_{cc} and S_{cw} were the cell-cell and cell-matrix adhesion coefficients, respectively. $\Omega(r)$ was taken to be a measure of how strongly points within the sensing region influence the adhesion velocity. The two variations of this measure considered by Gerisch and Chaplain (2008), and also used previously used by Armstrong et al. (2006), were

$$\Omega_1(r) = \frac{1}{2R} \quad \text{and} \quad \Omega_2(r) = \frac{1}{\pi R^2}.$$

These described the one- and two-dimensional case, respectively, where any point in the sensing region had the same influence on adhesion velocity. The alternative formulations

$$\Omega_2(r) = \frac{1}{R}\left(1 - \frac{r}{R}\right) \quad \text{and} \quad \Omega_2(r) = \frac{3}{\pi R^2}\left(1 - \frac{r}{R}\right)$$

were used when the influence was supposed to be decreasing the further the points were away from $\mathbf{x}$.

Sherratt et al. (2009) proposed a similar non-local PDE model of cancer invasion also based on Armstrong et al. (2006). Simulations of cancer cell profiles invading the ECM from both of these models delivered results of similar quality to those obtained by previous reaction-diffusion-taxis cancer invasion models. However, it generally appeared that including the non-local cell-cell adhesion term tended to slow down the cancer cells' invasion rate. Also, both Gerisch and Chaplain (2008) and Sherratt et al. (2009) found that for a given cell-matrix adhesion parameter, a large enough cell-cell adhesion parameter could be chosen to stop invasion completely in their computational simulations.

Chaplain et al. (2011) studied the nature of the proliferative properties of non-local PDE models analytically by proving some results based on Gerisch and Chaplain (2008). Furthermore, computational simulations illustrating the relative effects of cell-cell and cell-matrix adhesion on cancer invasion were provided.

Domschke et al. (2014) further developed work by Gerisch and Chaplain (2008), who had extended the continuous local haptotaxis-based PDE model proposed in Anderson et al. (2000) to include cell proliferation and ECM remodelling as well as cell-matrix and cell-cell adhesion by adding non-local terms. In particular, Domschke et al. (2014) introduced a subpopulation of cancer cells that arose from the initial cell population by mutation, which was modelled using a Heaviside function. The mutation resulted in a decrease in self-adhesion and an increase in cell-matrix adhesion, which caused the mutated cancer cells to spread more rapidly into the surrounding tissue—as coherent with the current biological understanding that EMT causes more invasive phenotypes.

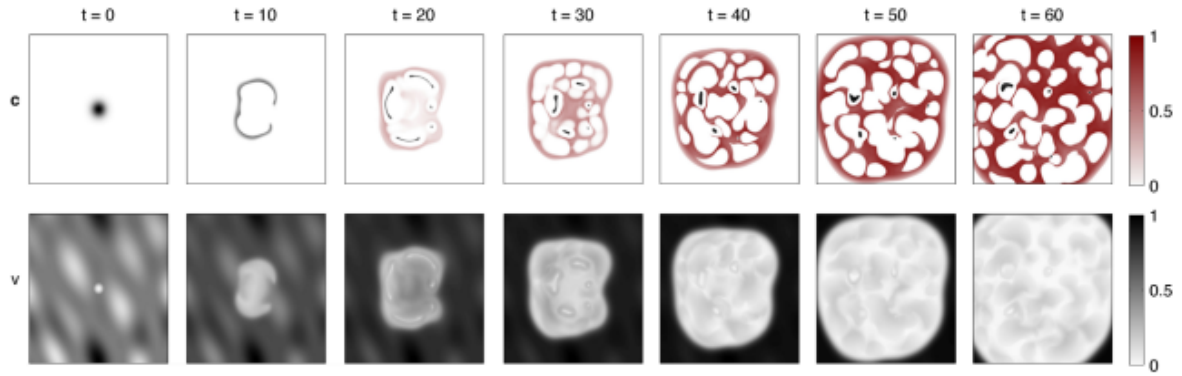

Figure 3.5: ***Example of simulation results from two species non-local partial integro-differential equation model by Domschke et al. (2014).*** *For the time steps $t = 0, 10, 20, 30, 40, 50, 60$, the top row shows the superimposed non-dimensionalised cancer cell densities of two subpopulations c_1 (black) and c_2 (red), while the bottom row shows the ECM density w. The red colour bar refers to c_2, the black one to both c_1 and w. Reproduced from Domschke et al. (2014) with permission from Elsevier.*

Domschke et al. (2014) further developed the model by Gerisch and Chaplain (2008) to study the influence of cell-cell and cell-matrix adhesion on tumour growth and development in more depth. In particular, they introduced a subpopulation of cancer cells that arose from the initial cell population by mutation, which was modelled using a Heaviside function. The mutation resulted in a decrease in self-adhesion and an increase in cell-matrix adhesion, which caused the mutated cancer cells to spread more rapidly into the surrounding tissue— coherent with the current biological understanding that EMT causes more invasive phenotypes, *cf.* Section 2.3.2. Simulations showed various heterogeneous cancer cell infiltration patterns arising from changes in the cell-cell and cell-matrix adhesion properties, which had been held fixed in previous models, as well as from altering initial conditions. Finally, the effects of letting adhesion coefficients depend on time, rather than taking them to be constant, were investigated. Figure 3.5 presents an example of the computational results obtained by Domschke et al. (2014).

3.2 Mathematical models of metastasis

While representing invasion and metastasis as uncoupled, independent processes would be misleading, we review respective models separately. The models in Section 3.1 examined how cancer cells invaded the healthy tissue as can be observed around a solid primary carcinoma. In this review of metastatic cancer models, we focus on mathematical approaches that describe how secondary (and higher degree) tumours form from these primary tumours.

As Section 2.3.4 accentuates, a variety of sub-processes at multiple temporal and spatial scales are involved in metastasis. As a result, different models are appropriate to shed light on these sub-processes—ultimately, it is the biological problem that we seek to find insight to that should determine the appropriate modelling approaches and techniques. A model of metastasis could, for example, address the following questions: When do metastases appear and how does their size develop over time? How does the metastatic cancer cell phenotype evolve? Given a primary tumour, what determines its metastatic spreading pattern? Which circumstances result in newly metastasised cancer cells remaining dormant (*micrometastatic dormancy*) rather than developing into a full-blown secondary tumour?

In what follows, an overview of some of the most prominent approaches to modelling various aspects of metastatic spread is presented. These are broadly categorised into those describing how successful metastatic cancer cell phenotypes evolve through epigenetic and genetic mutations on the one hand, and approaches that model the growth dynamics of metastases on the other hand. Note that a review of mathematical models of EMT and/or MET in the context of metastasis will be omitted. The reason is that, to our knowledge, the work in Chapter 5 of this thesis, which will be published in Franssen and Chaplain (2019), is the first metastasis model to include the roles of EMT and MET, and of the corresponding phenotypes of individual cancer cells in a spatially explicit manner.

We will consider both deterministic and stochastic models and will further group them according to the predominant mathematical technique involved. Each type of model is useful; the appropriate one should be chosen on the grounds of the biological circumstances and the modeller's aim. A deterministic modelling approach in the form of an

ODE or a PDE model delivers the same results each time the system is solved if the same parameter values are used. There is no stochasticity involved in the coefficients. However, many biological processes—in the context of cancer invasion and metastasis for example cell movement, phenotypic mutations, and survival of cells when entering the bloodstream to metastasise—present an element of stochasticity. Thus, mathematical models that capture potentially occurring stochasticity in the appropriate part of the model may present results that are biologically more realistic. For instance, cells movement in space could be stochastic, or the cell phenotype could mutate with some probability upon mitosis, or random noise can be included in an otherwise deterministic model. While the representation of inherently random biological processes by stochastic models may make them *prima facie* appear to be superior in many cases, the downside is that their analysis is generally more difficult. Deterministic models, on the contrary, are comparatively easily analysed, allowing us to study the different behaviours that a system can exhibit and further enabling us to determine over which parameter ranges these behaviours occur. Hence, a more profound understanding of the behaviour of the system of interest may be gained.

Information in this review chapter of metastasis models is drawn from personal reading as well as from the chapter *Mathematical Modeling of the Metastatic Process* by Scott et al. (2013b) and from the chapter *Mathematical Modeling of Cancer Metastases* by Ryser & Komarova (2015) published in Zhang (2015). Stochastic types of models reviewed are branching processes, Moran processes, cellular automata (which are not intrinsically stochastic—this depends on the rules imposed), *Markov Chain* (MC) models as well as stochastic-mechanistic models. Deterministic approaches to modelling metastasis considered here are ODE and PDE models.

3.2.1 Models describing the acquisition of a metastatic phenotype

Cancer starts with mutations in a small set of healthy cells. Further mutations over time can result in cells acquiring a metastatic phenotype that enables them to spread to distant sites in the body. In what follows, we introduce a group of models describing the acquisition of a metastatic phenotype.

In Michor et al. (2006); Michor and Iwasa (2006), Moran processes that allowed for mutation upon reproduction were used to study the dynamics of metastatic formation. As shown in Figure 3.6, a Moran process is a stochastic approach to modelling the evolution dynamics of a population that consists of a fixed number of individuals. These individuals can be of diverse phenotypes where each type has a different fitness assigned to it. At each time step, one individual in the population is chosen to replicate with a probability proportional to its fitness. So, in principle, any individual could be chosen to replicate but the higher an individual's fitness, the more likely it will do so. Consecutively, a randomly chosen individual will die during each time step. As a result, phenotypes of higher fitness tend to dominate the population as time progresses. While the earlier model by Michor et al. (2006) considered a scenario in which a single activating mutation in an oncogene like *myelocytomatosis viral oncogene homolog* (myc) or *rat sarcoma virus homolog* (ras) was necessary to enable cells to metastasise, their follow-up paper (Michor and Iwasa, 2006) studied the effect of metastasis suppressor gene (MSG) inactivation. If these MSGs

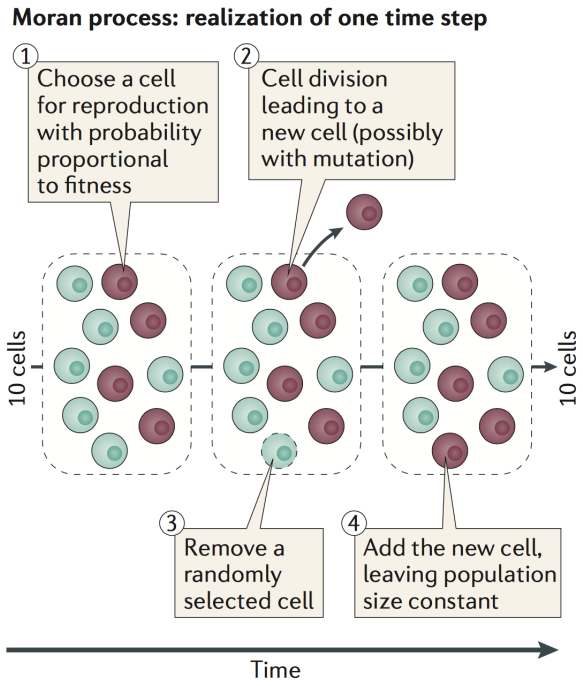

Figure 3.6: ***Schematic representation of a single time step in a Moran process.*** *Given a population consisting of a fixed number of individuals of diverse phenotypes (red and green cells) where each type has a different fitness associated to it, at each time step, one individual in the population is chosen to replicate with a probability proportional to its fitness. Consecutively, a randomly chosen individual will die during each time step. Reproduced from Altrock et al. (2015) with permission from Nature Publishing Group.*

were inactivated in both alleles, or an oncogene—like myc or ras—was activated in a single mutation, this promoted the ability of metastatic spread within the scope of the model. Further, cancer cells acquired either a fitness advantage or disadvantage over normal cells through the mutations in the model.

Results obtained in Michor et al. (2006); Michor and Iwasa (2006) include that the majority of metastases formed from mutations that provided mutated cells in the primary tumour with a fitness advantage. This allowed them to increase in number at the cost of cancer cells of other phenotypes in the primary tumour. Further, they found that their results fit in with experimental data by Ramaswamy et al. (2003) who observed that

> *'the metastatic potential of human tumors is encoded in the bulk of a primary tumor, thus challenging the notion that metastases arise from rare cells within a primary tumor that have the ability to metastasize'.*

An extension to the model by Michor et al. (2006) was published by Dingli et al. (2007). Since the cancer cell population in this model was allowed to grow, the modelling approach was no longer a Moran process in the strict sense. Instead, the growth of the primary tumour was now captured using a time-branching process. Two cases were distinguished. The cancer cells could either break free from the primary tumour but the tumour itself did not change in size or they could remain at the primary site, causing the tumour to grow exponentially. The dissemination probability of cancer cells depended on the tumour's

size. Overall, Dingli et al. (2007) found that the rate of metastatic formation depended on the interactions between the mutated cells' relative fitness, the likelihood that they were exported and the rate at which mutations occurred. The optimal combination giving the highest metastatic progression possible was unique to every tumour. For example, while one may, at first sight, assume that a higher dissemination probability of mutated cancer cells would benefit cancer spread, the authors found that the trade-off costs could have a destructive effect—even on an exponentially growing tumour. The reason for this was the potential lack of mutated cells that remained at the primary site and continued to proliferate there. While cells with mutations like myc and ras, which had a higher relative fitness assigned to them in the model in accordance with research on fibroblasts by Wyllie et al. (1987), flourished in the primary tumour and were able to seed plenty of metastases, the authors suggested that the phenomenon described above especially occurred in cells with mutations that had a lower relative fitness than normal cells, such as MSG activation (Steeg, 2004). These cells could only coexist if the tumour population was small. Also, complete export of the mutated cells could be observed in the model. Interestingly, this phenomenon is also reported to occur in cancer patients. For example, the articles by Greco (2014), Moran et al. (2016) and Ross et al. (2015) evolve around the phenomenon of *cancer of unknown primary site* (CUP), which is seen in approximately 3-5% of advanced cancers. A CUP consists of multiple metastases whose primary tumour of origin remains unknown to clinicians (Greco, 2014).

3.2.2 Models of metastatic growth dynamics

For reasons explained in Section 2.3.4, a seemingly successfully treated and recovered patient may relapse after some time due to cancerous regrowths at the primary site and/or due to undetected micrometastases and/or isolated dormant cancer cells that remain undiscovered upon initial treatment. Routinely preventing these small lesions of cancer cells from causing a relapse in every patient with drugs is not viable due to their often debilitating side effects. Ideally, a patient should receive a treatment dosage that is just sufficient to prevent a relapse. This requires the treatment to be adjusted in a case-specific manner so that it is only applied where and when necessary. An oncologist has the best chance of achieving this if they know where and how many metastases typically form, what their growth patterns are, how aggressively they grow, and of what size they are. However, at the time of removal of the primary tumour, an oncologist's knowledge is usually restricted to the size of detectable metastases and of the primary tumour.

In an attempt to shed light on metastatic growth dynamics, several deterministic and stochastic mathematical models have been proposed.

Saidel et al. (1976) combined experimental work on a murine model of primary fibrosarcoma with metastatic spread to the lungs with an ODE model in order to obtain lumped-parameter values that could not be measured experimentally. They compartmentalised their model into five metastatic stages shown in the blue boxes of Figure 3.7. The change in cancer cell number over time at the different stages was measured experimentally to subsequently parametrise the mathematical model. Next, the model was used to make predictions regarding e.g. vessel growth inhibition, inhibition of intravasation, lung vessel damage and tumour resection. *In silico* results were compared with experimental ones, where possible, and were described to be in good agreement.

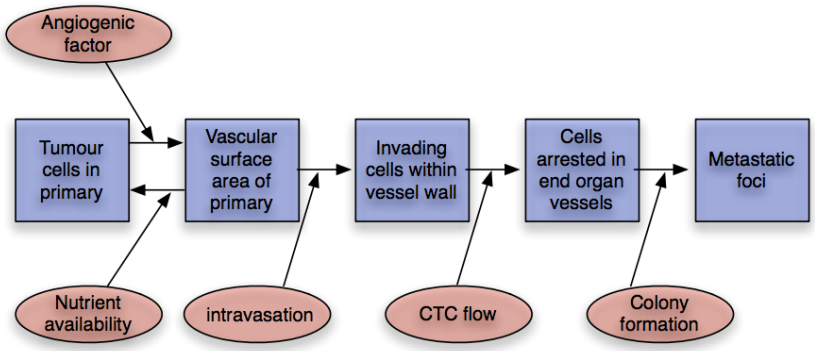

Figure 3.7: ***Compartmentalised translational ODE model by Saidel et al. (1976).*** *While the blue boxes represent the compartments, in which the size of the tumour cell populations can be measured experimentally, the brown ovals indicate the quantities derived from the model. Schematic representation reproduced from Scott et al. (2013b) with permission from Springer.*

Scott et al. (2013a) proposed a model of self-seeding to study the relative likelihood of primary and secondary seeding by assuming that a primary tumour consisted of a set of independent loci, on which tumours underwent saturating growth according to a logistic law. From these loci, cancer cells were shed and potentially returned to their original loci or formed new loci.

With the aim of investigating the validity and the implications of the current hypothesis that the immune system plays a pro-tumour role—rather than just an anti-tumour role—in metastasis (Cohen et al., 2015; Shahriyari, 2016), Rhodes and Hillen (2019) proposed a mathematical model of tumour-immune interactions at two anatomically distant sites. The model accounted for both pro- and anti-tumour effects of the immune system by considering the time-evolution of metastatic cancer cells, necrotic cells, cytotoxic immune cells and tumour-educated immune cells at the primary and secondary site through an ODE model. Following validation of the model against experimental data, immunotherapeutic interventions, primary resection surgeries and injuries at the metastatic site were modelled. Rhodes and Hillen (2019) concluded that the results of their model suggested that the immune-mediated theory of metastasis may explain e.g. metastatic dormancy or blow-up, as well as metastatic spread to secondary sites that present injury and the relatively poor performance of immunotherapies.

A PDE model for the colony size distribution of multiple metastatic tumours, as found in rapidly disseminating tumours in the liver (see Figure 3.8), lungs or brain was suggested by Iwata et al. (2000). Their model studied the evolution of the colony size distribution of metastatic tumours. The metastatic growth model initially considered a single cell, which grew according to Gompertzian growth. The resulting growing primary tumour shed single metastatic cancer cells—the larger the tumour, the more cells were shed. These single cells also grew into metastases at some rate and emitted further single cells, just like the cells of the primary tumour. The authors obtained an explicit solution which tended to an asymptotically stable colony size distribution of metastatic tumours. They concluded that this solution fitted data from *computer tomography* (CT) scans of clinically observed colony size distributions well. CT scans, like the one shown in Figure 3.8,

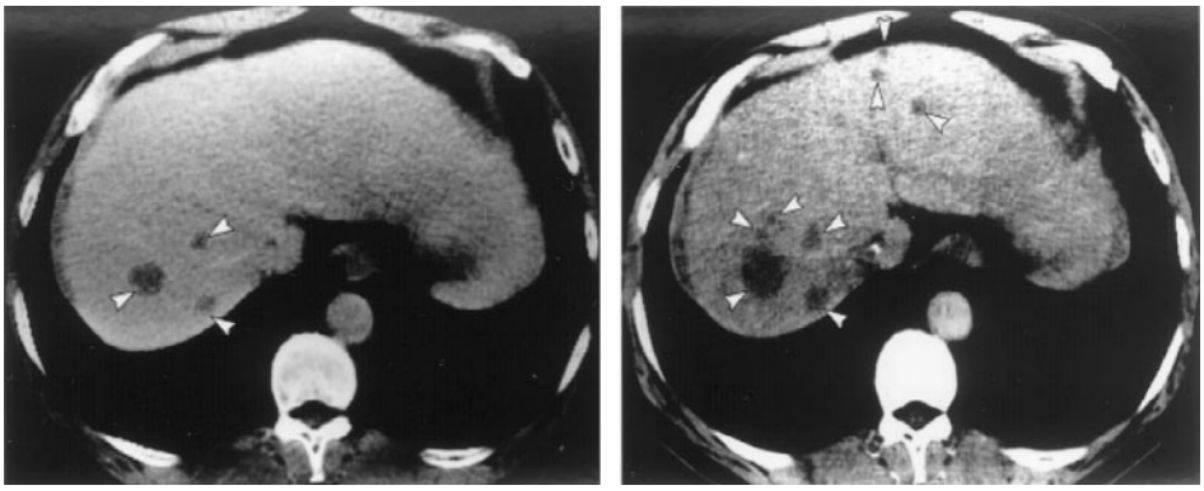

Figure 3.8: ***Examples of liver CTs with multiple metastatic tumours.*** *The CTs on the left and right were taken 432 and 559 days after the primary tumour diagnosis, respectively. By taking multiple CT images in the form of slices throughout the whole liver, the number and size of all detectable liver metastases (indicated by white arrows) can be measured. Reproduced from Iwata et al. (2000) with permission from Elsevier.*

are very commonly used in diagnosing and monitoring cancer and are thus generally readily available. Hence, a model like this one could potentially be well-parametrised to make clinically relevant predictions about subclinical (primary, secondary,...) metastatic burden and the future metastatic growth dynamics.

Many subsequent papers were based on the preliminary work of Iwata et al. (2000). For instance, the model was further analysed and solved numerically by Barbolosi et al. (2009) and Devys et al. (2009). It was then used in Benzekry (2011) to model metastasis density, while tumour growth and angiogenesis were accounted for by an ODE model by Hahnfeldt et al. (1999). It further formed the basis for a mathematical model by Benzekry et al. (2016), which connected presurgical primary tumour volume and post-surgical metastatic burden. Finally, an *in vivo* human xenograft model by Hartung et al. (2014) was also based on Iwata et al. (2000). This described primary tumour growth by a set of phenomenological models, and metastatic growth by a transport equation that was endowed with a boundary condition for metastatic emission.

In Xu and Prorok (1998); Bartoszyński et al. (2001); Hanin et al. (2006), similar growth laws to the ones described in Iwata et al. (2000) were used in fully stochastic models in order to predict the probability that a certain given distribution of metastatic colony size occurred at a given time by deriving joint conditional distribution functions. Each model was validated against one patient's data. After fitting the models, predictions about the patients' condition prior to diagnosis and about the natural history of their cancer were made.

While we reviewed the models by Michor et al. (2006); Michor and Iwasa (2006); Dingli et al. (2007) in Section 3.2.1, as they focus on the acquisition of a metastatic phenotype, Haeno and Michor (2010) proposed a model of similar type but allowed for tumour cell proliferation rates that are much larger than death rates. This way, the authors studied how tumour metastasis evolved in an *expanding* cancer cell population. They calculated

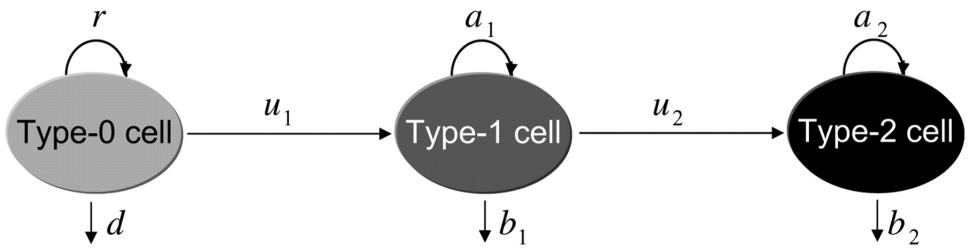

Figure 3.9: ***Continuous time-branching model by Haeno et al. (2007).*** *Type-0 cells, which are mutation-free, differentiate into type-1 cells, which carry one mutation, at rate u_1. Type-1 cells further mutate into type-2 cells, which carry two mutations, at rate u_2. Reproduction rates of each cell type are shown on top, death rates at the bottom. Reproduced from Haeno et al. (2007) with permission from Genetics Society of America.*

not only the probability that a tumour metastasises but also, at every particular point in time, the expected total number of cancer cells and metastasised cells. The model relied on estimated parameter values due to lack of clinical data on cell growth and death rates, on probabilities of metastatic export and on mutation frequency of cancer cells. Yet, it gave a theoretical example of how a mathematical model can be used to examine the effect of the choice of treatment (chemotherapy and/or tumour resection) and its timing on the period a patient survives. The model further indicated that the optimal treatment choice for a patient was tumour-specific. It was found to depend on factors such as how large the metastasis-enabling mutation rate was, on the death and birth rates of cells with and without the ability to metastasise, and on the export rate of metastatic cells. The authors further analysed their stochastic model and found that analytic approximations were in good agreement with results obtained by running the computational stochastic model. Regarding the expected patient survival time, the authors found that both chemotherapy and resection had life-prolonging effects, as to be expected.

Cisneros and Newman (2014) proposed another stochastic model that used a birth-death process to investigate whether metastasis occurs from many poorly adapted cancer cells or from a few well-adapted cancer cells.

Building on the work by Michor et al. (2006) and Michor and Iwasa (2006), which had investigated the dynamics of one and two mutations in MSGs in a cell population of constant size, respectively, Iwasa et al. (2006) and Haeno et al. (2007) studied the same scenario with one and two MSGs, respectively, while allowing for exponential tumour expansion using a continuous time-branching process. Both papers initially assumed the existence of a sole mutation-free (and hence treatment-sensitive) parent cancer cell. At each mitosis, a parental cell could turn into a resistant cell with a single mutation with a certain probability. In the work of Haeno et al. (2007), a cell with a single mutation could then further mutate into one with two mutations. In both models, these cell types were differentiated by their relative fitness. This was represented schematically in Figure 3.9. Furthermore, these models were suggested to have clinical relevance because a single genetic alteration suffices to induce resistance to an otherwise successful therapy. Knowing the probability that a tumour will become resistant to a drug during the course of treatment and the mean number of resistant cells that exist when a tumour has reached a detectable size could provide valuable insights that cannot be easily obtained experimentally.

Recently, Frei et al. (2019) introduced a stochastic model for cancer metastasis that took the form of a *branching stochastic process with settlement*. Particles in the model represented clusters of cancer cells. It was shown that the expected particle location, their locational variance, the furthest particle distribution, and the extinction probability satisfied an integro-differential equation with distributed delay. The uniqueness and existence of this equation were proven and then analysed. The framework was then validated against murine data on metastasis.

Liotta et al. (1976) considered the three left-most steps of metastatic cascade system shown in Figure 3.7, which they had conceptualised for their previous ODE model in Saidel et al. (1976), in a MC model that accounted for stochastic processes at the cell level. Instead of the flux of single cells between these compartments, the flux of tumour cell clusters was modelled. In line with experimental data, the model made the following assumptions:

- The number of cell clusters decreased as clusters increased in size.
- The larger the clusters, the lower their death rate and the higher the probability that they colonised as metastases.

Like before, model results were in good agreement with an experimental murine model regarding the number of macroscopic metastases as a function of time as well as the time-dependent probability of finding a mouse that is metastasis-free when it was sacrificed after ten to 30 days. This led the authors to the conclusion that therapeutic interventions which break up large clusters of cancer cells could reduce the number of metastases forming.

In a follow-up paper, Liotta et al. (1977) suggested a mathematical expression for the probability that no metastasis will have formed in their experimental murine model after a given period of time. This probability was found to be close to one ($\sim$1) at the beginning but it approached zero ($\rightarrow$0) as time progressed, suggesting that after a critical time period micrometastases will almost certainly have formed.

Another MC model was proposed by Newton et al. (2012) with the aim of quantifying pathways of metastatic progression for lung cancer. A transition matrix was calculated and its transition probabilities interpreted as random variables. This was used to construct a circular network of primary and metastatic locations that was based on postmortem tissue analysis of primary and metastatic tumour sites in 3827 autopsies from untreated lung cancer patients. The model was further developed in Newton et al. (2013). As an extension, this model was applied to breast cancer in Newton et al. (2015)—the circular chord diagramme showing a MC network of data on metastatic spread from 4181 breast cancer patients shown in Figure 2.15 is based on the work in Newton et al. (2015).

Finally, Margarit and Romanelli (2016) developed a patient-statistics-based absorbing MC model to analyse the metastatic routes between principal organs.

3.3 Conclusions from the literature review

In this chapter, we reviewed existing models of cancer invasion and metastasis. In the case of invasion, we considered both spatially local and non-local models. The metastasis models we reviewed either described the acquisition of a metastatic phenotype in cancer

cells or investigated metastatic growth dynamics. The models proposed in the remainder of the thesis are motivated by the gaps in the literature identified through this review.

In particular, we found that existing models of metastasis did not account for the spatiotemporal evolution of individual cancer cells in the—inherently spatial—invasion-metastasis cascade. The same applies to the location-dependent role of phenotypic variation and EMT-processes in cancer invasion and metastatic spread. These previously unexplored aspects are at the centre of the metastasis modelling framework introduced in Chapter 4, which is extended in Chapter 5:

- In Chapter 4, a spatially explicit hybrid multi-organ metastasis modelling framework is developed. It describes the invasive growth dynamics of individual cancer cells of epithelial-like and mesenchymal-like phenotype both at a primary site and at potential secondary metastatic sites in the body, as well as their transport from the primary to secondary sites.

- The phenotypic variation accounted for by the framework in Chapter 4 is extended in Chapter 5 to include cancer cells of an epithelial-like, a mesenchymal-like and a mixed phenotype. Furthermore, permanent and transient mutations between these cell phenotypes in the form of EMT and its reverse process MET are now included. Both of these mechanisms are implemented at the biologically appropriate locations of the invasion-metastasis cascade.

Furthermore, the literature review of cancer invasion models showed that—due to the large number of cells involved in the invasion process—continuum models are a popular and computationally efficient approach to modelling cancer invasion, *cf.* Section 3.1. This approach can reflect the biology of *epithelial-like* cancer cells and hence their spatiotemporal evolution well. However, as we have established in Section 2.4, EMT and MET—and intrinsically also cancer cells of mesenchymal phenotype—play a crucial role in cancer invasion (Godlewski et al., 2010). In particular, a distinguishing feature of mesenchymal-like cancer cells is their relative loss of cell-cell adhesion as shown in Figure 2.11. Hence, it would be biologically inaccurate to represent cells of mesenchymal phenotype using a continuum approach. To this end, we develop a model that represents the spatiotemporal evolution of epithelial-like and mesenchymal-like cancer cells in a biologically appropriate manner through a hybrid system of partial and stochastic differential equations in Chapter 6. As only a small proportion—and hence relatively small number—of cancer cells are of mesenchymal-like phenotype (Dongre and Weinberg (2019); *cf.* Section 2.4), the model retains computational efficiency. Thus, the three-dimensional spatio-temporal evolution of an appropriately large number of cancer cells can be simulated. As a result, the hybrid model can be accurately parametrised to predict experimental organotypic invasion assay results qualitatively and quantitatively. Thus, the novel modelling approach introduced in Chapter 6 allows us to bridge the gap between experimental and theoretical work frequently observed in existing invasion models.

Chapter 4

A mathematical framework for modelling the metastatic spread of cancer

The biological processes involved in the invasion-metastatic cascade are inherently spatial, *cf.* Chapter 2. Yet, from the literature review in Chapter 3, we conclude that, to our knowledge, no spatially explicit model to describe cancer invasion and metastatic spread exists, not to mention a model that combines all of the steps of the invasion-metastasis cascade—i.e. cancer cell invasion, intravasation, vascular travel, extravasation and regrowth at secondary sites in the body—in a spatial manner. To close this gap in the existing literature, we propose a novel spatial modelling framework of the metastatic spread of cancer in this chapter. This framework describes the invasive growth dynamics of individual cancer cells both at a primary site and at potential secondary metastatic sites in the body, as well as the transport from the primary to secondary sites. Throughout, the interdependent interactions between the cancer cells, the MDEs secreted by the cells, and the cells' microenvironment in the form of the ECM are accounted for. Furthermore, the individual-based framework models phenotypic variation by considering cancer cells of an epithelial-like and a mesenchymal-like phenotype. The work in this chapter has also previously been published in (Franssen et al., 2019).

4.1 Model setup

In this section, we introduce the ideas and assumptions that our modelling framework builds on. The corresponding model is described in Figure 4.1 in the form of a flowchart.

In order to account for the metastatic spread of cancer cells in a spatially explicit manner, we consider $G+1$ non-overlapping spatial domains. These consist of the spatial domain representing the primary tumour site, $\Omega_{\mathrm{P}} \subset \mathbb{R}^2$, as well as the $G \in \mathbb{N}$ spatial domains representing the sites of potential secondary metastatic spread, $\Omega_{\mathrm{S}}^a \subset \mathbb{R}^2$, where $a = 1, 2, ..., G$. In these spatial domains, we represent the MMP-2 concentration and the ECM density at position $\mathbf{x}$ at time t by the continuous functions $m(t, \mathbf{x})$ and $w(t, \mathbf{x})$, respectively, while capturing the spatiotemporal evolution of epithelial-like and mesenchymal-like cancer cells *individually*. We model the local cancer cell invasion by expanding the modelling approach used in Anderson and Chaplain (1998); Anderson et al.

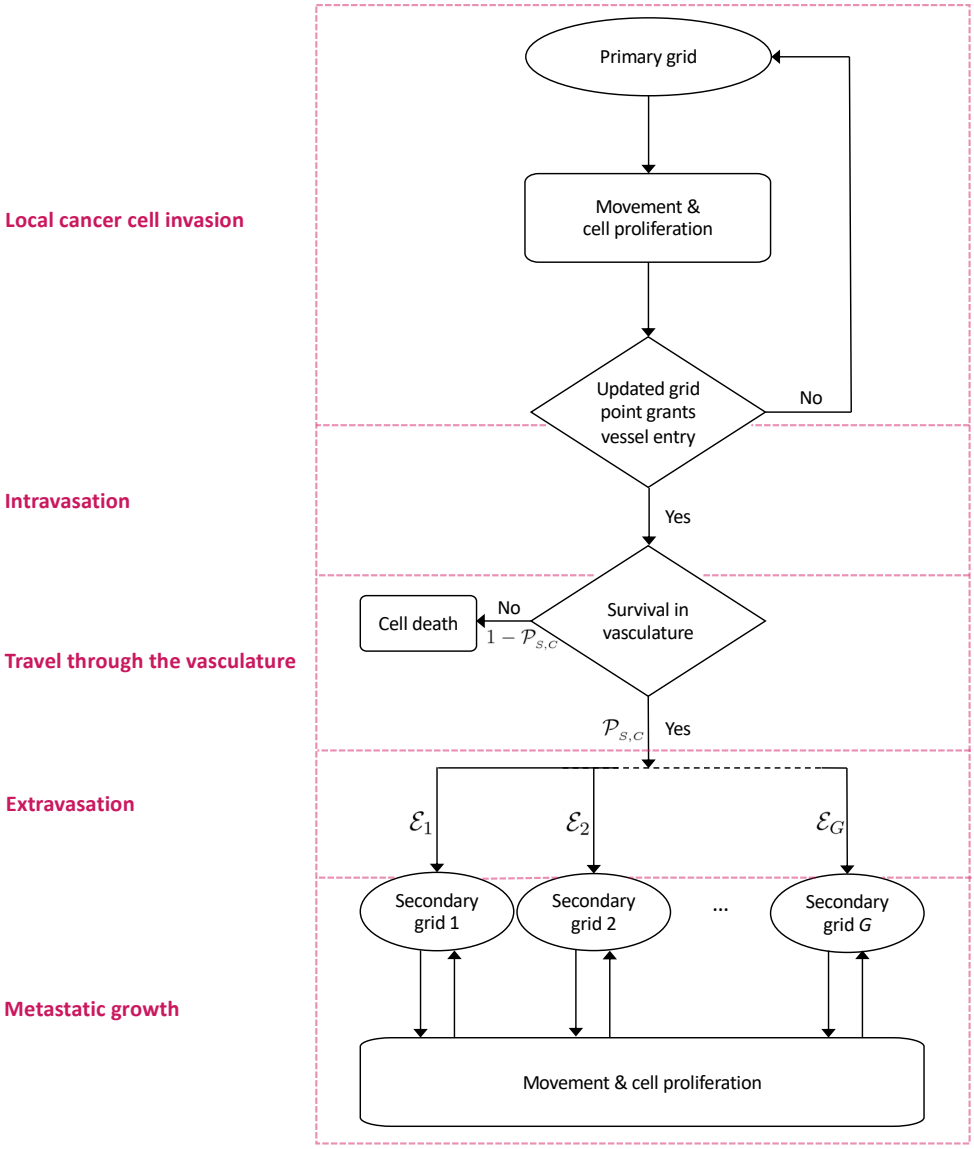

Figure 4.1: ***Flowchart of the invasion-metastasis hybrid model.*** *At each time step, each cancer cell on the primary grid moves and proliferates as explained in detail in the text. A cancer cell remains on the primary grid during the respective time step, unless it is placed on a grid point of the primary grid that represents a blood vessel. In the latter case, single CTCs and CTC clusters may enter the vasculature. They spend some number of time steps in the circulation and survive with a probability of $\mathcal{P}_S$ in the case of single CTCs and with a probability of $\mathcal{P}_C$ in the case of CTC clusters. Cancer cells that do not survive are removed from the simulation. Surviving CTCs and CTC clusters are placed onto one of G secondary grids with the respective probability $\mathcal{E}_1, \mathcal{E}_2, ..., \mathcal{E}_G$. Cancer cells on the secondary grids move and proliferate in the same way as the cancer cells on the primary grid (potentially with different parameter values to represent organ- and patient-specific differences in the local tumour microenvironment). For better orientation, the red boxes with their labels on the left correspond to the sections indicated in bold in Sections 2.3.2–2.3.5 and Section 4.1 of the text.*

(2000) to our specific biological problem. We include a second cancer cell phenotype and also additionally consider MT1-MMP, which is taken to be bound to the membranes of the mesenchymal-like cancer cells and thus follows their discrete spatiotemporal dynamics. We designate locations in the primary spatial domain to function as entry points into the vasculature and, similarly, impose a spatial map of exit locations from the vasculature onto the secondary metastatic domains. This allows cancer cells to travel from the primary tumour site to secondary sites via blood vessels.

We next consider one key step of the invasion-metastasis cascade after the other. To make the key steps more recognisable, we begin each paragraph by printing the description of the corresponding step of the invasion-metastasis cascade, *cf.* Sections 2.3.2–2.3.5, in bold. Further, the same step descriptions are used in the flowchart in Figure 4.1.

Local cancer cell invasion The movement of the individual epithelial-like and mesenchymal-like cancer cells in the spatial domains of our model is *derived* from the coupled PDEs (4.1.1) and (4.1.2) below. These equations describe the continuous spatiotemporal evolution of epithelial-like and mesenchymal-like cancer cell densities $c_{\mathsf{E}}(t,\mathbf{x})$ and $c_{\mathsf{M}}(t,\mathbf{x})$, respectively. Both cancer cell types are assumed to move via a combination of diffusive movement and haptotactic movement up the gradient of the ECM density $w(t,\mathbf{x})$. Thus, the conservation equations for the cancer cell densities $c_k(t,\mathbf{x})$—where $k=\mathsf{E},\mathsf{M}$—evolving with constant diffusion coefficient $]D_k \geq 0$ and constant haptotactic coefficient $\Phi_k \geq 0$ are given by

$$\frac{\partial c_k}{\partial t} + \nabla\cdot(\mathbf{J}_{\mathsf{diff}} + \mathbf{J}_{\mathsf{hapto}}) = 0.$$

Here

$$\mathbf{J}_{\mathsf{diff}} = -D_k\nabla c_k$$

is the flux used to describe solely the random movement of the cancer cells, and

$$\mathbf{J}_{\mathsf{hapto}} = \Phi_k c_k \nabla w$$

is the haptotactic flux. Moreover, we assume that cancer cells (and, implicitly, MT1-MMP) cannot leave the domain. This results in zero-flux boundary conditions, i.e. if $\mathbf{n}$ is an appropriate outward unit normal vector,

$$\mathbf{n}\cdot(-D_k\nabla c_k + \Phi_k c_k\nabla w) = 0$$

is imposed on the boundaries of every domain Ω_{P} and Ω_{S}^a, $a=1,2,...,G$. Consequently, the evolution of the density of epithelial-like cancer cells $c_{\mathsf{E}}(t,\mathbf{x})$ is governed by the following diffusion-haptotaxis equation:

$$\frac{\partial c_{\mathsf{E}}}{\partial t} = \overbrace{D_{\mathsf{E}}\nabla^2 c_{\mathsf{E}}}^{\text{diffusion}} - \overbrace{\Phi_{\mathsf{E}}\nabla\cdot(c_{\mathsf{E}}\nabla w)}^{\text{haptotaxis}}, \tag{4.1.1}$$

along with zero-flux boundary conditions. Here, $D_{\mathsf{E}} \geq 0$ is the constant cancer cell diffusion coefficient for epithelial-like cancer cells and $\Phi_{\mathsf{E}} \geq 0$ is their constant haptotactic sensitivity coefficient. Similarly, the mesenchymal-like cancer cell density $c_{\mathsf{M}}(t,\mathbf{x})$ evolves

according to

$$\frac{\partial c_{\mathsf{M}}}{\partial t} = \overbrace{D_{\mathsf{M}} \nabla^2 c_{\mathsf{M}}}^{\text{diffusion}} - \overbrace{\Phi_{\mathsf{M}} \nabla \cdot (c_{\mathsf{M}} \nabla w)}^{\text{haptotaxis}}, \tag{4.1.2}$$

along with zero-flux boundary conditions. Here, $D_{\mathsf{M}} \geq 0$ is the constant cancer cell diffusion coefficient for mesenchymal-like cancer cells and $\Phi_{\mathsf{M}} \geq 0$ is their constant haptotactic sensitivity coefficient.

However, we aim to model the cancer cells individually rather than as densities to allow to track the evolution of *single* mesenchymal-like and epithelial-like cancer cells with different phenotypes. To achieve this, we next discretise the spatial domains of our model using a uniform mesh and discretise the flow of the cell densities in equations (4.1.1) and (4.1.2). This way, we derive the movement coefficients of the *individual* epithelial-like and mesenchymal-like cancer cells to be those in equations (4.1.7) and (4.1.8).

For this, we fix a time step Δt and set $t_n = n\Delta t$. We discretise each of the $G+1$ square domains using, in the two dimensional case where $\mathbf{x} = (x, y) \in \mathbb{R}^2$, a uniform mesh of grid cells with size $\Delta x = \Delta y = \frac{1}{l}$. We continue by approximating the MMP-2 concentration m and the ECM density w by discrete values $m_{i,j}^n$ and $w_{i,j}^n$, respectively, and denote the number of epithelial- and mesenchymal-like cancer cells on grid point (x_i, y_j)—where $x_i = i\Delta x$ and $y_j = j\Delta y$ with $i, j \in [0, l] \cap \mathbb{N}_0$—at time t_n by ${c_{\mathsf{E}}}_{i,j}^{n}$ and ${c_{\mathsf{M}}}_{i,j}^{n}$, respectively.

Equations (4.1.1) and (4.1.2) are discretised using a five-point central difference scheme, as described in detail in Appendix A. This yields

$${c_{\mathsf{E}}}_{i,j}^{n+1} = \mathcal{P}_0 {c_k}_{i-1,j}^{n} + \mathcal{P}_1 {c_k}_{i+1,j}^{n} + \mathcal{P}_2 {c_k}_{i,j+1}^{n} + \mathcal{P}_3 {c_k}_{i,j-1}^{n} + \mathcal{P}_4 {c_k}_{i,j}^{n} \tag{4.1.3}$$

where $k = \mathsf{E}, \mathsf{M}$, for the discrete spatiotemporal evolution epithelial-like and mesenchymal-like cancer cells, respectively, together with zero-flux boundary conditions. We then extract the coefficients to obtain

$$\begin{aligned}
\mathcal{P}_0 : \mathcal{P}_{i-1,j}^n &:= \frac{\Delta t}{(\Delta x)^2} \left[D_k - \frac{\Phi_k}{4} \left(w_{i+1,j}^n - w_{i-1,j}^n \right) \right], \\
\mathcal{P}_1 : \mathcal{P}_{i+1,j}^n &:= \frac{\Delta t}{(\Delta x)^2} \left[D_k + \frac{\Phi_k}{4} \left(w_{i+1,j}^n - w_{i-1,j}^n \right) \right], \\
\mathcal{P}_2 : \mathcal{P}_{i,j+1}^n &:= \frac{\Delta t}{(\Delta x)^2} \left[D_k + \frac{\Phi_k}{4} \left(w_{i,j+1}^n - w_{i,j-1}^n \right) \right], \\
\mathcal{P}_3 : \mathcal{P}_{i,j-1}^n &:= \frac{\Delta t}{(\Delta x)^2} \left[D_k - \frac{\Phi_k}{4} \left(w_{i,j+1}^n - w_{i,j-1}^n \right) \right], \qquad (4.1.4) \\
\mathcal{P}_4 : \mathcal{P}_{i,j}^n &:= 1 - \frac{\Delta t}{(\Delta x)^2} \left[4D_k - \Phi_k \left(w_{i+1,j}^n + w_{i-1,j}^n + w_{i,j+1}^n + w_{i,j-1}^n - 4w_{i,j}^n \right) \right]. \qquad (4.1.5)
\end{aligned}$$

By approximating the ECM density w by linear functions in the x- and in the y-direction,

which will not affect the numerical results significantly since our numerical method is of first order accuracy, equation (4.1.5) simplifies to

$$\mathcal{P}_4 : \mathcal{P}_{i,j}^n \quad := 1 - \frac{4\Delta t}{(\Delta x)^2} D_k. \tag{4.1.6}$$

Furthermore, we can provide the notions of probabilities by

- choosing the positive parts of $\mathcal{P}_0$ to $\mathcal{P}_3$;
- noting that small values of Δt suffice to ensure that $\mathcal{P}_0, \mathcal{P}_1, \mathcal{P}_2, \mathcal{P}_3 \leq 1$.

Also, it follows from the above that $\mathcal{P}_4 \in [0, 1]$. Hence, we redefine $\mathcal{P}_0$–$\mathcal{P}_4$ as

$$\begin{aligned}
\mathcal{P}_0 : \mathcal{P}_{i-1,j}^n &:= \max\left(0, \frac{\Delta t}{(\Delta x)^2}\left[D_k - \frac{\Phi_k}{4}\left(w_{i+1,j}^n - w_{i-1,j}^n\right)\right]\right), \\
\mathcal{P}_1 : \mathcal{P}_{i+1,j}^n &:= \max\left(0, \frac{\Delta t}{(\Delta x)^2}\left[D_k + \frac{\Phi_k}{4}\left(w_{i+1,j}^n - w_{i-1,j}^n\right)\right]\right), \\
\mathcal{P}_2 : \mathcal{P}_{i,j+1}^n &:= \max\left(0, \frac{\Delta t}{(\Delta x)^2}\left[D_k + \frac{\Phi_k}{4}\left(w_{i,j+1}^n - w_{i,j-1}^n\right)\right]\right), \\
\mathcal{P}_3 : \mathcal{P}_{i,j-1}^n &:= \max\left(0, \frac{\Delta t}{(\Delta x)^2}\left[D_k - \frac{\Phi_k}{4}\left(w_{i,j+1}^n - w_{i,j-1}^n\right)\right]\right), \qquad (4.1.7) \\
\mathcal{P}_4 : \mathcal{P}_{i,j}^n &\quad = 1 - \sum_{q=0}^{3} \mathcal{P}_q. \qquad (4.1.8)
\end{aligned}$$

The resulting coefficients $\mathcal{P}_0, \mathcal{P}_1, \mathcal{P}_2, \mathcal{P}_3$ now correspond to the probabilities that, during the next time step, a cancer cell at grid point (x_i, y_j) moves left, right, up and down, respectively. $\mathcal{P}_4$ corresponds to the probability that a cancer cell remains at grid point (x_i, y_j) during the next time step. This way, the cancer cells move both by diffusion, and, as soon as a non-zero ECM density gradient exists in the local neighbourhood, also by haptotactic movement towards the higher ECM density.

Note that, if we had used a positivity-preserving numerical scheme, such as a second or higher order Runge-Kutta scheme, positivity of $\mathcal{P}_0$ to $\mathcal{P}_4$ would have been inherited from the positivity of the PDEs in equations (4.1.1) and (4.1.2). The explicit Euler approximation, however, introduces a small numerical error that could lead to negative coefficients. The renormalisation resulting from taking the positive parts of $\mathcal{P}_0$ to $\mathcal{P}_3$ and the re-expression of equation (4.1.6) as equation (4.1.8) has a small impact on the results in cases where any of the coefficients $\mathcal{P}_0$ to $\mathcal{P}_3$ would have been negative otherwise. Examples are for instance scenarios where no diffusion is included but the haptotactic term in one or more of $\mathcal{P}_0$ to $\mathcal{P}_3$ becomes negative. In these cases, our model predicts a slightly higher probability for the particular cell to remain where it is compared to the result we would have obtained if we had used a positivity-preserving numerical scheme. However, with the parameter values that we choose for our simulations, the impact of this spatially symmetric discrepancy is not significant. If anything, the spread of the cancer cells could slow down slightly in a symmetric manner. To study parameter values that imply for $\mathcal{P}_0$ to $\mathcal{P}_3$ to become negative regularly, however, we suggest to switch the numerical scheme.

At any time step $n \geq 0$, we then realise the individual-based cell movement from grid point to grid point using the following sub-model, which was proposed in Burgess et al. (2016, 2017):

1. On every grid we identify ${c_{\mathsf{M}}}_{i,j}^{n}$ on each grid point (x_i, y_j) by counting the number of (sizeless) mesenchymal-like cancer cells and thus the MMP-2 concentration and ECM density by calculating the numerical solutions defined by completing equations (A.0.1) and (A.0.2) with zero-flux boundary conditions and suitable initial conditions.

2. For each grid point (x_i, y_j) on every grid, we evaluate the movement probabilities to a neighbouring grid point for cancer cells on this grid point by substituting the local ECM densities into equations (4.1.7) and (4.1.8).

3. Five intervals are then defined based on the movement probabilities from equations (4.1.7) and (4.1.8), at each grid point (x_i, y_j):

$$\mathcal{R}_0 := [0, \mathcal{P}_0); \quad \mathcal{R}_p := \left[\sum_{q=0}^{p-1} \mathcal{P}_q, \sum_{q=0}^{p} \mathcal{P}_q\right), \ p = 1, 2, 3; \quad \text{and} \quad \mathcal{R}_4 := \left[\sum_{q=0}^{3} \mathcal{P}_q, 1\right].$$

4. At each grid point (x_i, y_j) of every grid, we generate a random number $z \in [0, 1]$ for every cancer cell on that grid point. Depending on which of the above intervals $\mathcal{R}_0$ to $\mathcal{R}_4$ the value of z falls into, the corresponding cancer cell will move left ($z \in \mathcal{R}_0$), move right ($z \in \mathcal{R}_1$), move up ($z \in \mathcal{R}_2$), move down ($z \in \mathcal{R}_3$), or remain on its current grid point ($z \in \mathcal{R}_4$).

5. If a cancer cell would have been placed outside the grid limits by Step 4, it remains in its grid position in compliance with the no-loss boundary conditions. The same applies if a cancer cell would have moved to a grid point already filled with the preferred carrying capacity of $\mathcal{Q}$ cells.

The model we described so far only accounts for the movement of the cancer cells. We thus need to additionally account for the *proliferation* of cancer cells. The two cancer cell types included in the model proliferate at different frequencies. The more proliferative epithelial-like cancer cells perform mitosis after $T_{\mathsf{E}} \in \mathbb{N}$ time steps, the less proliferative mesenchymal-like cell types after $T_{\mathsf{M}} \in \mathbb{N}$ time steps (with $T_{\mathsf{M}} > T_{\mathsf{E}}$). When proliferating, the cancer cells pass on their respective phenotype as well as their location so that a proliferating cancer cell is replaced by two daughter cells after the proliferative step has been performed. However, to account for competition for space and resources, the cancer cells on the respective grid point do not proliferate if there are $\mathcal{Q} \in \mathbb{N}$ cancer cells on a grid point at the time of proliferation. If this is the case, they may proliferate again after another time interval T_{E} or T_{M}, respectively.

With reference to the flowchart shown in Figure 4.1, the part of our approach described so far is summarised as *Movement & cell proliferation*, which, for the primary site, is depicted in the upper region of the flowchart.

The mesenchymal-like cancer cells in our model have the ability to express diffusible MMP-2. The MMP-2 concentration $m(t, x, y)$ hence develops according to the equation

$$\frac{\partial m}{\partial t} = \overbrace{D_m \nabla^2 m}^{\text{diffusion}} + \overbrace{\Theta c_{\mathsf{M}_n}}^{\text{expression}} - \overbrace{\Lambda m}^{\text{decay}}, \tag{4.1.9}$$

along with zero-flux boundary conditions

$$\mathbf{n} \cdot (-D_m \nabla m) = 0,$$

where $\mathbf{n}$ is an appropriate outward unit normal vector. Here, $c_{\mathsf{M}_n} \in \{0, 1, 2, ..., Q\}$ denotes the respective presence of up to Q mesenchymal-like cancer cells at a given position $\mathbf{x}$, following the notation by Stéphanou et al. (2006) and McDougall et al. (2012). Consequently, Θc_{M_n} represents the local expression of MMP-2 by the c_{M_n} mesenchymal-like cancer cells.

$D_m > 0$ is the constant MMP-2 diffusion coefficient; $\Theta > 0$ is the constant rate of MMP-2 concentration provided by mesenchymal-like cancer cells; and $\Lambda > 0$ is the constant rate at which MMP-2 decays. Note that the mesenchymal-like cancer cells also express MT1-MMP. However, MT1-MMP acts locally only where it is bound to the cancer cell membrane and its spatiotemporal evolution is hence congruent to that of the mesenchymal-like cancer cells. Therefore, we do not include a separate equation.

The diffusible MMP-2 degrades the ECM with a degradation rate of $\Gamma_2 > 0$. The MT1-MMP expressed on the membrane of the mesenchymal-like cancer cells also degrades the ECM, which is expressed through the degradation rate $\Gamma_1 > 0$. Hence, given that we are disregarding ECM-remodelling for simplicity, the evolution of the ECM density $w(t, x, y)$ is governed by the following PDE:

$$\frac{\partial w}{\partial t} = \overbrace{-(\Gamma_1 c_{\mathsf{M}_n} + \Gamma_2 m) w}^{\text{degradation}}. \tag{4.1.10}$$

Since the continuous evolution of the MMP-2 concentration and the ECM density is governed by equations (4.1.9) and (4.1.10), while the spatiotemporal evolution of the cancer cells (and, intrinsically, of the membrane-bound MT1-MMP) is captured by an individual-based model, this is a hybrid discrete-continuum approach to modelling cancer invasion. Because the movement probabilities are derived from equations (4.1.1) and (4.1.2), which are obtained using equations (4.1.9) and (4.1.10), the hybrid approach is of the kind pioneered by Anderson and Chaplain (1998) in the context of modelling tumour-angiogenesis, that was subsequently used to model tissue invasion by cancer cells (Anderson et al., 2000; Anderson, 2005) and spatial evolutionary games (Burgess et al., 2016, 2017).

Intravasation With the model setup we have described so far, the cancer cells can invade the tissue locally in the primary spatial domain but cannot reach the spatially separated secondary domains. To allow for metastatic spread, we account for the connection of the primary spatial domain to the secondary spatial domains by incorporating blood vessels in our modelling framework. Examples of primary and secondary domains are presented in Figure 4.2. To represent the entry points into the blood vessels, a number of

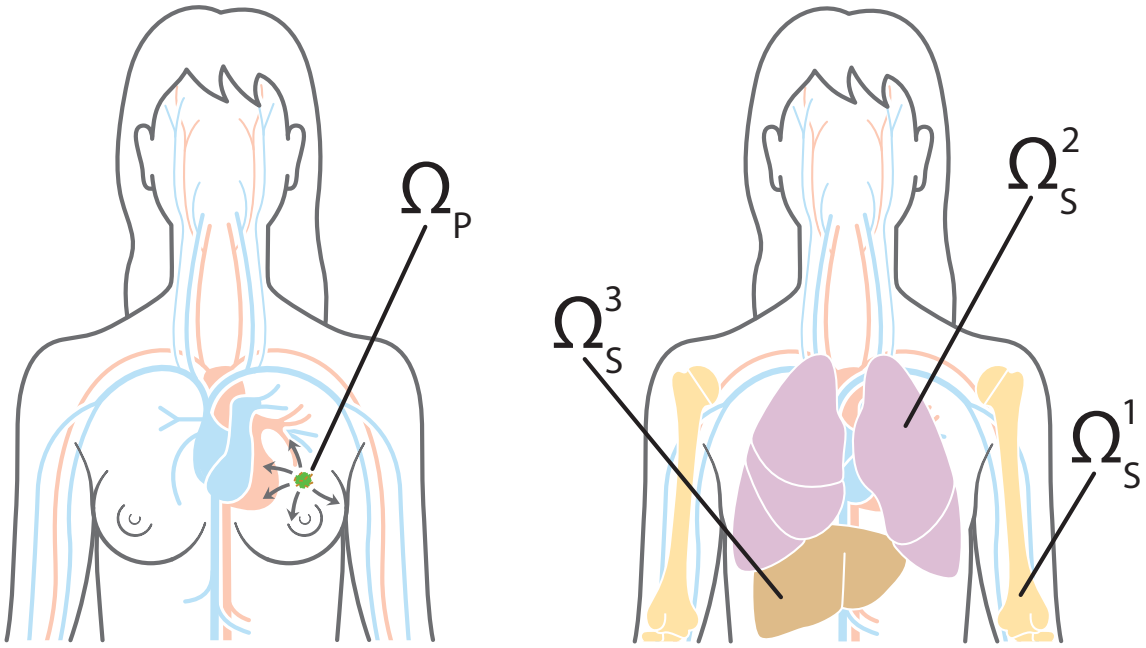

Figure 4.2: ***Primary and metastatic sites.*** *To give an example of how the general modelling framework can be applied to a specific clinical setting, in our simulations we chose the primary site* Ω_P*, which is shown on the left, to represent the breast, and potential secondary metastatic sites* Ω_S^1*,* Ω_S^2*,* Ω_S^3*, which are shown on the right, to represent the bones, the lungs and the liver, respectively. Cancer cells can reach the secondary sites by travelling through the blood system.*

$U_P \in \mathbb{N}_0$ normal blood vessels, as well as $V_P \in \mathbb{N}_0$ ruptured blood vessels, are distributed on the primary grid. The normal blood vessels take the size of one grid point, while ruptured vessels consist of a group of $A^b \in \mathbb{N}$, where $b = 1, 2, ..., V_P$, adjacent grid points and can thus have different shapes. Each secondary grid Ω_S^a also has, respectively, $U_S^a \in \mathbb{N}$ normal blood vessels, where $a = 1, 2, ..., G$ as before, that take the form of a single grid point each. On the primary grid, the grid points where the vessels are located allow the cancer cells to intravasate, while the respective grid points on the secondary grids allow for extravasation.

If, by the movement steps described above, a cancer cell on the primary grid is placed on a grid point that represents a blood vessel, it *may* leave the grid and enter the vasculature. Whether or not a cancer cell can successfully intravasate depends both on its phenotype and on the type of vessel it is placed on.

Whenever a mesenchymal-like cancer cell is moved to a grid point $(x_i, y_j) \in \Omega_P$, on which a *normal* single blood vessel is located, it will successfully enter the vasculature. Further, to represent collective invasion in the form of co-presence of mesenchymal-like and epithelial-like cancer cells, cancer cells of any type on the four neighbouring primary grid points $(x_{i+1}, y_j), (x_{i-1}, y_j), (x_i, y_{j+1})$ and (x_i, y_{j-1}) are forced into the vasculature together with the mesenchymal-like cancer cell on (x_i, y_j) as well as any other cells on (x_i, y_j). Hence, a mesenchymal-like cancer cell moving to a grid point on which a normal blood vessel is located results in either a single mesenchymal-like cancer cell or a cluster consisting of up to $5\mathcal{Q}$ cancer cells of any phenotype intravasating. However, if an

epithelial-like cancer cell is moved to a grid point $(x_i, y_j) \in \Omega_{\mathsf{P}}$ where a *normal* single vessel is located without a mesenchymal-like cell being present there, the epithelial-like cancer cell will not intravasate and the grid point (x_i, y_j) will be treated like any other grid point. This models the fact that epithelial-like cancer cells have been shown to be unable to actively intravasate on their own.

Further, a cancer cell on the primary grid can move to one of the grid points where a *ruptured* vessel is located. Contrary to the above-described scenario of entering a normal vessel, a cancer cell of any phenotype, which is placed on a grid point representing part of a ruptured vessel, can enter the circulation. The respective cancer cell takes with it any other cancer cells residing both on the grid points representing the ruptured blood vessel and on the regular grid points bordering the ruptured vessel. Biologically, the fact that cancer cells of any phenotype can intravasate mirrors that these blood vessels are already ruptured due to trauma or pressure applied by the expanding tumour, making the requirement of MDE-mediated degradation of the vessel wall redundant. The fact that other cancer cells on bordering grid points will enter the circulation together with cancer cells placed on grid points representing blood vessels captures some degree of the cell-cell adhesion found in collectively invading cancer cell clusters.

Travel through the vasculature If a cancer cell of either phenotype or a cluster of cancer cells successfully enters the vasculature either through a ruptured or a normal vessel, it will be removed from the primary grid and moved to the vasculature. Cancer cells and cancer cell clusters remain in the vasculature for some number of time steps $T_{\mathsf{V}} \in \mathbb{N}$, which biologically represents the average time the cancer cells spend in the blood system. If a cell would have normally been due to proliferate while in the vasculature, the proliferation is suppressed. It may proliferate again after another T_{E}, $T_{\mathsf{E/M}}$ or T_{M} time steps, as appropriate. Any cancer cells that enter a particular vessel at the same time are treated as one cluster and hence as a single entity once they are located in the vasculature. However, each cancer cell that is part of a cancer cell cluster disaggregates from its cluster with some probability $\mathcal{P}_d$ after $\left\lceil \frac{T_{\mathsf{V}}}{2} \right\rceil$ time steps. At the end of T_{V} time steps, the single cancer cells and the remaining cancer cell clusters are removed from the simulation unless they are randomly determined to survive. The survival probability is $\mathcal{P}_{\mathsf{S}}$ for single cancer cells and $\mathcal{P}_{\mathsf{C}}$ for cancer cell clusters.

Extravasation Any surviving cancer cells and cancer cell clusters are placed on one of the G secondary grids Ω^a_{S} with probability $\mathcal{E}_1, \mathcal{E}_2, ..., \mathcal{E}_G$, where $\sum_{a=1}^{G} \mathcal{E}_a = 1$. Also, on each specific secondary grid, the cancer cells extravasate through one of the randomly chosen U^a_{S} grid points that represent a blood vessel with equal probability. If the respective grid point cannot accommodate all of the entering cancer cells without violating the preferred carrying capacity $\mathcal{Q}$, the remaining cancer cells are randomly distributed onto the four non-diagonally neighbouring grid points until these are filled to preferred carrying capacity $\mathcal{Q}$. If there are further cancer cells to be placed onto the respective grid point at this instance, such cancer cells are killed to capture the effect of competition for space in combination with vascular flow dynamics.

Metastatic growth If and when cancer cells reach a secondary grid, they behave (i.e. replicate, move, produce MDEs etc.) there according to the same rules as on the primary grid, as indicated on the bottom of the flowchart in Figure 4.1. However, as the nature of the tumour microenvironment varies according to organs and particular patients, the parameter values can be adapted accordingly for each domain.

4.2 Implementation and model calibration

To perform numerical simulations, we first non-dimensionalised the system of equations (4.1.1), (4.1.2), (4.1.9) and (4.1.10), which—along with zero-flux boundary conditions—describes the spatiotemporal evolution of the epithelial-like cancer cell density $c_{\mathsf{E}}(t,x,y)$, of the mesenchymal-like cancer cell density $c_{\mathsf{M}}(t,x,y)$, of the ECM density $w(t,x,y)$, and of the MMP-2 concentration $m(t,x,y)$.

Like Anderson et al. (2000), we chose to rescale distance with an appropriate length scale $L = 0.2\,\mathrm{cm}$ (since 0.1–1 cm is estimated to be the maximum invasion distance of cancer cells at an early stage of cancer invasion) and time with an appropriate scaling parameter $\tau = \frac{L^2}{D}$. Here $D = 10^{-6}\,\mathrm{cm^2 s^{-1}}$ is a reference chemical diffusion coefficient suggested by Bray (1992), such that $\tau = 4 \times 10^4\,\mathrm{s}$, which corresponds to approximately 11 h. Setting $\tilde{t} = \frac{t}{\tau}$, $\tilde{x} = \frac{x}{L}$, $\tilde{y} = \frac{y}{L}$, $\tilde{c}_{\mathsf{E}}(\tilde{t},\tilde{x},\tilde{y}) = \frac{c_{\mathsf{E}}(t,x,y)}{\bar{c}_{\mathsf{E}}}$, $\tilde{c}_{\mathsf{M}}(\tilde{t},\tilde{x},\tilde{y}) = \frac{c_{\mathsf{M}}(t,x,y)}{\bar{c}_{\mathsf{M}}}$, $\tilde{m}(\tilde{t},\tilde{x},\tilde{y}) = \frac{m(t,x,y)}{\bar{m}}$ and $\tilde{w}(\tilde{t},\tilde{x},\tilde{y}) = \frac{w(t,x,y)}{\bar{w}}$, where $\bar{c}_{\mathsf{E}}, \bar{c}_{\mathsf{M}}, \bar{m}$ and $\bar{w}$ are appropriate reference parameters, substituting these into the system of PDEs (4.1.1), (4.1.2), (4.1.9) and (4.1.10) and dropping the tildes for better readability, yields

$$\frac{\partial c_{\mathsf{E}}}{\partial t} = D_{\mathsf{E}} \nabla^2 c_{\mathsf{E}} - \Phi_{\mathsf{E}} \nabla \cdot (c_{\mathsf{E}} \nabla w), \tag{4.2.1}$$

$$\frac{\partial c_{\mathsf{M}}}{\partial t} = D_{\mathsf{M}} \nabla^2 c_{\mathsf{M}} - \Phi_{\mathsf{M}} \nabla \cdot (c_{\mathsf{M}} \nabla w), \tag{4.2.2}$$

$$\frac{\partial m}{\partial t} = D_m \nabla^2 m + \Theta c_{\mathsf{M}} - \Lambda m, \tag{4.2.3}$$

$$\frac{\partial w}{\partial t} = -(\Gamma_1 c_{\mathsf{M}} + \Gamma_2 m) w, \tag{4.2.4}$$

where $D_{\mathsf{E}} = \frac{\tau d_{\mathsf{E}}}{L^2} = \frac{d_{\mathsf{E}}}{D}$, $\Phi_{\mathsf{E}} = \frac{\tau \phi_{\mathsf{E}} \bar{w}}{L^2} = \frac{\phi_{\mathsf{E}} \bar{w}}{D}$, $D_{\mathsf{M}} = \frac{\tau d_{\mathsf{M}}}{L^2} = \frac{d_{\mathsf{M}}}{D}$, $\Phi_{\mathsf{M}} = \frac{\tau \phi_{\mathsf{M}} \bar{w}}{L^2} = \frac{\phi_{\mathsf{M}} \bar{w}}{D}$, $D_m = \frac{\tau d_m}{L^2} = \frac{d_m}{D}$, $\Theta = \frac{\tau \theta \bar{c}_{\mathsf{M}}}{\bar{m}}$, $\Lambda = \tau\lambda$, $\Gamma_1 = \tau \bar{c}_{\mathsf{M}} \gamma_1$ and $\Gamma_2 = \tau \bar{m} \gamma_2$.

To obtain biologically realistic parameter values for our model, we consulted biological publications on the topic—Stokes et al. (1990); Bray (1992); Luzzi et al. (1998); Meng et al. (2004); Milo et al. (2009); Collier et al. (2011); Vajtai (2013); Aceto et al. (2014); Kuhn Laboratory (2017)—as well as comparable PDE models—Anderson et al. (2000); Deakin and Chaplain (2013). An overview of the parameter values used together with their mathematical and experimental origin can be found in Table 4.1.

We considered spatial domains of size $[0,1] \times [0,1]$, which corresponds to physical domains of size $[0, 0.2]\mathrm{cm} \times [0, 0.2]\mathrm{cm}$. In particular, we let the spatial domain Ω_{P} represent the primary site and the spatial domains Ω_{S}^1, Ω_{S}^2 and Ω_{S}^3 describe three metastatic sites. These spatial domains could represent *any* primary and secondary carcinoma sites. However, to give an example of a particular application, we considered a study of 4181 breast cancer patients at Memorial Sloan Kettering Cancer Center. Data and graphs from this study can be found at `http://kuhn.usc.edu/breast_cancer` (Kuhn Laboratory, 2017). We accordingly chose Ω_{P} to represent the primary site of the breast, and Ω_{S}^1, Ω_{S}^2 and Ω_{S}^3 to correspond to the common metastatic sites of bones, lungs and liver, respectively. Disregarding potential spread to any other metastatic sites, the data from the Kuhn Laboratory (2017) provided us with an extravasation probability of $\mathcal{E}_1 \approx 0.5461$ to the bones, of $\mathcal{E}_2 \approx 0.2553$ to the lungs, and of $\mathcal{E}_3 \approx 0.1986$ to the liver.

Table 4.1: ***Baseline parameter settings used in the simulations.*** *In the first column, non-dimensional parameters are indicated by upper-case notation—corresponding dimensional parameters using lower-case notation. In the fourth column, other mathematical modelling papers are referenced in brackets and biological papers without brackets.*

	Description	Non-dimensional value	Biological reference (Modelling reference)	Original value
Δt	Time step	1×10^{-3}		40 s
Δx, Δy	Space step	5×10^{-3}	Breast cell diameter in Vajtai (2013)	1×10^{-3} cm
$D_{\mathsf{M}}(d_{\mathsf{M}})$	Mesenchymal-like cancer cell diffusion coefficient	1×10^{-4}	Bray (1992) (Anderson and Chaplain (1998)) (Deakin and Chaplain (2013))	$1 \times 10^{-10}\,\mathrm{cm^2 s^{-1}}$
$D_{\mathsf{E}}(d_{\mathsf{E}})$	Epithelial-like cancer cell diffusion coefficient	5×10^{-5}	Bray (1992) (Anderson and Chaplain (1998)) (Deakin and Chaplain (2013))	$5 \times 10^{-11}\,\mathrm{cm^2 s^{-1}}$
$\Phi_{\mathsf{M}}(\phi_{\mathsf{M}})$	Mesenchymal haptotactic sensitivity coefficient	5×10^{-4}	Stokes et al. (1990) (Anderson and Chaplain (1998))	$2.6 \times 10^{3}\,\mathrm{cm^2 M^{-1} s^{-1}}$
$\Phi_{\mathsf{E}}(\phi_{\mathsf{E}})$	Epithelial haptotactic sensitivity coefficient	5×10^{-4}	Stokes et al. (1990) (Anderson and Chaplain (1998))	$2.6 \times 10^{3}\,\mathrm{cm^2 M^{-1} s^{-1}}$
$D_{\mathsf{m}}(d_{\mathsf{m}})$	MMP-2 diffusion coefficient	1×10^{-3}	Collier et al. (2011)	$1 \times 10^{-9}\,\mathrm{cm^2 s^{-1}}$
$\Theta(\theta)$	MMP-2 production rate	0.195	Biological constraints	$4.875 \times 10^{-6}\,\mathrm{M s^{-1}}$
$\Lambda(\lambda)$	MMP-2 decay rate	0.1	Estimated in (Deakin and Chaplain, 2013)	$2.5 \times 10^{-6}\,\mathrm{s^{-1}}$
$\Gamma_1(\gamma_1)$	ECM degradation rate by MT1-MMP	1	Based on (Deakin and Chaplain, 2013)	$1 \times 10^{-4}\,\mathrm{s^{-1}}$
$\Gamma_2(\gamma_2)$	ECM degradation rate by MMP-2	1	Based on (Anderson et al., 2000)	$1 \times 10^{-4}\,\mathrm{M^{-1} s^{-1}}$
T_V	Time CTCs spend in the vasculature	0.18	Meng et al. (2004)	7.2×10^{3} s
T_{M}	Epithelial doubling time	3	Milo et al. (2009)	1.2×10^{5} s
T_{E}	Mesenchymal doubling time	2	Milo et al. (2009)	8×10^{4} s
$\mathcal{P}_S$	Single CTC survival probability	5×10^{-4}	Luzzi et al. (1998)	5×10^{-4}
$\mathcal{P}_C$	CTC cluster survival probability	2.5×10^{-2}	Luzzi et al. (1998) Aceto et al. (2014)	2.5×10^{-2}
$\mathcal{E}_1$	Extravasation probability to bones	∼0.5461	Kuhn Laboratory (2017)	∼0.5461
$\mathcal{E}_2$	Extravasation probability to lungs	∼0.2553	Kuhn Laboratory (2017)	∼0.2553
$\mathcal{E}_3$	Extravasation probability to liver	∼0.1986	Kuhn Laboratory (2017)	∼0.1986

We discretised the four spatial domains to contain 201×201 grid points each. This corresponds to a non-dimensionalised space step of $\Delta x = \Delta y = 5 \times 10^{-3}$, which results in a dimensional space step of 1×10^{-3} cm, and thus roughly corresponds to the diameter of a breast cancer cell (Vajtai, 2013). We then chose a time step of $\Delta t = 1 \times 10^{-3}$, corresponding to 40 s. This condition is motivated by Anderson et al. (2000) and is employed as a means of increasing the accuracy and stability of the numerical scheme. The simulations were run for 48000 time steps, which corresponds to ∼22 days.

On each secondary grid, we chose $U_{\mathrm{S}}^1 = U_{\mathrm{S}}^2 = U_{\mathrm{S}}^3 = 10$ distinct grid points, on which blood vessels are located. For each grid, these blood vessels were placed randomly but at least two space step widths away from the respective grid's boundary. The same applies to the primary grid Ω_{P} but with the additional condition that the $U_{\mathrm{P}} = 8$ single grid points, where normal blood vessels are located, and the $V_{\mathrm{P}} = 2$ sets of five grid points, where ruptured blood vessels are placed, are located outside a quasi-circular region containing the 200 centre-most grid points. While these 10 randomly placed vessels are modelled to exist from the beginning, they represent those vessels that grow as a result of tumour-induced angiogenesis in the vascular tumour growth phase.

To represent a two-dimensional cross-section of a small avascular primary tumour, we placed a nodule that consisted of 388 randomly distributed cancer cells in the quasi-circular region of the 97 centre-most grid points of the primary grid. Throughout the simulation, we allowed for no more than $\mathcal{Q} = 4$ cancer cells on any grid point to account for competition for space. Hence, initially placing 388 cancer cells on the grid implies that the 97 centre-most grid points, which we chose to obtain a symmetric, quasi-circular region of about 100 grid points, are filled to the preferred carrying capacity with cancer cells. A randomly chosen 40% of these cancer cells were of epithelial-like phenotype and the remaining 60% of mesenchymal-like phenotype. The described initial condition ensures that the cancer cells are placed away from any pre-existing vessels to match the biology of an avascular tumour. The counters for the cell age are initially set to zero for all cells. Figure 4.3 gives an example of a typical initial mesenchymal-like cancer cell placement and vessel distribution on the primary grid.

In accordance with Table 4.1, we chose the mesenchymal-like cancer cell diffusion coefficient to be $D_{\mathrm{M}} = 1 \times 10^{-4}$, the epithelial-like cancer cell diffusion coefficient to be $D_{\mathrm{E}} = 5 \times 10^{-5}$, and the mesenchymal and epithelial haptotactic sensitivity coefficients to be $\Phi_{\mathrm{M}} = \Phi_{\mathrm{E}} = 5 \times 10^{-4}$. Moreover, we used the MMP-2 decay rate $\Lambda = 0.1$ that was estimated in Deakin and Chaplain (2013) and chose the MMP-2 production rate to be about twice as large, $\Theta = 0.195$.

We further assumed that, once in the vasculature, a single CTC had a survival probability of $\mathcal{P}_S = 5 \times 10^{-4}$, which is of the order of the micro- and macrometastatic growth success rates proposed in Luzzi et al. (1998). We chose the success rate for metastatic growth to be our survival probability because our model in its current state disregards cancer cell death at secondary sites so that any successfully extravasated cancer cell will initiate micrometastatic growth over time. CTC clusters had a survival probability $\mathcal{P}_C = 50\mathcal{P}_S = 2.5 \times 10^{-2}$, in agreement with the finding by Aceto et al. (2014) that the survival probability of CTC clusters is between 23 and 50 times higher than that of single CTCs. Surviving single CTCs and CTC clusters exited onto the secondary grids after spending $T_V = 0.18$ in the blood system, which corresponds to 2 hours and hence to the breast cancer-specific clinical results in Meng et al. (2004).

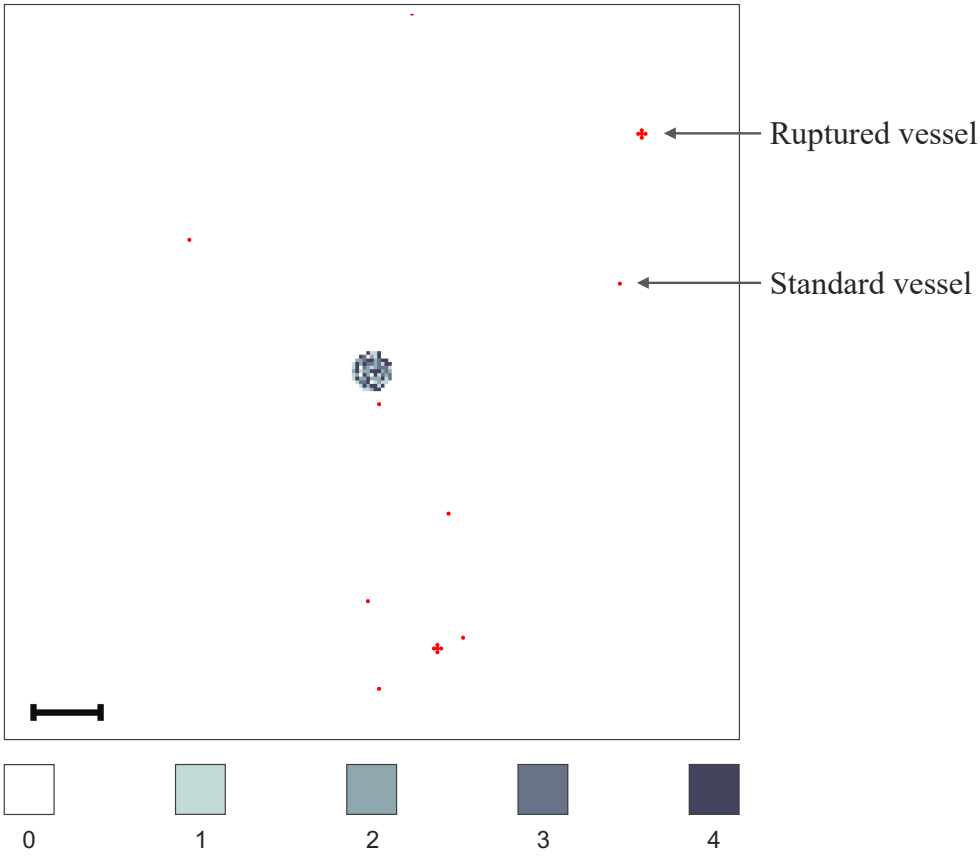

Figure 4.3: ***Sample vessel distribution and initial condition for the mesenchymal-like cancer cells.*** *The plot shows (in red) ten randomly distributed blood vessels on the primary grid, two of which are so-called ruptured vessels that consist of five rather than one grid point. In the centre of the grid, the initial distribution of the mesenchymal-like cancer cells is shown. There are between* 0 *(white) and* 4 *(black) cancer cells on a grid point. As the initial distribution of cancer cells represents a two-dimensional section through an avascular tumour, the blood vessels are placed at some distance away from the initial nodule of cancer cells. The scale bar denotes* 0.02 cm.

Further, we assumed a uniform initial ECM density of $w(t, x, y) = 1$ across all the spatial domains, while the initial MMP-2 concentration was $m(t, x, y) = 0$. We chose the other parameters as shown in Table 4.1 and assumed that epithelial-like cancer cells divide by mitosis every time span $T_{\mathsf{E}} = 2$ and mesenchymal-like cancer cells every $T_{\mathsf{M}} = 3$. This corresponds to approximately 22 hours and 33 hours, respectively, which is consistent with the average doubling times found in breast cancer cell lines (Milo et al., 2009).

In Appendix B, we provide pseudo-code that yields insight into the computational implementation of this mathematical multi-organ model.

4.3 Results

To verify that our modelling framework is suitable to capture the key steps of the invasion-metastasis cascade, we first ran simulations with the base parameters shown in Table 4.1. As indicated by the headings throughout this section, we then varied these base parameters across biologically realistic ranges to further confirm that our framework delivers biologically realistic results and to gain insight into the underlying biology. For each of the parameter studies, we took the average results from running the simulation three times—unless stated otherwise—and indicated error bars to display the standard deviation in the corresponding plots. While the statistical reliability could be improved by increasing the number of samples, we only use these measures to examine the general qualitative tendencies of our model. Hence, we have restricted the analysis at this point. This way, we studied the effect that changing the initial ratio of epithelial-like to mesenchymal-like cancer cells, the number of blood vessels in the primary site, and the survival probability of cancer cells had on the overall cancer dynamics. We investigated the roles of MMP-2 and MT1-MMP as well as their role in comparison to one another. Finally, we changed the parameters to describe haptotaxis-dominated rather than diffusion-dominated cancer cell movement at the end of this section to re-examine the role of membrane-bound versus diffusible MDEs. We compared the outcomes of these simulations to a range of experimental and clinical results.

The computational time to run a simulation on a standard desktop computer was approximately 35 minutes.

Simulations with base parameters

When using the settings outlined in the previous section, we observed in our simulations that both epithelial-like and mesenchymal-like cancer cells invaded the tissue surrounding the primary tumour, which is represented by the primary grid, over 22 days. This is shown in the simulation results in the two upper rows of panels in Figure 4.4, respectively. The epithelial-like cancer cells formed the bulk of the central tumour mass, while the mesenchymal-like cancer cells were predominantly found at the outermost tissue-invading edge. The maximum observed invasion distance of the cancer cells over this period was approximately 0.13 cm. The pattern of MMP-2 concentration for the same simulation roughly followed the distribution of the mesenchymal-like cancer cells as shown in the third row of panels in Figure 4.4. The ECM density, which is depicted in the bottom row of Figure 4.4, also followed the evolution of the MMP-2 concentration but in a more uniform fashion.

In addition to the cancer cell invasion on the primary grid, we also observed metastatic spread of single cancer cells, as well as of homogeneous and heterogeneous cancer cell clusters, to the grids representing the secondary sites of the bones (Figure 4.5), the lungs (Figure 4.6) and the liver (Figure 4.7). The results obtained here showed that the first metastatic spread occurred at the site of the bones. As shown in the panel on the top left of Figure 4.5, after 11 days we already observed a micrometastatic lesion of epithelial-like cancer cells with an approximate diameter of 0.04 cm on the grid that represented the bones, but in none of the other locations. Since this micrometastasis was seeded by a single extravasated epithelial-like cancer cell, no mesenchymal-like cancer cells are

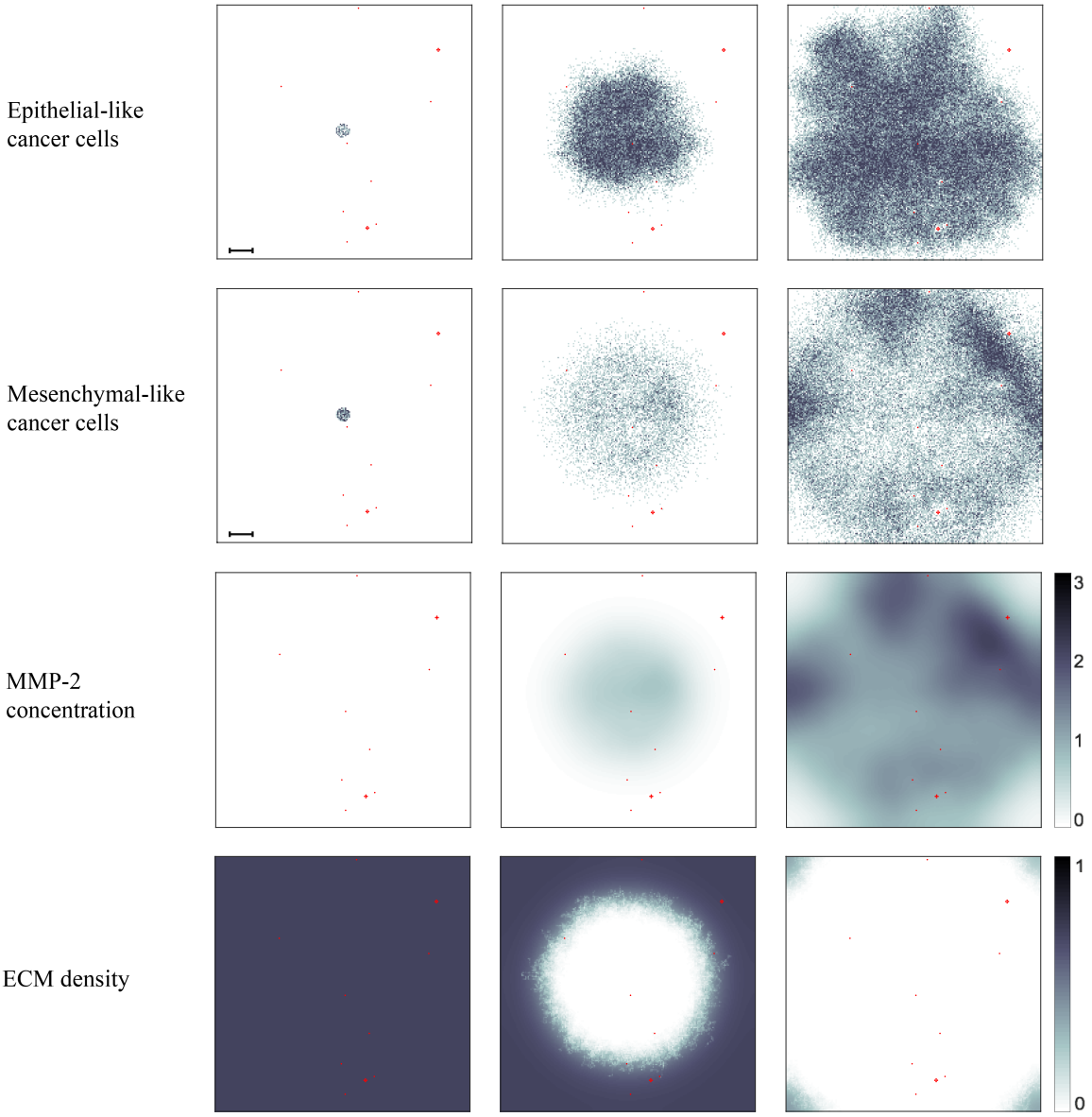

Figure 4.4: ***Simulation results on the primary grid.*** *Primary tumour dynamics after 0 days,* $\sim$11 *days and* $\sim$22 *days (left to right). For each time step, the distribution of epithelial-like cancer cells (top row) and mesenchymal-like cancer cells (second row) is shown, with the discrete number of cancer cells per grid point ranging from* 0 *(white) to* 4 *(black) on each of the panels. The MMP-2 concentration (third row) continuously varies between* 0 *(white) and* 3.0936 *(black), and the ECM density (bottom row) between* 0 *and* 1*. Red dots represent blood vessels. There are* 8 *normal blood vessels of the size of one grid point as well as* 2 *ruptured blood vessels, which extend over* 5 *grid points each. If cancer cells are moved to these grid points, they may enter the vasculature and can potentially extravasate at secondary sites. The dynamics of the cancer cells at the secondary sites are presented in Figures 4.5–4.7. The scale bar denotes* 0.02 cm *and applies to all of the panels.*

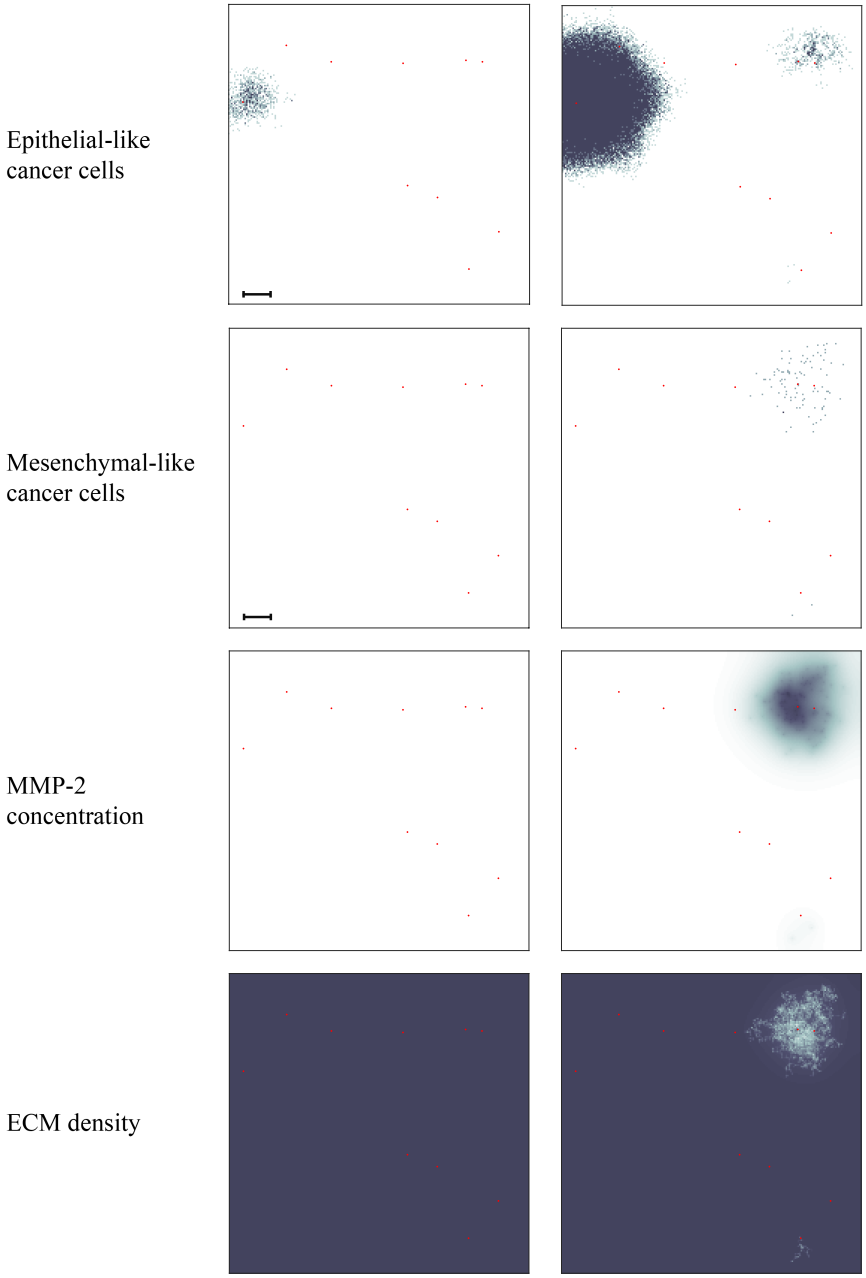

Figure 4.5: ***Simulation results on secondary grid representing the bones.*** *Distribution of epithelial-like cancer cells, mesenchymal-like cancer cells, MMP-2 concentration and ECM density (top to bottom row of panels) at the secondary site representing the bones, shown after* $\sim$11 *days (left) and* $\sim$22 *days (right). The number of cancer cells per grid point varies between* 0 *(white) and* 4 *(black) in the first row of panels and between* 0 *(white) and* 2 *(black) in the second row of panels. The MMP-2 concentration ranges from* 0 *(white) to* 3.4737×10^{-2} *(black) and the ECM density from* 0.17559 *(light grey) to* 1 *(black). The red grid points represent blood vessels, through which cancer cells can extravasate. The scale bar denotes* 0.02 cm *and applies to all panels.*

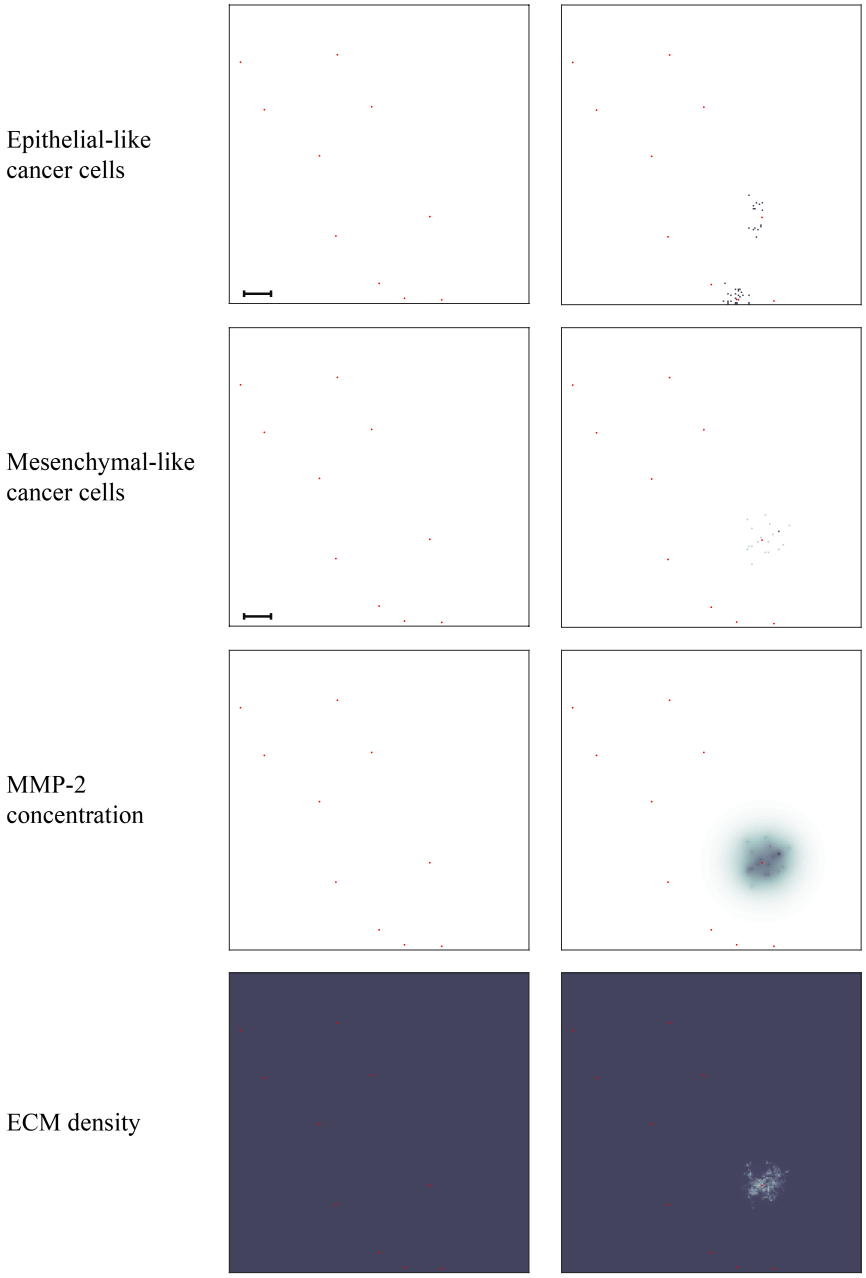

Figure 4.6: ***Simulation results on secondary grid representing the lungs.*** *Distribution of epithelial-like cancer cells, mesenchymal-like cancer cells, MMP-2 concentration and ECM density (top to bottom row of panels) at the secondary site representing the bones, shown after* $\sim$11 *days (left) and* $\sim$22 *days (right). The number of cancer cells per grid point varies between* 0 *(white) and* 2 *(black) in the upper panels and* 0 *(white) and* 3 *(black) in the lower panels. The MMP-2 concentration ranges from* 0 *(white) to* 1.5876×10^{-2} *(black) and the ECM density from* 0.41137 *(light grey) to* 1 *(black). The red grid points represent blood vessels, through which cancer cells can extravasate. The scale bar denotes* 0.02 cm *and applies to all panels.*

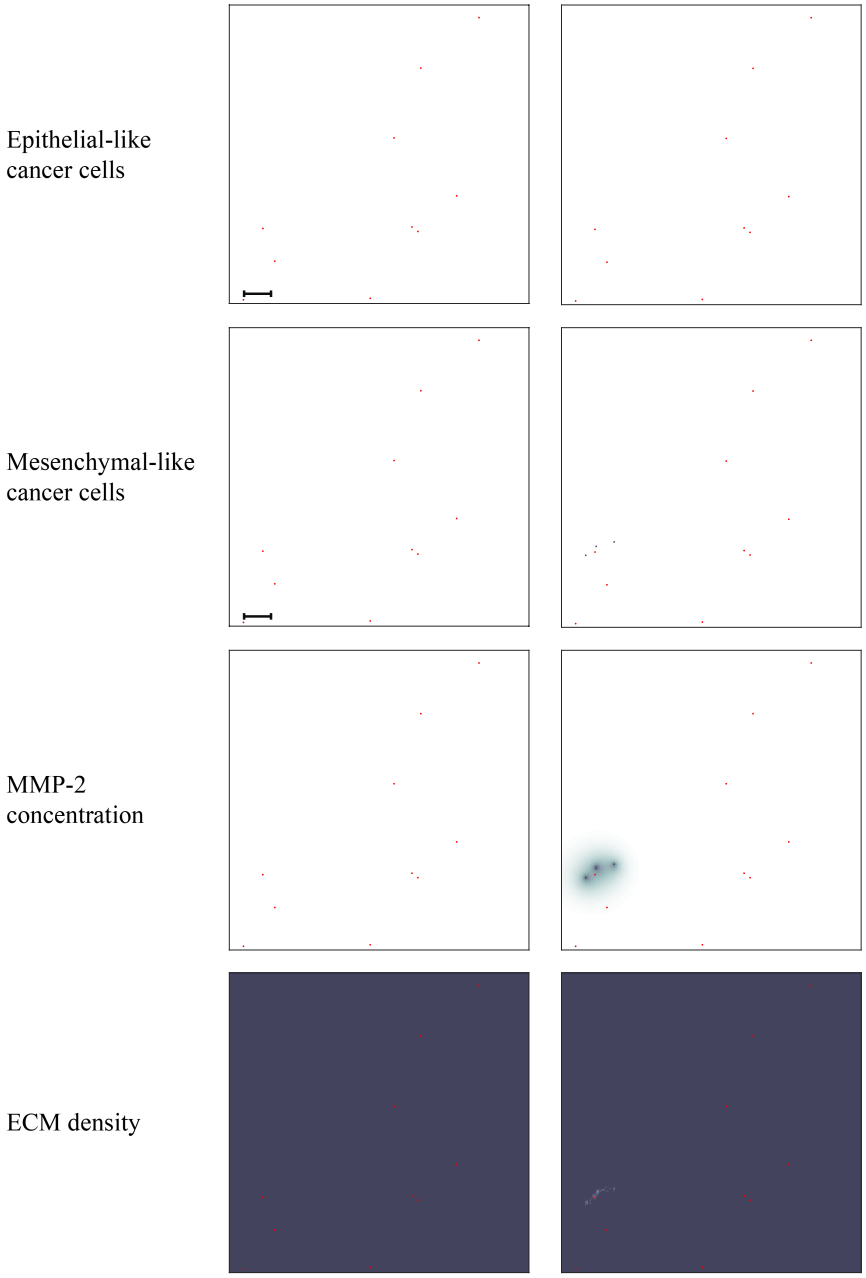

Figure 4.7: ***Simulation results on secondary grid representing the liver.*** *Distribution of epithelial-like cancer cells, mesenchymal-like cancer cells, MMP-2 concentration and ECM density (top to bottom row of panels) at the secondary site representing the bones, shown after* $\sim$11 *days (left) and* $\sim$22 *days (right). The first row of panels does not contain any epithelial-like cancer cells, while the panel on the bottom right of the second row contains three single mesenchymal-like cancer cells indicated in black. The MMP-2 concentration ranges from* 0 *(white) to* 3.7129×10^{-3} *(black) and the ECM density from* 0.58015 *(light grey) to* 1 *(black). The red grid points represent blood vessels, through which cancer cells can extravasate. The scale bar denotes* 0.02 cm *and applies to all panels.*

present. Yet, after 22 days we discovered metastatic spread at all three of the secondary locations in the body that we considered in our simulations. On the grid representing the bones, we found that the earliest micrometastasis, which consisted of epithelial-like cancer cells only, had rapidly increased in diameter to approximately 0.1 cm (see top right panel of Figure 4.5). Additionally, a second micrometastasis consisting of both epithelial-like and mesenchymal-like cancer cells had formed at the top right of the same grid. This phenotypically heterogeneous micrometastasis developed from the extravasation of a heterogeneous cancer cell cluster. Finally, we observed a set of four epithelial-like and two mesenchymal-like DTCs at the bottom right of the grid corresponding to the bones. The latter two formations were results of heterogeneous cancer cell clusters spreading to the bones. While the secondary site that represented the bones showed by far the largest cancer cell load after 22 days, we detected a further two micrometastases at the secondary site of the lungs, as shown in the panels on the right of Figure 4.6. Here, the micrometastasis at the bottom of the grid consisted of epithelial-like cancer cells only, while the top micrometastasis contained both cancer cell types as it had grown out of a heterogeneous cancer cell cluster. Finally, the liver showed the least secondary spread in the form of three mesenchymal-like DTCs that arrived as a single cluster, as shown in the panel on the right in the second row of panels of Figure 4.7.

Changing the initial ratio of epithelial- to mesenchymal-like cancer cells

By keeping the total initial amount of cancer cells constant at 388 but varying the initial percentage of epithelial-like cancer cells between 0% and 100% in steps of 10%, we found that having solely epithelial-like cells at the start of the simulation had a significant negative impact on tumour growth. We counted an average of 62932 cancer cells at the end of our simulation time span of 22 days as compared to about 48% more cancer cells (i.e. 93115 cancer cells) in the case of an even initial distribution.

Starting the simulation solely with mesenchymal-like cancer cells had a similar, yet weaker, dampening effect: Compared to simulation with an even initial distribution, it reduced growth to 86425, and thus by about 7.7%. Otherwise, we generally found that a higher percentage of epithelial-like cancer cells at the start coincided with a lower number of mesenchymal-like cancer cells at the end of the simulations. At the same time, the number of epithelial-like cancer cells after 22 days increased. We observed that the maximum number of cancer cells occurred under initial conditions with even parts of mesenchymal-like and epithelial-like cancer cells but that the combined cancer cell count at the end of the simulation was relatively stable if we varied the initial number of epithelial-like cancer cells between 0% and 90% (see Figure 4.8).

With regards to shedding from the primary tumour, and hence also to chances of successful metastasis, we found that a higher initial percentage of mesenchymal-like cancer cells correlated to a higher number of intravasating single cancer cells and cancer cell clusters, likely as a result of an overall higher number of mesenchymal-like cancer cells (see Figure 4.9). If we started our simulation with mesenchymal-like cancer cells only, we observed an average total of 634 intravasations by single cancer cells or cell clusters—compared to only 7 over the same time range in the case of the average of simulations that included epithelial-like cancer cells only. When we set the number of ruptured

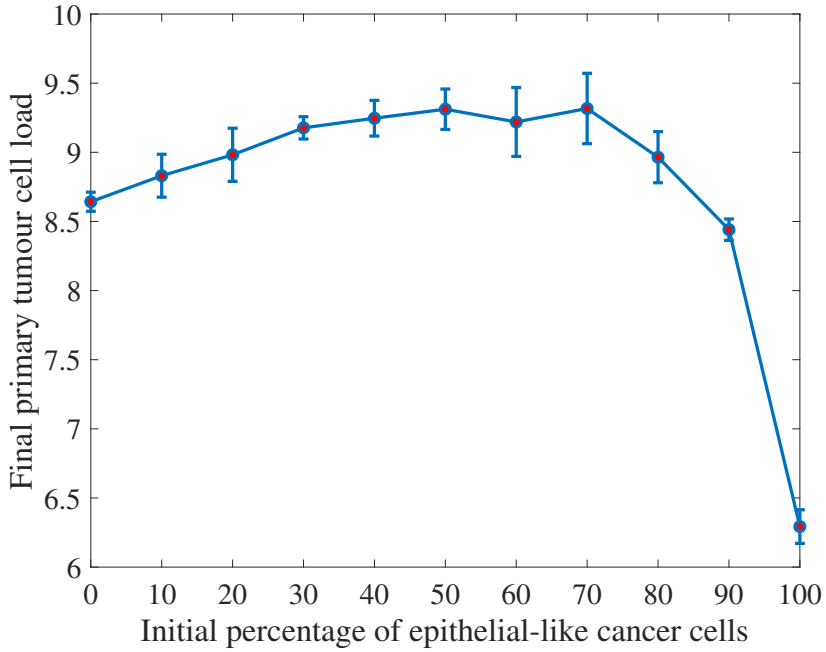

Figure 4.8: ***Co-presence of epithelial- and mesenchymal-like cancer cells increases the overall primary tumour cancer cell load.*** *The absence of mesenchymal-like cancer cells hinders cancer cell invasion and tumour growth. The final primary tumour cancer cell load on the vertical axis is given in units of* 10^4 *and refers to simulation results after approximately* 22 *days.*

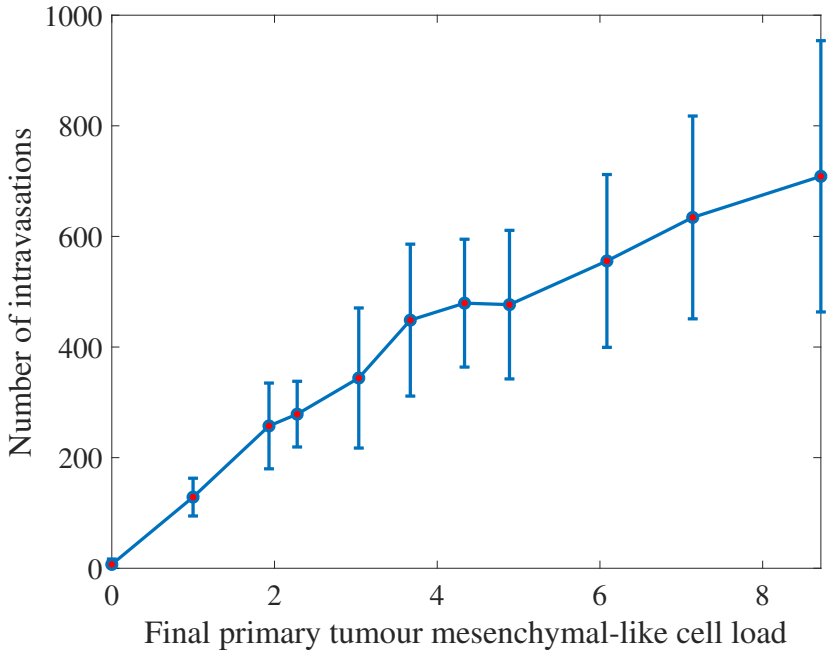

Figure 4.9: ***Higher numbers of mesenchymal-like cancer cells at the primary site correspond to an increased intravasation count.*** *The final primary tumour cancer cell load on the horizontal axis is given in units of* 10^4 *and refers to simulation results after approximately* 22 *days.*

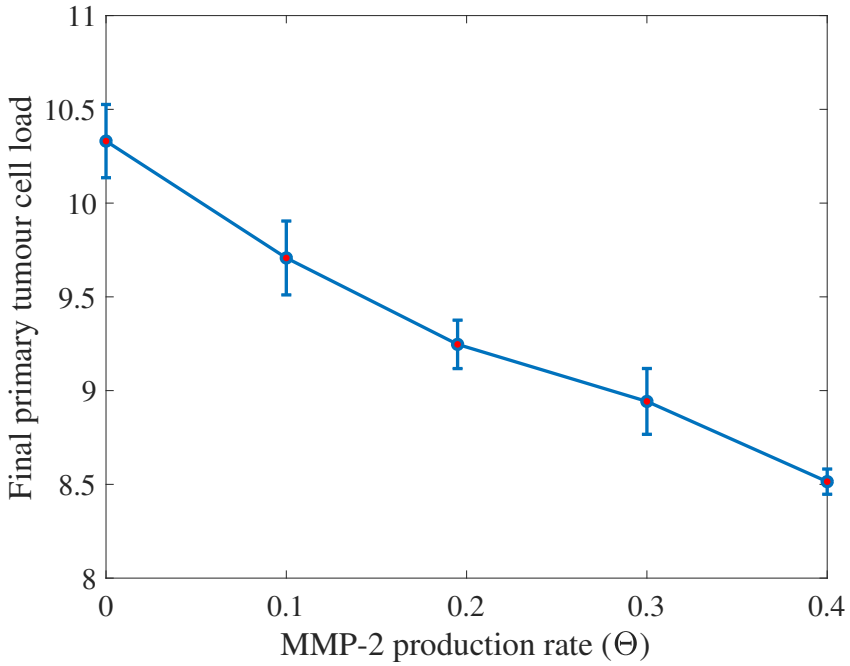

Figure 4.10: ***A higher MMP-2 production rate lowers the final primary tumour cancer cell load.*** *The final primary tumour cancer cell load on the vertical axis is given in units of* 10^4 *and refers to simulation results after approximately* 22 *days.*

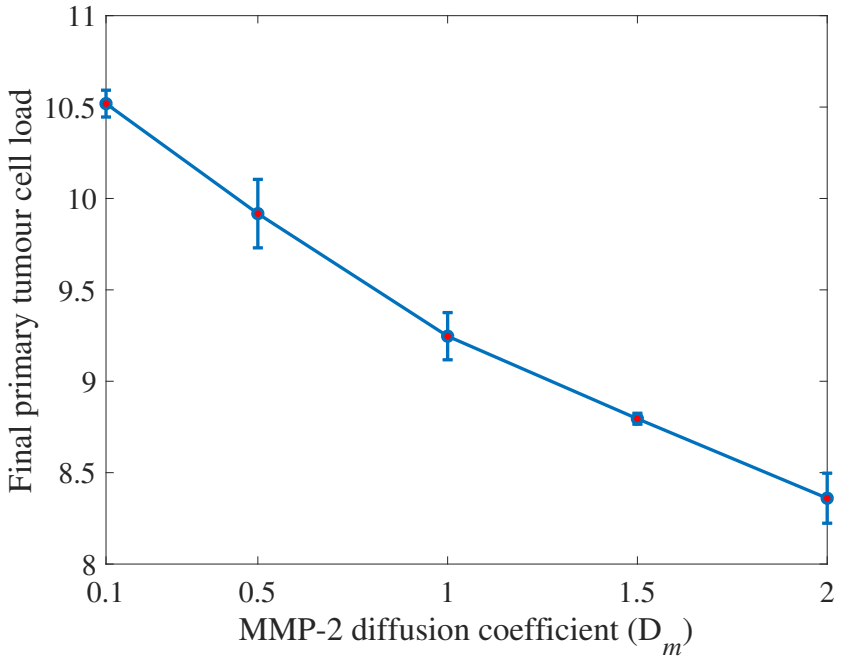

Figure 4.11: ***A higher MMP-2 diffusion coefficient corresponds to a lower final primary tumour cancer cell load.*** *The MMP-2 diffusion coefficient on the horizontal axis is given in units of* 10^{-3} *and the final primary tumour cancer cell load on the vertical axis in units of* 10^4*. The results were measured after approximately* 22 *days.*

vessels in the primary grid to 0 and considered 10 normal vessels only, we observed no intravasations.

Changing the survival probability of cells in the vasculature

As Aceto et al. (2014) suggested that the probability of cluster survival in the vasculature ($\mathcal{P}_C$) is 23 to 50 times higher than that for single CTCs ($\mathcal{P}_S$), in the next simulations, we examined the effects of changing the probability of cluster survival in the vasculature to be $\mathcal{P}_C = 23\mathcal{P}_S = 1.15 \times 10^{-2}$—so to take the value of the lower rather than the upper bound suggested by the authors. For this purpose, we did not allow cancer cell clusters to break up in the vasculature. Averaged over 12 simulations, the observed cluster survival was caused to be changed from 2.503×10^{-2} (with $\mathcal{P}_C = 2.5 \times 10^{-2}$) to 1.137×10^{-2}. While this change had no significant effect on the number of single cells and clusters intravasating, it did reduce the average number of extravasating cancer cell clusters, as expected.

The role of MMP-2

To investigate the role of MMP-2 in the spatiotemporal evolution of the cancer cells, we varied both the MMP-2 production rate and the MMP-2 diffusion coefficient.

Modifying the MMP-2 production rate to take values $\Theta \in \{0, 0.1, 0.195, 0.3, 0.4\}$ suggested that a lower MMP-2 production rate correlates to a higher overall cancer cell load after ∼22 days—for each cancer cell type individually as well as for both cell types combined. This resulted mainly from changes in cancer cell numbers on the primary grid. The corresponding plot in Figure 4.10 highlights this.

Next, we observed that increasing the MMP-2 diffusion coefficient over the range of values $D_m \in \{0.1, 0.5, 1, 1.5\} \times 10^{-3}$ decreased the total cancer cell load on the primary grid after 22 days. The total number of intravasations and, coherently, the metastatic cancer cell load decreased as well. This is shown in Figure 4.11.

The effects of MMP-2 degradation alone

We next set the MT1-MMP degradation rate to be $\Gamma_1 = 0$ to examine the situation in which the diffusible MMP-2 is the only MDE in our system. We then varied the MMP-2 production rate, as we had done before when studying the effects of varying the MMP-2 production rate in the presence of MT1-MMP, to be $\Theta \in \{0, 0.1, 0.195, 0.3, 0.4\}$.

Generally, we found that the total primary cancer cell load after 22 days was significantly reduced compared to simulations in which MT1-MMP was present. For instance, comparing against simulations with our baseline MMP-2 production rate of $\Theta = 0.195$, the total primary cancer cell load was between 8.2% and 58.0% lower. However, invasion was still possible.

The role of MDEs in the context of haptotaxis-dominated cancer cell movement

In all of the above simulations, we have considered diffusion-dominated cancer cell movement. We next investigated the roles of MT1-MMP and MMP-2 in cancer cell invasion in the scenario of haptotaxis-dominated cancer cell movement. For this, we changed our epithelial-like and mesenchymal-like non-dimensional cancer cell diffusion coefficients to be $D_{\mathsf{E}} = 5 \times 10^{-11}$ and $D_{\mathsf{M}} = 1 \times 10^{-10}$, respectively. Further, we focussed on cancer cell invasion in the primary grid in these simulations and hence set the number of normal and ruptured vessels to zero. *Ceteris paribus*, we then re-examined the effectiveness of invasion involving solely MT1-MMP as well as solely MMP-2 in a system with haptotaxis-dominated cancer cell movement. We first set the MT1-MMP degradation rate to be $\Gamma_1 = 0$, allowing us to represent the situation in which the diffusible MMP-2 is the only MDE in our system. We then, as before, varied the MMP-2 production rate to be $\Theta \in \{0, 0.1, 0.195, 0.3, 0.4\}$. As opposed to our findings when studying diffusion-dominated cancer cell movement, we observed that invasion was no longer possible for the same range of MMP-2 production rates. The final cancer cell numbers on the primary grid averaged below a ten-fold increase in cell population when compared to the original nodule of 388 cancer cells. Moreover, the final cancer cell constellation was located at the centre of the grid due to the very low invasion distance of the cancer cells.

When we increased the MT1-MMP degradation coefficient back to the baseline $\Gamma_1 = 1$ but set the MMP-2 production rate to be $\Theta = 0$, we found that the cancer cells did invade with an average total of 18312 cancer cells after approximately 22 days. By decreasing the MT1-MMP degradation coefficient to $\Gamma_1 = 0.5$, we observed an even larger cancer cell load of 28157.

Simulation results coincide with experimental evidence that stresses the importance of MT1-MMP in cancer invasion

We next ran simulations with an initial cell distribution and domain size that matched the experiments conducted by Sabeh et al. (2009), who embedded HT-1080 cancer cells into 3D type I collagen gels as central nodules of diameter 1.5×10^{-2}–2×10^{-2} cm. Coherently, we increased the diameter of our initial centred quasi-circular nodule to 1.5×10^{-2} cm and let it consist of 700 cancer cells, 40% (i.e. 280) of which were epithelial-like and 60% (i.e. 420) mesenchymal-like. Further, we decreased our domain size to be $0.1\,\text{cm} \times 0.1\,\text{cm}$ to match that in the experimental conditions of Sabeh et al. (2009).

Figure 4.12 shows the spatiotemporal evolution of epithelial-like and mesenchymal-like cancer cells under these experimental conditions after running a simulation for 16 days. As expected, we still observed that invasion by both epithelial-like and mesenchymal-like cancer cells was possible when both MDEs were present (i.e. with $\Theta = 0.195$, $\Gamma_1 = 1$) and when solely MT1-MMP was present (i.e. with $\Theta = 0$, $\Gamma_1 = 1$), while invasion was not possible when solely MMP-2 was expressed (i.e. with $\Theta = 0.195$, $\Gamma_1 = 0$). These results are shown in the left, middle and right column of panels of Figure 4.12, respectively. Out of the three mechanisms, invasion under the expression of MT1-MMP alone yielded the highest average invasion depth. We further observed that the switch from diffusion-dominated to haptotaxis-dominated cancer cell movement triggered more

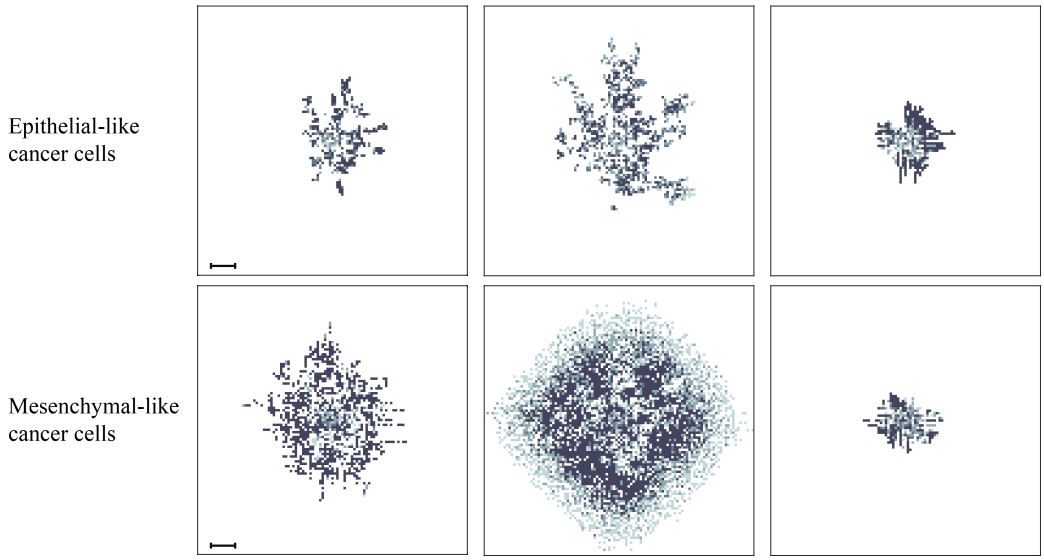

Figure 4.12: ***Simulation results for a heterogeneous cancer cell population subject to haptotaxis-dominated movement.*** *To match the domain size and initial cell count of experiments by Sabeh et al. (2009), we started the simulation by placing* 420 *mesenchymal-like cancer cells and* 280 *epithelial-like cancer cells in a quasi-circular region with diameter* $1.5 \times 10^{-2}\,\mathrm{cm}$ *at the centre of a* $0.1\,\mathrm{cm} \times 0.1\,\mathrm{cm}$ *grid (initial conditions not shown). Depicted is the distribution of epithelial-like (upper panels) and mesenchymal-like (lower panels) cancer cells after* 16 *days. Left to right, the invasive patterns in presence of both MDEs (*$\Theta = 0.195$, $\Gamma_1 = 1$*), in presence of MT1-MMP only (*$\Theta = 0$, $\Gamma_1 = 1$*) and in presence of MMP-2 only (*$\Theta = 0.195$, $\Gamma_1 = 0$*) are shown for both cancer cell phenotypes. The scale bar denotes* $0.01\,\mathrm{cm}$ *and applies to all panels.*

prominent finger-like protrusions in the invasive pattern of the epithelial-like cancer cells in the scenarios where either both MDEs or MT1-MMP alone were present, which is shown in the left and in the middle panel of the top row of Figure 4.12, respectively.

However, Sabeh et al. (2009) used a *homogeneous* HT-1080 cancer cell population, and thus cells of mesenchymal origin, in their experiments to examine the role of MT1-MMP and MMP-2 in cancer invasion. To fully match the experimental conditions of Sabeh et al. (2009), we next changed our initial conditions to consider a cancer cell population consisting of 700 mesenchymal-like cancer cells only, as shown in the third row of panels in Figure 4.13. Sabeh et al. (2009) electroporated multicellular clusters of HT-1080 cancer cells of diameter 1.5×10^{-2}–$2 \times 10^{-2}\,\mathrm{cm}$ either with a control *small interfering RNA* (siRNA), which leaves the diffusible *matrix metalloproteinase-1* (MMP-1) and MMP-2 as well as the non-diffusible MT1-MMP activated; or with MMP-1 and MMP-2 siRNAs, which leaves MT1-MMP alone activated but silences the diffusible MDEs MMP-1 and MMP-2; or with MT1 siRNA, which silences MT1-MMP but leaves MMP-1 and MMP-2 activated. These electroporated multicellular clusters were then embedded centrally in 3D type I collagen gels. The initial experimental setups and their respective evolution after 3 days are shown—left to right—in the two upper rows of panels in Figure 4.13. Since the evolution of the two diffusible MDEs, MMP-1 and MMP-2, in the experiments can be jointly accounted for by the MMP-2 equation of our model, our modelling framework

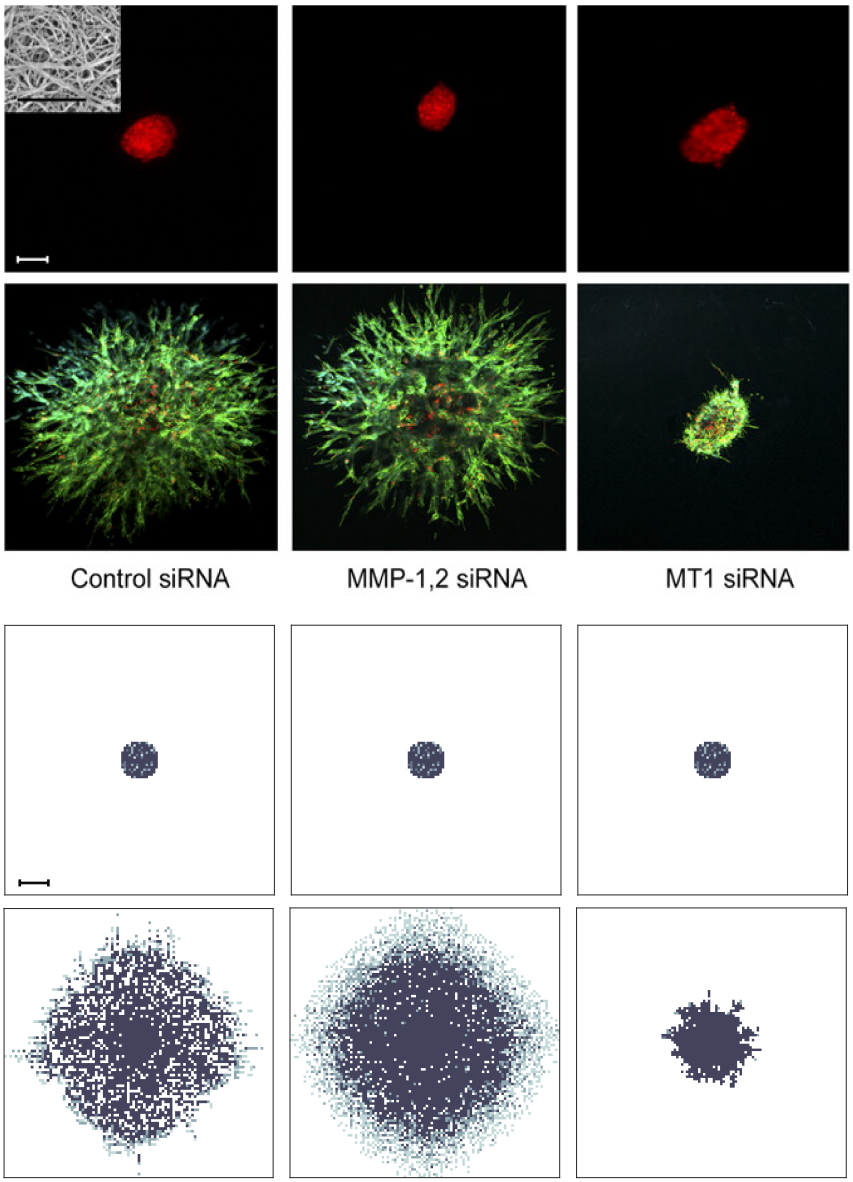

Figure 4.13: ***Experimental findings by Sabeh et al. (2009) (black panels) compared to simulation results (white panels).*** *The top row of panels shows the initial experimental conditions in Sabeh et al. (2009), where HT-1080 cancer cells were embedded into 3D type I collagen gels as central nodules of diameter* 1.5×10^{-2}–$2 \times 10^{-2}\,\mathrm{cm}$. *The cancer cell spheroids had previously been electroporated with a control siRNA; MMP-1 and MMP-2 siRNAs; MT1 siRNA (left to right). Their invasion after* 3 *days is shown in the second row of panels. We matched the experimental conditions (see text). The bottom row of panels shows the distribution of the mesenchymal-like cancer cells after* 16 *days in the case where the mesenchymal-like cancer cells are subject to haptotaxis-dominated movement. The number of cancer cells per grid point ranges from* 0 *(white) to* 4 *(black) on each of the panels. Comparing the six panels on the bottom with those on the top, we find the simulation results to be in good qualitative agreement with the experimental results by Sabeh et al. (2009). The scale bar denotes* $0.01\,\mathrm{cm}$ *and applies to all panels. Reproduced from Sabeh et al. (2009) with permission from Rockefeller University Press.*

can replicate the above-described experimental settings well. We did this by, again, considering a system with both MDEs (i.e. with $\Theta = 0.05$, $\Gamma_1 = 1$), with MT1-MMP only (i.e. with $\Theta = 0$, $\Gamma_1 = 1$) and with MMP-2 only (i.e. with $\Theta = 0.05$, $\Gamma_1 = 0$), respectively. When looking at the invasion results after 720 time steps, which corresponds to 16 days, we observed similar results as in the case of a mixed initial cancer cell population. As the first panel of the bottom row of Figure 4.13 shows, invasion was possible with both MDEs present. Yet, the invasion depth—measured by the distance between the cancer cell that has invaded the furthest from the centre of the grid from the centre of the grid—was slightly lower compared to the case where we allowed for MT1-MMP expression alone, which is shown in the second panel of the bottom row of the same figure. Finally, we again found that invasion was not possible in the presence of MMP-2 alone as the third panel of the bottom row of Figure 4.13 shows. As Figure 4.13 suggests, these results are qualitatively in good agreement with the experiments by Sabeh et al. (2009).

Moreover, it would be interesting to repeat the experiments by Sabeh et al. (2009) using a cancer cell population consisting of both epithelial-like and mesenchymal-like cancer cells to examine whether the invasion assays would resemble those shown in Figure 4.12.

Finally, due to our awareness that Sabeh et al. (2009) used cancer cells of mesenchymal origin only in their experiments, we further sought to reproduce the results of experiments by Gaggioli et al. (2007), who studied the invasion of *squamous cell carcinoma* (SCC) *cells*, which are of epithelial origin. They found that SCC cells rely on fibroblasts for their invasion, which are cells of mesenchymal-like type that are capable of matrix remodelling, like the mesenchymal-like cancer cells in our model. In the absence of fibroblasts, the authors observed that the cancer cells were unable to invade. While we showed that a mixed population of epithelial-like and mesenchymal-like cancer cells was indeed able to invade when both MDEs are present (see panels on the left of Figure 4.12), we ran the same simulations again with epithelial-like cancer cells only. This showed that the epithelial-like cancer cells in our model were unable to invade on their own, as observed experimentally by Gaggioli et al. (2007). (Data not shown—similar to bottom right panel of Figure 4.13.)

4.4 Discussion

In carrying out the computational simulations, we found that such a modelling framework provides biologically realistic outcomes and gives further insight into the mechanisms underpinning the invasion-metastasis cascade at the cellular scale. Tumour shape and metastatic distribution were predicted to appear as one would expect in a cancer patient who has not yet received treatment. In particular, we found that the mesenchymal-like cancer cells formed a ring-shaped leading front along the tumour edge, which was also seen in experiments (Nurmenniemi et al., 2009). Nurmenniemi et al. (2009) further observed an average maximum invasion depth of 5.47×10^{-2} cm over 14 days, when culturing HSC-3 cancer cells, a human oral squamous carcinoma cell line with high metastatic potential, on top of myoma tissue. This translates into an average estimated invasion speed of approximately 4.52×10^{-8} cm s^{-1}. It suggests that our observed maximum invasion depth of $\sim$0.13 cm in 22 days and resulting average estimated invasion speed of approximately 6.77×10^{-8} cm s^{-1} is a realistic result, given that migration speed varies between

cancer cell lines. The distribution of the cancer cell spread between the secondary sites that we considered in our model—measured via the metastatic cancer cell load and number of metastases at the respective sites—further matched the clinical data of 4181 breast cancer patients underlying our simulations, which is summarised in Figure 2.15. As Figure 4.5 indicates, the largest micrometastasis, which resulted from the earliest metastatic spread, occurred at the site of the bones. This is the most frequently observed site of metastatic spread from primary breast cancer in the data processed by the Kuhn Laboratory (2017). Overall, we observed two further successful extravasations to the site of the bones, resulting in both phenotypically homogeneous and heterogeneous secondary growth at this site. The second heaviest cancer cell load, in the form of one heterogeneous micrometastasis and one consisting of epithelial-like cancer cells only, was found in the lungs. The least metastatic spread occurred to the liver with only three mesenchymal-like DTCs being observed, which arrived jointly as part of the same successfully extravasated mesenchymal-like cancer cell cluster. While, of course, stochasticity underpins the results of the metastatic spread, we again found that our results matched the clinical observations summarised in Figure 2.15. To our knowledge, there are currently no data available that claim to deliver an accurate estimation of the typical metastatic load from primary breast cancer to secondary sites over a specified time frame. However, we believe our result is biologically appropriate with regards to its timing, in correspondence with the conclusion reached by Obenauf and Massagué (2015) in their review of the metastatic traits that allow cancer cells to colonise various secondary sites, who suggested that CTCs and metastatic spread can be detected soon after vascularisation of the primary tumour, as in our simulations. Nonetheless, Obenauf and Massagué (2015) argue that the most limiting step of the invasion-metastasis cascade is not the dissemination through the vasculature, which we account for in our model, but the transition from infiltration of a secondary site to overt colonisation. To achieve this final step of colonisation, which is not (yet) part of our modelling framework, the cancer cells need to survive secondary site-derived detrimental signals and simultaneously exploit secondary site-derived survival signals (Obenauf and Massagué, 2015). Also, observed dormancy of tumours over extended periods may occur in the form of pre-angiogenic micrometastases that, at a later point in time, acquire the ability to become vascularised (Chambers et al., 2002). As avascular tumours can grow up to 0.1–0.2 cm via diffusion only (Folkman, 1990), all metastatic spread observed in our simulation is assumed to fall into this pre-angiogenic category.

In addition to obtaining expected simulation outcomes on the cell-level, both for primary tumour growth and secondary spread, by using the baseline parameter settings in Table 4.1, we obtained other biologically realistic and relevant results from the simulations by varying key parameters.

Changing the initial ratio of mesenchymal-like cancer cells to epithelial-like cancer cells emphasised the importance of co-presence of the two cancer cell types for rapid invasive tumour growth. In particular, it highlighted that cancer cell invasion relies on the expression of MDEs (and MT1-MMP in particular), which are required to clear the collagen in the normal tissue of its covalent cross-links, as proposed by Sabeh et al. (2009). These results further suggested that a relatively small percentage of MDE-expressing cancer cells suffices to induce rapid cancer cell invasion.

We observed that higher numbers of mesenchymal-like cancer cells at the primary tumour location increased the number of cancer cell intravasations. Also, cancer cells from primary tumours consisting of a homogeneous epithelial-like cell population did not intravasate (unless ruptured vessels were present, in which case minimal shedding occurred). This coincides with experimental findings by Tsuji et al. (2009). Results from their mouse model indicated that cancer cells originating from primary tumours of homogeneously mesenchymal-like phenotype could intravasate. The same applied to cancer cells that stemmed from tumours consisting of a combination of epithelial-like and mesenchymal-like cancer cells. On the contrary, no intravasations were observed when the primary tumour consisted of epithelial-like cancer cells only.

The fact that we, as opposed to Tsuji et al. (2009), found a small amount of successfully intravasated cancer cells, even when our tumour consisted of epithelial-like cancer cells only, was to be expected. This was a result of our inclusion of ruptured vessels in the model, which we considered following the biological findings by Bockhorn et al. (2007). Since these blood vessels are ruptured due to trauma or pressure applied from the expanding tumour, no MDEs are required to degrade the vessel wall and thus any cell type can intravasate through a ruptured blood vessel. We verified that the ruptured vessels were indeed the cause of this discrepancy by rerunning the simulations with an initial nodule consisting of epithelial-like cancer cells only on a primary grid that solely contained normal blood vessels.

Furthermore, we showed that our model was able to reproduce the survival probabilities of single CTCs and of CTC clusters observed in experiments by Luzzi et al. (1998); Aceto et al. (2014).

Regarding the role of the MDEs in our model, we found that both less MMP-2 production as well as less MMP-2 diffusion caused faster cancer cell invasion and thus a higher metastatic cancer cell load after 22 days. If the MMP-2 was too diffusive or too abundant, it degraded the ECM very rapidly. The result was a ring-shaped area around the tumour edge, in which the ECM was fully degraded. This caused the influence of haptotaxis on cancer cell movement to diminish or even to cease completely. Hence, a more local or decreased degradation caused the cancer cells to invade the tissue more rapidly.

When we reduced the MMP-2 production rate to zero, we observed that the cancer cells could effectively invade in the presence of MT1-MMP only, which coincides with the experimental results by Sabeh et al. (2009). On the contrary, when we set the MT1-MMP degradation rate to zero and studied the effects of MMP-2 degradation alone, we found that the final total primary cancer cell load was significantly reduced compared to simulations with MT1-MMP present, which showed again the same tendency as the results by Sabeh et al. (2009). However, contrary to the findings in these experiments, invasion was still possible in our model when considering diffusion-dominated cancer cell movement.

To further investigate the reason for this, we reduced the diffusion coefficients of both the mesenchymal-like and the epithelial-like cancer cells, resulting in haptotaxis-dominated rather than diffusion-dominated cancer cell movement. We then studied the invasion of a mixed cancer cell population, consisting of 40% epithelial-like and 60% mesenchymal-like cancer cells, as well as of homogeneous cell populations consisting of mesenchymal-like or epithelial-like cancer cells only, under various MDE-related condi-

tions. These conditions were the presence of both MT1-MMP and MMP-2 as well as settings with solely MT1-MMP or solely MMP-2 present. We chose these MDE-related conditions as they correspond to those in experiments conducted by Sabeh et al. (2009). We first ran simulations with a heterogeneous initial cancer cell population and then, to fully match the experimental conditions of Sabeh et al. (2009), with mesenchymal-like cancer cells alone. In both cases, we found that invasion was not possible in the presence of MMP-2 alone, while invasion was possible when we considered MT1-MMP expression alone. Invasion was also possible with both MDEs present but the invasion depth was slightly decreased compared to when we considered MT1-MMP alone. In the case of a heterogeneous initial cell population, we again observed that the mesenchymal-like cancer cells formed the invading edge of the tumour by occurring most abundantly around the central cluster of epithelial-like cancer cells. Further, the epithelial-like cancer cells formed a pattern of finger-like protrusions. The simulation results observed in the case of a homogeneously mesenchymal-like cancer cell population were in qualitative agreement with the experimental results by Sabeh et al. (2009). For these *in vitro* experiments, HT-1080 cancer cell spheroids were electroporated with a control siRNA, MMP-1 and MMP-2 siRNAs, or MT1 siRNA. These multicellular clusters were then embedded in 3D type I collagen gels as central nodules of diameter 1.5×10^{-2}–2×10^{-2} cm. The invasive patterns of the HT-1080 cells under the various conditions were then studied after 3 days. Our model's results in comparison to those of Sabeh et al. (2009) are shown in Figure 4.13. Finally, we also matched experimental results by Gaggioli et al. (2007) confirming that in the case of an initial population of epithelial-like cancer cells only, invasion is not possible. However, the same epithelial-like population mixed with mesenchymal-like cancer cells could invade.

Chapter 5

A mathematical multi-organ model for bidirectional epithelial-mesenchymal transitions in the metastatic spread of cancer

As explained in Section 2.4, EMT, MET and the associated changes in cancer cell phenotypes play a pivotal role during the invasion-metastatic cascade. Yet, we found that no spatially explicit models that describe the role of EMT and MET in metastatic spread—as opposed to their role in invasion alone—exist, *cf.* Section 3.2. Consequently, none of the existing models capture the site- and location-dependent occurrence of EMT and MET in all of the steps of the invasion-metastasis cascade—i.e. in cancer cell invasion, intravasation, vascular travel, extravasation and during regrowth at new sites in the body—in a spatial manner. Moreover, to our knowledge, the simulations from existing spatiotemporal ECM invasion models that account both for epithelial and mesenchymal cancer cell populations as well as for the transition between these two phenotypic states, such as Domschke et al. (2017), lack the inclusion of intermediate partial-EMT phenotypes, *cf.* Section 3.1. However, it has recently become evident that cancer cells of partial-EMT phenotype are crucial to the EMT process, as explained in Section 2.4.

To close this gap in the literature, in this chapter, we develop an extension to the spatially explicit hybrid modelling framework from Chapter 4. The resulting model describes the invasive growth dynamics of the primary tumour, by—*inter alia*—accounting for EMT, as well as metastatic growth in the early avascular stages at potential secondary metastatic sites, by accounting for MET. Furthermore, we introduce changes to the existing framework that allow us to differentiate between the cell behaviour on the various organs as well as to account for dormancy and death of metastasised cancer cells as a result of the potential immune response at and maladaptation to secondary sites. As in Chapter 4, we continue to model the transport from primary to secondary sites.

Next, we introduce the ideas and assumptions that the EMT/MET-extension of the metastasis framework builds on. Only new, EMT-related features will be established here. The existing underlying metastasis framework in Section 4.1, onto which the alterations described in this chapter are imposed, should be consulted for any non-EMT-specific aspects. This work is also submitted for publication in Franssen and Chaplain (2019).

5.1 Model setup

As in Section 4.1, we use $G+1$ non-overlapping spatial domains to represent the primary tumour site, $\Omega_{\mathsf{P}} \subset \mathbb{R}^2$, as well as the $G \in \mathbb{N}$ spatial domains representing the sites of potential secondary metastatic spread, $\Omega_{\mathsf{S}}^a \subset \mathbb{R}^2$, where $a = 1, 2, ..., G$. As previously, we represent the MMP-2 concentration and the ECM density at position $\mathbf{x}$ at time t in these spatial domains by the continuous functions $m(t, \mathbf{x})$ and $w(t, \mathbf{x})$, respectively, while capturing the spatiotemporal evolution of epithelial, partial-EMT and mesenchymal cancer cells as well as of the membrane-bound MT1-MMP in a discrete approach, *cf.* Anderson and Chaplain (1998); Anderson et al. (2000); Franssen et al. (2019). Also analogously to Section 4.1, we allow cancer cells to travel from primary to secondary sites via the vasculature by designating locations in the primary spatial domain to function as entry points into blood vessels and, similarly, impose a spatial map of exit locations from the vasculature onto the secondary metastatic domains.

The EMT-related features that are novel to the metastatic framework are explained according to which key step of the invasion-metastasis cascade—i.e. cancer cell invasion, intravasation, vascular travel, extravasation and metastatic growth—they belong to. To enhance the clarity of presentation, as in Section 4.1, we begin each paragraph by printing the description of corresponding the step in bold. We also label the respective sections in the flowchart presented in Figure 5.1, which visually describes the model, accordingly.

Local cancer cell invasion As explained in detail in Section 4.1, the evolution of the MMP-2 concentration and of the ECM density are modelled in a continuum approach. To account for the inclusion of partial-EMT cancer cells in our model, we extend equations (4.1.9) and (4.1.10) from the existing model slightly. Accordingly, the spatiotemporal evolution of the MMP-2 concentration $m(t, \mathbf{x})$ is given by

$$\frac{\partial m}{\partial t} = \overbrace{D_m \nabla^2 m}^{\text{diffusion}} + \overbrace{\Theta_{\mathsf{M}} c_{\mathsf{M}_n} + \Theta_{\mathsf{E/M}} c_{\mathsf{E/M}_q}}^{\text{expression}} - \overbrace{\Lambda m}^{\text{decay}}, \tag{5.1.1}$$

along with zero-flux boundary conditions. Here, analogous to the notation in Section 4.1, we let $c_{\mathsf{M}_n} \in \{0, 1, 2, ..., N\} \cap \mathbb{N}_0$, and $c_{\mathsf{E/M}_q} \in \{0, 1, 2, ..., M\} \cap \mathbb{N}_0$, with $c_{\mathsf{M}_n} + c_{\mathsf{E/M}_q} \leq Q$, denote the presence of up to a total of Q mesenchymal-like or partial-EMT cancer cells at a given position $\mathbf{x}$, following the notation by Stéphanou et al. (2006); McDougall et al. (2012). Consequently, $\Theta_{\mathsf{M}} c_{\mathsf{M}_n}$ and $\Theta_{\mathsf{E/M}} c_{\mathsf{E/M}_q}$ represent the local expression of MMP-2 by the c_{M_n} mesenchymal-like and the $c_{\mathsf{E/M}_q}$ partial-EMT cancer cells, respectively. $D_m \geq 0$ is the MMP-2 diffusion coefficient, and $\Theta_{\mathsf{M}} \geq 0$ and $\Theta_{\mathsf{E/M}} \geq 0$ are the rates of MMP-2 concentration provided by mesenchymal-like cancer cells and the partial-EMT cancer cells, respectively. Finally, $\Lambda \geq 0$ is the rate at which MMP-2 decays. Note that the mesenchymal-like and partial-EMT cancer cells also express MT1-MMP. However, MT1-MMP acts only locally where it is bound to the cancer cell membrane and its spatiotemporal evolution is hence congruent to that of the mesenchymal-like and of the partial-EMT cancer cells. Therefore, we do not include a separate equation.

Both the MT1-MMP expressed on the membranes of the mesenchymal-like and the partial-EMT cancer cells and the diffusive MMP-2 they secrete degrade the ECM. In the respective equation (5.1.2), this is expressed through the degradation rates $\Gamma_{\mathsf{M}} > 0$

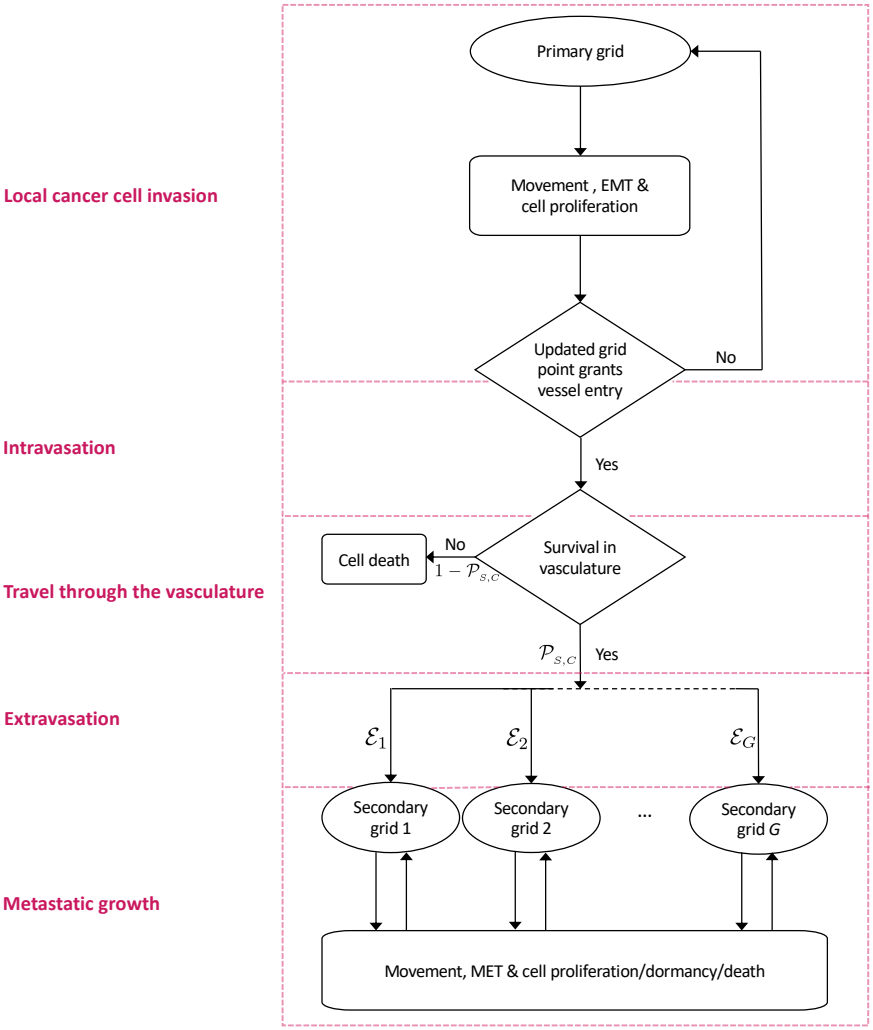

Figure 5.1: ***Flowchart of the extended invasion-metastasis hybrid model.*** *At each time step, each cancer cell on the primary grid may move, may perform EMT with some (location-dependent) probability, and may proliferate. A cancer cell remains on the primary grid during the respective time step, unless it is placed on a grid point that represents a blood vessel. In the latter case, single CTCs and CTC clusters may enter the vasculature. They spend a number of time steps in the circulation and survive with a probability of* $\mathcal{P}_S = \mathcal{P}_{\mathsf{E}}$, $\mathcal{P}_{\mathsf{M}}$ *or* $\mathcal{P}_{\mathsf{E/M}}$ *in the case of single CTCs of epithelial, mesenchymal and partial-EMT phenotype, respectively, and with a probability of* $\mathcal{P}_C$ *in the case of CTC clusters. Cancer cells that do not survive are removed from the simulation. Surviving CTCs and CTC clusters are placed onto one of* G *secondary grids with the respective probability* $\mathcal{E}_1, \mathcal{E}_2, ..., \mathcal{E}_G$*. Cancer cells on the secondary grids move and proliferate like cancer cells on the primary grid (potentially with different parameter values to represent organ- and patient-specific differences in the local tumour microenvironment). However, partial-EMT cells may now revert to cells of an epithelial phenotype via MET and cancer cells may die or remain dormant. The labelled red boxes on the left correspond to the steps of the invasion-metastasis cascade described in Sections 2.3.2–2.3.5 and 2.4.1–2.4.4 as well as to the non-EMT-specific features of the model indicated in bold in Section 4.1.*

and $\Gamma_{\mathsf{E/M}} > 0$ in the case of the MT1-MMP bound to the membranes of partial-EMT and of mesenchymal-like cancer cells, respectively, and for the diffusive MMP-2 by the degradation rate $\Gamma_m > 0$. Hence, given that we are disregarding ECM-remodelling for simplicity, the evolution of the ECM density $w(t, \mathbf{x})$ is governed by the following PDE:

$$\frac{\partial w}{\partial t} = \overbrace{-(\Gamma_{\mathsf{M}} c_{\mathsf{M}_n} + \Gamma_{\mathsf{E/M}} c_{\mathsf{E/M}_q} + \Gamma_m m)w}^{\text{degradation}}, \tag{5.1.2}$$

along with no-flux boundary conditions.

For the cancer cell migration on the grid, we adopt a discrete approach that is further explained in Chapter 4. The movement probabilities of the cancer cells on the grid are given as follows:

$$\begin{aligned}
\mathcal{P}_0 : \mathcal{P}^n_{i-1,j} &:= \max\left(0, \frac{\Delta t}{(\Delta x)^2}\left[D_k - \frac{\Phi_k}{4}\left(w^n_{i+1,j} - w^n_{i-1,j}\right)\right]\right), \\
\mathcal{P}_1 : \mathcal{P}^n_{i+1,j} &:= \max\left(0, \frac{\Delta t}{(\Delta x)^2}\left[D_k + \frac{\Phi_k}{4}\left(w^n_{i+1,j} - w^n_{i-1,j}\right)\right]\right), \\
\mathcal{P}_2 : \mathcal{P}^n_{i,j+1} &:= \max\left(0, \frac{\Delta t}{(\Delta x)^2}\left[D_k + \frac{\Phi_k}{4}\left(w^n_{i,j+1} - w^n_{i,j-1}\right)\right]\right), \\
\mathcal{P}_3 : \mathcal{P}^n_{i,j-1} &:= \max\left(0, \frac{\Delta t}{(\Delta x)^2}\left[D_k - \frac{\Phi_k}{4}\left(w^n_{i,j+1} - w^n_{i,j-1}\right)\right]\right), \qquad (5.1.3) \\
\mathcal{P}_4 : \mathcal{P}^n_{i,j} &:= 1 - \sum_{q=0}^{3} \mathcal{P}_q, \qquad (5.1.4)
\end{aligned}$$

where $k = \mathsf{E}, \mathsf{E/M}, \mathsf{M}$ and—as throughout this chapter—$0 \leq D_{\mathsf{E}} \leq D_{\mathsf{E/M}} \leq D_{\mathsf{M}}$ and $0 = \Phi_{\mathsf{E}} \leq \Phi_{\mathsf{E/M}} \leq \Phi_{\mathsf{M}}$. $\mathcal{P}_0, \mathcal{P}_1, \mathcal{P}_2, \mathcal{P}_3$ and $\mathcal{P}_4$ correspond to the probabilities that, during the next time step, a cancer cell at grid point (x_i, y_j) moves left, right, up, down, and not at all, respectively (Stéphanou et al., 2006; McDougall et al., 2012; Franssen et al., 2019). Rules for proliferation and phenotypic transitions of the cancer cells, as well as—on the secondary grids—for cell death and dormancy, are then included as described below.

The more proliferative cancer cells of epithelial phenotype perform mitosis after time interval T_{E} and the less proliferative partial-EMT and mesenchymal-like cancer cells after time interval $T_{\mathsf{E/M}}$ and T_{M} (with $T_{\mathsf{E}} \leq T_{\mathsf{E/M}} \leq T_{\mathsf{M}}$), respectively. As previously in Section 4.1, when proliferating, the cancer cells pass on their location so that a proliferating cancer cell is replaced by two daughter cells. Generally, during a proliferative step, cells are replaced by cells of their respective phenotype. However, following the biological findings presented in Section 2.4, the extended model allows for location-dependent full and partial EMT on the primary grid. For simplicity, this is implemented upon proliferation. As also explained schematically on the left-hand side of Figure 5.2, the EMT mutations on the primary grid occur as follows:

- Cancer cells of epithelial phenotype may be replaced by a set of daughter cells consisting of one cell of epithelial and one of partial-EMT phenotype with probability $\mathcal{P}^{\mathsf{E/M}}_{\mathsf{EMT}} > \mathcal{P}^{\mathsf{M}}_{\mathsf{EMT}}$ when proliferating;

- If at least one neighbouring grid point of a cancer cell of epithelial phenotype is unoccupied, it may be replaced by a set of daughter cells consisting of one of epithelial and one of partial-EMT phenotype with an additional probability $\mathcal{P}_{\mathsf{EMT}}^{\mathsf{E/M}^*}$;

- Cancer cells of epithelial and of partial-EMT phenotype may be replaced by a set of daughter cells consisting of one cell of epithelial or of partial-EMT phenotype, respectively, and one of mesenchymal phenotype with probability $\mathcal{P}_{\mathsf{EMT}}^{\mathsf{M}} > 0$ when proliferating.

As before, to account for competition for space and resources, the cancer cells on the respective grid point do not proliferate if there are already $\mathcal{Q} \in \mathbb{N}$ cancer cells on a grid point at the time of proliferation. Thus, $\mathcal{Q}$ represents the preferred carrying capacity in our model. If proliferation is not possible due to spatial constraints, the concerned cell may proliferate again after another T_{E}, $T_{\mathsf{E/M}}$ or T_{M} time steps, respectively.

Intravasation As in Section 4.1, to represent the entry points into the blood vessels, a number of $U_{\mathsf{P}} \in \mathbb{N}_0$ normal blood vessels, as well as $V_{\mathsf{P}} \in \mathbb{N}_0$ ruptured blood vessels, are distributed throughout the primary grid. The normal blood vessels take the size of one grid point, while ruptured vessels consist of a group of $A^b \in \mathbb{N}$, where $b = 1, 2, ..., V_{\mathsf{P}}$, adjacent grid points and can thus have different shapes. The entry rules for cancer cells of epithelial and mesenchymal phenotype remain as described in Section 4.1. Moreover, in this extended framework, the cancer cells of partial-EMT phenotype are treated in the same way as those of mesenchymal phenotype—they may intravasate into both normal and ruptured vessels, unlike epithelial-like cancer cells, and are able to carry epithelial-like cancer cells into the vasculature with them.

Travel through the vasculature Cancer cells and cancer cell clusters remain in the vasculature for some time interval of length $T_{V} \in \mathbb{N}$, which biologically represents the average time the cancer cells spend in the blood system. If a cell would have normally been due to proliferate while in the vasculature, the proliferation is suppressed. It may proliferate again after another T_{E}, $T_{\mathsf{E/M}}$ or T_{M} time steps, as appropriate. Any cancer cells that enter a particular vessel at the same time are treated as one cluster and hence as a single entity once they are located in the vasculature. However, each cancer cell that is part of a cancer cell cluster disaggregates from its cluster with some probability $\mathcal{P}_d$ after spending a time interval of $\left\lceil \frac{T_V}{2} \right\rceil$ in the vasculature. After the time interval T_{V}, the single cancer cells and the remaining cancer cell clusters are removed from the simulation unless they are randomly determined to survive. In accordance with the findings in Section 2.4, the survival probability is $\mathcal{P}_{\mathsf{E}} = \mathcal{P}_{\mathsf{M}} > 0$ for single cancer cells of epithelial and mesenchymal phenotype, $\mathcal{P}_{\mathsf{E/M}} > \mathcal{P}_{\mathsf{E}}, \mathcal{P}_{\mathsf{M}}$ for single cancer cells of partial-EMT phenotype, and $\mathcal{P}_{C} > \mathcal{P}_{\mathsf{E/M}}$ for cancer cell clusters.

Metastatic growth On the secondary grids Ω_{S}^a, where $a = 1, 2, ..., G$, the same phenotypes of cancer cells are accounted for as on the primary grid. Also, the same movement probabilities from equations (5.1.4) and (5.1.3) are used to describe their movement. However, we allow for organ-specific adjustment of the cell movement through differentiation of the respective diffusion and haptotactic coefficients, $D_k^{\Omega_{\mathsf{S}}^a}$ and $\Phi_k^{\Omega_{\mathsf{S}}^a}$, $k = \mathsf{E}, \mathsf{E/M}, \mathsf{M}$, $a = 1, 2, ..., G$.

Moreover, at the primary site, we modelled the assumption of well-adaptedness of the cancer cells to their tumour microenvironment of origin by considering proliferation every

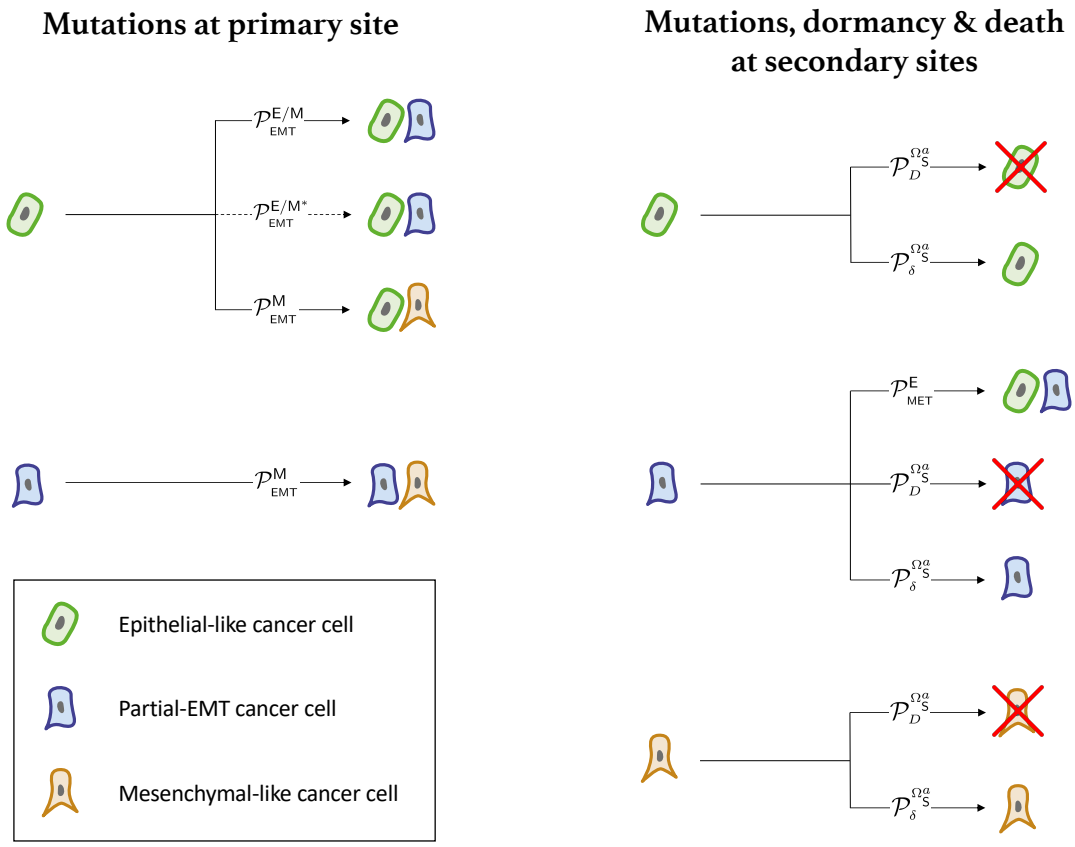

Figure 5.2: ***Schematic representation of possible EMT mutations at the primary site (left) and of MET mutations, cell death and dormancy at the secondary sites (right).*** *Upon proliferation, each of the cells of the three phenotypes on the left of each arrow may undergo one of three fates instead of the usual proliferation: (A) It may be replaced by one cancer cell of the same and one of a different phenotype; (B) it may die (indicated by the red cross); or (C) it may remain dormant. (B) and (C) occur at secondary sites only (shown on the right). The dashed line on the top left indicates that this additional probability* $\mathcal{P}_{\text{EMT}}^{\text{E/M}^*}$ *for cancer cells to mutate only applies to cancer cells at the tumour edge (see text). Note that, for enhanced readability, the illustration omits the representation of non-mutated proliferation, which results in the substitution of one parent cell by two daughter cells of its phenotype. Also, if the carrying capacity is reached on a grid point prior to proliferation, proliferation—and thus mutations—do not occur.*

fixed time interval T_k, $k = \mathsf{E}, \mathsf{E/M}, \mathsf{M}$, if the preferred carrying capacity Q permits. At the secondary sites, the cancer cells may not be as well-adapted to their new tumour microenvironment and may be exposed to the response of the immune system upon arrival. Furthermore, how well the cancer cells are adapted may vary between secondary organ tissues, *cf.* Section 2.4. To account for this, we make several adjustments to the proliferative step on the secondary grids, which are summarised schematically on the right-hand side of Figure 5.2. Firstly, cancer cells may die with some grid-specific probability $\mathcal{P}_D^{\Omega_\mathsf{S}^a}$ immediately prior to each potential proliferation. Secondly, a cell may not proliferate with some grid-specific probability $\mathcal{P}_\delta^{\Omega_\mathsf{S}^a}$ when proliferation is due to account for cancer cell dormancy. Besides this, if cancer cells do proliferate during a time step, we account for MET at the secondary sites in agreement with the biological findings presented in Section 2.4. Hence, cancer cells of partial-EMT phenotype on the secondary grids may be replaced by a set of daughter cells consisting of one cancer cell of epithelial and one of partial-EMT phenotype with probability $\mathcal{P}_{\mathsf{MET}}^{\mathsf{E}} > 0$ when proliferating. EMT does not occur on the secondary grids. However, as before, proliferation is capped as soon as a maximum of Q cancer cells per grid point is reached.

5.2 Implementation and model calibration

To perform numerical simulations, we non-dimensionalised the system of equations (5.1.1), (5.1.2), (4.1.1), (4.1.2) and the respective equation for the partial-EMT cancer cells obtained by e.g. substituting $\mathsf{E/M}$ for E in equation (4.1.1), analogously to our previous model in Section 4.2. As Anderson et al. (2000); Franssen et al. (2019), we chose to rescale distance with an appropriate length scale $L = 0.2\,\text{cm}$ (since 0.1–1 cm is estimated to be the maximum invasion distance of cancer cells at an early stage of cancer invasion) and time with an appropriate scaling parameter $\tau = \frac{L^2}{D}$. Here, $D = 10^{-6}\,\text{cm}^2\text{s}^{-1}$ is a reference chemical diffusion coefficient suggested by Bray (1992), such that $\tau = 4 \times 10^4\,\text{s}$, which corresponds to approximately 11 h.

We considered spatial domains of size $[0, 1] \times [0, 1]$. This corresponds to physical domains of size $[0, 0.2]\text{cm} \times [0, 0.2]\text{cm}$. In particular, we let the spatial domain Ω_P represent the primary site and the spatial domains Ω_S^1, Ω_S^2 and Ω_S^3 describe three potential metastatic sites. These spatial domains could represent *any* primary and secondary carcinoma sites. However, to give an example of a specific application, we chose Ω_P to represent the primary site of the breast, and Ω_S^1, Ω_S^2 and Ω_S^3 to correspond to the bones, lungs and liver, respectively, which are commonly observed metastatic sites in breast cancer.

The four spatial domains were discretised to contain 201×201 grid points each. Using the notation $\mathbf{x} = (x, y) \in \mathbb{R}^2$, as in Chapter 4, this corresponds to a non-dimensionalised space step of $\Delta x = \Delta y = 5 \times 10^{-3}$, which results in a dimensional space step of $1 \times 10^{-3}\,\text{cm}$, and thus roughly corresponds to the diameter of a breast cancer cell (Vajtai, 2013). We then chose a time step of $\Delta t = 1 \times 10^{-3}$, corresponding to 40 s. This condition is motivated by Anderson et al. (2000). It is employed as a means of increasing the accuracy and stability of the numerical scheme while still maintaining appropriate computational efficiency. We ran our simulation for a period corresponding to $\sim$24 days.

On each secondary grid, we chose $U_\mathsf{S}^1 = U_\mathsf{S}^2 = U_\mathsf{S}^3 = 10$ distinct grid points, on which blood vessels are located. For each grid, these blood vessels were placed randomly but at

least two grid step widths away from the respective grid's boundary. The same applies to the primary grid Ω_{P} but with the additional condition that the $U_{\mathsf{P}} = 8$ single grid points, where normal blood vessels are located, and the $V_{\mathsf{P}} = 2$ sets of five grid points, where ruptured blood vessels are placed, are located outside a quasi-circular region containing the 200 centre-most grid points. While these 10 randomly placed vessels are modelled to exist from the beginning, they represent those vessels that grow as a result of tumour-induced angiogenesis in the vascular tumour growth phase—hence they are placed away from the initial avascular epithelial tumour mass.

To represent a two-dimensional cross-section of a small avascular primary tumour, we placed a nodule that consisted of 288 randomly distributed epithelial-like cancer cells in the quasi-circular region of the 97 centre-most grid points of the primary grid. To account for competition for space, we allowed for no more than $\mathcal{Q} = 4$ cancer cells on any grid point. This preferred carrying capacity of $\mathcal{Q} = 4$ was applied throughout the simulation. The described initial condition ensured that the cancer cells were placed away from any pre-existing vessels to match the biology of an avascular tumour in epithelial tissue. The counters for the cell age and proliferation were initially set to zero for all cancer cells. Figure 4.3 provides an example of a typical initial placement of the epithelial-like cancer cells as well as a sample vessel distribution on the primary grid.

In accordance with the ranges provided in Table 5.1, we chose the epithelial-like cancer cell diffusion coefficient to be $D_{\mathsf{E}} = 1 \times 10^{-4}$, the partial-EMT cancer cell diffusion coefficient to be $D_{\mathsf{E/M}} = 2.5 \times 10^{-4}$ and set the mesenchymal-like cancer cell diffusion coefficient to $D_{\mathsf{M}} = 5 \times 10^{-4}$. The epithelial, partial-EMT and mesenchymal haptotactic sensitivity coefficients were $\Phi_{\mathsf{E}} = 5 \times 10^{-5}$, $\Phi_{\mathsf{E/M}} = 1 \times 10^{-3}$ and $\Phi_{\mathsf{M}} = 2 \times 10^{-3}$, respectively. These parameter values were chosen in accordance with Anderson and Chaplain (1998); Deakin and Chaplain (2013) based on biological data on cell movement in Bray (1992) in combination with the biological constraint that EMT enhances cell invasiveness and motility, which we express in terms of diffusion and haptotactic movement in this model.

Moreover, we used the MMP-2 decay rate $\Lambda = 0.1$ that was estimated in Deakin and Chaplain (2013). We chose the MMP-2 production rate of the mesenchymal-like cancer cells to be about twice as large ($\Theta_{\mathsf{M}} = 0.195$), the MMP-2 production rate of partial-EMT cancer cells to be the same as the MMP-2 decay rate ($\Theta_{\mathsf{E/M}} = 0.1$), and for the epithelial-like cancer cells to not produce any MMP-2 ($\Theta_{\mathsf{E}} = 0$). This choice of parameters is motivated by the qualitative biological observation that breast cancer cells which have undergone EMT produce more MMPs (Radisky and Radisky, 2010; Dongre and Weinberg, 2019).

Taking into consideration the qualitative and quantitative biological findings in Sections 2.3 and 2.4, we further assumed that, once in the vasculature, single CTCs of epithelial and mesenchymal phenotypes had a survival probability of $\mathcal{P}_{\mathsf{E}} = \mathcal{P}_{\mathsf{M}} = 2 \times 10^{-4}$, while those of partial-EMT phenotype survived the travel through the vasculature with probability $\mathcal{P}_{\mathsf{E/M}} = 6 \times 10^{-4}$. The survival probability of CTC clusters was set to $\mathcal{P}_C = 2.5 \times 10^{-2} \approx 42 \times \mathcal{P}_{\mathsf{E/M}}$, in accordance with the finding by Aceto et al. (2014) that the survival probability of CTC clusters is between 23 and 50 times higher than that of single CTCs. Surviving single CTCs and CTC clusters exited onto the secondary grids after spending a period of $T_V = 0.18$ in the blood system, which corresponds to 2 h and hence to the breast cancer-specific clinical results in Meng et al. (2004).

Further, we assumed a uniform initial MMP-2 concentration of $m(0, \mathbf{x}) = 0$ across all

the spatial domains. We varied the initial ECM density according to the organ each grid represents using clinical measurements of ECM densities in organs from (ICRP, 2009). These are presented in Table 5.1. For this, we took $w(0, \mathbf{x}) = 1$, $\mathbf{x} \in \Omega_{\mathsf{P}}$, on the primary grid that represents the breast as our reference density. We then rescaled the initial ECM densities on the secondary grids relative to this initial density. For the bones, the lungs and the liver, respectively, this yielded $w(0, \mathbf{x}) \approx 0.9608$, for $\mathbf{x} \in \Omega_{\mathsf{S}}^1$, $w(0, \mathbf{x}) \approx 1.0392$, for $\mathbf{x} \in \Omega_{\mathsf{S}}^2$, and $w(0, \mathbf{x}) \approx 1.0294$, for $\mathbf{x} \in \Omega_{\mathsf{S}}^3$. We assumed that epithelial-like cancer cells divide by mitosis every interval $T_{\mathsf{E}} = 2$, the partial-EMT cancer cells every interval $T_{\mathsf{E/M}} = 3$, and the mesenchymal-like cancer cells every $T_{\mathsf{E}} = 6$. This corresponds to approximately 22 hours, 33 hours and 67 hours, respectively, which is consistent with the average doubling times found in breast cancer cell lines (Milo et al., 2009; NCI, 2015; Hughes et al., 2008). Moreover, we assumed that on the primary site, upon proliferation of a cancer cell of epithelial or partial-EMT phenotype, one of the daughter cells mutates into a mesenchymal-like cancer cell with probability $\mathcal{P}_{\mathsf{EMT}}^{\mathsf{M}} = 1 \times 10^{-2}$. Similarly, one daughter cell of each epithelial-like cancer cell may mutate into a partial-EMT cancer cell with a probability of $\mathcal{P}_{\mathsf{EMT}}^{\mathsf{E/M}} = 2 \times 10^{-2}$ throughout the grid. Moreover, there is an additional probability from partial EMT of $\mathcal{P}_{\mathsf{EMT}}^{\mathsf{E/M}^*} = 0.15$ if the epithelial-like cancer cell is located at the edge of the tumour, *cf.* Puram et al. (2017). While these parameter values could not be inferred directly from the literature at this point as, to our knowledge, no quantitative results are available, they are constrained by the biology presented in Dongre and Weinberg (2019). In particular, they are based on the fact that cancer cells of partial-EMT phenotype—especially at the leading tumour edge (Puram et al., 2017)—are observed more frequently than those of full mesenchymal-like phenotype at the primary site. Instead of representing the adaptation to each grid through these parameter settings, we determined the relative likelihood of metastasis-formation at the three secondary sites by consulting data on the transition probabilities of primary breast cancer to the metastatic sites of the bones, lungs and liver, respectively. As in Franssen et al. (2019), we used data gathered by the Kuhn Laboratory (2017) in a study of 4181 breast cancer patients. As shown in Figure 4 of Franssen et al. (2019), the one-step transition probability from the breast to the bones was 23.1%, to the lungs was 15.3% and to the liver was 11.0%. Since we focus solely on the spread to these three metastatic sites and spread to other organs is included in the terms accounting for vascular death, we obtain the relative likelihoods of spread to the bones, lungs and liver, which are $\mathcal{P}_{\mathsf{S}}^1 \approx 0.5461$, $\mathcal{P}_{\mathsf{S}}^2 \approx 0.2553$, and $\mathcal{P}_{\mathsf{S}}^3 \approx 0.1986$, respectively.

At the secondary sites, cancer cells of partial-EMT phenotype were replaced by a set of daughter cells consisting of one cell of epithelial and one of partial-EMT phenotype with probability $\mathcal{P}_{\mathsf{MET}}^{\mathsf{E}} = 0.5$ during proliferation. Again, this parameter value could not be inferred directly from the literature at this point as, to our knowledge, such quantitative information is not available. However, it is constrained by the biological result presented in Dongre and Weinberg (2019) that metastases tend to resemble the phenotypic make-up of the tumours at the primary site with a high number of epithelial-like cancer cells. Due to a lack of organ-specific data on differences in the tumour microenvironments that could affect the diffusion and haptotactic coefficients of the cancer cells of various phenotypes—as well as their dormancy and death probabilities—at the time of writing, we restricted the differentiation between organs to their local initial ECM density at this stage. Accordingly, we took $D_k^{\Omega_{\mathsf{S}}^a} = D_k$ and $\Phi_k^{\Omega_{\mathsf{S}}^a} = \Phi_k$, where $k = \mathsf{E}, \mathsf{E/M}, \mathsf{M}$ on all

grids in our model. Similarly, the dormancy and death probabilities on all secondary sites were $\mathcal{P}_{\delta}^{\Omega_a^S} = 0.5$ and $\mathcal{P}_{D}^{\Omega_a^S} = 0.05$, $a = 1, 2, 3$. As data from the literature could not be sourced to approximate these values at this point, we chose these probabilities to qualitatively agree with the results by Luzzi et al. (1998). We postpone updating the parameter values until data on dormancy and death of cancer cells at secondary sites in the body become available. An overview of the parameter values mentioned herein can be found in Table 5.1.

In Appendix B, we provide pseudo-code that provides insight into the computational implementation of this mathematical multi-organ model.

Table 5.1: ***Baseline parameter settings used in the simulations.*** *In the first column, non-dimensional parameters are indicated by upper-case notation. Corresponding dimensional parameters are stated in brackets using lower-case notation. In the fourth column, we reference other mathematical modelling papers in brackets and biological papers without brackets. Epithelial-like, partial-EMT and mesenchymal-like cancer cells are represented by the acronyms ECC, PCC and MCC, respectively.*

	Description	Non-dimensional value	Biological reference (Modelling reference)	Original value from cited source
Δt	Time step	1×10^{-3}		40 s
Δx, Δy	Space step	5×10^{-3}	Breast cell diameter in Vajtai (2013)	1×10^{-3} cm
D_{E} (d_{E})	ECC diffusion coefficient	1×10^{-4}	Bray (1992) (Anderson and Chaplain (1998)) (Deakin and Chaplain (2013))	$1 \times 10^{-10}\,\mathrm{cm^2 s^{-1}}$
$D_{\mathsf{E/M}}$ ($d_{\mathsf{E/M}}$)	PCC diffusion coefficient	2.5×10^{-4}	Bray (1992) (Anderson and Chaplain (1998)) (Deakin and Chaplain (2013))	$1 \times 10^{-10}\,\mathrm{cm^2 s^{-1}}$
D_{M} (d_{M})	MCC diffusion coefficient	5×10^{-4}	Bray (1992) (Anderson and Chaplain (1998)) (Deakin and Chaplain (2013))	$1 \times 10^{-10}\,\mathrm{cm^2 s^{-1}}$
Φ_{E} (ϕ_{E})	ECC haptotactic sensitivity coefficient	5×10^{-5}	Stokes et al. (1990) (Anderson and Chaplain (1998))	$2.6 \times 10^{3}\,\mathrm{cm^2 M^{-1} s^{-1}}$
$\Phi_{\mathsf{E/M}}$ ($\phi_{\mathsf{E/M}}$)	PCC haptotactic sensitivity coefficient	1×10^{-3}	Stokes et al. (1990) (Anderson and Chaplain (1998))	$2.6 \times 10^{3}\,\mathrm{cm^2 M^{-1} s^{-1}}$
Φ_{M} (ϕ_{M})	MCC haptotactic sensitivity coefficient	2×10^{-3}	Stokes et al. (1990) (Anderson and Chaplain (1998))	$2.6 \times 10^{3}\,\mathrm{cm^2 M^{-1} s^{-1}}$
D_{m} (d_{m})	MMP-2 diffusion coefficient	1×10^{-3}	Collier et al. (2011)	$1 \times 10^{-9}\,\mathrm{cm^2 s^{-1}}$
Θ_{E} (θ_{E})	MMP-2 production rate by ECCs	0	Biological constraints in Radisky and Radisky (2010)	
$\Theta_{\mathsf{E/M}}$ ($\theta_{\mathsf{E/M}}$)	MMP-2 production rate by PCCs	0.1	Biological constraints in Radisky and Radisky (2010)	
Θ_{M} (θ_{M})	MMP-2 production rate by MCCs	0.195	Biological constraints in Radisky and Radisky (2010)	
Λ (λ)	MMP-2 decay rate	0.1	Based on (Deakin and Chaplain, 2013)	$2.5 \times 10^{-6}\,\mathrm{s^{-1}}$

Γ_1 (γ_1)	ECM degradation rate by MT1-MMP	1	Based on (Deakin and Chaplain, 2013)	$1 \times 10^{-4}\,\mathrm{s}^{-1}$
Γ_2 (γ_2)	ECM degradation rate by MMP-2	1	Based on (Anderson et al., 2000)	$1 \times 10^{-4}\,\mathrm{M}^{-1}\mathrm{s}^{-1}$
T_V	Time CTCs spend in the vasculature	0.18	Meng et al. (2004)	$7.2 \times 10^3\,\mathrm{s}$
T_{E}	ECC doubling time	2	Milo et al. (2009); NCI (2015)	$8 \times 10^4\,\mathrm{s}$
$T_{\mathsf{E/M}}$	PCC doubling time	3	Milo et al. (2009); NCI (2015)	$1.2 \times 10^5\,\mathrm{s}$
T_{M}	MCC doubling time	6	Milo et al. (2009); NCI (2015) Hughes et al. (2008)	$2.4 \times 10^5\,\mathrm{s}$
$\mathcal{P}_\delta^{\Omega_{\mathsf{S}}^{1,2,3}}$	Probability no cell proliferation when due on $\Omega_{\mathsf{S}}^{1,2,3}$	0.5	Qualitative biological constraints (see text)	
$\mathcal{P}_D^{\Omega_{\mathsf{S}}^{1,2,3}}$	Probability cell death before proliferation on $\Omega_{\mathsf{S}}^{1,2,3}$	0.05	Qualitative biological constraints (see text)	
$\mathcal{P}_{\mathsf{E}} = \mathcal{P}_{\mathsf{M}}$	Epithelial/mesenchymal CTC survival probability	2×10^{-4}	Luzzi et al. (1998)	
$\mathcal{P}_{\mathsf{E/M}}$	Partial-EMT CTC survival probability	6×10^{-4}	Luzzi et al. (1998)	
$\mathcal{P}_C$	CTC cluster survival probability	2.5×10^{-2}	Luzzi et al. (1998) Aceto et al. (2014)	
$\mathcal{P}_{\mathsf{S}}^1$	Probability for surviving cells to extravasate to bones	$\sim$0.5461	Kuhn Laboratory (2017)	$\sim$0.5461
$\mathcal{P}_{\mathsf{S}}^2$	Probability for surviving cells to extravasate to lungs	$\sim$0.2553	Kuhn Laboratory (2017)	$\sim$0.2553
$\mathcal{P}_{\mathsf{S}}^3$	Probability for surviving cells to extravasate to liver	$\sim$0.1986	Kuhn Laboratory (2017)	$\sim$0.1986
$\mathcal{P}_{\mathsf{EMT}}^{\mathsf{M}}$	Probability for full EMT on Ω_P	1×10^{-2}	Biological constraints in Dongre and Weinberg (2019)	
$\mathcal{P}_{\mathsf{EMT}}^{\mathsf{E/M}}$	Probability for partial EMT on Ω_P	2×10^{-2}	Biological constraints in Dongre and Weinberg (2019)	
$\mathcal{P}_{\mathsf{EMT}}^{\mathsf{E/M}^*}$	Additional probability for partial EMT on Ω_P at tumour edge	0.15	Qualitative information in Puram et al. (2017)	
$\mathcal{P}_{\mathsf{MET}}^{\mathsf{E}}$	Probability for partial MET on $\Omega_{\mathsf{S}}^{1,2,3}$	0.5	Biological constraints in Dongre and Weinberg (2019)	
$w(0,\mathbf{x})$, $\mathbf{x} \in \Omega_{\mathsf{P}}$	Breast initial ECM density	1	ICRP (2009)	$1.020\,\mathrm{g\ cm}^{-3}$
$w(0,\mathbf{x})$, $\mathbf{x} \in \Omega_{\mathsf{S}}^1$	Bone initial ECM density	0.9608	ICRP (2009)	$0.980\,\mathrm{g\ cm}^{-3}$
$w(0,\mathbf{x})$, $\mathbf{x} \in \Omega_{\mathsf{S}}^2$	Lung initial ECM density	1.0392	ICRP (2009)	$1.060\,\mathrm{g\ cm}^{-3}$
$w(0,\mathbf{x})$, $\mathbf{x} \in \Omega_{\mathsf{S}}^3$	Liver initial ECM density	1.0294	ICRP (2009)	$1.050\,\mathrm{g\ cm}^{-3}$

5.3 Results

To verify that our modelling framework can capture the key steps of the invasion-metastasis cascade, we ran simulations with the parameters shown in Table 5.1. The computational time to run a simulation on a standard desktop computer was about 45 minutes. We provide sample results showing the primary and the three secondary grids at various times in the range of 0 to 24 days during one sample simulation in Figure 5.3 and Figures 5.4–5.6, respectively. We chose results on the primary grid to show the spatiotemporal dynamics on day 0, 11 and 22 so that they can be contrasted to those in Section 4.3. For the secondary sites, we chose to present sample results for times that best give evidence of the various mechanisms related to metastatic spread, MET and the consequences of the immune response at secondary sites that are described through this modelling framework. However, this does not imply that these phenomena are limited to the times and locations depicted in Figures 5.3–5.6 in that particular or in other simulations. The results discussed in this section refer to this single simulation unless it is explicitly stated that they refer to the 20 simulations shown in Figure 5.9. These were run with the same conditions—including the vessel locations on all grids—as the sample simulation apart from that the 288 initial epithelial-like cancer cells were newly distributed randomly in the central 97 grid points each time. Also, different seeds for the random number generator were used for each simulation, which affects various processes such as the movement and mutations of the cancer cells.

As described in Section 5.2, we started the simulations with a small nodule of epithelial-like cancer cells of diameter $\sim 1.5 \times 10^{-2}$ cm (see also Figure 4.3). These were located on the primary grid representing the breast, which had an ECM of uniform density and contained no partial-EMT cancer cells, no mesenchymal-like cancer cells and no MMP-2, as shown in the left-most column of Figure 5.3. As the middle column of Figure 5.3 shows, after 11 days, the epithelial-like cancer cells had invaded the local tissue, covering a nearly circular area of approximately 0.1 cm diameter. Moreover, some partial-EMT and mesenchymal-like cancer cells could be observed on the primary grid. Their occurrence arose from cancer cells of previously epithelial-like phenotype via (partial) EMT. Both of these cell types occurred sparsely within a quasi-circular region with an approximate diameter of 0.18 cm. Additionally, the partial-EMT cancer cells populated a ring-shaped area at the edge of the tumour more densely. The MMP-2 concentration broadly followed the distribution of the partial-EMT cells and ranged from 0 to 0.38. Moreover, the ECM had been degraded in the centre of the grid and a density gradient could be observed at the edge of this near-circular region. After 22 days, the area occupied by the epithelial-like cancer cells in the centre of the tumour had expanded further. Also, the ring-like area populated with partial-EMT cancer cells at the tumour edge had grown and become more densely populated. The mesenchymal-like cancer cells were now sparsely spread throughout the whole grid. In general, we observed that areas on the grid near vessels were sparsely occupied, if at all. The distribution of the MMP-2 concentration still broadly followed the evolution of the partial-EMT cancer cells, now ranging from 0.76 to 2.66. The ECM on the domain that we considered had now been fully degraded.

In addition to the cancer cell invasion on the primary grid, we also observed metastatic spread to the grids representing the secondary sites. For the model in Chapter 4, we

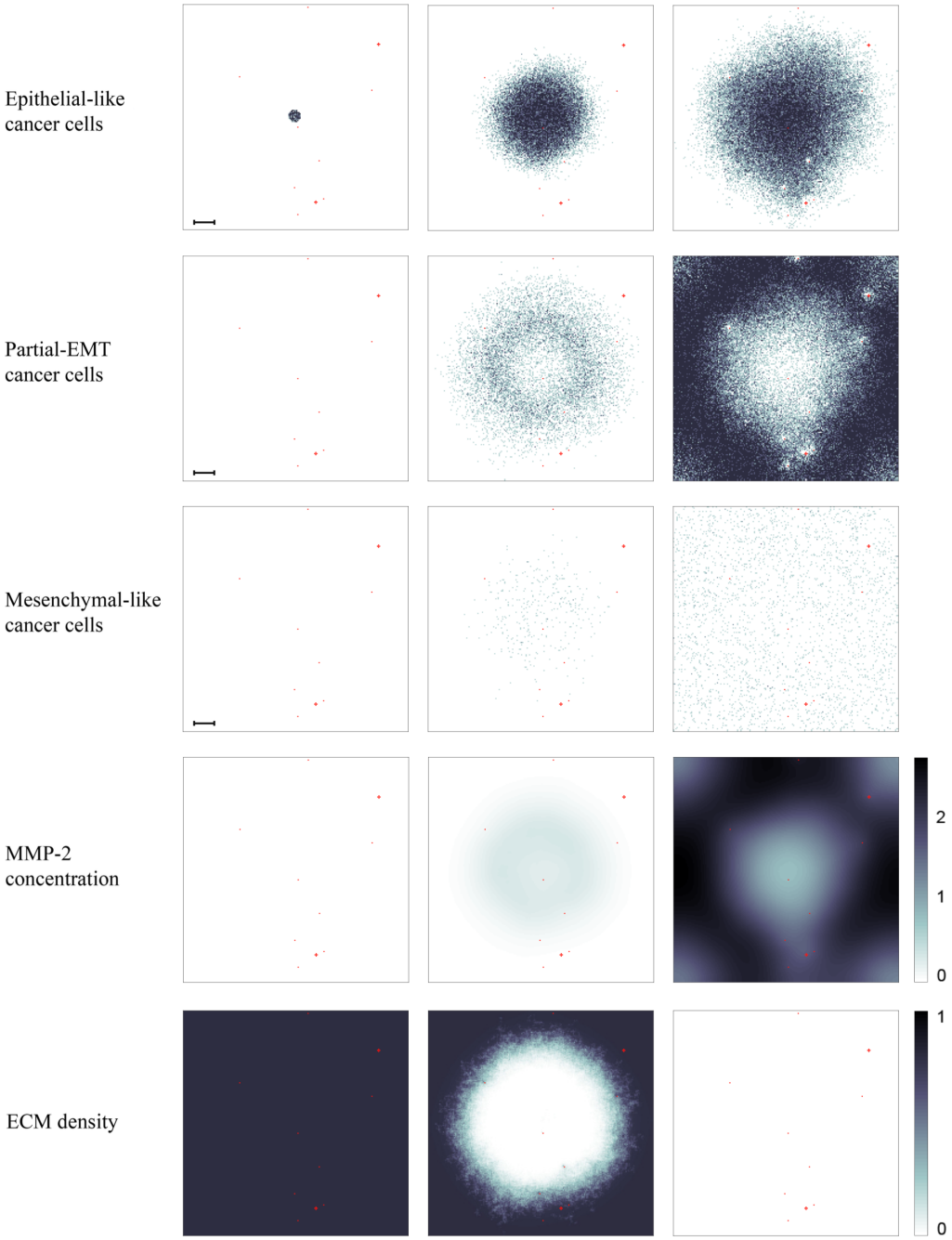

Figure 5.3: ***Simulation results on the primary grid.*** *Primary tumour dynamics after 0,* $\sim$11*, and* $\sim$22 *days. For each time step, the distribution of epithelial-like, partial-EMT and mesenchymal-like cancer cells (first to third row) is shown, with the discrete number of cancer cells per grid point ranging from* 0 *(white) to* 4 *(black) on each of the panels. The MMP-2 concentration (fourth row) continuously varies between* 0 *(white) and* 2.6602 *(black), and the ECM density (bottom row) between* 0 *and* 1*. Red dots represent blood vessels. There are* 8 *normal blood vessels of the size of one grid point as well as* 2 *ruptured blood vessels, which extend over* 5 *grid points each. If cancer cells are moved to these grid points, they may enter the vasculature and may extravasate at a secondary site, cf. Figures 5.4–5.6. The scale bar denotes* 0.02 cm *and applies to all of the panels.*

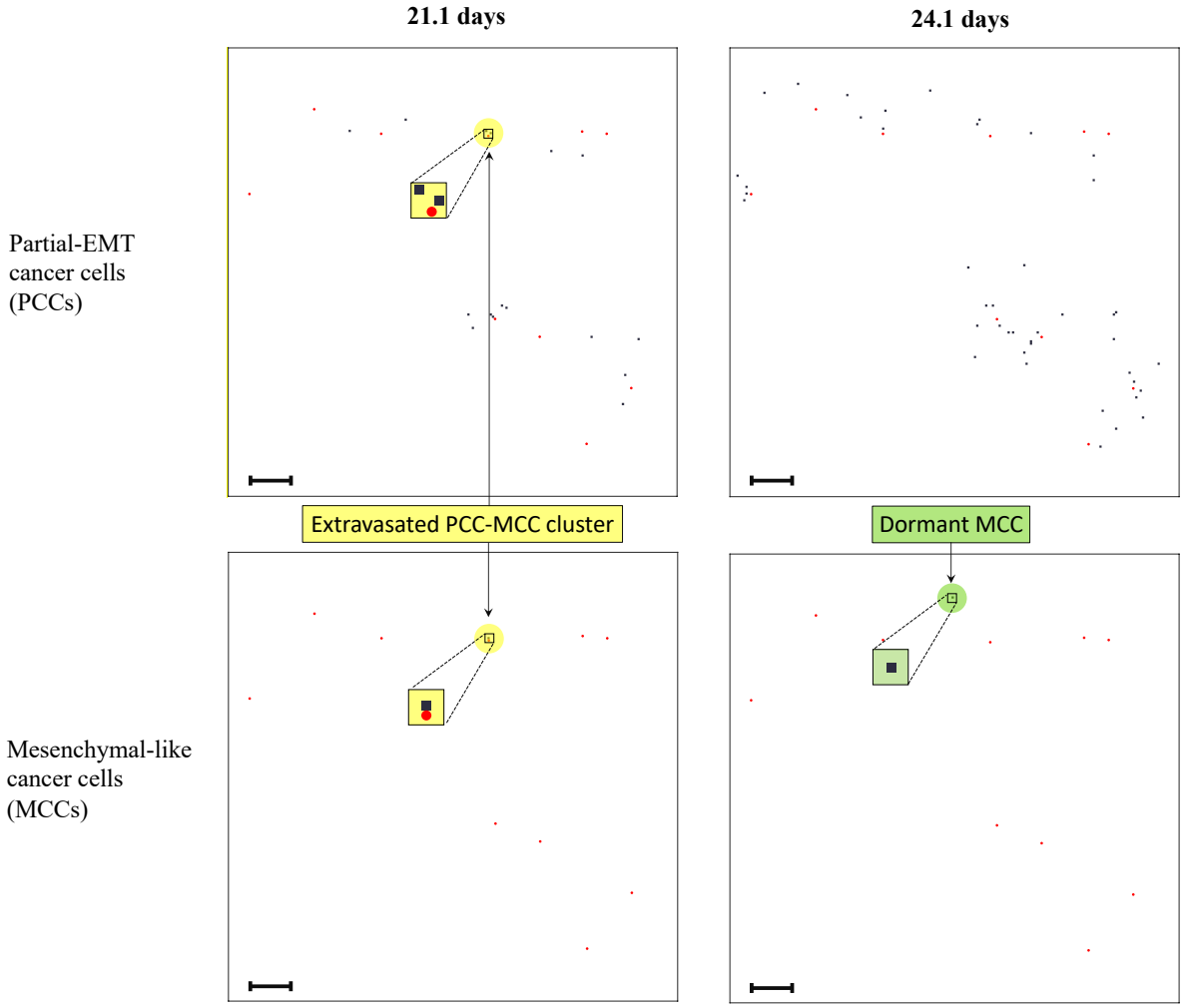

Figure 5.4: ***Cluster extravasation and dormancy on secondary grid representing the bones.*** *Distribution of partial-EMT cancer cells (upper panels) and mesenchymal-like cancer cells (lower panels) at the secondary site representing the bones is shown after* $\sim$21 *days (left) and* $\sim$24 *days (right). The number of cancer cells per grid point varies between* 0 *(white) and* 1 *(black). Around day 21, a cluster consisting of two partial-EMT and one mesenchymal-like cancer cell extravasates onto the grid of the bones (yellow). Moreover, over the 3 day period between the panels on the left and on the right, the mesenchymal-like cancer cell, which normally has a doubling-time of* $\sim$2.78 *days, remains dormant (green). The scale bar denotes* 0.02 cm.

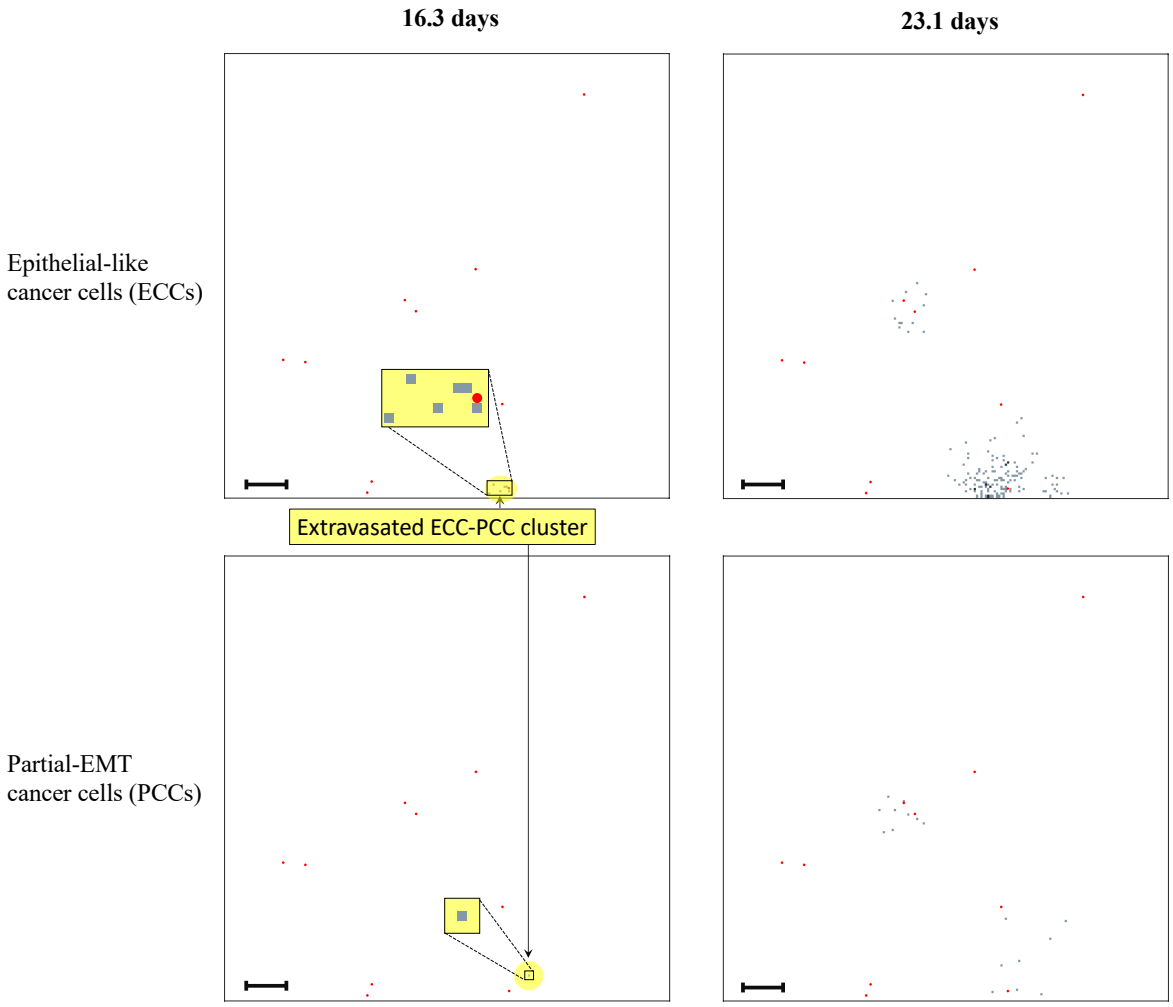

Figure 5.5: ***Cluster extravasation and largest metastatic lesion on secondary grid representing the lungs.*** *Distribution of epithelial-like cancer cells (upper panels) and partial-EMT cancer cells (lower panels) at the secondary site representing the lungs is shown after* $\sim$16 *days (left) and* $\sim$23 *days (right). The number of cancer cells per grid point varies between* 0 *(white) and* 2 *(black). Around day 16, a cluster consisting of six epithelial-like and one partial-EMT cancer cell extravasates onto the grid of the lungs (yellow). This early extravasation of a relatively large cluster of epithelial-like cancer cells results in the largest metastatic growth which can be observed in the right half of the panels on the right. The scale bar denotes* 0.02 cm.

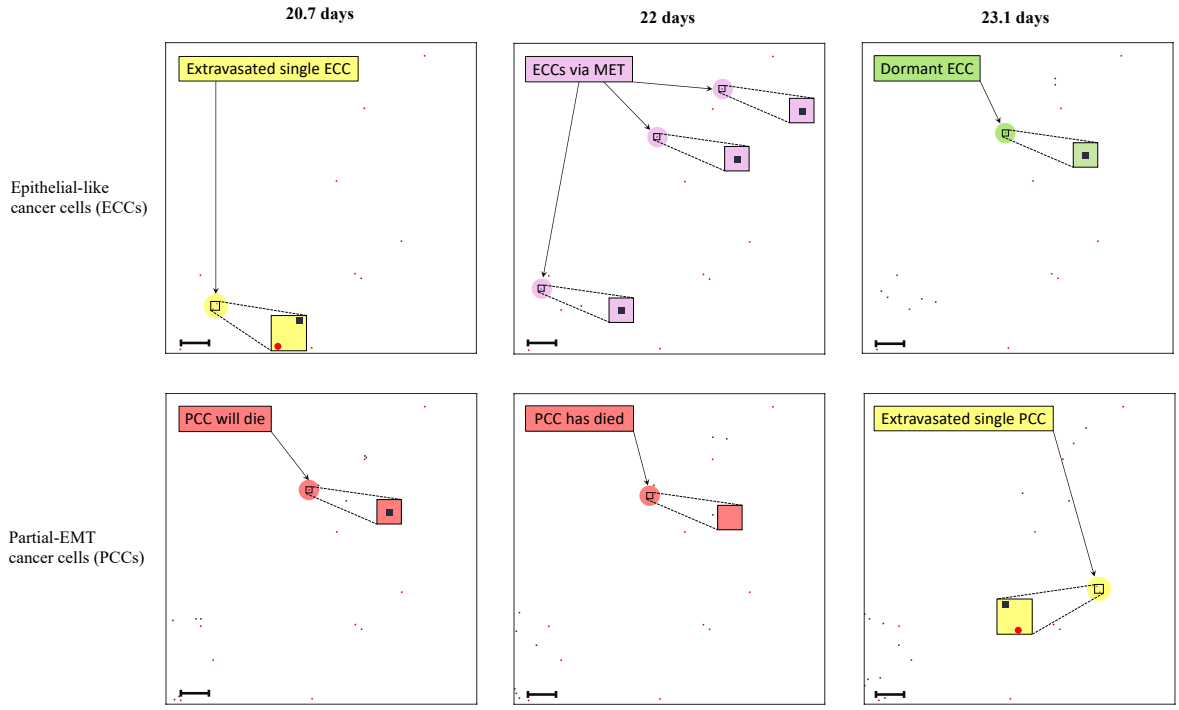

Figure 5.6: ***Single cell extravasations, MET, dormancy and cell death on secondary grid representing the liver.*** *Distribution of epithelial-like cancer cells (upper panels) and partial-EMT cancer cells (lower panels) at the secondary site representing the liver is shown after* $\sim$*21 days,* $\sim$*22 days and* $\sim$*23 days (left to right). The number of cancer cells per grid point varies between* 0 *(white) and* 1 *(black). On day 20 and 23, a single epithelial-like and a single partial-EMT cancer cell extravasate onto the grid of the liver (yellow). No extravasations took place during the presented period. Hence, the three epithelial-like cancer cells that occurred in the period between 20.7 and 22 days in the upper middle panel (pink) are a result of MET of the partial-EMT cancer cells presented in the bottom row of panels. Over the same period, a partial-EMT cancer cell dies (red). Moreover, over the 1.1 days between the panels in the middle and on the right, an epithelial-like cancer cell, which normally has a doubling-time of* $\sim$*0.93 days, remains dormant (green). The scale bar denotes* 0.02 cm.

showed all of the secondary grids at the same time instances as the primary grid, so after approximately 11 and 22 days, *cf.* Section 4.3. Moreover, we included the spatiotemporal dynamics of the ECM density and of the MMP-2 concentration for each of the grids at these times. For these results, we hence refer to this previous work. In this chapter, we focus on the presentation of the additional phenomena captured through this extension of the model instead. As the newly introduced features are connected to the cells of various phenotypes that are included in the model, at the secondary sites we only show their evolution, while omitting the presentation of the MMP-2 and ECM dynamics. To give examples of how the various mechanisms that this model describes are instantiated in the simulations, we show the grids of the bones (Figure 5.4), the lungs (Figure 5.5) and the liver (Figure 5.6) at various times ranging from 16.3 to 24.1 days. The particular times differ between the secondary grids as they were chosen to best present how the

phenomena occur in the simulations. Yet, within each grid, the time instances shown are such that the cell phenotypes depicted in the corresponding panels are at least the length of a cell doubling interval apart to allow all cells in the respective grid to have proliferated, if applicable, at least once.

We proceed by describing the results at the secondary sites grouped by the mechanisms that we aim to highlight (Figures 5.4–5.6) rather than grid-by-grid, as these mechanisms typically occur on all secondary grids. Furthermore, we present the corresponding dynamics of the cell-phenotype evolution of the population sizes on the secondary grids in Figures 5.7 and 5.8. Finally, we ran another 20 simulations, *cf.* Figure 5.9, to examine whether the results in Figures 5.7 and 5.8 from the single sample simulation is generally representative.

Extravasations

We observed extravasations of single cancer cells of various phenotypes, as well as of homogeneous and heterogeneous cancer cell clusters. Examples of a selection of these extravasations are highlighted in yellow on the grids representing the various secondary organs. Figure 5.6 shows samples of recently extravasated single cancer cells of epithelial and of partial-EMT phenotypes on the grid representing the liver. Figures 5.4 and 5.5 show examples of extravasated cancer cell clusters consisting of mixed phenotypes. These consist of two partial-EMT and one mesenchymal-like cancer cell on the grid that represents the bones, and of six epithelial-like and one partial-EMT cancer cell in the case of the grid representing the lungs.

During the 22 day period over which the simulation on the primary grid is presented in Figure 5.3, we observed 6 extravasations of single cells, as well as 11 of clusters consisting of two cells, 6 of clusters consisting of three cells and 1 extravasation each of clusters consisting of six and of seven cells. Another general observation was that during the simulated 24 day period, only one mesenchymal-like cancer cell successfully extravasated onto a secondary grid. All other extravasations were performed by single cancer cells as well as by homo- and heterogeneous cancer cell clusters, which were mainly of partial-EMT phenotype but also of epithelial-like phenotype. The highest number of extravasations of either a cancer cell or a cancer cell cluster was observed onto the grid of the bones.

In the 20 simulations that we ran to examine the mean numbers of cancer cells of the various phenotypes on secondary grids, *cf.* Figure 5.9, we observed the earliest extravasations to secondary grids by mesenchymal-like cancer cells after 9.3 days, by partial-EMT cancer cells after 2 days and by epithelial-like cancer cells after 1.4 days. In other simulations, there were no extravasations by epithelial-like or mesenchymal-like cancer cells during the 24.1 days we ran the simulations for.

MET

On the grid representing the liver, no extravasations took place during the period between 20.7 and 23.1 days, i.e. during the period shown in Figure 5.6. Hence, the three epithelial-like cancer cells that occurred during the period between 20.7 and 22 days, which are highlighted in pink in the upper row of panels, are a result of MET of the partial-EMT cancer cells presented in the bottom row of panels. If MET occurred during a

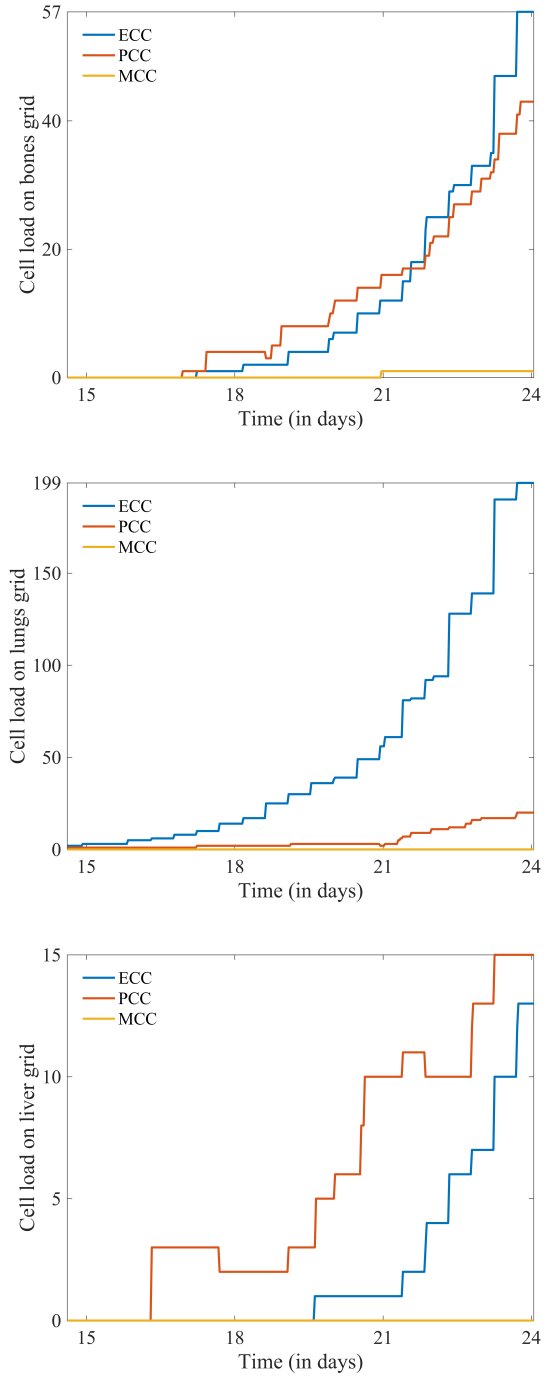

Figure 5.7: ***Phenotype-specific cell load over time on secondary grids.*** *Plots of total number of epithelial-like (ECC; blue), partial-EMT (PCC; red) and mesenchymal-like (MCC; yellow) cancer cells on the grids of the bones, lungs and liver (top to bottom) in the period between 14.6 and 24.1 days. On each grid, the initial growth arises from extravasating cells. The stepwise, mostly non-negative growth pattern thereafter largely occurs from proliferation of cells as well as further extravasations. For ECCs, part of the growth also results from PCCs that undergo MET. As MET during PCC proliferation results in one PCC and one ECC, MET typically causes the PCC growth to slow down. Negative growth, as e.g. observed in the PCC population on the top 'bones' grid after day 18, is always a result of cell death. Throughout, MCCs remain rare on secondary grids.*

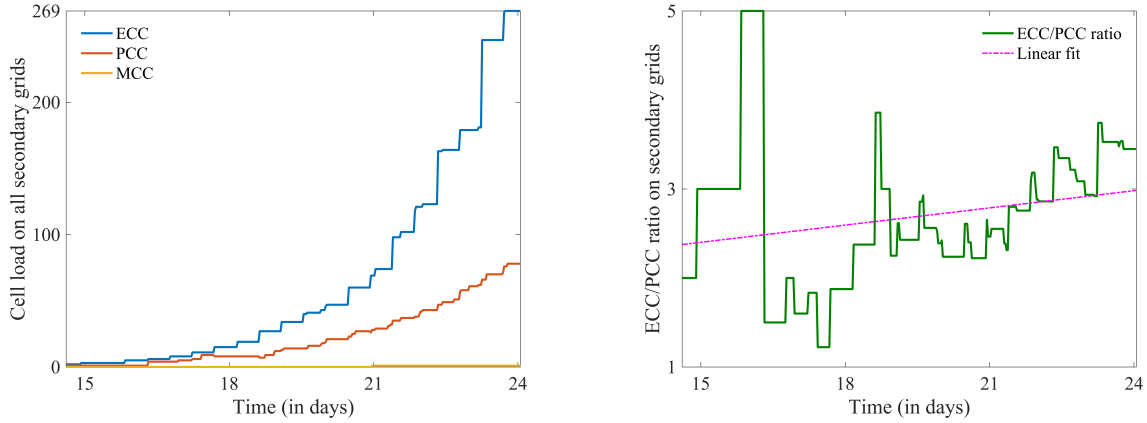

Figure 5.8: ***Trends in phenotype-specific cell load on secondary grids overall.*** *Left: Combined total cell load on the secondary grids of cancer cells of epithelial-like (ECC; blue), partial-EMT (PCC; red) and mesenchymal-like (MCC; yellow) phenotype between the period of 14.6 and 24.1 days. The number of ECCs grows most rapidly over time—their growth is caused by extravasations, MET and proliferation. PCCs grow steadily but less rapidly. Their growth is slower due to their larger proliferation interval but also due to a subset of PCCs undergoing MET during proliferation. Only 1 MCC is observed during the time period. Right: Plot of the ratio of ECCs to PCCs over the same time frame (green). Throughout, there are more ECCs than PCCs and the ratio increases with time for the reasons explained above. The best linear fit line (pink) highlights this trend.*

proliferative step, the respective partial-EMT cancer cell was replaced by one cancer cell of its phenotype as well as one of epithelial-like phenotype. Overall, the phenomenon of MET caused the growth rate of epithelial-like cancer cells to increase while slowing the growth rate of partial-EMT cancer cells at secondary sites. This trend is captured in the plots in Figure 5.8.

While any partial-EMT cancer cell can potentially undergo MET, the mesenchymal-like cancer cells cannot change phenotype. The sole mesenchymal-like cancer cell in Figure 5.4 is an example of such a phenotypically stable cell.

Metastatic growth

The by far largest micrometastatic lesion during the simulation period presented itself on the grid of the lungs, shown in Figure 5.5. It resulted from a cluster consisting of six epithelial-like cancer cells and one partial-EMT cancer cell that extravasated relatively early—after approximately 16 days. All other lesions remained comparatively small during the same 23 day period, consisting of less than 20 cancer cells of almost exclusively epithelial-like and partial-EMT phenotypes. This is also reflected in the evolution of the total cell number on the three grids represented through the plots in Figure 5.7. As time progressed, a tendency towards a higher percentage of epithelial-like cancer cells at secondary sites was observed, as Figure 5.8 suggests.

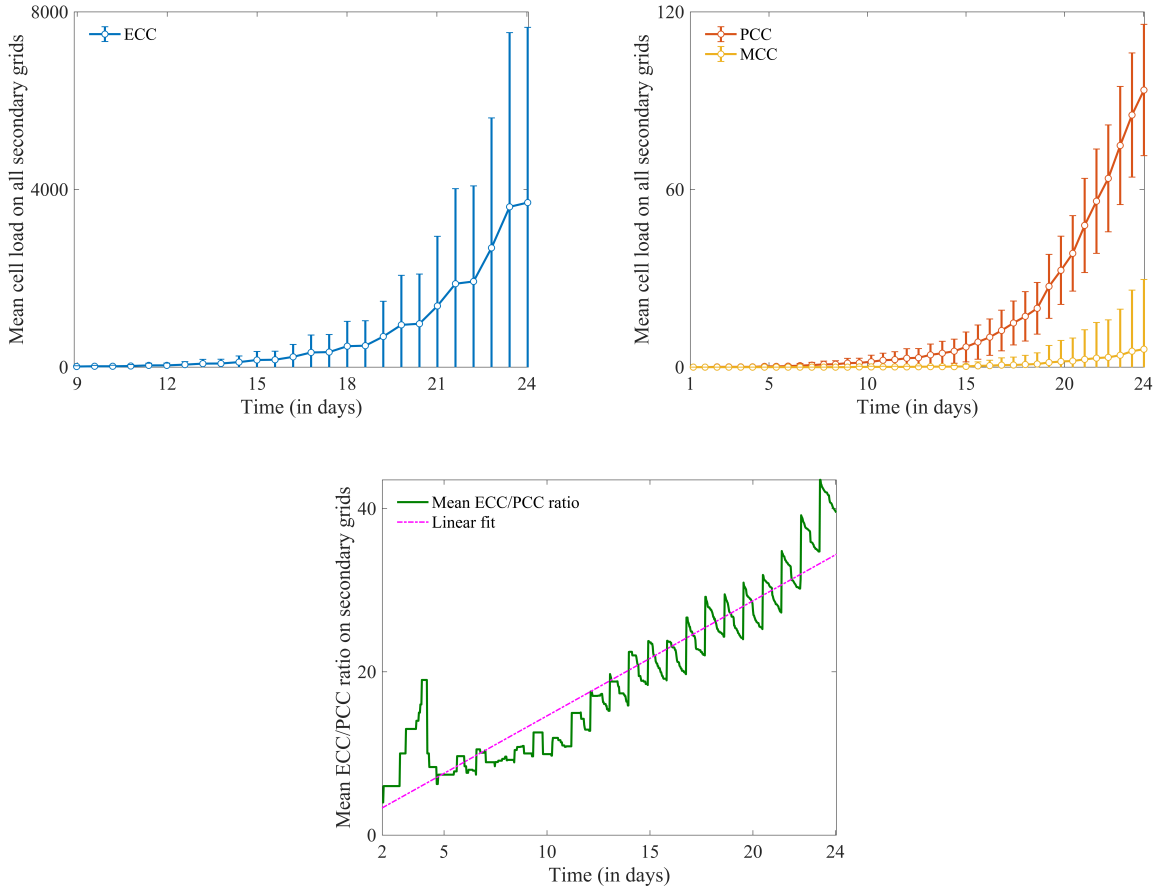

Figure 5.9: ***Trends in phenotype-specific cell load on secondary grids overall—showing the mean (line) and standard derivation (whiskers) from 20 simulations.*** *All 20 simulations were run with the same conditions as the sample simulation in Figure 5.8 apart from that the 288 initial epithelial-like cancer cells were newly distributed randomly in the central 97 grid points and that different seeds for the random number generator were used for each simulation. Top left: Mean combined total load of cancer cells of epithelial-like (ECC; blue) phenotype on the secondary grids between the period of 9 and 24.1 days. The number of ECCs grows most rapidly over time—their growth is caused by extravasations, MET and proliferation. Top right: Mean combined total load of cancer cells of partial-EMT (PCC; red) and mesenchymal-like (MCC; yellow) phenotype on the secondary grids between the period of 1 and 24.1 days. Generally, PCCs grow steadily but less rapidly than ECCs. Their growth is slower due to their longer proliferation interval but also because a subset of PCCs undergoes MET during proliferation. MCCs also tend to grow in number over time, yet very slowly. This is due to their long doubling time. Bottom: Plot of the mean ratio of ECCs to PCCs between the period of 2 and 24.1 days (green). Throughout, there are on average more ECCs than PCCs and the mean ratio increases with time. The best linear fit line (pink) highlights this trend.*

In the 20 simulations that we ran to examine the mean numbers of cells of the various phenotypes on secondary grids, *cf.* Figure 5.9, we observed a comparatively large standard deviation with respect to the mean number of epithelial-like cancer cells on the secondary grids. This is likely caused by the large variation in the time of the first extravasation by epithelial-like cancer cells: This occurred after as little as 1.4 days during one of the 20 simulations, while no epithelial-like cancer cells at all extravasated during another. Due to the exponential growth observed in the early stages of secondary spread when space is not yet a significantly limiting factor, large metastases can form if the extravasation occurred early on. The same applies to a lesser extent to the other two cell phenotypes. The standard deviation of the number of cells on the secondary grids over time is lower for these cell types as these cell types need to come into existence on the primary grid before they are able to spread. Also, they are less proliferative and, in the case of partial-EMT cancer cells, subject to MET on the secondary grids.

Dormancy

Given that we have chosen the periods between the time instances presented through the panels in Figures 5.4 to 5.6 to be such that there exists at least one opportunity for each cancer cell to reproduce, these figures show examples of dormant cancer cells at the secondary site of the bones and the liver, respectively. Due to their dormancy, the respective mesenchymal-like and epithelial-like cancer cells do not proliferate while other cells on the grids may. The two examples of dormant cells discussed in this section are highlighted in green in the respective figures.

Death due to maladaptation & immune response

Figure 5.6 shows an example of a partial-EMT cancer cell that dies in the period between 20.7 and 22 days. Other examples of cell death on secondary sites become evident when examining the cell population growth plots for the partial-EMT cells on each of the secondary sites shown in Figure 5.7. Negative growth, as e.g. observed in the partial-EMT population on the top 'bones' grid after day 18, on the middle 'lungs' grid at day 21, and on the bottom 'liver' grid after day 17 and 22, is always a result of cell death. The fact that we only observe cell death in the partial-EMT population through these plots does not imply that cell death does cannot occur in the cell populations of other phenotypes. The epithelial-like cancer cells in the model tend to proliferate mostly synchronously. Hence, rare potential cell deaths are likely to be overshadowed in the plots in Figure 5.7 by an even larger positive cell growth at the same time instance. The same applies to potential other partial-EMT cell deaths.

5.4 Discussion

In this chapter, we have extended the mathematical framework for the metastatic spread of cancer introduced in Chapter 4 to include EMT and MET. As a result, the framework now additionally accounts for transitions of cancer cells between an epithelial, a newly introduced partial-EMT and a mesenchymal phenotypic state. This is achieved in a location-dependent fashion—both with respect to the steps of the invasion-metastasis

cascade and with respect to the intra-tumoural location of the cancer cells. This way, the modelling framework captures the phenomena of EMT and MET in their physiological context. Furthermore, we include organ-specific differences in the local tissue of the secondary sites involved in our model by accounting for their ECM density following biological findings in (ICRP, 2009). Finally, the extended framework now also takes into account cancer cell dormancy and death as a result of maladaptation to the new tumour microenvironments at the secondary sites as well as due to the local immune response.

Through computational simulations, we found that the extended metastasis modelling framework provides biologically realistic outcomes and gives further insight into the above-described mechanisms that underpin the invasion-metastasis cascade at the cellular scale. Tumour shape and metastatic distribution at the primary site were predicted to appear as one would expect in a cancer patient who has not yet received treatment. In particular, we found that the partial-EMT cancer cells formed a ring-shaped leading front along the tumour edge, which was also seen in experiments (Nurmenniemi et al., 2009) as well as in human tissue, as shown in Figure 2.16 from Puram et al. (2017).

Nurmenniemi et al. (2009) further observed an average maximum invasion depth—measured as the distance from the centre of the grid to the cell furthest away from the centre—of 5.47×10^{-2} cm over 14 days when culturing HSC-3 cancer cells, a human oral squamous carcinoma cell line with high metastatic potential, on top of myoma tissue. This translates into an estimated average invasion speed of approximately 4.52×10^{-8} cm s^{-1}. It suggests that our observed maximum invasion depth of $\sim 9 \times 10^{-2}$ cm in 11 days by partial-EMT and mesenchymal-like cancer cells, which remained roughly the same during the 20 simulations that we ran, and the resulting estimated average for the invasion speed of approximately 9.38×10^{-8} cm s^{-1} are realistic results, given that migration speed varies between cancer cell lines and that the displacement of the cancer cells is likely a result of a combination of migration and proliferation.

The number of extravasations of single cancer cells or of a cancer cell cluster per secondary site further matched the clinical data of 4181 breast cancer patients, which underlie our simulations. The bones are the most frequently observed site of metastatic spread from primary breast cancer in the data processed by the Kuhn Laboratory (2017)—correspondingly, we observed the highest number of extravasations to the grid representing this site.

To our knowledge, there are currently no data available that claim to deliver an accurate estimation of the typical metastatic load from primary breast cancer to secondary sites over a specified time frame. However, we believe our results are biologically appropriate with regards to their timings. They are in correspondence with the conclusion reached by Obenauf and Massagué (2015) in their review of the metastatic traits that allow cancer cells to colonise various secondary sites, suggesting that CTCs and metastatic spread can be detected soon after vascularisation of the primary tumour, as in our simulations.

The types of extravasations that we observed through the simulations in our model coincide with the biological evidence presented in Section 2.4 that CTCs of all phenotypes appear to be able to extravasate (Banyard and Bielenberg, 2015). Furthermore, only a low proportion of extravasations included mesenchymal-like cancer cells—the bulk of extravasating cells were of partial-EMT phenotype and others of epithelial phenotype.

As discussed above, the highest number of extravasations was observed onto the grid of the bones. Yet, as Figure 4.6 indicates, the largest micrometastasis, which resulted from

the early metastatic spread of a large cluster consisting predominantly of epithelial-like cancer cells, occurred at the site of the lungs, where only two extravasations were observed over the total time period that we considered. This emphasises that cancerous spread is highly complex and difficult to predict, a feature represented through the stochasticity involved in multiple processes of our model. Examples of such processes are (partial) EMT at the primary site, the survival of CTCs and the potential partial or full dissemination of CTC clusters in the vasculature, the determination of the secondary site of extravasation, as well as MET, dormancy and cell death at secondary sites. Furthermore, the fact that the largest growth stemmed from a cluster consisting of predominantly epithelial-like cancer cells highlights that this cell type with its distinguishing feature of rapid proliferation is generally the one best adapted to growth in the tumour microenvironment at secondary sites. This observation and our observation that—as time progresses—increasing numbers of partial-EMT cancer cells transit to an epithelial-like phenotype coincide with two of the biological findings discussed in Section 2.4. The first such finding is that the bulk of cancer cells at secondary sites are of epithelial-like phenotype (Pastushenko and Blanpain, 2018) as well as some of partial-EMT phenotype (Dongre and Weinberg, 2019). The second finding in agreement with our results is the observation by Ruscetti et al. (2015) that macrometastases at the secondary site of the lungs consisted mainly of epithelial-like cancer cells while smaller lesions presented few epithelial-like cancer cells and thus mainly cells with some degree of mesenchymal-traits. Finally, our model accounts for the biological evidence presented in Ocaña et al. (2012) and Kröger et al. (2019) that cancer cells of a stable mesenchymal-like phenotype are unable to transform via MET and hence fail to give rise to metastatic growth at secondary sites.

Chapter 6

A 3D hybrid discrete-continuum model of EMT-/MET-dependent cancer cell invasion

In this chapter, we introduce a three-dimensional hybrid discrete-continuum mathematical model of cancer cell invasion. This model accounts not only for collective epithelial and for individual mesenchymal invasion strategies but also for the transition between these two phenotypic cell states, i.e. for EMT and MET. It is based on the two-dimensional model for cancer invasion introduced in Sfakianakis et al. (2018a). In this thesis, we extend this model to a third dimension and use it to represent organotypic invasion assay experiments by Nurmenniemi et al. (2009). Subject to some alterations, the work is aimed to be published.

Due to the number of cells involved in cancer invasion, continuum models are a popular and computationally efficient approach to modelling cancer invasion, *cf.* Section 3.1. This approach can reflect the biology of epithelial-like cancer cells and hence their spatiotemporal evolution well. However, as we have established in Section 2.4, EMT and MET—and intrinsically also cancer cells of mesenchymal phenotype—play a crucial role in cancer invasion (Godlewski et al., 2010). In particular, a distinguishing feature of mesenchymal-like cancer cells is their loss of cell-cell adhesion (see Figure 2.11). Hence, it would be biologically inaccurate to represent cells of mesenchymal phenotype using a continuum approach. As only a small proportion—and hence relatively small number—of cancer cells are of mesenchymal-like phenotype (Dongre and Weinberg (2019); *cf.* Section 2.4), the model in this chapter retains computational efficiency while representing the spatiotemporal evolution of epithelial-like and mesenchymal-like cancer cells in a biologically appropriate manner. This is achieved by representing the epithelial-like cancer cells, which make up the bulk of cells in the model, in a continuum PDE approach and the more sparsely occurring mesenchymal-like cancer cells through an individual-based SDE approach.

As we present in Section 6.3, the resulting model predicts the experimental organotypic assay results by Nurmenniemi et al. (2009) qualitatively and quantitatively accurately. Hence, the modelling approach allows us to bridge the often-existent gap between experimental and theoretical work. To demonstrate this, the resulting model was parametrised to accurately represent the organotypic invasion assays of OSCCs in an

experimental organotypic invasion model proposed by Nurmenniemi et al. (2009), which is described in Section 2.5. Parameter values were extracted from the literature wherever possible. Missing parameter values were inferred using inverse parameter estimation. Finally, a sensitivity analysis was carried out to give information about the biological relevance of the parameters.

6.1 Model setup

For the construction of this invasion model, we formulate a coupled hybrid system of partial and stochastic differential equations that describe the evolution of epithelial-like and mesenchymal-like cancer cells, respectively. We continue by outlining in Section 6.1.3 how the transitions from one phenotypic state to the other—via EMT and MET—are modelled mathematically. It is to be noted that, while both the model described in Chapters 4 and 5, and the model introduced in this section are of *hybrid* nature, they are each 'hybrid' in a different sense. The previously introduced metastasis framework is a hybrid approach because the evolution of the diffusive MMP-2 and the ECM is modelled in a continuum approach while the movement of the cancer cells is modelled using a (continuum-derived) discrete modelling approach and cell-specific processes like proliferation and mutations are then added onto the discrete model. In contrast, in the coupled discrete-continuum approach introduced in this section, epithelial-like cancer cells are *always* modelled in a continuum approach while mesenchymal-like cancer cells are represented as a collection of discrete particles *throughout*.

This is achieved through the density-based and particle-based submodels outlined in Sections 6.1.1 and 6.1.2. These submodels are *coupled* via density-to-particle and particle-to-density operators introduced in Section 6.1.3. The setup of the two submodels mirrors biological features that distinguish the cancer cells of the two phenotypes. Epithelial-like cancer cells typically appear as cell sheets with strong intercellular adhesion. This adhesion becomes diminished during the EMT process. EMT is captured through the density-to-particle operator in Section 6.1.5. This causes resulting mesenchymal-like cancer cells to typically appear individually (see Figure 2.11 for a graphical representation). However, cell-cell attachment and hence the epithelial phenotypic state can be regained via MET, which is represented by the particle-to-density operator in Section 6.1.4.

Another important difference between the models is that the individual cancer cells in the metastasis framework in Chapters 4 and 5 move on a grid while the individually modelled mesenchymal cancer cells in this model can take any position in the spatial domain like in the cells in the CBMs explained in Section 3.1.1.

6.1.1 Density-based submodel

Through the density-based submodel, we capture the spatiotemporal evolution of the epithelial-like cancer cells. We assume that these cells compete for space and resources with the mesenchymal-like cancer cells and with the ECM. Moreover, the epithelial-like cancer cells in our model proliferate. This causes (mechanical) pushing forces to develop between them, which we incorporate in the model through a small diffusion term. Finally, we assume that epithelial-like cancer cells do not migrate actively—neither in the form

a directed response to extracellular cues via hapto- or chemotaxis nor in the form of random migration.

In our model, the above processes are accounted for via macroscopic deterministic PDEs. Namely, we denote by $\Omega \subset \mathbb{R}^3$ a Lipschitz domain suitable for the experimental settings to be modelled, and by $c_{\mathsf{E}}(\mathbf{x},t)$, $c_{\mathsf{M}}(\mathbf{x},t)$, $m(\mathbf{x},t)$, and $w(\mathbf{x},t)$, where $\mathbf{x} \in \Omega$ and $t \geq 0$, the densities of the epithelial-like cancer cells, the mesenchymal-like cancer cells (whenever applicable), the diffusible MMP-2, and the ECM, respectively, in coherence with the notation in the other chapters of this thesis. As in Chapters 4 and 5, the subscripts E and M indicate the epithelial and the mesenchymal phenotype, respectively.

Although we model the time evolution of the mesenchymal-like cancer cells through their particle formulation (see Section 6.1.2), they also participate in the time evolution of the epithelial-like cancer cells via their corresponding density formulation c_{M}. The mesenchymal-like cancer cells transition between their particle and density formulations via the *particle-to-density* process explained in Section 6.1.3.

The considerations above are incorporated in the following (deterministic) PDE that governs the spatiotemporal evolution of the epithelial-like cancer cells:

$$\begin{aligned}\frac{\partial}{\partial t}c_{\mathsf{E}}(\mathbf{x},t) &= \overbrace{D_{\mathsf{E}}\Delta c_{\mathsf{E}}(\mathbf{x},t)}^{\text{diffusion}} - \overbrace{\nu_{\mathsf{E}}^{\mathrm{EMT}}(\mathbf{x},t)c_{\mathsf{E}}(\mathbf{x},t)}^{\text{EMT}} + \overbrace{\nu_{\mathsf{M}}^{\mathrm{MET}}(\mathbf{x},t)c_{\mathsf{M}}(\mathbf{x},t)}^{\text{MET}} \\ &+ \overbrace{\rho_c^{\mathsf{E}}c_{\mathsf{E}}(\mathbf{x},t)\left(1-c_{\mathsf{E}}(\mathbf{x},t)-c_{\mathsf{M}}(\mathbf{x},t)-w(\mathbf{x},t)\right)}^{\text{proliferation}}, \end{aligned} \tag{6.1.1}$$

where $\nu_{\mathsf{E}}^{\mathrm{EMT}}(\mathbf{x},t) = \nu_{\mathsf{E}}\mathcal{X}_{\mathcal{E}(t)}(\mathbf{x})$ and $\nu_{\mathsf{M}}^{\mathrm{MET}}(\mathbf{x},t) = \nu_{\mathsf{M}}\mathcal{X}_{\mathcal{M}(t)}(\mathbf{x})$, with $\mathcal{E}(t), \mathcal{M}(t) \subset \Omega$, and D_{E}, ν_{E}, $\nu_{\mathsf{M}}, \rho_c^{\mathsf{E}} \geq 0$. Note that in equation (6.1.1), for simplicity, we assume that EMT takes place in randomly chosen sub-sets, denoted by $\mathcal{E}(t) \subset \Omega$. We understand $\mathcal{E}(t)$ to be the set union of a number of sub-sets each having the size of a single biological cell, *cf.* equation (6.1.9) and Section 6.1.2. Similarly, we assume that MET gives rise to $\mathcal{M}(t)$, another union of sub-sets, each of the size of a cancer cell, *cf.* equation (6.1.13).

We further suppose that both epithelial-like and mesenchymal-like cancer cells produce diffusible MMP-2, which are assumed to diffuse in the environment and decay with a constant rate. This yields the following PDE for the spatiotemporal evolution of MMP-2:

$$\frac{\partial}{\partial t}m(\mathbf{x},t) = \overbrace{D_m\Delta m(\mathbf{x},t)}^{\text{diffusion}} + \overbrace{\rho_m^{\mathsf{E}}c_{\mathsf{E}}(\mathbf{x},t) + \rho_m^{\mathsf{M}}c_{\mathsf{M}}(\mathbf{x},t)}^{\text{production}} - \overbrace{\lambda_m m(\mathbf{x},t)}^{\text{decay}}, \tag{6.1.2}$$

with D_m, ρ_m^{E}, ρ_m^{M}, $\lambda_m \geq 0$ constants. Note, however, that within the scope of this thesis, we set these coefficients to zero so that only the membrane-bound MT1-MMP degrades the ECM, *cf.* (Sabeh et al., 2009) and models in previous chapters.

Similarly, we model the ECM as an immovable component of the system that neither diffuses nor otherwise translocates. The ECM is described by a non-uniform density profile, which is degraded by both membrane-bound and diffusive MMPs. We model

the matrix degradation to be dependent on the cancer cell/MMP-2-complex instead of MMP-2 alone. This is a simplification of the activation of MMP-2 by membrane-bound MT1-MMP, TIMP2 and pro-MMP-2, previously explained in Figure 2.8 in Section 2.3.2. Additionally, for simplicity, no reconstruction of the matrix is assumed. Overall, the spatiotemporal evolution for the ECM is then given by the equation

$$\frac{\partial}{\partial t} w(\mathbf{x}, t) = \overbrace{-\left(\lambda_w^{\mathsf{E}} c^{\mathsf{E}}(\mathbf{x}, t) + \lambda_w^{\mathsf{M}} c^{\mathsf{M}}(\mathbf{x}, t)\right) m(\mathbf{x}, t) w(\mathbf{x}, t)}^{\text{degradation}}, \tag{6.1.3}$$

with $\lambda_w^{\mathsf{E}},\ \lambda_w^{\mathsf{M}} \geq 0$ constants.

The reaction-diffusion system (6.1.1)–(6.1.3), which could be extended to an *advection-reaction-diffusion* (ARD) system if it involved chemo- or haptotaxis in equation (6.1.1), is solved numerically using a method developed in Kolbe et al. (2016); Sfakianakis et al. (2017), which we describe in some detail in Appendix C.

6.1.2 Particle-based submodel

We next give an outline of the particle-based submodel that describes the spatiotemporal evolution of the single mesenchymal-like cancer cells. Like the remainder of the model, the methods and techniques used therein are motivated by work in Sfakianakis et al. (2018a). However, prior to their application of modelling the spatiotemporal evolution of mesenchymal-like cancer cells in Sfakianakis et al. (2018a), similar methods and techniques had been used in other scientific fields. An example is the classical *particle-in-cell method*, first proposed in Harlow (1962), which has its main application in plasma physics. Another example is the *smoothed-particle hydrodynamics method* used in astrophysics and ballistics, see e.g. Gingold and Monaghan (1977). The stochastic nature of the ODEs obeyed by the particles is motivated by the seminal work in Stratonovich (1966). For the combination of the two cancer cell formulations—i.e. for the bidirectional transition between the epithelial-like and mesenchymal-like cancer cell formulations via an atomistic and a continuum formulation for both the epithelial-like and mesenchymal-like cancer cell populations—we are inspired by Blanc et al. (2007); Kitanidis (1994); Makridakis et al. (2013); Tompson and Dougherty (1992).

We consider the mesenchymal-like cancer cells to be a discrete collection of isolated mass particles that migrate through the tissue via *biased random motion*. We model this biased random motion strategy using SDEs. In particular, we consider a system of $N = N(t) \in \mathbb{N}$ mesenchymal-like cancer cells, which we index by $p \in P = \{1, \ldots, N\}$. We account for their positions $\mathbf{x}_p(t) \in \mathbb{R}^3$ and their masses $m_p(t) \geq 0$. Then the overall mass distribution of the particle system $\{(\mathbf{x}_p, m_p),\ p \in P\}$ is given by

$$\tilde{\tilde{c}}(\mathbf{x}, t) = \sum_{p \in P} m_p(t) \delta(\mathbf{x} - \mathbf{x}_p(t)) \tag{6.1.4}$$

where $\delta(\cdot - \mathbf{x}_p(t))$ is the Dirac distribution centred at $\mathbf{x}_p \in \mathbb{R}^3$. Using the characteristic function

$$\zeta(\mathbf{x}) = \mathcal{X}_{K_0}(\mathbf{x}), \quad \mathbf{x} \in \mathbb{R}^3, \tag{6.1.5}$$

we redefine $\tilde{\tilde{c}}(\mathbf{x}, t)$ in equation (6.1.4) as

$$\tilde{c}(\mathbf{x}, t) = \int_{\Omega} \tilde{\tilde{c}}(\mathbf{x}', t)\zeta(\mathbf{x} - \mathbf{x}')d\mathbf{x}' \overset{(6.1.4)}{=} \sum_{p \in P} m_p(t)\zeta(\mathbf{x} - \mathbf{x}_p(t)). \tag{6.1.6}$$

Here K_0 is a—for reasons of simplicity—cuboid domain that represents the volume occupied by a physical cell. The *biased random motion* of the particles that represent the mesenchymal-like cancer cells is modelled through the combination of two independent processes. Firstly, we consider directed motion that represents the haptotactic response of the cells to gradients of the ECM-bound adhesion sites. Secondly, we include persistent random motion, which we understand as Brownian motion. Both of these cell-migration processes are combined in an SDE of the form

$$d\mathbf{X}_t^p = \mu(\mathbf{X}_t^p, t)dt + \sigma(\mathbf{X}_t^p, t)d\mathbf{W}_t^p, \quad \text{for } p \in P, \tag{6.1.7}$$

where $\mathbf{X}_t^p$ represents the position of the particles in physical space (here $\mathbb{R}^3$), and $\mathbf{W}_t^p$ is a Wiener process with independent and normally distributed increments. The modelling assumption that the mesenchymal-like cancer cells undergo directed motion is encoded in equation (6.1.7) via the *drift* coefficient μ, and their random motion via the *diffusion* coefficient σ. The contribution of these coefficients to equation (6.1.7) can be understood as follows. During a short time interval of duration δt, the changes of the stochastic process $\mathbf{X}_t^p$ (i.e. of the position of the particle p in physical space) follow a normal distribution with expectation $\mu(\mathbf{X}_t^p, t)\delta t$ and variance $\sigma(\mathbf{X}_t^p, t)^2\delta t$.

Remark: Note that, in the special case that we consider here where $\mu(\mathbf{x}, t) = \mu\,\mathbf{x}$ and $\sigma(\mathbf{x}, t) = \sigma\mathbf{x}$, with $\mu \in \mathbb{R}$ and $\sigma \geq 0$, the stochastic process that solves equation (6.1.7) can be numerically computed and hence approximated by the corresponding *half-step explicit Euler-Maruyama particle motion scheme*

$$\mathbf{X}_{t+\tau}^p = \mathbf{X}_t^p + \mu\mathbf{X}_t^p\tau + \sigma\mathbf{Z}^p\sqrt{\tau}, \quad \text{for} \quad p \in P\,. \tag{6.1.8}$$

Here, $\tau > 0$ is the time step of the scheme and $\mathbf{Z}^p$ is a vector of normally distributed values of zero mean and unit variance, *cf.* Kloeden and Platen (2013).

During every time step τ, a provisional new position of each particle is computed via equation (6.1.8). This allows estimating the speed of the respective particle. If this speed exceeds the maximal (biological) mesenchymal-like cancer cell particle speed s, the provisional new position of the respective particle is adjusted in its magnitude to comply with s. The direction of the particle displacement is not affected.

The mesenchymal-like cancer cells participate in several dynamical processes—such as in the EMT, the MET and the proliferation of the epithelial-like cancer cells; in the production of MMPs; and in the degradation of the ECM. Yet, the particle motion scheme in equation (6.1.8) does not include any reaction processes. Instead, we account for these processes in the following way:

- As mesenchymal-like cancer cells undergo MET and become epithelial-like cancer cells, they are transformed to density via the *density-to-particle* operator that will be introduced in Section 6.1.3 and the respective mesenchymal-like cancer cells are removed from the system of mesenchymal-like cancer cell particles. The additional epithelial-like cancer cell density that is created via MET augments the existing

epithelial-like cancer cell density and participates in the system of equations (6.1.1)–(6.1.3) in a regular fashion. Conversely, a part of the epithelial-like cancer cell density undergoes EMT and becomes mesenchymal-like cancer cell density. This is then transformed into particles via the *particle-to-density* operator defined in Section 6.1.3. These newly formed mesenchymal-like cancer cells are then added to the system of existing mesenchymal-like cancer cell particles.

- At every (time instance and) time step of the method, the full distribution of mesenchymal-like cancer cell particles is transformed temporarily to density via the *particle-to-density* operator (without undergoing MET to epithelial-like cancer cells). The mesenchymal-like cancer cell density then participates in the proliferation of the epithelial-like cancer cells, in the production of the MMPs, and in the degradation of the ECM, as equations (6.1.1)–(6.1.3) describe.

6.1.3 Phase transitions between particles and densities

We assume that the domain $\Omega \subset \mathbb{R}^3$ is sufficiently large and regular to be uniformly partitioned into equal cuboid partition cells $\{M_i, i \in I\}$ as

$$\Omega = \bigcup_{i \in I} M_i, \tag{6.1.9}$$

where all cuboid partition cells M_i are translations of the *generic cell* K_0. Every measurable function $c : \Omega \times (0, \infty) \to \mathbb{R}$ can be represented by its simple-function decomposition

$$\sum_{i \in I} c_i(t) \mathcal{X}_{M_i}(\mathbf{x}), \tag{6.1.10}$$

where $\mathcal{X}_{M_i}$ is the characteristic function of $M_i \subset \Omega$, and $c_i(t)$ the mean value of $c(\cdot, t)$ over M_i. That is

$$c_i(t) = \frac{1}{K} \int_{M_i} c(\mathbf{x}, t) d\mathbf{x}. \tag{6.1.11}$$

where K is the volume of K_0 and in effect of all M_i. Furthermore, a particle, indexed by $p \in P$, can be represented in its *particle formulation* through its position and its mass

$$\left(\mathbf{x}_p(t),\, m_p(t)\right), \tag{6.1.12}$$

or in its *density formulation* by the characteristic function with density value

$$\frac{m_p(t)}{K} \mathcal{X}_{K_p}(\mathbf{x}). \tag{6.1.13}$$

Here, as before, K_p is the translation of the generator cell K_0 centred at $\mathbf{x}_p$. Note that, clearly, equation (6.1.13) implies that the mass m_p of the particle is uniformly distributed over K_p. The sets K_p, $p \in P$, in equation (6.1.13) and the M_i, $i \in I$, in equation (6.1.10) are equivalent up to translations but they do not coincide in general. The M_i, $i \in I$, form a fixed partition of the domain, *cf.* equation (6.1.9), whereas the K_p, $p \in P$, 'follow' the position of the particles in equation (6.1.13). Based on this 'dual' description of the particles in equations (6.1.12) and (6.1.13), we assign the *particle-to-density* and the *density-to-particle transition operators* in the next two sections.

6.1.4 Particle-to-density transition operator for MET

Let $\big\{(\mathbf{x}_p^{\mathsf{M}}, m_p^{\mathsf{M}}),\ p \in P\big\}$ be a collection of particles that represent mesenchymal-like cancer cells. Using equation (6.1.6), we define the *particle-to-density* operator $\mathcal{F}$ as

$$\big\{(\mathbf{x}_p^{\mathsf{M}}, m_p^{\mathsf{M}}),\ p \in P\big\} \xrightarrow{\mathcal{F}} c(\mathbf{x}, t). \tag{6.1.14}$$

To define the function $c(\mathbf{x}, t)$, we go through all the particles that represent mesenchymal-like cancer cells and consider their corresponding density formulation according to equation (6.1.13). The support K_p of every particle overlaps with several of the partition cells M_i, $i \in I$. We assign the corresponding portion of the particle mass to every partition cell M_i:

$$m_p^{\mathsf{M}}\big|_{M_i} = \frac{m_p^{\mathsf{M}}}{K}\big|K_p \cap M_i\big|. \tag{6.1.15}$$

In a similar fashion, we account for the contribution of all particles $p \in P$ to a partition cell M_i:

$$c_i(t) = \sum_{p\in P} \frac{1}{K} m_p^{\mathsf{M}}\big|_{M_i} \overset{(6.1.15)}{=} \sum_{p\in P} \frac{m_p^{\mathsf{M}}(t)}{K^2}\big|K_p \cap M_i\big|, \quad \text{for } i \in I\,. \tag{6.1.16}$$

In view of equations (6.1.10) and (6.1.16), we deduce the density function $c(\mathbf{x}, t)$ over the full domain Ω to be

$$c(\mathbf{x}, t) = \sum_{i\in I} c_i(t)\mathcal{X}_{M_i}(\mathbf{x}), \quad \mathbf{x} \in \Omega. \tag{6.1.17}$$

For simplicity, within the scope of this thesis, we assume that each of the mesenchymal-like cancer cell particles $\big\{(\mathbf{x}_p^{\mathsf{M}}, m_p^{\mathsf{M}}),\ p \in P\big\}$ undergo MET to become an epithelial-like cancer cell (below abbreviated as *ECC*) randomly through the process

$$\big\{(\mathbf{x}_p^{\mathsf{M}}, m_p^{\mathsf{M}}),\ p \in P\big\} \xrightarrow{\text{MET}} \overbrace{\big\{(\mathbf{x}_p^{\mathsf{E}}, m_p^{\mathsf{E}}),\ p \in P^{\text{MET}}\big\}}^{\text{newly created ECC particles}}. \tag{6.1.18}$$

The resulting epithelial-like cancer cell particles are instantaneously transformed to density via the *particle-to-density* operator $\mathcal{F}$ given in equation (6.1.14):

$$\big\{(\mathbf{x}_p^{\mathsf{E}}, m_p^{\mathsf{E}}),\ p \in P^{\text{MET}}\big\} \xrightarrow{\mathcal{F}} c_{\text{MET}}^{\mathsf{E}}.$$

Consequently, the MET can be expressed in operator form as

$$\mathcal{R}^{\text{MET}}\left(c^{\mathsf{E}}, \big\{(\mathbf{x}_p^{\mathsf{M}}, m_p^{\mathsf{M}}),\ p \in P\big\}\right) = (c^{\mathsf{E}} + c_{\text{MET}}^{\mathsf{E}}, \{(\mathbf{x}_p^{\mathsf{M}}, m_p^{\mathsf{M}}),\ p \in \tilde{P}^{\text{new}}\}), \tag{6.1.19}$$

where $\tilde{P}^{\text{new}}$ is a re-enumeration of the set difference $P \setminus P^{\text{MET}}$.

Figure 6.1 shows a graphical representation of the *particle-to-density* operator $\mathcal{F}$. For ease of presentation, this is depicted in two dimensions.

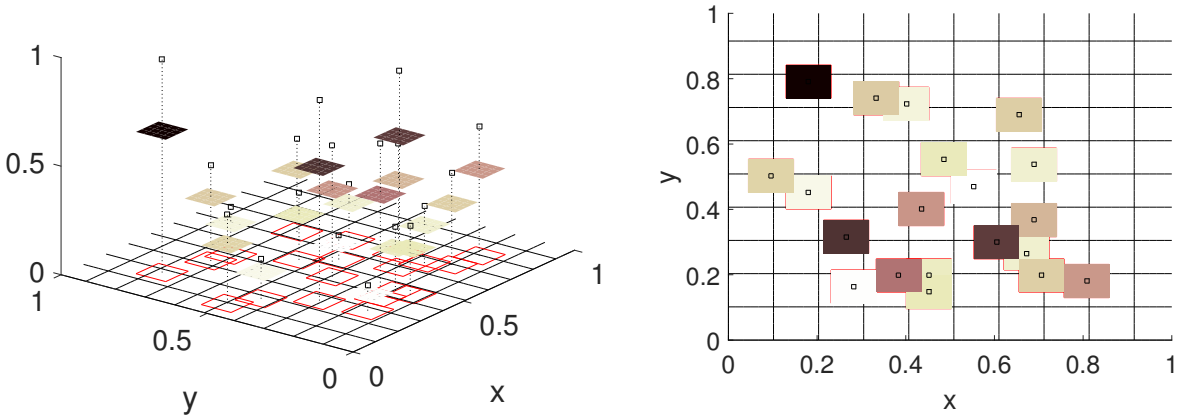

Figure 6.1: ***Two-dimensional graphic representation of the particle-to-density operator $\mathcal{F}$.*** *Left: We consider a support K_p ($p \in P$) around the location x_p of every particle. The mass of every particle m_p—each represented by a point—is uniformly distributed over the respective support K_p. The grid represents the partitioning of the domain. Right: A view from above reveals that the supports K_p can overlap with several cells of the partition. The corresponding masses are assigned to the partition cells using equation* (6.1.16)*. We have chosen to show this in two rather than three dimensions for ease of presentation.*

6.1.5 Density-to-particle transition operator for EMT

Given a density function $c = c(\mathbf{x}, t)$, we define the *density-to-particle* operator $\mathcal{B}$ for a general particle as

$$c(\mathbf{x}, t) \xrightarrow{\mathcal{B}} \{(\mathbf{x}_p(t), m_p(t)),\ p \in P\}\,. \tag{6.1.20}$$

We assign one particle with mass

$$m_i(t) = \int_{M_i} c(\mathbf{x}, t) d\mathbf{x} \tag{6.1.21}$$

and position

$$\mathbf{x}_i(t) = \text{ the (bary-)centre of } M_i \tag{6.1.22}$$

to every cuboid partition cell M_i, $i \in I$. Figure 6.2 shows a graphical representation of the *density-to-particle* operator $\mathcal{B}$—in two dimensions for ease of presentation.

In this thesis, the density-to-particle transition is used to model the EMT process. As in the case of MET in Section 6.1.4, EMT is—at this stage—represented using a simplified approach where a randomly chosen part of the epithelial-like cancer cells (in density formulation) $c^{\mathsf{E}}_{\mathrm{EMT}}$ undergoes EMT to give rise to mesenchymal-like cancer cells. For this, the full domain is discretised into partition cuboids M_i, $i \in I$, as represented graphically for the two-dimensional case in Figure 6.1. EMT takes place with some probability in each cuboid that contains some material. The larger the amount of material in a cuboid, the higher the probability that one cell undergoes EMT. We perform this process in steps. First, the randomly chosen part of the epithelial-like cancer cell density $c^{\mathsf{E}}_{\mathrm{EMT}}$ transitions to mesenchymal-like cancer cell density:

$$c^{\mathsf{E}}_{\mathrm{EMT}} \xrightarrow{\mathrm{EMT}} c^{\mathsf{M}}_{\mathrm{EMT}}.$$

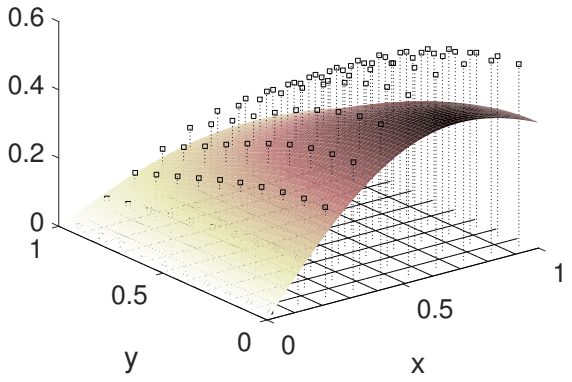

Figure 6.2: ***Graphical representation of the density-to-particle operator $\mathcal{B}$.*** *The mass m_i of the density function $c(\mathbf{x}, t)$ (surface) is computed over every partition cell M_i, $i \in I$ (quadrilateral grid on the xy-plane) using equation* (6.1.21)*. We then define the particle as $(\mathbf{x}_i, m_i)$, where the location $\mathbf{x}_i$ is given by equation* (6.1.22)*. We have chosen to show this in two rather than three dimensions for ease of presentation.*

This mesenchymal-like cancer cell density is immediately transformed to me- senchymal-like cancer cell particles via the *density-to-particle* operator $\mathcal{B}$ given in equation (6.1.20):

$$c^{\mathsf{M}}_{\mathrm{EMT}} \xrightarrow{\mathcal{B}} \left\{(\mathbf{x}^{\mathsf{M}}_p, m^{\mathsf{M}}_p),\ p \in P^{\mathrm{EMT}}\right\}. \tag{6.1.23}$$

Here $\mathbf{x}^{\mathsf{M}}_p$ and m^{M}_p are given by equations (6.1.21) and (6.1.22), respectively, and P^{EMT} is the set of indices corresponding to the particles that perform EMT. Subsequently, the family of existing mesenchymal-like cancer cell particles—below abbreviated as *MCC*—is updated with these newly created particles. It is hence given by the disjoint union

$$\overbrace{\left\{(\mathbf{x}^{\mathsf{M}}_p, m^{\mathsf{M}}_p),\ p \in P\right\}}^{\text{existing MCC particles}} \uplus \overbrace{\left\{(\mathbf{x}^{\mathsf{M}}_p, m^{\mathsf{M}}_p),\ p \in P^{\mathrm{EMT}}\right\}}^{\text{newly created MCC particles}} = \left\{(\mathbf{x}^{\mathsf{M}}_p, m^{\mathsf{M}}_p),\ p \in P^{\mathrm{new}}\right\}, \tag{6.1.24}$$

where P^{new} is a re-enumeration of the multiset $P \uplus P^{\mathrm{EMT}}$. Overall, the EMT operator consequently reads as

$$\mathcal{R}^{\mathrm{EMT}}(c^{\mathsf{E}}, \left\{(\mathbf{x}^{\mathsf{M}}_p, m^{\mathsf{M}}_p),\ p \in P\right\}) = (c^{\mathsf{E}} - c^{\mathsf{E}}_{\mathrm{EMT}}, \left\{(\mathbf{x}^{\mathsf{M}}_p, m^{\mathsf{M}}_p),\ p \in P^{\mathrm{new}}\right\}). \tag{6.1.25}$$

6.1.6 Interactions between particles

We understand the particles as isolated cancer cells or cancer-cell aggregates of similar sizes and masses. To maintain similar masses, we split and merge the particles according to their mass and position. In the particular case that a particle represents an isolated cancer cell, we set m_{ref} to be the reference cell mass, *cf.* Table 6.1. Moreover, because particles are represented as points, we take K_0 to be the substantiation of a particle into

three dimensions, i.e. the mass of the cancer cell is modelled to be distributed evenly throughout the cube K_0. We then proceed as follows:

Splitting. A *large particle* $(\mathbf{x}_p, m_p)$ with mass $m_p > \frac{4}{3}\, m_{\text{ref}}$ is *split* into two smaller particles $(\mathbf{x}_p^1, m_p^1)$, $(\mathbf{x}_p^2, m_p^2)$ of the same position $\mathbf{x}_p^1 = \mathbf{x}_p^2 = \mathbf{x}_p$ and each of mass $m_p^1 = m_p^2 = \frac{1}{2}\, m_p$. From that moment onwards, these two particles are considered to be distinct from each other.

Merging. A *small particle* $(\mathbf{x}_p, m_p)$ with mass $m_p < \frac{2}{3}\, m_{\text{ref}}$ is *merged* with another small particle $(\mathbf{x}_q, m_q)$ if they are close to each other, i.e. if

$$\|\mathbf{x}_p - \mathbf{x}_q\| < \operatorname{diam}(K_0),$$

where $\|\cdot\|$ describes the two-dimensional Euclidean norm. The resulting particle is set to have the cumulative mass of the two particles and to be located at their centre of mass

$$\left(\frac{m_p \mathbf{x}_p + m_q \mathbf{x}_q}{m_p + m_q}, m_p + m_q\right). \tag{6.1.26}$$

If more than two small particles are found in merging distance at the same time, they are merged pair-wise in the order they have been created.

Given that the distance between the particles is sufficiently small, iterations of the *merging* and *splitting* processes lead to particles with masses $m_p \in \left[\frac{2}{3}\, m_{\text{ref}}, \frac{4}{3}\, m_{\text{ref}}\right]$, i.e. particles with masses that are close to the reference cell mass m_{ref}.

Besides the merging and splitting procedures, we do not consider other processes that alter the masses of the particles. Moreover, we do not consider any further interactions between the particles in this work (such as competition for free space or development of collision forces) as we try to be consistent with the dynamics that are usually assumed by macroscopic deterministic models similar to that in equations (6.1.1)–(6.1.3). If two or more particles occupy the same position in this model, this can be understood as a comparatively high local cell density.

6.2 Implementation and model calibration

We choose our domain to be of size $8500\,\mu\text{m} \times 8500\,\mu\text{m} \times 8500\,\mu\text{m}$ following the experimental settings of Nurmenniemi et al. (2009) described in Section 2.5.3.

The construction of the initial ECM density distribution is based on discrete principles. For this, we first created a random landscape of a predefined size—e.g. an 8×8 random matrix for two-dimensional experiments or an $8\times8\times8$ random matrix for three-dimensional experiments. These random values are chosen from a normal distribution between the predefined minimum and maximum ECM density value and, respectively, will serve as the *'heights of the hills'* and *'depths of the valleys'* of the final ECM landscape. With subsequent refinements and periodic interpolations, we increased the dimensionality of the matrix. This way, from the 8×8 matrix in two dimensions we deduced a 16×16 matrix, from which we deduced a 32×32 matrix and so on—as shown in Figure 6.3. At every stage of the refinement process, we introduced some small Gaussian noise in each

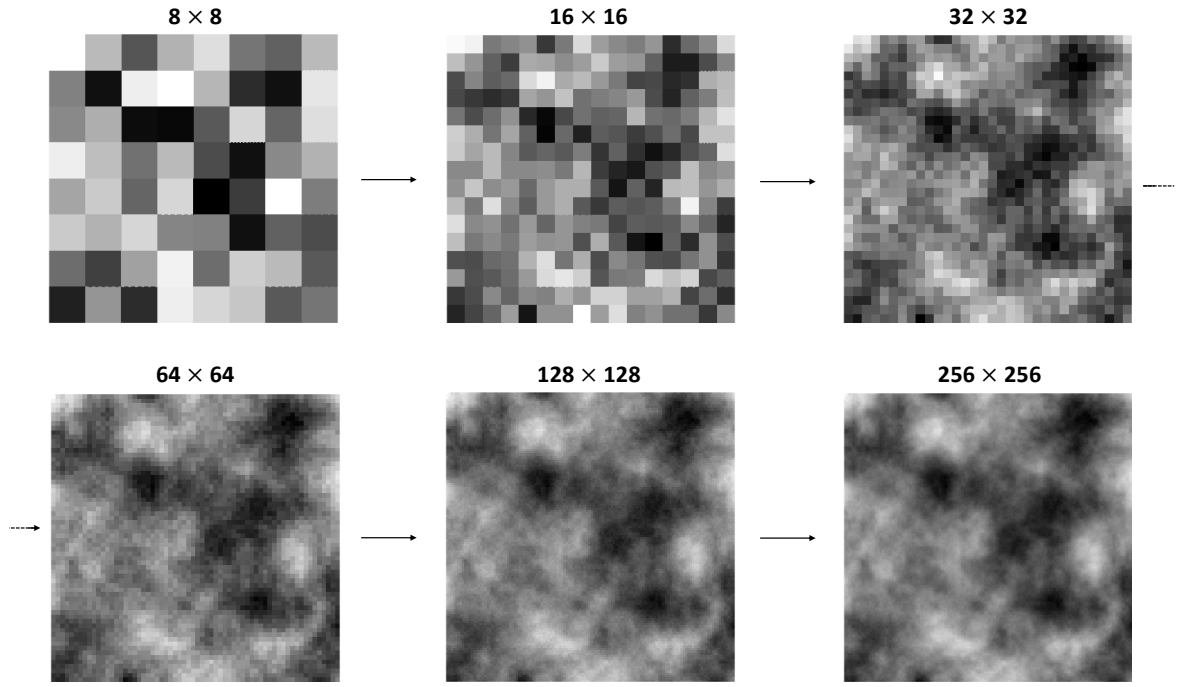

Figure 6.3: ***Construction of a sample initial ECM density distribution in two dimensions.*** *The initial ECM density distribution that we ultimately use in our model is a result of multiple refinements. Here, we show the process in two dimensions starting with an 8×8 random matrix (top left panel). This matrix is progressively refined to a 256×256 matrix (bottom right panel) via repeated periodic interpolations. The result is a sample two-dimensional initial ECM density distribution with values between* $0.9 \times w_{\mathsf{max}}$ *and* w_{max}*, where* $w_{\mathsf{max}} = 1.06\,\mathrm{g}^{-1}\mathrm{cm}^3$ *(ICRP, 2009). The corresponding process was applied in three dimensions up to a refinement of 64×64×64 for our simulations.*

of the values. The process in two dimensions up to the deduction of a 256×256 matrix is described visually in Figure 6.3.

In what follows, we additionally provide a pseudo-algorithm for the construction of the ECM to explain how the construction of the ECM is based on discrete principles. For the sake of simplicity of presentation, we here consider the one-dimensional case and the domain $[0, 1)$.

- An initial approximation of the ECM is set by deciding on the number of the major 'hills' and 'valleys' per direction along the grid. In our one-dimensional example, we choose an initial rough structure of the ECM with 8 'hills' and 'valleys', i.e. we approximate the ECM as

$$\sum_{i=1}^{8} c_i^{(8)} \mathcal{X}_{C_i^{(8)}}(x), \quad x \in [0, 1),$$

where $C_i^{(8)} = [x_{i-1/2}^{(8)}, x_{i+1/2}^{(8)})$, $x_{i-1/2}^{(8)} = (i-1)\Delta x^{(8)}$, $i = 1, ..., 8$, $\Delta x^{(8)} = \frac{1}{8}$, and where the coefficients $c_i^{(8)}$ are uniformly distributed random numbers chosen within

the interval $[0, 1)$.

- Subsequently, a refinement takes place. The domain $[0, 1)$ is now discretised by $C_i^{(16)} = [x_{i-1/2}^{(16)}, x_{i+1/2}^{(16)})$, $\Delta x^{(16)} = \frac{1}{16}$, $i = 1, ..., 16$, $x_{i-1/2}^{(16)} = (i-1)\Delta x^{(16)}$. Accordingly, the ECM is then approximated by the simple function

$$\sum_{i=1}^{16} c_i^{(16)} \mathcal{X}_{C_i^{(16)}}(x), \quad x \in [0, 1).$$

  The new coefficients $c_i^{(16)}$ interpolate—with some random noise—between the previous values:

$$c_i^{(16)} = \left(1 + 0.002\left(r_i^{(16)} - 0.5\right)\right) \frac{c_{\lfloor i/2 \rfloor}^{(8)} + c_{\lfloor i/2 \rfloor + 1}^{(8)}}{2}, \quad i = 1, \ldots, 16,$$

  where $\lfloor \cdot \rfloor$ represents the floor function, and where $r_i^{(16)}$ are uniformly distributed random numbers within $[0, 1)$. We note that the first and last coefficients, $c_1^{(16)}$ and $c_{16}^{(16)}$, are computed periodically with respect to the $c_\cdot^{(8)}$-values. The rescaling factor 0.002 is chosen to that the multiplicative randomness/noise is adjusted to 0.1% of the interpolated value.

- In a similar manner, the resolution of the ECM increases further so that the ECM is approximated by

$$\sum_{i=1}^{32} c_i^{(32)} \mathcal{X}_{C_i^{(32)}}(x), \quad x \in [0, 1],$$

  where $C_i^{(32)} = [x_{i-1/2}^{(32)}, x_{i+1/2}^{(32)})$, $x_{i-1/2}^{(32)} = (i-1)\Delta x^{(32)}$, $\Delta x^{(32)} = \frac{1}{32}$, $i = 1, ..., 32$, and $c_i^{(32)} = \left(1 + 0.002\left(r_i^{(32)} - 0.5\right)\right) \frac{c_{\lfloor i/2 \rfloor}^{(16)} + c_{\lfloor i/2 \rfloor + 1}^{(16)}}{2}, \quad i = 1 \ldots 32.$

- The refinements are repeated until the desired resolution is reached.

- At a final stage when the desired resolution of the ECM is reached, the values of the density of the matrix are rescaled between the biological range of a minimum and maximum ECM density.

We initially considered a single layer of epithelial-like cancer cells to reside on the upper non-uniform matrix surface. This way, our initial conditions correspond to those in the experiments by Nurmenniemi et al. (2009), for which 7×10^5 epithelial-like cancer cells and no mesenchymal-like cancer cells were placed on top of each myoma disc. For the three-dimensional model with $\mathbf{x} = (x, y, z) \in \Omega$, this single layer of epithelial-like cells is translated to cell density as

$$c(t, \mathbf{x}) = c(t, x, y, z) = \begin{cases} 1, & z > z_{\mathsf{max}} - 1.5 \times 10^{-3} \\ 0, & \text{else.} \end{cases}$$

Here, 1.5×10^{-3} is the non-dimensional diameter of a single cell corresponding to the the average diameter of 15 to 20 µm of a HSC-3 cell (Japanese Collection of Research

Table 6.1: ***Parameter settings for the simulations.*** *Epithelial-like HSC-3 cells and mesenchymal-like HSC-3 cells are abbreviated* ECC *and* MCC*, respectively. At this instance, we only model the activity of membrane-bound, non-diffusive MMPs like MT1-MMP following the experimental results by Sabeh et al. (2009) shown in Figure 4.13. We achieve this by setting the coefficients D_m, ρ_m^{E}, ρ_m^{M} and λ_m in equation* (6.1.2) *to zero. We also set the initial conditions for the diffusible MMP to be $m(\mathbf{x}, 0) = 1$. This allows for possible extensions of the model that include diffusible MMPs, while continuing to account for the effects of membrane-bound MMPs in our model via equation* (6.1.3)*. Note that ν_{E} and ν_{M} have different units as the former refers to a density of cancer cells and the latter to individual cancer cells.*

	Description	**Value**	**Range**	**Reference**
D_{E}	ECC density diffusion coefficient	$8.64 \times 10^{-8}\,\mathrm{cm}^3$	$1 \times 10^{-9} - 1 \times 10^{-12}\,\mathrm{cm}^2\mathrm{s}^{-1}$	Chaplain and Lolas (2005) Brú et al. (2003)
ρ_c^{E}	ECC density proliferation coefficient	$1.2\ \mathrm{d}^{-1}$	$1.2\ \mathrm{d}^{-1}$	Fujinaga et al. (2014)
σ	MCC particle diffusion coefficient	$3.3675\ \mathrm{cm\ d}^{-\frac{1}{2}}$		Parameter estimation
μ	MCC particle drift coefficient	$7.4595 \times 10^{-2}\,\mathrm{d}^{-1}$		Parameter estimation
s	Maximum MCC particle speed	$2.16\ \mathrm{cm\ d}^{-1}$	$1.83 \times 10^{-5} - 3.83 \times 10^{-5}\,\mathrm{cm\ s}^{-1}$	Butler et al. (2010)
m_{ref}	MCC particle reference mass	$2.3 \times 10^{-9}\,\mathrm{g\ cell}^{-1}$	$2.3 \times 10^{-9} - 3.3 \times 10^{-9}\,\mathrm{g\ cell}^{-1}$	Park et al. (2008)
$\lvert V_0 \rvert$	MCC particle reference volume	$2.3 \times 10^{-9}\,\mathrm{cm}^3$	$2.2 \times 10^{-9} - 5.2 \times 10^{-9}\,\mathrm{cm}^3$	Puck et al. (1956)
ν_{E}	EMT rate	$7.502 \times 10^{-2}\,\mathrm{M\ cm}^{-3}\mathrm{d}^{-1}$		Parameter estimation
ν_{M}	MET rate	$4.7697 \times 10^{-1}\ \mathrm{d}^{-1}$		Parameter estimation
w_{max}	Maximum (initial) ECM density	$1.06\ \mathrm{g\ cm}^{-3}$	$1.02 - 1.05\ \mathrm{g\ cm}^{-3}$	ICRP (2009)
λ_w	ECM degradation rate by ECCs & MCCs	$1.8383 \times 10^{-4}\,\mathrm{M\ cm}^{-3}\mathrm{d}^{-1}$		Parameter estimation

Bioresources Cell Bank, 2015). z describes the height of the three-dimensional domain and z_{max} is the height of the upper surface of the myoma assay without the upper initial cell layer placed on it. Figure 6.5 shows this domain.

Throughout, we implement the model with the zero Neumann boundary conditions for the densities in the model in equations (6.1.1)–(6.1.3). However, since the MMPs accounted for in this set of simulations are membrane-bound and hence follow the spatiotemporal evolution of the cancer cells and since the ECM is immovable, we practically only need to enforce the boundary conditions for the cancer cells modelled through equation (6.1.1). Furthermore, to represent the experimental conditions of Nurmenniemi et al. (2009) through our simulations, we do not allow particles to escape the domain. If a particle would have escaped the domain, we force it to remain on the boundary of the domain instead, retracted along its linear movement trajectory. During the next time step, such a particle again moves according to the model, i.e. according to equation (6.1.7).

6.2.1 Parameter values

To ensure that our simulations are biologically realistic, we use parameter values from the literature wherever possible. These are summarised in Table 6.1 together with their source. Five of the parameter values shown in Table 6.1 could not be sourced from the literature. These were estimated using inverse parameter estimation, as explained in

Section 6.2.2.

Moreover, through the settings for the current simulations, we model the activity of membrane-bound, non-diffusive MMPs like MT1-MMP alone by setting D_m, ρ_m^{E}, ρ_m^{M} and λ_m to zero. We chose to do this in agreement with the results shown in Figure 4.13, which indicate that MT1-MMP is both necessary and sufficient for cell invasion. As MT1-MMP is created on the cell membranes and remains there, its impact through its magnitude is proportional to the density of the cancer cells. However, the model may allow for the inclusion of diffusive MMPs in the future and hence include equation (6.1.2) in the general model introduced in Section 6.1.1.

Finally, a rigorous dimensional analysis is non-trivial for a model on multiple scales like this one and hence postponed to future work.

6.2.2 Parameter estimation

The model described in Section 6.1 depends on the parameters shown in Table 6.1, some of which cannot directly be measured experimentally and need to be indirectly identified. In the case of our simulations, these are the ECM degradation rate λ_w, the diffusion coefficient σ and the drift coefficient μ of the mesenchymal-like cancer cell particles, and the EMT and MET rates ν_{E} and ν_{M}. We employ a combination of global and local optimisation methods for the parameter identification process of these parameters.

The global optimisation method we use is called *enhanced scatter search* (eSS) (Egea et al., 2009). It belongs to the wider class of stochastic global optimisation methods called *metaheuristics* (Glover and Kochenberger, 2006). Like other stochastic optimisation methods, eSS draws an initial diverse population of guesses out of the parameter space and conditionally initiates intense local searches.

As the local optimisation method, we employed the *interior point method*, for details on which we refer to Karmarkar (1984); Byrd et al. (2000). This is an iterative linear and non-linear convex optimisation method that achieves optimisation by going through the middle of the bounded polyhedron in the parameter space. Due to its robustness, it is very well-suited for a problem of mixed stochastic-deterministic nature like this one.

Due to the stochastic nature of our model, repeated applications of the minimisation methods lead to different (optimal) parameter results. We hence compute a large sample of results and identify the confidence interval, which is 95% in our work. The sample determined through the global optimisation method is then passed over to the local optimisation process as the computational polyhedron in the parameter space. All the implementations take place with MATLAB. For the metaheuristic part, we use the *MEtaheuristics for bIoinformatics Global Optimization* (MEIGO) toolbox (Egea et al., 2010).

We denote the parameters determined through the combination of global and local optimisation as

$$\mathcal{P}^{\text{est}} = \left\{ p_i^{\text{est}},\ i = 1 \dots 5 \right\} \left(\stackrel{\text{def.}}{=} \left\{ \lambda_w, \sigma, \mu, \nu_{\mathsf{E}}, \nu_{\mathsf{M}} \right\} \right), \tag{6.2.1}$$

and estimate them by minimising the discrepancy/error between the experimental measurements and the model predictions. This is measured here by the *objective functional*

$$E^{\mathrm{obj}} = \big| |\mathcal{W}^{\mathrm{mea}}|_X - |\mathcal{W}^{\mathrm{mod}}|_X \big|. \tag{6.2.2}$$

The 'norm' $|W^{\mathrm{mea}}|_X$ denotes the experimentally measured quantities and $|\mathcal{W}^{\mathrm{mod}}|_X$ the corresponding numerical values from the model.

To minimise the objective functional in equation (6.2.2), we employ optimisation techniques (see above), which can heuristically be outlined as follows:

a) For an initial parameter set $\mathcal{P}^{\mathrm{est}}$, like the one in equation (6.2.1), the model in Section 6.1 is solved numerically to give $\mathcal{W}^{\mathrm{mod}}$.

b) Via equation (6.2.2), these model predictions $\mathcal{W}^{\mathrm{mod}}$ are compared with the experimentally measured data $\mathcal{W}^{\mathrm{mea}}$ to yield the objective functional values E^{obj}.

c) A new parameter set $\mathcal{P}^{\mathrm{est}}$ for equation (6.2.1) is chosen via the interior point method with the aim of decreasing the value of the objective functional E^{obj}.

The steps a) to c) of the above algorithm are repeated until a parameter set is identified that either minimises the objective functional or satisfies other stopping criteria.

For the simulations in this thesis, in particular, we minimised the maximal invasion depth of the epithelial-like cancer cells as well as their invading cell area (using equal weights). The experimental meaning of these quantities is explained in Section 2.5.4 and Figures 2.22 and 2.23 in particular.

The parameter values resulting from the parameter estimation are shown in Table 6.1.

6.2.3 Sensitivity analysis

Each one of the parameters in the model in Section 6.1 has a different impact on the model's dynamics and its solution. A profound understanding of the impact of the model parameters is crucial both for drawing biological conclusions and for quantifying biological processes. Moreover, the sensitivity analysis is useful for the calibration and for the further development of the model.

We study the impact of the parameters both qualitatively and quantitatively by performing a *local sensitivity analysis*. To this end, we consider a particular experimental setting and a reference parameter set to compute a reference solution. We then vary one reference parameter after the other and compute the corresponding solutions. Consecutively, we compare these solutions with the reference solution and thus quantify the effect that the variation in the parameters has on the solution.

In more detail, the parameters that we study with respect to their effect are

$$\mathcal{P}^{\mathrm{sens}} = \Big\{ \lambda_w, \sigma, \mu, \nu_{\mathsf{E}}, \nu_{\mathsf{M}} \Big\} \overset{\mathrm{def.}}{=} \Big\{ p_i^{\mathrm{sens}},\ i = 1, ..., 5 \Big\}. \tag{6.2.3}$$

We denote the *reference parameter set* as

$$\mathcal{P}^{\mathrm{ref}} = \Big\{ p_i^{\mathrm{ref}},\ i = 1, ..., 5 \Big\} \tag{6.2.4}$$

and compute with it the reference solution $\mathcal{W}^{\mathrm{ref}}$. *Ceteris paribus*, we perturb the reference parameters $p_i^{\mathrm{ref}} \in \mathcal{P}^{\mathrm{ref}}$ individually, which gives new values p_i^{per}. For each perturbation of the parameters, the new parameter set, denoted by

$$\mathcal{P}_i^{\mathrm{per}} = \big\{ p_i^{\mathrm{per}},\ i = 1, ..., 5 \big\}, \tag{6.2.5}$$

differs from the reference set $\mathcal{P}^{\text{ref}}$ only with regards to the value of the parameter p_i. With the perturbed parameter set $\mathcal{P}_i^{\text{per}}$ and the same model conditions (initial conditions, boundary conditions, etc.), we compute the corresponding solution $\mathcal{W}_i^{\text{per}}$ and compare it to the reference solution $\mathcal{W}^{\text{ref}}$. For this, we use the *sensitivity function*

$$\mathcal{S}_i = \frac{\left| |\mathcal{W}_i^{\text{per}}|_X - |\mathcal{W}^{\text{ref}}|_X \right|}{|p_i^{\text{per}} - p_i^{\text{ref}}|}, \tag{6.2.6}$$

where $|\cdot|_X$ denotes a suitably chosen 'norm'. Note that because we consider the maximal invasion depth and the invading cell area with equal weights, we are not interested in the sign of the sensitivity function. However, if we solely considered one of the measurements as our solution, also accounting for the sign rather than the absolute value of the denominator alone would indicate the direction of change induced by the parameter set $\mathcal{P}_i^{\text{per}}$ with respect to $\mathcal{P}^{\text{ref}}$ (see e.g. Figure 6.7).

The perturbations of the parameters are small and hence the divided differences in equation (6.2.6) can also be viewed as approximations of the corresponding partial derivatives of the solution $\mathcal{W}$ around the reference parameter set $\mathcal{P}^{\text{ref}}$. In essence, $\mathcal{S}_i$ represents the (absolute) rate at which the solution $\mathcal{W}$ changes, in the sense of the 'norm' $|\cdot|_X$, with respect to the parameter i.

The *local sensitivity* follows from accounting for all the parameters of $\mathcal{P}^{\text{sens}}$. It can be used to deduce biological information and meaning. For instance, it lets us rank the influence of various parameters on the system, which enables us to gain a more comprehensive understanding of the influence of the different input parameters and their variation on the model outcomes (Alam et al., 2016).

6.3 Results

To produce the simulations presented in the top row of Figure 6.4 through our model, we accounted for the experimental conditions used in Nurmenniemi et al. (2009) as closely as possible. Nurmenniemi et al. (2009) used myoma organotypic assays as their ECM. Using results by (ICRP, 2009) on the average density of human uterine ECM and reproducing its homogeneity as described in Section 6.2 and Figure 6.3, we reconstructed the qualitative features of the myoma assay important to our model. We further ensured that our simulations were run on a domain similar to the assays used in Nurmenniemi et al. (2009) by running the simulations on an $8500\,\mu\text{m} \times 8500\,\mu\text{m} \times 8500\,\mu\text{m}$ square domain. In the experiments, this domain was cylindrical with a diameter of $8000\,\mu\text{m}$ and a height of $3000\,\mu\text{m}$. However, the $6\,\mu\text{m}$ thick slices that were ultimately analysed by Nurmenniemi et al. (2009) were only approximately of size $600\,\mu\text{m} \times 600\,\mu\text{m}$ (see Figure 6.4), taken perpendicular to the myoma disc surface, starting at its upper surface. As Figure 6.4 shows, we also examined slices of dimension $600\,\mu\text{m} \times 600\,\mu\text{m} \times 6\,\mu\text{m}$ from the larger three-dimensional domain as shown in Figure 6.5 as well.

Moreover, our initial conditions correspond to those in the experiments by Nurmenniemi et al. (2009), for which 7×10^5 epithelial-like cancer cells and no mesenchymal-like cancer cells were placed on top of each myoma disc—we initially considered a single layer of epithelial-like cancer cells, which were described by a density profile, to reside on the upper non-uniform matrix surface. The time evolution of this initial density is subject

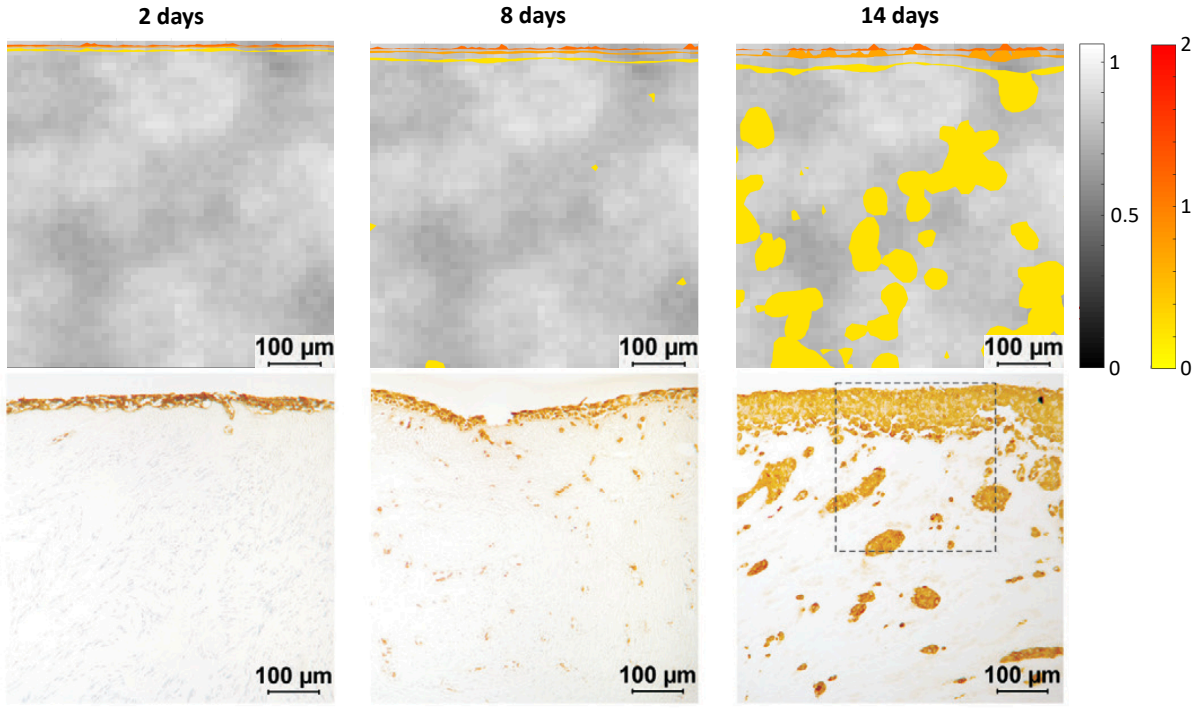

Figure 6.4: ***HSC-3 myoma invasion simulations and experimental results.*** *The spatiotemporal evolution of an initially uniformly dense epithelial-like cancer cell population placed on top of an ECM of heterogeneous density is depicted after 2, 8 and 14 days (left to right). Sample simulation results are shown in the top row of panels and corresponding experimental results of HSC-3 myoma invasion assays by Nurmenniemi et al. (2009) in the bottom row. All panels show slices of a three-dimensional assay of* $6\,\mu\mathrm{m}$ *thickness. The density of the epithelial-like cancer cells is represented via yellow and orange isosurfaces corresponding to the outer colour bar. We have chosen to present the isosurfaces corresponding to 0.1, 0.75 and 1.5 of the average tumour density for reasons explained in Section 6.4. The heterogeneous ECM density (grey) corresponds to the inner colour bar. EMT spawns mesenchymal-like cancer cells (not depicted here), which are able to invade the ECM via haptotaxis and thus much more rapidly than the slowly diffusing epithelial-like cancer cells at the cost of proliferative potential. The reverse process, MET, creates the 'islands' of epithelial-like cancer cells observed in the middle and right panels corresponding to days 8 and 14. These eventually reconnect with the invading tumour mass, as shown in the top left of right panels, which correspond to results on day 14. Bottom row of panels is modified from Nurmenniemi et al. (2009) with permission from Elsevier.*

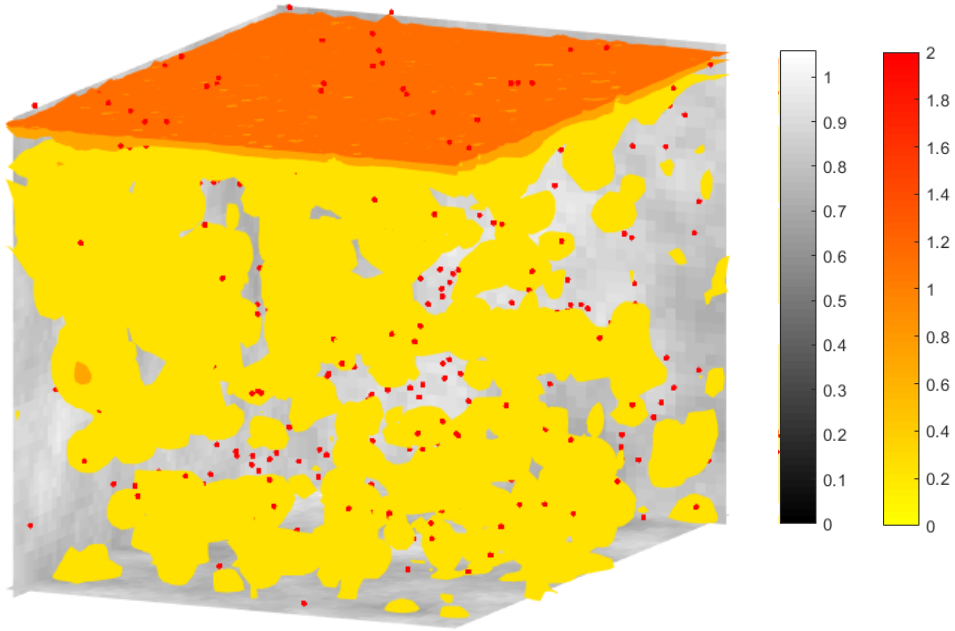

Figure 6.5: ***HSC-3 myoma invasion simulation results in 3D.*** *A sample simulation result of a HSC-3 myoma invasion assays of dimensions* $8500\,\mu\text{m} \times 8500\,\mu\text{m} \times 8500\,\mu\text{m}$ *after 14 days is shown. The ECM of non-uniform density, colouring of which corresponds to the first colour bar, is shown in the background. Epithelial-like cancer cell densities are visualised through contour plots in correspondence with the second colour bar. Mesenchymal-like cancer cell particles are represented by red dots.*

to equations (6.1.1)–(6.1.3). Primarily due to its diffusion term, equation (6.1.1) causes a slight propagation of the epithelial-like cancer cell front. This becomes most apparent in the earlier stages of the time evolution—before new islands are formed, which also contribute to the tumour growth. At the same time, EMT takes place and gives rise to isolated mesenchymal-like cancer cells, which are represented by particles. These are shown as red dots in Figure 6.5. However, the mesenchymal-like cancer cell particles are omitted in the top row of panels of Figure 6.4 to mimic the staining for epithelial markers in the corresponding panels that show the experimental findings by Nurmenniemi et al. (2009) in the bottom row of panels of the same figure. The migration of the particles takes the form of a random haptotaxis-biased motion, which is modelled by the system of SDEs in equation (6.1.7). During their invasion of the ECM, these particles, which represent mesenchymal-like cancer cells, undergo MET with a probability rate described in Table 6.1. This gives rise to islands consisting of epithelial-like cancer cells away from the non-invasive cell area on top of the ECM. These epithelial-like cancer cell islands are now described by a density profile and their spatiotemporal evolution is hence once again modelled through the continuum model in equations (6.1.1)–(6.1.3). Growth of these islands results in one of the following phenomena:

- The islands may merge with the upper layer of epithelial-like cancer cells on top of the ECM if they are sufficiently close to the top of the assay. This causes the non-invasive cell layer to grow rapidly.

- The islands become part of the invading cell area if they are placed at a sufficiently large distance from the top of the ECM.

Figure 2.23 describes the definition of the invading versus non-invading cell area as applied in the analysis of the experimental results by Nurmenniemi et al. (2009)—and hence also in the analysis of our simulation results—in more detail.

6.4 Discussion

Through the computational simulations we carried out, we found that our three-dimensional hybrid discrete-continuum model of EMT- and MET-dependent cancer cell invasion provides qualitatively and quantitatively biologically realistic outcomes. The spatiotemporal evolution of the cancer cell invasion in the experimental organotypic assays by Nurmenniemi et al. (2009) was predicted realistically. In this section, we will discuss some issues regarding the visualisation of the simulation results. We continue by describing the insights to our model that we have won through our sensitivity analysis. From this, we derive conclusions about the impact of various parameters in the model.

Visualisation of the 3D model

Regarding the visualisation of the top row of panels in Figure 6.4, we had to choose which isosurfaces to show due to the three-dimensional nature of the problem. Due to the diffusion term included in equation (6.1.1), as well as typically in all deterministic macroscopic models of cancer invasion, the entire domain is covered with some—even negligibly small—tumour cell density. As a result, the thresholds for the visualisation of all isosurfaces are required to be set—including, arguably most crucially, the threshold for the lowest isosurface, which is shown in yellow in Figure 6.4. For this, we computed the average cell—and hence tumour—density, which is

$$d_T = \frac{m_{\mathsf{ref}}}{|V_0|} = 1$$

for the parameters in Table 6.1. We then visualised the isosurfaces at $0.1d_T$, $0.75d_T$ and $1.5d_T$. Similarly, visualisation methods of experiments are also subject to overlooking phenomena that are below some threshold which can be accounted for.

Insights from the parameter sensitivity analysis

The simulations shown in Figure 6.4 were run using the estimated parameter values in Table 6.1. As described in Section 6.2.3, these values were obtained by minimising the error between our simulation results and the experimental results with respect to the maximal invasion depth of the epithelial-like cancer cells, as well as their total non-invasive and invasive area. For the experiments in Nurmenniemi et al. (2009), these were measured as explained in Section 2.5.4 and Figures 2.22 and 2.23 in particular. The quantification of the experimental results after 14 days was visualised in Figure 2.21, yielding a median of $5.4700 \times 10^{-2}\,\mu\mathrm{m}$ for the maximal invasion depth of the epithelial-like cancer cells, and of $3.5270 \times 10^{-4}\,\mu\mathrm{m}^2$ and $3.6710 \times 10^{-4}\,\mu\mathrm{m}^2$ for their total non-invasive and invasive

area, respectively. Through the parameter estimation of the values used in Table 6.1, we obtained $7.0130 \times 10^{-2}\,\mu\text{m}$, $3.9884 \times 10^{-4}\,\mu\text{m}^2$ and $3.0398 \times 10^{-4}\,\mu\text{m}^2$, respectively. Note that the maximal invasion depth in the experiments of Nurmenniemi et al. (2009) was the mean of the three epithelial-like cancer cells that had invaded the domain the furthest. To ensure to work as closely to the experimental measurements as possible, we adapted this approach when measuring our simulation outcomes.

To perform the measurements from our simulations, we started with the three-dimensional part of the epithelial-like tumour density profile. From this, we extracted nine vertical slices from the middle of the domain. For every slice, we identified the non-invading area of the tumour, which is defined as the upper connected part of the epithelial-like density profile. Computationally, areas of the domain are connected if there exists a path within the epithelial-like density profile that connects occupied computational cells. Thus, the non-invading area that is occupied by epithelial-like cancer cells in each slice is determined.

By subtracting the non-invading area of the tumour from the area of overall epithelial-like density profile, we then identified the invading area of the tumour. We computed the area that this part of the tumour occupies as well as the maximum invasion depth. The latter is given by the mean of the three computational cells with the lowest z-value that are occupied by epithelial-like cancer cell density. The invasion depth is measured as the shortest distance between the respective invading cell and the lower boundary of the non-invasive area, parallel to the vertical z-axis.

Finally, the invasion index is computed using the formula (2.5.4) that is proposed to measure the experiments in Nurmenniemi et al. (2009), i.e.

$$\text{invasion index} = 1 - \frac{\text{non-invading area}}{\text{invading area} + \text{non-invading area}}.$$

These computed quantities are next compared to the experimental data. As absolute errors that would result from the differences between the experimental and simulation measurements provided above are not directly comparable due to e.g. differences in units, we compute the (unit-less) relative errors e_1, e_2 and e_3 instead by dividing the absolute errors by the mean of the experimental measurement. Through addition of the errors and subsequent division by 3, we determined the L_1 *mean relative error*, which was 0.2558. We further determined the relative *root mean square* (RMS) error

$$\sqrt{\frac{1}{3}\sum_{n=1}^{3} e_n^2}, \tag{6.4.1}$$

which is commonly used in biological problems of this type and took value 0.2959. Due to the stochasticity involved in our model, these errors can vary between simulations even when the same parameters are explored. The obtained measurements were fairly satisfactory given the dimension and the stochasticity involved in our model and therefore no formal statistical analysis was performed at this stage.

We also used the RSM error for our sensitivity analysis. As explained in Section 6.2.3, we can compute the local sensitivity of the model by varying each of the originally unknown model parameters $\mathcal{P}^{sens} = \left\{\lambda_w, \sigma, \mu, \nu_{\mathsf{E}}, \nu_{\mathsf{M}}\right\} \overset{\text{def.}}{=} \left\{p_i^{\text{sens}},\ i = 1, ..., 5\right\}$—one after the

other—around its respective reference value p_i^{ref}. In this thesis, we computed the backward and forward sensitivity gradients by taking, respectively. Through this, we gained two pieces of information:

- The signs of the backward and forward gradients indicate whether the reference value p_i^{ref} is (close to) the minimiser. A combination of negative- and positive-signs implies that the sensitivity decreases and increases around the reference value p_i^{ref}.
- The magnitude of the two gradients indicates how sensitive the result is to the variation of this parameter p_i and to which direction it should be varied to minimise the result even more.

In our case, this analysis step is carried out with respect to the RMS error (6.4.1). In what follows, we give details of the respective sensitivity gradients and explain the results.

The parameter sensitivity analysis results for the ECM degradation rate ($p_1^{\text{sens}} = \lambda_w$) are shown in Figure 6.6a. The sensitivity gradients were -110.2882 and 80.5483, respectively, for the experiments run with, *ceteris paribus*, values $0.5p_1^{\text{ref}}$ and $2p_1^{\text{ref}}$—instead of $p_1^{\text{ref}} = 1.8383 \times 10^{-4}\,\text{M cm}^{-3}\text{d}^{-1}$. The change in the sign of the sensitivity gradients implies that the minimum of the RMS error is attained around the reference value p_1^{ref}. This is an indication that the reference parameter was sufficiently well estimated. Furthermore, the strong gradients imply that the RMS error is quite sensitive to the ECM degradation rate.

Figure 6.6b shows the results from the parameter sensitivity analysis for the mesenchymal-like cancer cell particle diffusion coefficient ($p_2^{\text{sens}} = \sigma$). The sensitivity gradients were 0.0033 and 0.0032, respectively, for the experiments run with, *ceteris paribus*, values $0.5p_2^{\text{ref}}$ and $2p_2^{\text{ref}}$—instead of $p_2^{\text{ref}} = 3.3675\,\text{cm d}^{-\frac{1}{2}}$. The two positive signs imply that the error increases as the parameter value increases. This should serve as an indication to reduce the reference parameter value $p_2^{\text{ref}} = 3.3675\,\text{cm d}^{-\frac{1}{2}}$ and to perform the sensitivity analysis again thereafter and re-evaluate. However, as the magnitude of the gradient—and hence the sensitivity of the RMS error to the variation in the particle diffusion coefficient—is small, no strong benefit is to be expected from this repeated minimisation of the RMS error. Hence, we conclude that the reference parameter value p_2^{ref} is acceptable.

In Figure 6.6c, the results from the parameter sensitivity analysis for the mesenchymal-like cancer cell particle drift coefficient ($p_3^{\text{sens}} = \mu$) are presented. -0.3658 and 0.2830 were the sensitivity gradients for the experiments run with, *ceteris paribus*, values $0.5p_3^{\text{ref}}$ and $2p_3^{\text{ref}}$—instead of p_3^{ref}—respectively. As in the case of the ECM degradation rate, the change in sign indicates that the minimiser of the RMS error is (close to) the reference value $p_3^{\text{ref}} = 7.4595 \times 10^{-2}\,\text{d}^{-1}$. However, by direct comparison, we deduce that the RMS error is less sensitive to this parameter than to the ECM degradation rate.

The results of the parameter sensitivity analysis for the EMT rate ($p_4^{\text{sens}} = \nu_{\mathsf{E}}$) are shown in Figure 6.6d. The sensitivity gradients were -3.3807 and 8.2855, respectively, for the experiments run with, *ceteris paribus*, values $0.5p_4^{\text{ref}}$ and $2p_4^{\text{ref}}$—instead of $p_4^{\text{ref}} = 7.502 \times 10^{-2}\,\text{M cm}^{-3}\text{d}^{-1}$. Again, the change in sign indicates that the minimiser of the RMS error is attained around the reference value $p_4^{\text{ref}} = 7.502 \times 10^{-2}\,\text{M cm}^{-3}\text{d}^{-1}$. Moreover, the RMS error is more sensitive to the EMT rate than it is to particle adhesion coefficient but less sensitive than it is to the ECM degradation rate.

Finally, the results of the parameter sensitivity analysis for the MET rate ($p_5^{\text{sens}} = \nu_{\mathsf{M}}$) are shown in Figure 6.6e. The sensitivity gradients were -0.2091 and 0.2201, respectively,

Figure 6.6: ***Sensitivity analysis results.*** *For each of the five estimated parameters* $\mathcal{P}^{\text{sens}} = \{\lambda_w, \sigma, \mu, \nu_{\text{E}}, \nu_{\text{M}}\} \overset{\text{def.}}{=} \{p_i^{\text{sens}},\ i = 1, ..., 5\}$*, the relative 'root mean square' (RMS) error* (6.4.1) *was computed for 20 simulations of the experiment. In each plot, the results obtained from the reference parameter set* $\mathcal{P}^{\text{ref}}$ *are shown (green), as well as results from parameter sets with the decreased (red) and increased (blue) parameter values,* $0.5p_i^{\text{ref}}$ *and* $2p_i^{\text{ref}}$*, respectively. Throughout, the means are represented by a horizontal dashed line in the respective colour. For result interpretation, see text.*

(a) ***ECM degradation rate*** *(*$p_1^{\text{sens}} = \lambda_w$*).*

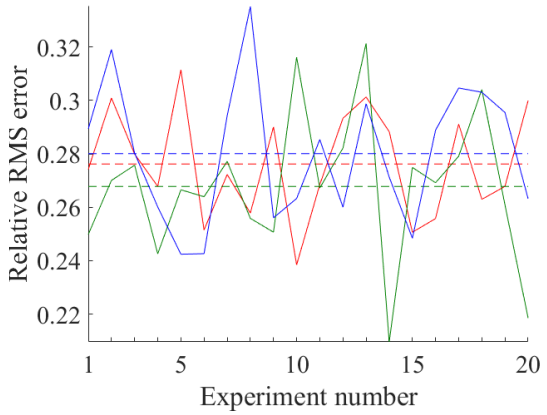

(b) ***Particle diffusion coefficient*** *(*$p_2^{\text{sens}} = \sigma$*).*

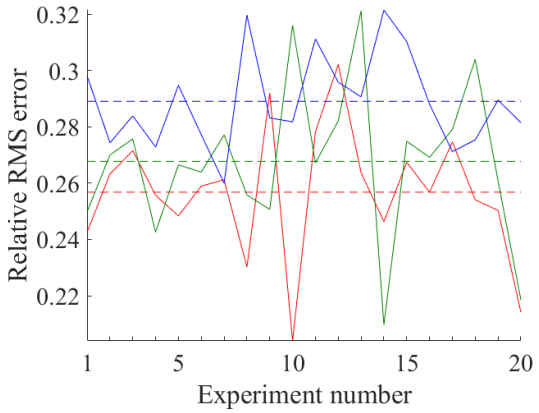

(c) ***Particle adhesion coefficient*** *(*$p_3^{\text{sens}} = \mu$*).*

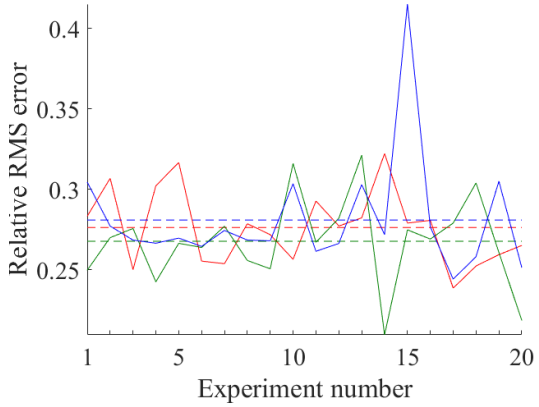

(d) ***EMT rate*** *(*$p_4^{\text{sens}} = \nu_{\text{E}}$*).*

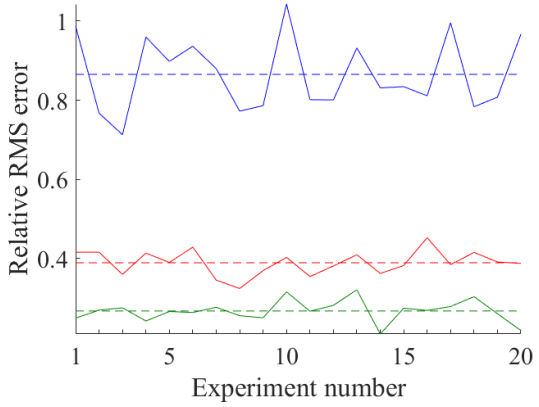

(e) ***MET rate*** *(*$p_5^{\text{sens}} = \nu_{\text{M}}$*).*

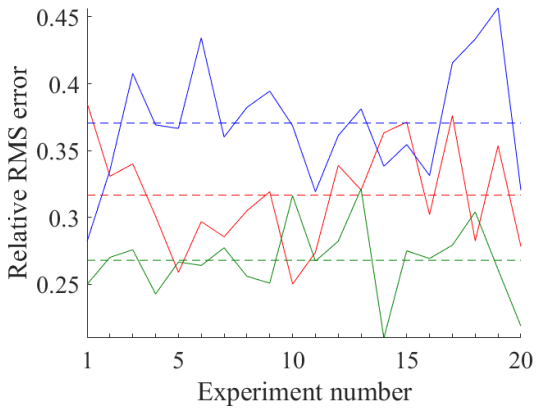

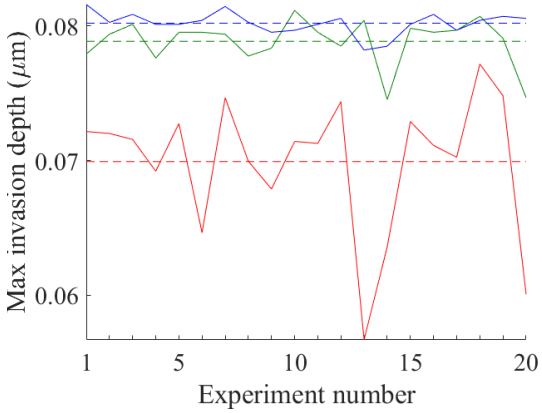

Figure 6.7: ***Sensitivity analysis for particle diffusion coefficient against maximal invasion depth of the epithelial-like cancer cells.*** *For the estimated parameter* $p_2^{\text{sens}} = \sigma$*, the maximal invasion depth of the epithelial-like cancer cells was computed for 20 simulations of the experiment. In the plot, the results obtained from the reference parameter set* $\mathcal{P}^{\text{ref}}$ *are shown in green; the results from parameter sets with the decreased and increased parameter values* $0.25p_2^{\text{ref}}$ *and* $4p_2^{\text{ref}}$*, respectively, are shown in red and blue, respectively. The means were computed and represented by a horizontal dashed line in the respective colour. For result interpretation, see text.*

for the experiments run with, *ceteris paribus*, the values $0.5p_5^{\text{ref}}$ and $2p_5^{\text{ref}}$—instead of $p_5^{\text{ref}} = 4.7697 \times 10^{-1}$ d^{-1}. As before, the change in sign indicates that the minimiser of the RMS error is (close to) the reference value $p_5^{\text{ref}} = 4.7697 \times 10^{-1}$ d^{-1}. Moreover, the RMS error is less sensitive to the MET rate than it is to the ECM degradation rate, the particle adhesion coefficient, and to the EMT rate parameters.

In summary, the sensitivity analysis showed that the parameter values P^{sens} that we determined as a result of the parameter sensitivity analysis (see Table 6.1) are sufficiently close to the minimiser of the RMS error and hence a good fit to our model. Furthermore, the RMS error shows different degrees of sensitivities to the parameters. If we order the five parameters from least to highest sensitivity, we get: particle diffusion coefficient, MET rate, particle adhesion coefficient, EMT rate, ECM degradation rate.

Note that we have performed our sensitivity analysis with respect to the relative RMS error, which consisted of the maximal invasion depth of the epithelial-like cancer cells, as well as of the non-invasive and invasive area—all with equal weights, as we described at the beginning of this section. We decided to minimise the total RMS error (6.4.1) rather than just one of these three values to take into account all of the quantitative output provided in Nurmenniemi et al. (2009). If we perform the sensitivity analysis against one of these three quantities only, rather than against the complete error, we can learn more about how this particular quantity changes as a particular parameter is varied, which provides us with further insights. Figure 6.7 shows an example of this kind of result—the reference particle diffusion coefficient p_2^{ref} (green line) is decreased and increased and computed against the maximal invasion depth of the epithelial-like cancer cells. The plot shows that increasing the particle diffusion coefficient to $4p_2^{\text{ref}}$ (blue line) only slightly increases the maximal invasion depth. However, a smaller particle diffusion coefficient of $0.25p_2^{\text{ref}}$ (red line) corresponds to a comparatively much stronger decrease

in invasion depth, which arises due to the lower cell motility. As a result, we obtain an average maximal invasion depth closer to the median of 5.4700×10^{-2} µm measured experimentally by Nurmenniemi et al. (2009). When linking this back to the results from the parameter sensitivity analysis that accounted for the relative RMS error rather than solely for the maximal invasion depth, which is shown in Figure 6.6b, we find that decreasing the particle diffusion coefficient does not benefit us significantly in our aim to approximate the RMS error against experimental data.

Chapter 7

Perspectives

In this thesis, we have established a first framework for modelling both the invasion and the metastatic spread of cancer cells in a cell-based, spatially explicit manner in Chapter 4. In this initial outline of the model, we have focussed on capturing the main steps involved in the invasion-metastasis cascade. This framework can be developed in many ways to include further biological detail.

To give an example of this, we have extended the model to additionally account for transitions of cancer cells between an epithelial, a partial-EMT and a mesenchymal phenotypic state in Chapter 5. Moreover, we have included the phenomena of cell death and dormancy due to suboptimal adaptivity of metastasised cancer cells to the new tumour microenvironments at secondary sites. Finally, in agreement with biological data, we have differentiated the tissue for different organs in our simulations in this chapter.

Further possible future extensions to the model are elucidated in Section 7.1. Also, one idea for future work—the representation of the fitness of cells of different phenotypes according to their adaptivity to their (potentially spatiotemporally varying) local environment by using game theory—is elaborated in detail in an initial model in Section 7.2 with corresponding sample simulation results.

In Section 7.3, we explore future work related to the three-dimensional hybrid model of cancer invasion that explicitly takes into account the transition from collectively invading epithelial-like cancer cells to individually invading mesenchymal-like cancer cells, which we introduced in Chapter 6.

7.1 Extensions to the metastasis modelling framework

With regards to future extensions of the metastasis model introduced in Chapter 4, which we further extended in Chapter 5, the inclusion of a third spatial dimension would further enhance the model's attention to biological detail. We have not prioritised this in the early-stage development of this invasion-metastasis cascade modelling framework as we believe that this would not change the overall characteristics of the model's qualitative insights.

Biomechanical properties are also not yet accounted for in this modelling framework but are important, especially for processes such as intravasation, travel through the vasculature and extravasation. For this reason, we are planning to couple our modelling framework to a biomechanical haemodynamics model.

To create an organ-specific model, we have taken into account differences in the local tumour microenvironment of primary and secondary organs in the body in two ways. Firstly, we distinguished between the relative differences in ECM density between the organs according to biological measurements in (ICRP, 2009). Secondly, we aligned the relative likelihood of successful secondary spread to the organs in our model to the metastatic transition probabilities of breast cancer from large patient studies (Kuhn Laboratory, 2017). This is, of course, a simplification of the actual physiology in many ways. For instance, in reality, differences between organs are not limited to the relative densities of their ECM. As explained in detail in Barney et al. (2016), the tissue-specific differences in the tumour microenvironment found in the organs are manifold and only marginally established. They include, for instance, the genetic markers associated with tissue-specific metastasis, the healthy cells typically found in these tissues, the ECM stiffness and protein composition, and the tissue dimensionality. Further, these and other features will not only differ between organs but also when considering the same organ in any number of patients. Also, the tumour microenvironments have been shown to change with time. They could thus be modelled as a landscape that evolves over time to capture e.g. the process of pre-metastatic niche formation that has been observed both in mouse models and clinical studies (McAllister and Weinberg, 2014). For this reason, it is our long-term goal to include the metastatic programmes of the various organs in our model once more is known about them. Until then, we will continue using the transition probabilities from a large study such as (Kuhn Laboratory, 2017) to differentiate between the relative success of metastatic spread to the various organs.

Often, solitary DTCs and micrometastases are non-proliferating, or *dormant*, even years after primary tumour diagnosis (Luzzi et al., 1998; Chambers et al., 2002; Pantel and Speicher, 2016). In fact, in the aforementioned experiments by Luzzi et al. (1998) on liver metastases in mice, examination of the liver tissue after two weeks after the intraportal injection of cancer cells showed that 95 % of all solitary DTCs were dormant but only 3.3% of the cells in tumours, which were of cross-sectional size 0.45×0.15 mm to 2.8×1.4 mm. Other cells may not survive due to activation of the immune system at the secondary sites. In our current model, dormant and apoptotic DTCs are accounted for through grid- and phenotype-unspecific probabilities only. Furthermore, we do not distinguish between cells at secondary sites that are part of a growing tumour and those that are solitary DTCs with regards to the probability of death and dormancy. We could include cancer cell dormancy and immune system activation at secondary sites more explicitly as part of the above-mentioned extension in the organ-specific differentiation of the respective organ tissue. This way, it could be studied in more detail how these changes in the microenvironment of dormant cancer cells over time affect growth activation of previously latent micrometastases, which was suggested, amongst others, by McAllister and Weinberg (2014).

Breast cancer cell intravasation and dissemination occurs through a *tumour microenvironment of metastasis* (TMEM)-mediated mechanism. TMEMs are microanatomical structures consisting of three different cell types that are in direct physical contact with one another (Karagiannis et al., 2017). Since we model individual cell dynamics, our framework can easily be adapted to model TMEM involvement in metastatic spread of breast cancer by including an additional cancer cell type and calibrating its phenotype.

In the current modelling approach, we account for the fact that EMT and MET have

been observed to occur in specific steps of the invasion-metastasis cascade as well as in specific locations within the primary tumour. For instance, partial EMT appears to be triggered predominantly at the primary site and towards the tumour boundary as observed *in situ*—see Figure 2.16 and Puram et al. (2017). Also, in the early stages of colonisation at a secondary site, MET has been found to be the predominant mutation. It would be desirable to additionally include a *physiological* motivation for the mutations we model, like e.g. developed in Sfakianakis et al. (2017). In particular, we aim to incorporate the physiological motivation by accounting for the role of hypoxia as a trigger for EMT and MET as described below. While the full spectrum of mechanisms underlying the induction of EMT remains elusive to date (Wang et al., 2016), it is assumed that tumour-induced hypoxia plays an important role in the process (Imai et al., 2003; Yang et al., 2008; Wang et al., 2016; Petrova et al., 2018). The hypoxic environment in the tumour activates its main effector *hypoxia-inducible factor-1* (HIF-1) (Petrova et al., 2018), which in turn activates EMT-TFs like Snail and Twist (Imai et al., 2003; Yang et al., 2008), thus promoting EMT and metastatic phenotypes. A biological model that connects the occurrence of tumour-induced hypoxia with EMT and angiogenesis via CAFs has recently been proposed in Petrova et al. (2018). The hypothesis is made that rapid tumour growth, which reduces the oxygen concentration in tumour and stroma regions far away from vessels since the diffusion of oxygen is limited to 100–200 µm, creates hypoxic regions. Epithelial-like cancer cells in these regions produce signalling molecules that transform normal fibroblasts as well as other healthy cells in the stroma to CAFs (Zeisberg et al., 2007; Petrova et al., 2018). These CAFs have been shown to produce stiff aligned ECM. This differently organised ECM is, in turn, hypothesised to induce EMT in premalignant epithelial cells and to support cell migration in breast cancer (Dumont et al., 2013). CAFs have further been shown to promote angiogenesis via the production of vascular endothelial growth factor-C (VEGF), C-X-C motif chemokine 12 (CXCL12) and basic fibroblast growth factor (FGF-2) (Pietras and Östman, 2010), making hypoxia an angiogenic stimulus (Carmeliet and Jain, 2000). Our modelling framework meets the prerequisites for an extension that includes the biological phenomena described above. Therefore, in future work, we will connect the EMT features currently included in the metastasis framework with the prevalence of tumour-induced acutely and chronically hypoxic regions as well as with angiogenesis.

Including tumour-induced angiogenesis as a result of hypoxia in the framework would furthermore allow to capture metastatic growth beyond the current avascular stage and to thus include the development of larger, vessel-growth activating (macro-)metastases. Incorporating tumour-induced angiogenesis in our framework would also allow us to include reseeding in a more realistic manner. In this thesis, we have investigated the classic, unidirectional view of metastatic progression. However, it is hypothesised that *self-seeding* from primary to primary tumour, *primary reseeding* from a metastatic site back to the primary tumour, and *metastatic reseeding*, where metastases form out of existing metastases, also play a role in metastatic spread. These processes could easily be included in this modelling framework, in particular in the context of allowing for colonisation by considering tumour-induced angiogenesis at the secondary sites. Of course, we could also replace the currently static initial vessel distribution by including vascular growth resulting from tumour-induced angiogenesis. For this, an earlier attempt by Powathil et al. (2012) to model the transportation of oxygen to the tumour through newly formed vessels

as well as hypoxia-induced quiescence of cancer cells could be modified and extended.

For ethical reasons, modern-day data concerning metastatic spread, such as those by the Kuhn Laboratory (2017), stem from studies in which the primary tumours were removed prior to the observations of when the tumour would reoccur or present detectable metastases. We could easily modify our model to include both successful resections of the primary tumour and/or of metastases as well as tumour resections that accidentally leave a small residue of cancer cells. Finally, we could model resections at various times to examine the effects of delayed surgical interventions on the disease outcome. Additionally, other treatment regimes could be modelled. One example is the inclusion of chemotherapy in the framework, especially once have we account for angiogenesis, in a similar way to (Powathil et al., 2012, 2013). Other approaches to modelling chemo-, radio-, nano- and immunotherapy, as well as targeted, hormone and combination therapy have recently been reviewed by Chamseddine and Rejniak (2019). Some of these could function as a basis to modelling treatment approaches by extending this framework.

Finally, the effect of mutations on cell phenotypes can easily be included in this cell-based modelling framework, as shown in Chapter 5. In this context, the biological observation that mesenchymal-like, partial-EMT and epithelial-like phenotypes occur on a spectrum rather than as three discrete states (Campbell, 2018) is another detail that could be included in the framework. Existing spatial models that consider multiple or continuous phenotypic states of cancer cells include (Lorz et al., 2015; Świerniak and Krześlak, 2016; Domschke et al., 2017; Lorenzi et al., 2018). Game theory could be applied to study the competition and hence evolution of cell phenotypes in the various local environments that evolve over time (*cf.* pre-metastatic niche formation) in the body. In the next section, some preliminary work to incorporating spatial game theory into our metastasis framework will be introduced.

7.2 Using game theory to capture interactions of cells of different phenotypes in various tumour microenvironments—an initial model

Game theory has its roots in economics. It was first used by Antoine Cournot to analyse the economic phenomenon of the duopoly (Cournot, 1838). Over 100 years later, the mathematician John von Neumann and the economist Oskar Morgenstern first formalised the theory mathematically in their classic book *Theory of games and economic behaviour* (Von Neumann and Morgenstern, 2007).

Economic game theory formally studies cooperation and conflict between several interdependently interacting agents. In his book *Game Theory: Analysis of Conflict*, Roger Myerson defines it as 'the study of mathematical models of conflict and cooperation between intelligent rational decision-makers' (Myerson, 2013). Understanding the interactions of rational decision-makers in an environment defined by scarce resources using the formalised language of game theory can underpin strategic decision-making. The impact of game theory has, however, not remained limited to economics. Social scientists and scientists from various fields such as psychology, political science, logic, computer science and biology soon also found a useful analytic tool in game theory (Myerson, 2013).

Problems that have been tackled using game theory since include, for instance, choosing the optimal policy for a presidential candidate, finding the best vaccination policy, salary negotiations (Von Neumann and Morgenstern, 2007) as well as population dynamics in ecology, which is also known as *evolutionary game theory* (EGT). Early EGT models did not consider spatial dimensions but well-mixed populations instead. However, it was established in Nowak and May (1992, 1993); Nowak et al. (1994); Durrett and Levin (1994) that the inclusion of spatial effects can change the outcome of a game compared to the corresponding well-mixed scenario. In particular, accounting for spatial dimensions can lead to the long-term stable coexistence of species in cases where, in the well-mixed game-theoretic scenario, coexistence cannot occur.

The concept of including game theory in the metastasis framework introduced in this section is based on the preliminary non-cancer-specific multi-grid model published in Burgess (2013); Burgess et al. (2016, 2017). However, EGT has already found applications in the context of cancer, most of which focus on the selection for certain tumour phenotypes. Several papers that model malignant tumour growth were reviewed in Hummert et al. (2014). In particular, Anderson et al. (2009) used EGT to study the evolution of aggressive cancer cell phenotypes. The go-or-grow dichotomy observed to occur between cancer cell phenotypes was examined in a non-spatial manner in Mansury et al. (2006) and spatially defined as occurring on a fixed lattice of a graph in Basanta et al. (2008a). Basanta et al. (2008b) and Archetti (2014) modelled the effect of differences between the metabolic pathway of cancer cells and normal cells, which is known as the *Warburg effect*, and Basanta et al. (2012) modelled interactions between tumour cells and healthy cells. Models by Tomlinson and Bodmer (1997) and Bach et al. (2001) were concerned with angiogenesis via growth factor production by cancer cells—the Tomlinson and Bodmer (1997) model was later extended in Bach et al. (2003) to become one of the early models that considered *spatial* EGT. The review by Hummert et al. (2014) concluded that applications of EGT to date had predominantly been used to examine the role of interactions between individual cells as well as, linked to this, the emergence of new phenotypic traits. Moreover, the authors remarked that most cancer-specific EGT models at the time had not accounted for space—despite the discovery of the importance of spatial dimensions for the game-theoretic outcomes in evolutionary games in a general, non-cancer-specific setting about a decade before the publication of the review. Instead, the majority of cancer-specific publications considered a well-mixed population of cells, often expressed in terms of proportions rather than absolute numbers of cells.

Since then, a few papers have used *spatial* EGT in the context of cancer modelling. For instance, Kaznatcheev et al. (2015) presented cancer dynamics as an evolutionary game between two cell phenotypes. In line with the go-or-grow dichotomy, rapidly proliferating cancer cells were considered alongside invasive cancer cells. These invasive cells arose from the former via mutations that were triggered by differences in environmental factors. In particular, spatial structure—as anatomically found in the neighbourhood of static boundaries representing e.g. blood vessels or basement membranes—promoted the invasive phenotype in this model. This led the authors to the conclusion that the local neighbourhood structure has important effects in game-theoretic modelling and that these would be overlooked when only considering scenarios including well-mixed populations.

You et al. (2017) analysed a spatial game of metastatic castrate-resistant prostate cancer in the form of a spatially-explicit agent-based approach. They also examined how

this game compared to the corresponding non-spatial game. Because for almost all their case studies the predictions of the spatial model differed from those of a non-spatial one and because of the intrinsic spatial heterogeneity within tumours, they concluded that spatial cancer models are likely needed to capture the key elements of tumour growth.

Given the effects observed from the inclusion of space in non-cancer-specific EGT models, we agree with Hummert et al. (2014); Kaznatcheev et al. (2015); You et al. (2017); Zhang et al. (2017): To study tumourigenesis—which is intrinsically spatially heterogeneous as tumours do not consist of well-mixed cell populations—appropriately with EGT, spatial effects should be taken into account. If space *is* taken into account, EGT can be a powerful tool to study the long-term spatial evolution of cells of different phenotypes in various physiological locations. These can, for instance, be organs where primary and secondary tumours form in the body, as our initial model in the next section elucidates.

7.2.1 Model setup

For our initial model, we consider the spatiotemporal evolution of cells of two different phenotypes, A and B. When relating the model to the setting of cancer invasion and metastasis, the cell types could, for instance, represent cancer cells and healthy cells. The cells move on a spatial domain $\Omega \subset \mathbb{R}^2$ by random diffusion only, which corresponds to the cells performing an unbiased random walk in the discretised model. The ECM density and the MDE concentrations accounted for previously in the metastasis framework in Section 4.1 are not included at this point.

As in Section 4.1, the movement of the cells of the two phenotypes A and B is obtained via the FTCS discretisation of the respective PDEs, which are

$$\frac{\partial c_k}{\partial t} = \overbrace{D_{c_k} \nabla^2 c_k}^{\text{random motility}}, \tag{7.2.1}$$

where $k = \mathsf{A}, \mathsf{B}$, along with reflective boundary conditions. Here, $D_{c_k} > 0$ is the constant cell diffusion coefficient for cells of type A and B, respectively.

Again, analogously to Section 4.1, we fix a time step Δt and set $t_n = n\Delta t$. We choose a square domain, which we discretise using a uniform mesh of grid cells with size $\Delta x = \Delta y = \frac{1}{l}$. Furthermore, we set $x_i = i\Delta x$ and $y_j = j\Delta y$, where $i, j \in [0, l] \subset \mathbb{N}_0$. We continue by expressing the number of cells of type A and B on grid point (x_i, y_j) at time t_n by ${c_{\mathsf{A}}}_{i,j}^{n}$ and ${c_{\mathsf{B}}}_{i,j}^{n}$, respectively. The resulting discretised equation is then solved for $c_{i,j}^{n+1}$, the number of cancer cells at grid point (x_i, y_j) at time t_{n+1}. Finally, substituting $\Delta x = \Delta y$ yields the discretised equations

$$c_{ki,j}^{n+1} = \mathcal{P}_0 c_{ki-1,j}^{n} + \mathcal{P}_1 c_{ki+1,j}^{n} + \mathcal{P}_2 c_{ki,j+1}^{n} + \mathcal{P}_3 c_{ki,j-1}^{n} + \mathcal{P}_4 c_{ki,j}^{n},$$

where

$$\begin{aligned}
\mathcal{P}_0 : \mathcal{P}^n_{i-1,j} &:= D_{c_k} \frac{\Delta t}{(\Delta x)^2}, \\
\mathcal{P}_1 : \mathcal{P}^n_{i+1,j} &:= D_{c_k} \frac{\Delta t}{(\Delta x)^2}, \\
\mathcal{P}_2 : \mathcal{P}^n_{i,j+1} &:= D_{c_k} \frac{\Delta t}{(\Delta x)^2}, \\
\mathcal{P}_3 : \mathcal{P}^n_{i,j-1} &:= D_{c_k} \frac{\Delta t}{(\Delta x)^2}, \\
\mathcal{P}_4 : \mathcal{P}^n_{i,j} \quad &:= 1 - 4D_{c_k} \frac{\Delta t}{(\Delta x)^2}.
\end{aligned}$$

The coefficients $\mathcal{P}_0, \mathcal{P}_1, \mathcal{P}_2$ and $\mathcal{P}_3$ correspond to the probabilities that, during the next time step, a cancer cell at grid point (x_i, y_j) moves left, right, up and down, respectively. $\mathcal{P}_4$ is the probability that a cancer cell remains at grid point (x_i, y_j) during the next time step. Subsequently, the movement submodel—as outlined in bullet points 1. to 5. in Section 4.1 but with the obvious adjustment that ECM density and MMP-2 concentration are not considered in this early stage of model development—is applied.

As in Section 4.1, the proliferation rules are added onto the discrete model. Only this time, proliferation is a result of the local interaction of cells, which is represented through game theory. As soon as there are two or more cells from either species on the same grid point, each cell performs up to one interaction per time step with another cell. If there are exactly two cells on the same grid point, they interact; if there are three, two randomly chosen ones interact; if there are four cells, two pairs—chosen at random—interact exactly once; and so on. Self-interaction does not exist in this model. All cells enter the model with a payoff of 0 but as a result of these interactions, the cells accumulate payoff. The payoff from a single interaction with another cell is phenotype-specific (Table 7.1 shows an example). Once a cell's accumulated payoff is larger than or equal to 1, it produces one offspring cell of its phenotype on the grid point that it is located on and its own payoff is reduced by 1. This is also known as *non-synchronous generation* (as opposed to *synchronous generation* where the accumulated payoff is translated into offspring at a certain point in time, for example when a cell dies). Finally, cells die after a set amount of T_D time steps.

7.2.2 Implementation

We considered four scenarios. In all scenarios, the spatial domains were taken to be of size $[0, 1] \times [0, 1]$. We took $\Delta t = 0.05$ and $\Delta x = \Delta y = \frac{1}{l}$, where $l = 30$ for *Scenario 1* and *2* and $l = 100$ for *Scenario 3* and *4*. Throughout, each cell had a lifespan of $100\Delta t$. Also, all cells started with a payoff of 0 and accumulated phenotype-dependent payoff from interactions on their grid point as described in Table 7.1. To relate the model to the setting of cancer invasion and metastasis, we chose to consider one type B cell amongst an abundance of type A cells as the initial settings in all our simulations. The initially rare type B cell could, for instance, represent a cancer cell that is found in tissue otherwise containing healthy cells. The healthy cells could be represented by the initially abundant presence of type A cells. A physiological scenario like this could exist either when a

tumour first begins forming at a primary site in the body or as a result of metastatic spread to secondary sites.

For *Scenario 1* and *2*, the initial population consisted of 8999 cells of type A, which were randomly spread out on the grid, and one cell of type B at the centre of the grid.[1] This gave an average of five cells per grid point, like in Burgess et al. (2017), where, however, a square grid with 100 grid cells in each direction together with an initial population of 49999 type A cells and one type B cell was used. For *Scenario 1*, the cells of either phenotype moved to any of the four neighbouring grid points with probability $\mathcal{P}_0 = \mathcal{P}_1 = \mathcal{P}_2 = \mathcal{P}_3 = 0.0000625$ and remained in their position with a probability of $\mathcal{P}_4 = 0.99975$ during a time step. For *Scenario 2*, we took $\mathcal{P}_0 = \mathcal{P}_1 = \mathcal{P}_2 = \mathcal{P}_3 = 0.000125$ and the probability for cells to remain in their position to be $\mathcal{P}_4 = 0.9995$.

For *Scenario 3* and *4*, we had 9999 type A cells spread out randomly on the grid and one type B cell in the middle of the grid. This yielded an average of one cell per grid point. For *Scenario 3*, we used the same movement probabilities as for *Scenario 2*. For *Scenario 4*, we also allowed for the two cell types to have different diffusion coefficients, resulting in type A moving to any of the four neighbouring grid points with probability $\mathcal{P}_0 = \mathcal{P}_1 = \mathcal{P}_2 = \mathcal{P}_3 = 0.0375$, while type B cells did so with probability $\mathcal{P}_0 = \mathcal{P}_1 = \mathcal{P}_2 = \mathcal{P}_3 = 0.075$ during each time step.

Table 7.1: ***Payoff matrix of the game between cells of phenotype*** **A** ***and*** **B.**

	Type A cell	Type B cell
Type A cell	$p_{\mathsf{AA}} = 0.02$	$p_{\mathsf{AB}} = 0$
Type B cell	$p_{\mathsf{BA}} = 0.1$	$p_{\mathsf{BB}} = 0.001$

7.2.3 Results

Exemplary results for *Scenario 1* highlighted that stochasticity plays an important role in the EGT model. The results shown in Figures 7.1 and 7.2 were run using the exact same settings. Yet, in the simulations presented in Figure 7.1, the cells of type B never invaded the tissue but remained on the initial grid point instead. This led to the extinction of this cell type within three generations, i.e. after $300\Delta t$. On the contrary, in Figure 7.2, the cells of type B established themselves for a period that was more than one magnitude larger ($3200\Delta t$). Both cell types coexisted during this period. However, over time, the type B cells locally depleted the type A cells on the grid points which they resided on. It was only when the cells of type B had died out that the cells of type A repopulated the respective area of the grid (see final three panels of Figure 7.2). Yet, both simulations have in common that the type B cells did not establish themselves in the long run, while the type A cells eventually covered the entire grid with an overall stable number of cells that only fluctuated minimally. In future work, we will quantify the effects of the observed stochasticity by analysing the numbers of cells of phenotype A and B and the area occupied by type B cells over time in a larger number of simulations.

[1] We also ran simulations starting solely with type A cells. Type B cells were introduced by random mutations upon offspring generation only. Due to the performance limitations of the MATLAB model, however, we eventually decided to focus on mutations at a later stage.

Figure 7.1: ***First set of sample results for*** **Scenario 1.** *Spatiotemporal evolution of cells of type* A *(left panels) and of type* B *(right panels) after* $0, 100\Delta t, 250\Delta t$ *and* $10000\Delta t$ *is shown. Initially, 8999 cells of type* A *were randomly distributed and one cell of type* B *placed in the centre of the* 30×30 *grid (first row of panels). During each time step, the cells moved to one of four neighbouring grid points with probability* 0.0000625 *and accumulated phenotype-dependent payoffs according to Table 7.1. Each cell had a lifespan of* $100\Delta t$*. Type* B *cells died out after 3 generations while type* A *cells remained spread throughout the grid in the long term.*

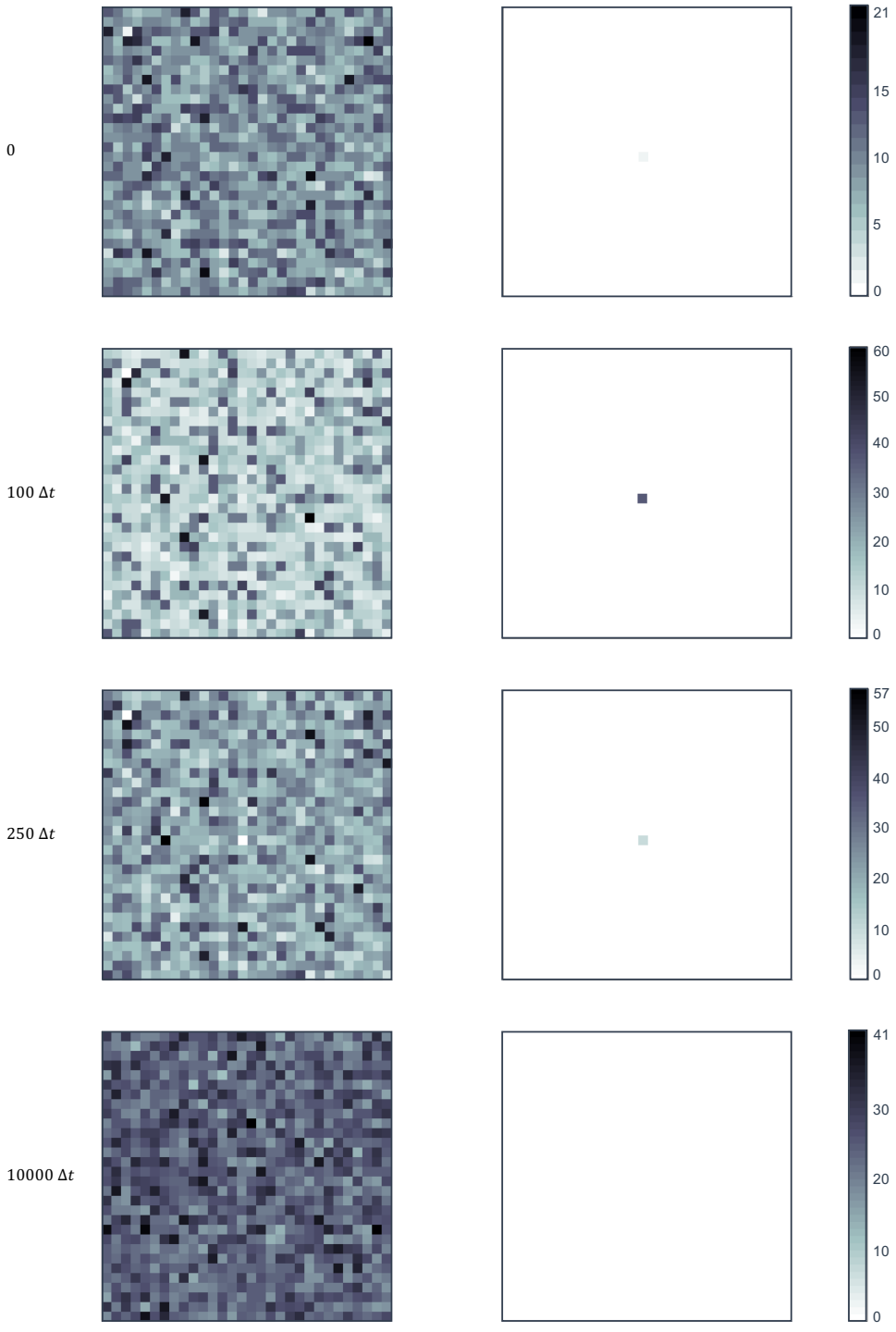

Figure 7.2: ***Second set of sample results for*** **Scenario 1.** *Plots show the spatiotemporal evolution of cells of type* A *(left panels) and of type* B *(right panels) at* 0, $250\Delta t$, $600\Delta t$, $1200\Delta t$, $1700\Delta t$, $2300\Delta t$, $3150\Delta t$, $3200\Delta t$ *and* $3250\Delta t$. *The simulation was run using the same parameter values as in Figure 7.1. Yet, type* B *cells died out after 32—rather than 3—generations. Also, type* B *cells invaded the grid and caused type* A *cells to become locally degraded while they continued to exist. Once type* B *cells had died out, type* A *cells re-populated the space and remained spread throughout the grid thereafter.*

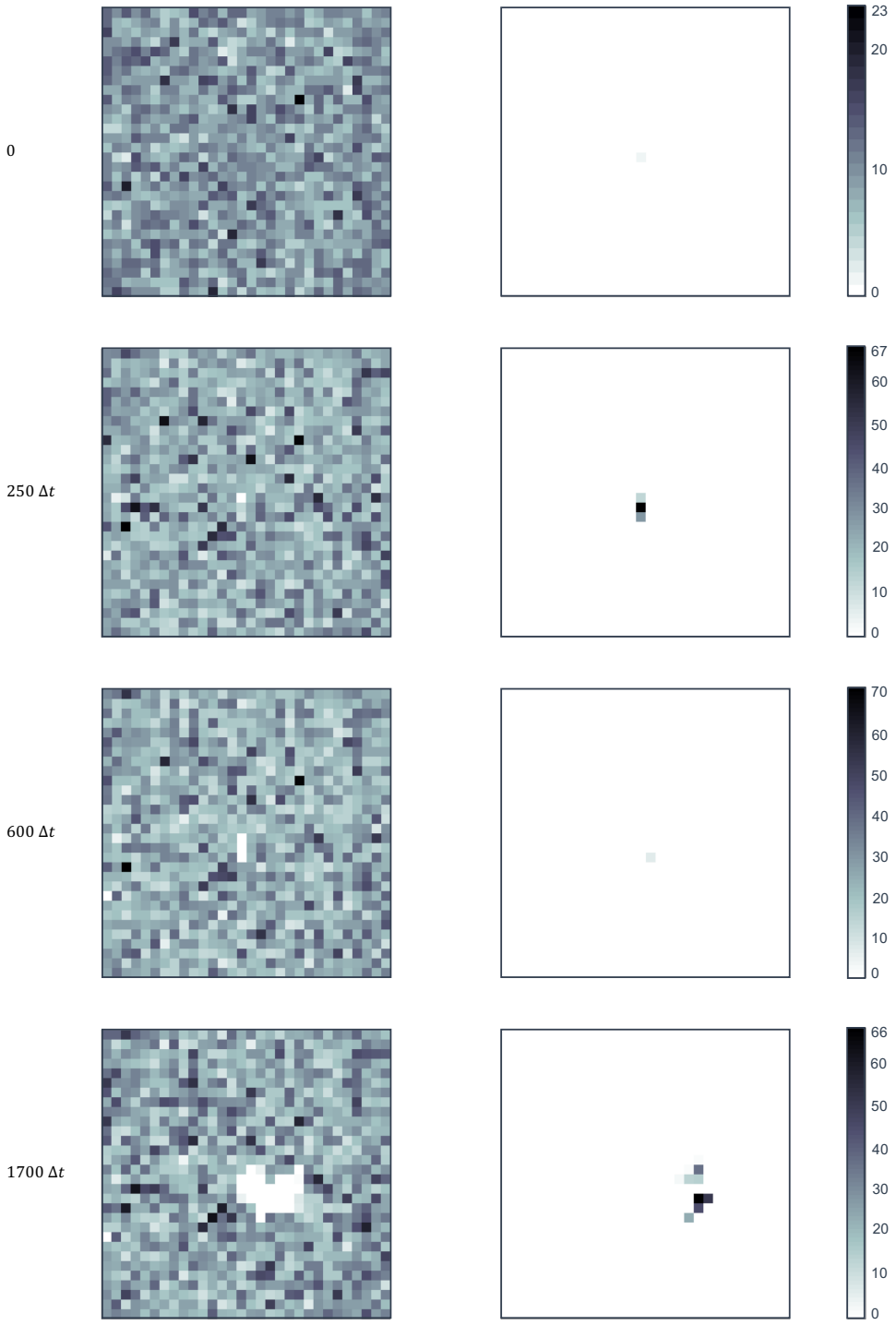

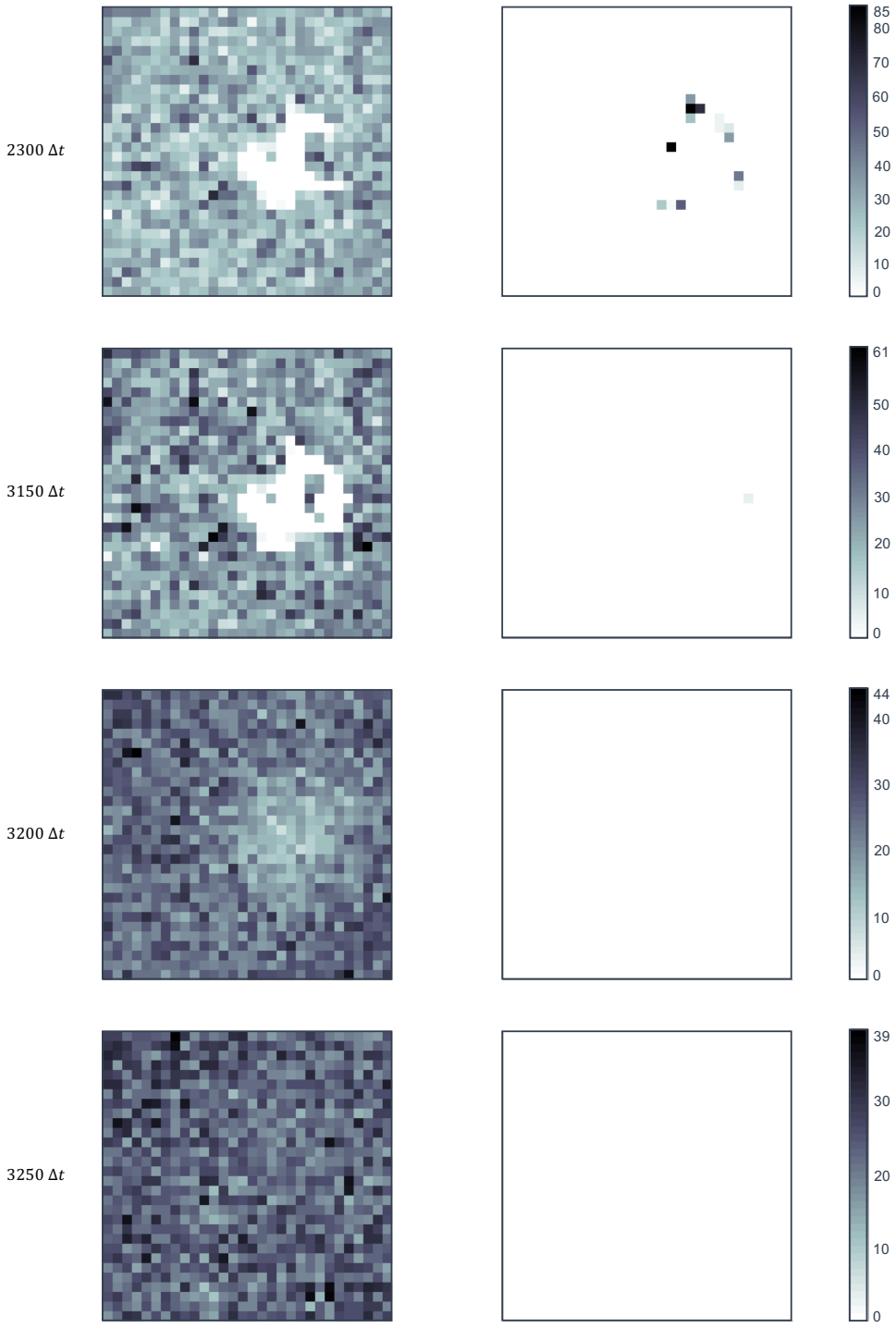
2300 Δt
3150 Δt
3200 Δt
3250 Δt
85
80
70
60
50
40
30
20
10
0
61
50
40
30
20
10
0
44
40
30
20
10
0
39
30
20
10
0

Figure 7.3: ***Sample results for*** **Scenario 2.** *Plots show the spatiotemporal evolution of cells of type* A *(left panels) and of type* B *(right panels) at* 0, $400\Delta t$, $1400\Delta t$, $2600\Delta t$, $3200\Delta t$, $5000\Delta t$, $9000\Delta t$ *and* $15200\Delta t$. *The same parameter values as in* Scenario 1 *were used apart from that the movement probability to one of four neighbouring grid points was doubled to be* 0.000125. *Type* B *cells invaded the grid fully in a ring-shaped wavefront and died out after 50 generations. The invasion caused some type* A *cells to locally die out while others continued to exist in clusters. Once type* B *cells had died out, type* A *cells did not re-populate the space. They also died out after 152 generations.*

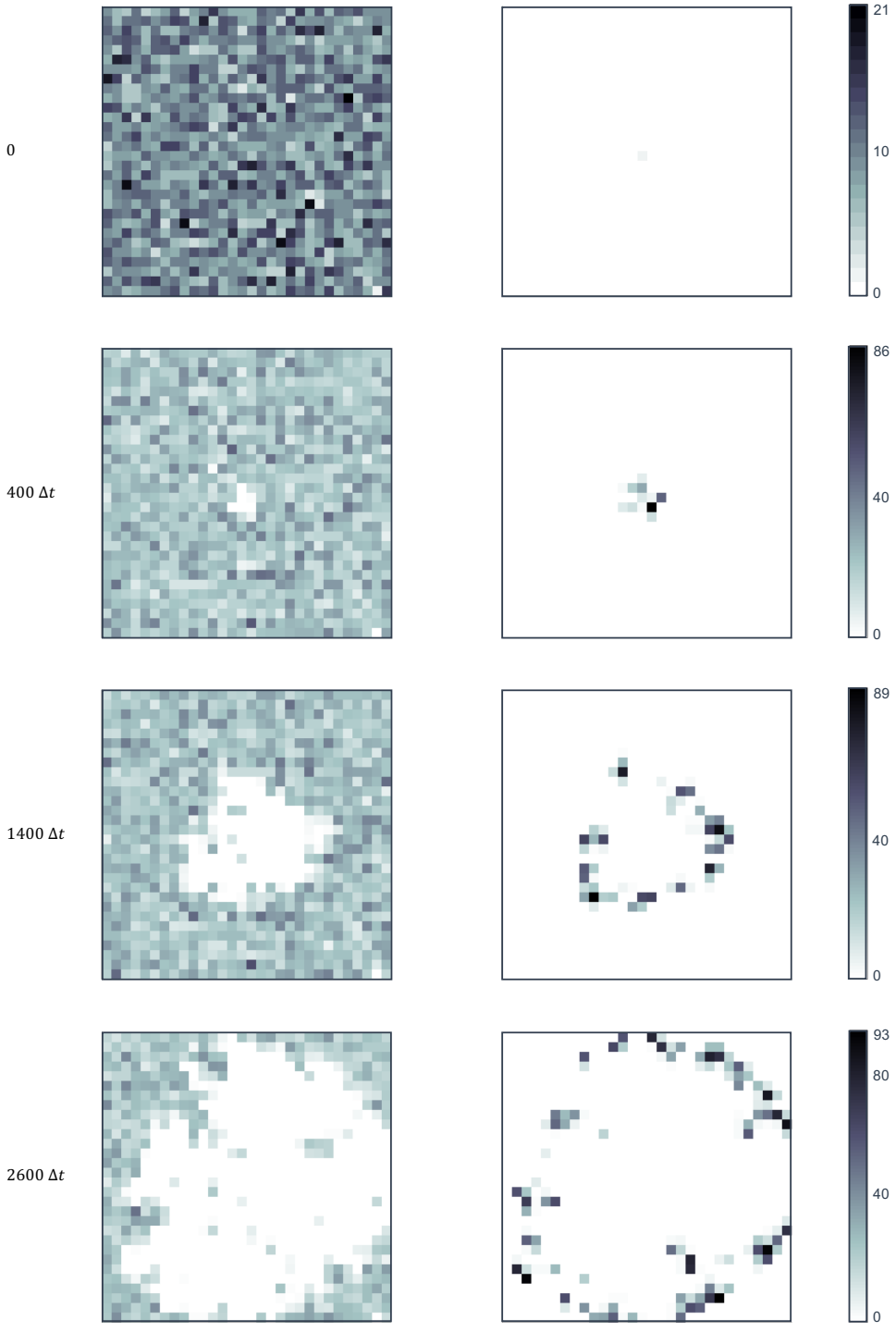

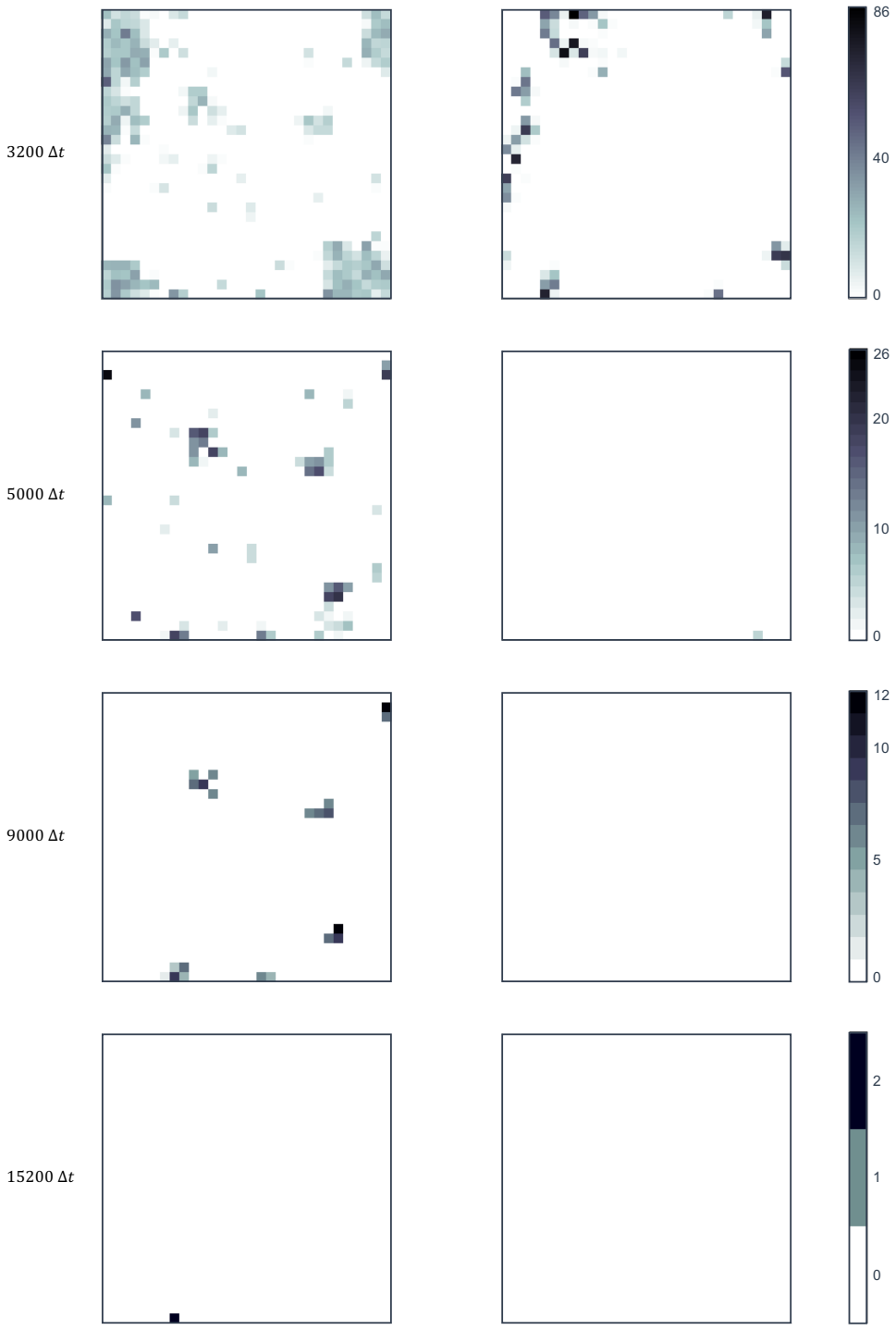
3200 Δt
5000 Δt
9000 Δt
15200 Δt
86
40
0
26
20
10
0
12
10
5
0
2
1
0

Figure 7.4: ***Sample results for*** **Scenario 3.** *The spatiotemporal evolution of cells of type* A *(left panels) and type* B *(right panels) after* 0, $100\Delta t$, $500\Delta t$, $700\Delta t$ *and* $900\Delta t$ *is shown. Initially, 9999 cells of type* A *were randomly distributed and one cell of type* B *placed in the centre of the* 100×100 *grid (first row of panels). The movement probabilities were taken as in Figures 7.1 and 7.2. The cells received phenotype-dependent payoff upon encounter according to Table 7.1. Each cell had a lifespan of* $100\Delta t$*. The cells of type* B *did not invade the tissue and did not even proliferate once. The cells of type* A *also did not stably sustain over time so that all cells had died out after 10 generations.*

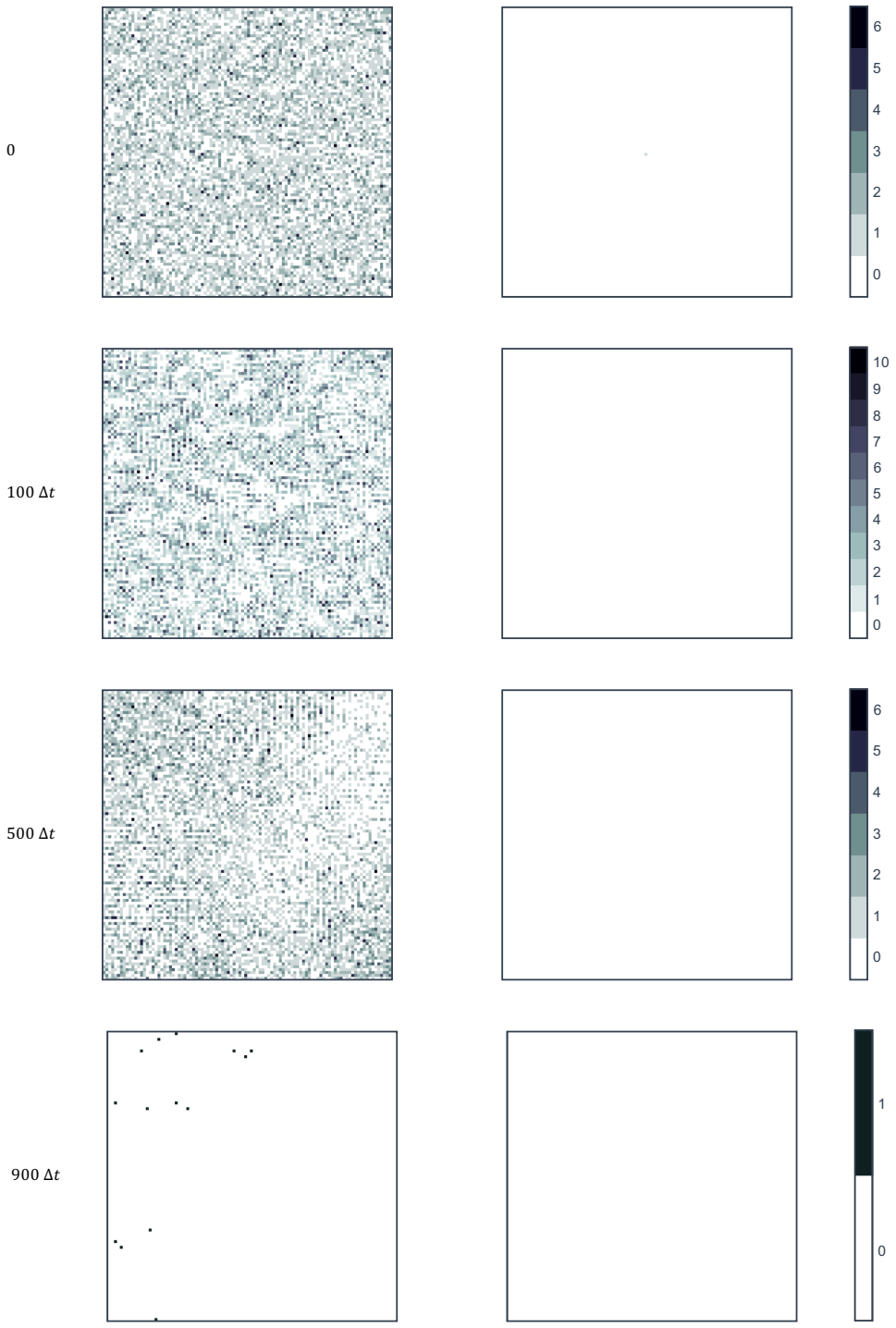

Figure 7.5: ***Sample results for*** **Scenario 4.** *Plots show the spatiotemporal evolution of cells of type* A *(left panels) and of type* B *(right panels) at* 0*,* $100\Delta t$*,* $300\Delta t$*,* $400\Delta t$ *and* $550\Delta t$*. Simulations were run with the same conditions as in Figure 7.5 apart from that, during each time step, the cells of type* A *moved to either of the four neighbouring grid points with probability* 0.0375*, while type* B *cells did so with probability* 0.075*. The cells of type* B *invaded the tissue and locally depleted the cells of type* A*. However, the cells of type* A *did not stably continue to exist over time regardless of the existence of type* B *cells. Hence, all cells had died out after 6 generations.*

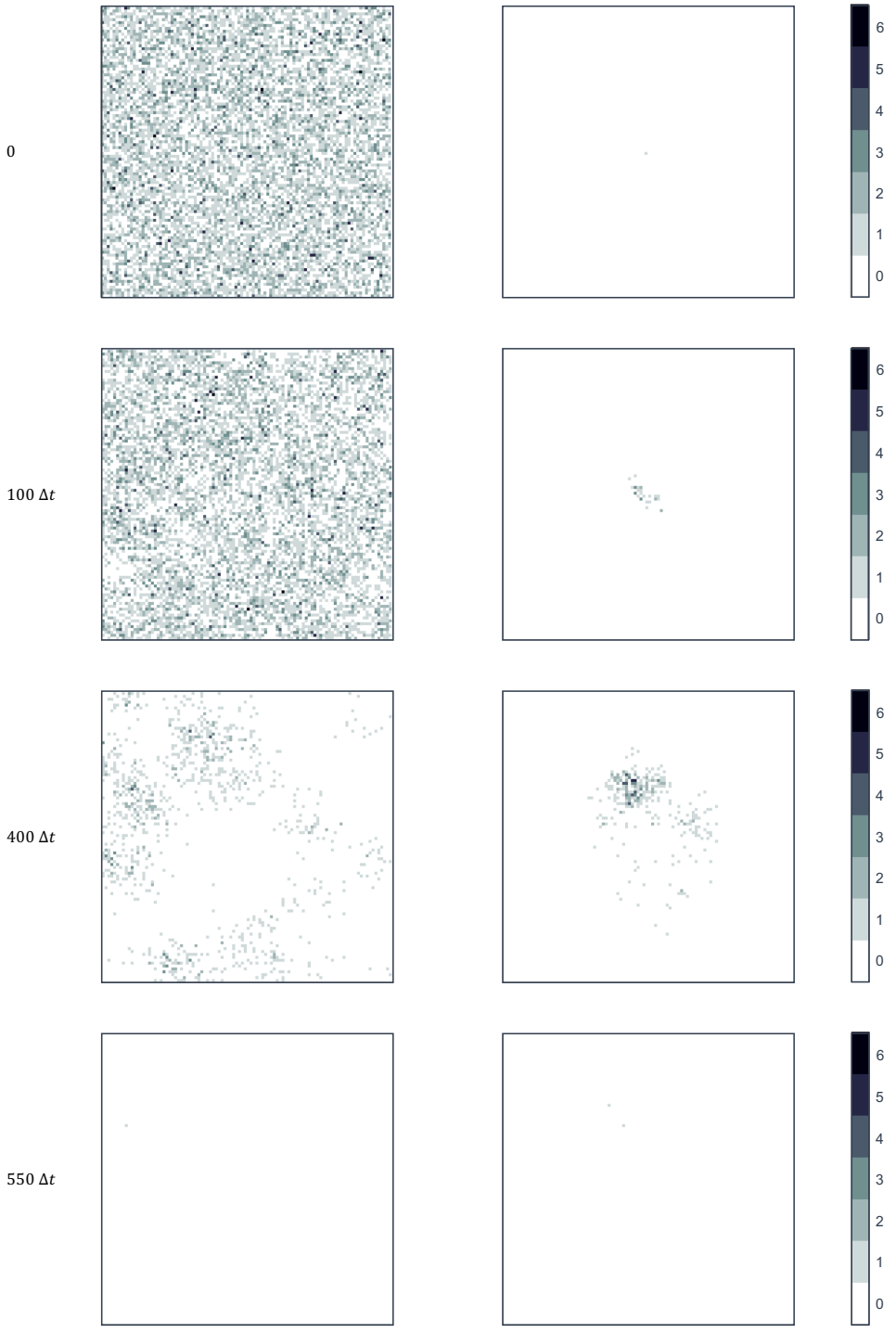

The panels shown in Figure 7.3 represent sample results for *Scenario 2*, in which cells are twice as likely to move during each time step as they were in *Scenario 1*. The resulting movement probabilities and the average number of cells per grid point in *Scenario 2* coincided with those in Burgess et al. (2017). Like Burgess et al. (2017), we observed a ring-shaped wavefront of type B cells that invaded the grid (see Figure 7.3). This caused the cells of type A that were initially spread randomly throughout the grid to become depleted in the regions where the cells of type B had resided. However, small groups of cells of type A remained on the grid throughout and beyond the 51-generation survival period of cells of type B. The clusters consisting of type A cells remained on the grid for an additional period of 153 generations thereafter.

Comparing the sample results for *Scenario 2* to the stable coexistence of both cell types observed in Burgess et al. (2017) led us to believe that boundary effects may have played a role in the extinction of both populations. Thus, we decided to run simulations on a larger 100×100 grid for *Scenario 3* and *4*. However, as it was computationally too costly to model an initial average population density of 5 cells per grid point, simulations for *Scenario 3* and *4* contained an initial average of 1 cell per grid point. The results shown in Figure 7.4 are representative of simulations with settings of *Scenario 3*. Apart from the grid size, the only difference to *Scenario 2* was the initial (average) population distribution—all other parameters were taken to be the same. The change in initial conditions typically resulted in type B cells failing to reproduce. Also, all A cells died out after 10 generations.

Finally, for *Scenario 4* we increased the movement probabilities during each time step to 0.0375 for the type A cells and to 0.075 for the B cells, *ceteris paribus*. We observed that type B cells were now able to invade the grid and to locally deplete the type A cells. While this allowed type B cells to survive for 6 generations, it decreased the survival period of type A cells compared to *Scenario 3* from 10 to 6 generations.

7.2.4 Discussion

We chose the interaction of cells to result in the payoff accumulation shown in Table 7.1, which resembles that of a classical prisoner's dilemma game. In the language of EGT, this makes type A cells *cooperators* and type B cells *defectors*. When a type A cell meets another type A cell, both cells receive a payoff of $p_{\mathsf{AA}} = 0.02$. However, type A cells receive no payoff when paired with a type B cell. While such an interspecific encounter is unproductive for type A cells, it highly pays off for type B cells, which gain the game's highest payoff of $p_{\mathsf{BA}} = 0.1$ during such an encounter. Yet, when type B cells encounter type B cells, they only receive a very small payoff of $p_{\mathsf{BB}} = 0.001$. In a biological sense, type B cells are parasitic on type A cells. Depending on the conditions of a game, they can more or less successfully invade the type A population (see Figures 7.1 to 7.5), which receives no benefit from the invasion by cells of type B. We hypothesise that, in the simulations depicted in Figures 7.1 to 7.5, this becomes evident from the fact that type A cells become locally depleted if type B cells reside on the same grid points for some length of time. Also, as Figure 7.2 shows, if the population of type A is fit enough (in the sense of motility, payoff accumulation and the number of cells per grid point) to establish itself in the long term, it re-populates the temporarily depleted regions of the grid that were previously occupied by type B cells. Notably, cells of type B also depend on the

existence of type A cells for survival as they do not produce sufficient offspring to sustain in the long run by intraspecific interaction alone—due to a lack of payoff accumulation. This explains why type B cells die out in the simulations depicted in Figures 7.1 to 7.5 after the cells of type A have been locally depleted.

Through simulations with settings as described above, we propose two further hypotheses, which are still subject to more systematic investigations:

1. Given an initially random distribution of type A cells, the average number of cells per grid point plays an important role. In *Scenarios 1* and *2*, an average of 5 cells per grid point resulted in a stable existence of type A cells over a long time. However, in *Scenarios 3* and *4*, the type A cells died out regardless of the existence of type B cells. A proposed explanation is that the cells do not have enough partner cells to interact with in order to collect payoff and thus to generate enough offspring when the grid is uniformly sparsely populated.

2. Stochasticity plays an important role in this type of model. As Figures 7.1 and 7.2 exemplify, the fate of the initially the rare invader of type B seems to heavily depend on what happens during the early time steps of a simulation. The relative success or failure of a type B cell to spread likely depends on

   (a) the initial local conditions it finds in its local environment—here in the form of resident cells of type A in its local neighbourhood, which is a result of the initially random spread of the type A cells, and

   (b) the fact that the B cell may or may not move, and hence spread, during the initial time steps.

If we consider the initial type B cell in our simulations to represent a cancer cell that is found in tissue otherwise containing healthy type A cells, the respective physiological scenario could exist either at a primary site when cancer begins to form and may or may not be eliminated by the healthy tissue, or at secondary sites after cancer cells extravasate. With respect to secondary spread—as we consider in Chapters 4 and 5—we could, for example, differentiate between the adaptivity of cancer cells to the new local tumour microenvironment via differences in the payoff values that the cells accumulate via the interactions and/or via differences in their movement probabilities at each organ. For instance, cancer cells stemming from a primary breast tumour may be generally better adapted for spread to the tissue of the bones than to the liver's tissue, *cf.* Figure 2.15. In this case, *Scenario 1* could represent the metastatic spread to the grid representing the bones. The payoff values in Table 7.1 could then be adapted such that $p_{\mathsf{BA}} = 0.08$ rather than $p_{\mathsf{BA}} = 0.1$ for cells on the domain representing the metastatic spread of a breast cancer cell to the liver.

Also, by starting with a few rather than solely one cell of type B, we could represent the arrival of a cluster of cancer cells at a secondary site. Moreover, we could distinguish the payoff that cancer cells gain from interactions according to their various phenotypes, which could also evolve over time e.g. via mutations. This would allow us to model the degree of success of cancer cells of various phenotypes after arriving at secondary sites as a consequence of metastatic spread. As an example, in the context of the model introduced in Chapter 5, the various phenotypes of cells involved could be epithelial-like,

partial-EMT and mesenchymal-like, and the mutations could take the form of EMT and MET. Importantly, the phenotypes occurring along the epithelial-mesenchymal spectrum and hence the respective mutations could be taken to occur in smaller steps rather than as 3 discrete types of cancer cells as currently in Chapter 5.

Simulating cell interactions using spatial EGT can be computationally costly. This imposed limits on the simulations we chose to run using this initial model that was implemented using MATLAB. For instance, we limited the number of cells included in the simulation either by choosing a relatively small grid with a high population density (*Scenario 1* and *Scenario 2*) or a larger grid with relatively low population density (*Scenario 3* and *Scenario 4*). Yet, if the respective code is written in a lower-level language, like that of the C++ model introduced in Chapters 4 and 5, high-performance computing could allow simulations over long time periods. Running these could be used to investigate what the long-term outcome of cancer invasion and metastatic spread would be in tumour microenvironments representing various organs.

All results presented here are preliminary results that require further theoretical investigation as well as quantification e.g. by running multiple simulations with the same settings to inform us of the relative frequency of the results. This could, for example, be achieved through recording the number of cells of type A and of type B over time as well as through the maximal invasion depth and/or the area invaded by species B at any point throughout the simulations. However, we are looking to increase the complexity of the underlying model e.g. by allowing for mutations, haptotaxis and more realistic payoff tables that may (locally) evolve over time to represent local changes in the tumour microenvironment. Hence, we postpone more in-depth investigations to a later point.

7.3 Extensions to the 3D hybrid discrete-continuum model of EMT-/MET-dependent cancer cell invasion

Our long-term research aim is to create a multiscale full-organism modelling framework of cancer invasion and metastatic spread. To achieve this, we will extend the current work to include the representation of the single-cell scale, interactions between cells, as well as the dynamics at the scale of the tissue in the domains accounted for in a more biologically realistic manner.

Such a multiscale full-body framework can aid the understanding of the impact of changes on the various scales on the overall disease evolution. It can hence be used to model disease progression as well as the impact of treatment approaches in various combinations and doses. This way, we can, for instance, learn about optimal dosing of a particular drug in a particular patient or drug interactions, as explained in Chapter 1 and Figure 1.1, while taking into consideration spatiotemporal dynamics of cancer cell spread. Full-body and multi-organ models designed for purposes such as predicting the absorption, distribution, metabolism and excretion (ADME) of synthetic or natural chemical substances in humans and other animal species already exist, often in the form of *physiologically based pharmacokinetic* (PKPB) models, see e.g. review in van Hasselt and van der Graaf (2015). Some full-body models for pharmacokinetics also include mul-

tiple scales—Chen et al. (2014), for instance, included the subcellular, cellular, and the whole-body level in their model for immunogenicity. Such models typically represent multiple organs as compartments and do not account for spatiotemporal effects as the presence of e.g. drugs, antigens or oxygen in the respective compartments is modelled in an ODE approach. However, as the spatial homogeneity typically associated with carcinomas is crucial to their disease evolution, the multiscale full-body modelling framework we intend to construct would allow to understand and predict the disease and, later on, its treatment in more biological detail.

To achieve enhancements on the smallest scale, we will combine this model, which describes the motility of mesenchymal-like cancer cells through SDEs, with models that account for cell motility in a biologically more realistic sense, *cf.* Sfakianakis et al. (2018b).

On the scale of cell-cell interactions, we are looking to include a merging and splitting process that reflects the underlying biology in more detail. Within the scope of our model, large particles, which biologically correspond to clusters of cells, arise from EMT through the density-to-particle operator in Section 6.1.5. In the current simulations, we have set m_{ref}, which determines the cluster size through the splitting and merging processes in Section 6.1.6, to be such that any clusters of cells disaggregate into single cells. This is to account for the fact that we consider a binary epithelial-mesenchymal spectrum so that the mesenchymal-like cancer cells do not attach to other cells. If we decided to include phenotypes along the EMT-spectrum (*cf.* Figure 2.11), this could be adjusted to account for the existence of cell clusters in addition to the epithelial-like cancer cell sheets that we consider in the current model. Conversely, merging of small particles in Section 6.1.6 is included in the model to account for close-range cell-cell interactions. This property of the model will be investigated further in future work. Further possible extensions of the model include accounting for cell-cell communication mediated by their filopodia as well as the ECM (e.g. via durotaxis).

On the same scale, we will include the production of diffusible MMPs like MMP-2 by the cancer cells in the model rather than relying on ECM degradation by membrane-bound MMPs like MT1-MMP only.

Finally, on the largest scale, the current work, which models experiments on domains that represent organotypic assays, will be transferred to organs in the body where carcinomas typically develop. In the next step, the metastatic spread from this site in the body to other sites will be accounted for through multiple domains in a multi-organ model, *cf.* Chapters 4 and 5. We will then be able to provide a unified modelling framework to account for a wide range of scales, spanning from the migration of individual cells to whole-organism phenomena. The fundamental components for this extensive effort have been provided in this thesis.

Bibliography

Aceto, N., Bardia, A., Miyamoto, D. T., Donaldson, M. C., Wittner, B. S., Spencer, J. A., Yu, M., Pely, A., Engstrom, A., Zhu, H., et al. (2014). Circulating tumor cell clusters are oligoclonal precursors of breast cancer metastasis. *Cell*, 158(5):1110–1122.

Alam, M., Abedi, V., Bassaganya-Riera, J., Wendelsdorf, K., Bisset, K., Deng, X., Eubank, S., Hontecillas, R., Hoops, S., and Marathe, M. (2016). *Chapter 6: Agent-Based Modeling and High Performance Computing*, pages 79–111.

Alberts, B., Bray, D., Hopkin, K., Johnson, A., Lewis, J., Raff, M., Roberts, K., and Walter, P. (2013). *Essential cell biology*. Garland Science.

Altrock, P. M., Liu, L. L., and Michor, F. (2015). The mathematics of cancer: integrating quantitative models. *Nat. Rev. Cancer*, 15(12):730.

Andasari, V., Gerisch, A., Lolas, G., South, A. P., and Chaplain, M. A. J. (2011). Mathematical modeling of cancer cell invasion of tissue: biological insight from mathematical analysis and computational simulation. *J. Math. Biol.*, 63(1):141–171.

Anderson, A. R. A. (2005). A hybrid mathematical model of solid tumour invasion: the importance of cell adhesion. *Math. Med. Biol.*, 22(2):163–186.

Anderson, A. R. A. and Chaplain, M. A. J. (1998). Continuous and discrete mathematical models of tumor-induced angiogenesis. *Bull. Math. Biol.*, 60(5):857–899.

Anderson, A. R. A., Chaplain, M. A. J., Newman, E. L., Steele, R. J. C., and Thompson, A. M. (2000). Mathematical modelling of tumour invasion and metastasis. *Comput. Math. Methods Med.*, 2(2):129–154.

Anderson, A. R. A., Hassanein, M., Branch, K. M., Lu, J., Lobdell, N. A., Maier, J., Basanta, D., Weidow, B., Narasanna, A., Arteaga, C. L., , and Reynolds, A. B. (2009). Microenvironmental independence associated with tumor progression. *Cancer Res.*, 69(22):8797–8806.

Araujo, R. P. and McElwain, D. S. (2004). A history of the study of solid tumour growth: the contribution of mathematical modelling. *Bull. Math. Biol.*, 66(5):1039.

Archetti, M. (2014). Evolutionary dynamics of the warburg effect: glycolysis as a collective action problem among cancer cells. *J. Theor. Biol.*, 341:1–8.

Armstrong, A. J., Marengo, M. S., Oltean, S., Kemeny, G., Bitting, R. L., Turnbull, J. D., Herold, C. I., Marcom, P. K., George, D. J., and Garcia-Blanco, M. A. (2011). Circulating tumor cells from patients with advanced prostate and breast cancer display both epithelial and mesenchymal markers. *Mol. Cancer Res.*, 9(8):997–1007.

Armstrong, N. J., Painter, K. J., and Sherratt, J. A. (2006). A continuum approach to modelling cell–cell adhesion. *J. Theor. Biol.*, 243(1):98–113.

Åström, P., Heljasvaara, R., Nyberg, P., Al-Samadi, A., and Salo, T. (2018). Human tumor tissue-based 3D in vitro invasion assays. In *Proteases and Cancer*, pages 213–221. Springer.

Bach, L. A., Bentzen, S., Alsner, J., and Christiansen, F. B. (2001). An evolutionary-game model of tumour–cell interactions: possible relevance to gene therapy. *Eur. J. Cancer*, 37(16):2116–2120.

Bach, L. A., Sumpter, D. J., Alsner, J., and Loeschcke, V. (2003). Spatial evolutionary games of interaction among generic cancer cells. *Comput. Math. Methods Med.*, 5(1):47–58.

Banyard, J. and Bielenberg, D. R. (2015). The role of EMT and MET in cancer dissemination. *Connect. Tissue Res.*, 56(5):403–413.

Barbolosi, D., Benabdallah, A., Hubert, F., and Verga, F. (2009). Mathematical and numerical analysis for a model of growing metastatic tumors. *Math. Biosci.*, 218(1):1–14.

Barney, L. E., Jansen, L., Polio, S., Galarza, S., Lynch, M. E., and Peyton, S. (2016). The predictive link between matrix and metastasis. *Curr. Opin. Chem. Eng.*, 11:85–93.

Bartoszyński, R., Edler, L., Hanin, L., Kopp-Schneider, A., Pavlova, L., Tsodikov, A., Zorin, A., and Yakovlev, A. Y. (2001). Modeling cancer detection: tumor size as a source of information on unobservable stages of carcinogenesis. *Math. Biosci.*, 171(2):113–142.

Basanta, D., Hatzikirou, H., and Deutsch, A. (2008a). Studying the emergence of invasiveness in tumours using game theory. *Eur. Phys. J. B*, 63(3):393–397.

Basanta, D., Scott, J. G., Fishman, M. N., Ayala, G., Hayward, S. W., and Anderson, A. R. A. (2012). Investigating prostate cancer tumour–stroma interactions: clinical and biological insights from an evolutionary game. *Br. J. Cancer*, 106(1):174.

Basanta, D., Simon, M., Hatzikirou, H., and Deutsch, A. (2008b). Evolutionary game theory elucidates the role of glycolysis in glioma progression and invasion. *Cell Prolif.*, 41(6):980–987.

Benzekry, S. (2011). Mathematical analysis of a two-dimensional population model of metastatic growth including angiogenesis. *J. Evol. Equ.*, 11(1):187–213.

Benzekry, S., Tracz, A., Mastri, M., Corbelli, R., Barbolosi, D., and Ebos, J. M. (2016). Modeling spontaneous metastasis following surgery: an in vivo-in silico approach. *Cancer Res.*, 76(3):535–547.

Bianconi, E., Piovesan, A., Facchin, F., Beraudi, A., Casadei, R., Frabetti, F., Vitale, L., Pelleri, M. C., Tassani, S., Piva, F., and Perez-Amodio, S. (2013). An estimation of the number of cells in the human body. *Ann. Hum. Biol.*, 40(6):463–471.

Bill, R. and Christofori, G. (2015). The relevance of EMT in breast cancer metastasis: Correlation or causality? *FEBS letters*, 589(14):1577–1587.

Blanc, X., Le Bris, C., and Lions, P.-L. (2007). Atomistic to continuum limits for computational materials science. *ESIAM Math. Model. Numer. Anal.*, 41(2):391–426.

Bockhorn, M., Jain, R. K., and Munn, L. L. (2007). Active versus passive mechanisms in metastasis: do cancer cells crawl into vessels, or are they pushed? *Lancet Oncol.*, 8(5):444–448.

Braun, S., Vogl, F. D., Naume, B., Janni, W., Osborne, M. P., Coombes, R. C., Schlimok, G., Diel, I. J., Gerber, B., Gebauer, G., and Pierga, J. (2005). A pooled analysis of bone marrow micrometastasis in breast cancer. *N. Engl. J. Med.*, 353(8):793–802.

Bray, D. (1992). Cell movements. *New York: Garland Publishing*.

Brú, A., Albertos, S., Subiza, J. L., García-Asenjo, J. L., and Brú, I. (2003). The universal dynamics of tumor growth. *Biophys. J.*, 85(5):2948–2961.

Burgess, A. E. F. (2013). *Applications of spatial game theory to host-parasitiod interactions: an individual-based modelling approach*. PhD thesis, University of Dundee.

Burgess, A. E. F., Lorenzi, T., Schofield, P. G., Hubbard, S. F., and Chaplain, M. A. J. (2017). Examining the role of individual movement in promoting coexistence in a spatially explicit prisoner's dilemma. *J. Theor. Biol.*, 419:323–332.

Burgess, A. E. F., Schofield, P. G., Hubbard, S. F., Chaplain, M. A. J., and Lorenzi, T. (2016). Dynamical patterns of coexisting strategies in a hybrid discrete–continuum spatial evolutionary game model. *Math. Model. Nat. Phenom.*, 11(5):49–64.

Burton, A. C. (1966). Rate of growth of solid tumours as a problem of diffusion. *Growth*, 30(2):157–176.

Butler, K. L., Ambravaneswaran, V., Agrawal, N., Bilodeau, M., Toner, M., Tompkins, R. G., Fagan, S., and Irimia, D. (2010). Burn injury reduces neutrophil directional migration speed in microfluidic devices. *PloS One*, 5(7):e11921.

Byrd, R., Gilbert, J., and Nocedal, J. (2000). A trust region method based on interior point techniques for nonlinear programming. *Math. Program.*, 89(1):149–185.

Byrne, H. M. (2010). Dissecting cancer through mathematics: from the cell to the animal model. *Nat. Rev. Cancer*, 10(3):221.

Campbell, K. (2018). Contribution of epithelial-mesenchymal transitions to organogenesis and cancer metastasis. *Curr. Opin. Cell Biol.*, 55:30–35.

Carmeliet, P. and Jain, R. K. (2000). Angiogenesis in cancer and other diseases. *Nature*, 407(6801):249.

Carragher, N., Walker, S., Carragher, L. S., Harris, F., Sawyer, T., Brunton, V., Ozanne, B., and Frame, M. (2006). Calpain 2 and Src dependence distinguishes mesenchymal and amoeboid modes of tumour cell invasion: a link to integrin function. *Oncogene*, 25(42):5726.

Cavallaro, U. and Christofori, G. (2001). Cell adhesion in tumor invasion and metastasis: loss of the glue is not enough. *Biochim. Biophys. Acta*, 1552(1):39–45.

Chaffer, C. L. and Weinberg, R. A. (2011). A perspective on cancer cell metastasis. *Science*, 331(6024):1559–1564.

Chambers, A. F., Groom, A. C., and MacDonald, I. C. (2002). Metastasis: Dissemination and growth of cancer cells in metastatic sites. *Nat. Rev. Cancer*, 2(8):563–572.

Chamseddine, I. M. and Rejniak, K. A. (2019). Hybrid modeling frameworks of tumor development and treatment. *Wiley Interdiscip. Rev. Syst. Biol. Med.*, page e1461.

Chaplain, M. A. J., Lachowicz, M., Szymańska, Z., and Wrzosek, D. (2011). Mathematical modelling of cancer invasion: the importance of cell–cell adhesion and cell–matrix adhesion. *Math. Models Methods Appl. Sci.*, 21(04):719–743.

Chaplain, M. A. J. and Lolas, G. (2005). Mathematical modelling of cancer cell invasion of tissue: The role of the urokinase plasminogen activation system. *Math. Models Methods Appl. Sci.*, 15(11):1685–1734.

Chaplain, M. A. J. and Lolas, G. (2006). Mathematical modelling of cancer invasion of tissue: dynamic heterogeneity. *Netw. Heterog. Media*, 1(3):399–439.

Chen, Q., Zhang, X. H.-F., and Massagué, J. (2011). Macrophage binding to receptor VCAM-1 transmits survival signals in breast cancer cells that invade the lungs. *Cancer Cell*, 20(4):538–549.

Chen, X., Hickling, T., and Vicini, P. (2014). A mechanistic, multiscale mathematical model of immunogenicity for therapeutic proteins: part 1—theoretical model. *CPT Pharmacometrics Syst. Pharmacol.*, 3(9):1–9.

Cheung, K. J. and Ewald, A. J. (2016). A collective route to metastasis: Seeding by tumor cell clusters. *Science*, 352(6282):167–169.

Cisneros, L. H. and Newman, T. J. (2014). Quantifying metastatic inefficiency: rare genotypes versus rare dynamics. *Phys. Biol.*, 11(4):046003.

Cohen, E. N., Gao, H., Anfossi, S., Mego, M., Reddy, N. G., Debeb, B., Giordano, A., Tin, S., Wu, Q., Garza, R. J., and Cristofanilli, M. (2015). Inflammation mediated metastasis: immune induced epithelial-to-mesenchymal transition in inflammatory breast cancer cells. *PLoS One*, 10(7):e0132710.

Collier, I. E., Legant, W., Marmer, B., Lubman, O., Saffarian, S., Wakatsuki, T., Elson, E., and Goldberg, G. I. (2011). Diffusion of MMPs on the surface of collagen fibrils: the mobile cell surface–collagen substratum interface. *PLoS ONE*, 6(9):e24029.

Cook, L. M., Araujo, A., Pow-Sang, J. M., Budzevich, M. M., Basanta, D., and Lynch, C. C. (2016). Predictive computational modeling to define effective treatment strategies for bone metastatic prostate cancer. *Sci. Rep.*, 6:1–12.

Cournot, A.-A. (1838). *Recherches sur les principes mathématiques de la théorie des richesses par Augustin Cournot*. Chez L. Hachette.

Deakin, A. (1975). Model for the growth of a solid in vitro tumor. *Growth*, 39(1):159–165.

Deakin, N. E. (2015). *Mathematical modelling of cancer growth and spread: the role of matrix metalloproteinases*. PhD thesis, University of Dundee.

Deakin, N. E. and Chaplain, M. A. J. (2013). Mathematical modeling of cancer invasion: the role of membrane-bound matrix metalloproteinases. *Front Oncol*, 3:70.

Deutsch, A. and Dormann, S. (2005). *Cellular automaton modeling of biological pattern formation*. Springer.

Devys, A., Goudon, T., and Lafitte, P. (2009). A model describing the growth and the size distribution of multiple metastatic tumors. *Discrete Cont. Dyn.-B*, 12:731–767.

Diepenbruck, M. and Christofori, G. (2016). Epithelial–mesenchymal transition (EMT) and metastasis: yes, no, maybe? *Curr. Opin. Cell. Biol.*, 43:7–13.

Dingli, D., Michor, F., Antal, T., and Pacheco, J. M. (2007). The emergence of tumor metastases. *Cancer Biol. Ther.*, 6(3):383–390.

Domschke, P., Trucu, D., Gerisch, A., and Chaplain, M. A. J. (2014). Mathematical modelling of cancer invasion: implications of cell adhesion variability for tumour infiltrative growth patterns. *J. Theor. Biol.*, 361:41–60.

Domschke, P., Trucu, D., Gerisch, A., and Chaplain, M. A. J. (2017). Structured models of cell migration incorporating molecular binding processes. *J. Math. Biol.*, 75(6-7):1517–1561.

Dongre, A. and Weinberg, R. A. (2019). New insights into the mechanisms of epithelial-mesenchymal transition and implications for cancer. *Nat. Rev. Mol. Cell Biol.*, 20:69–84.

Dormann, S. and Deutsch, A. (2002). Modeling of self-organized avascular tumor growth with a hybrid cellular automaton. *In Silico Biol.*, 2(3):393–406.

Dumont, N., Liu, B., DeFilippis, R. A., Chang, H., Rabban, J. T., Karnezis, A. N., Tjoe, J. A., Marx, J., Parvin, B., and Tlsty, T. D. (2013). Breast fibroblasts modulate early dissemination, tumorigenesis, and metastasis through alteration of extracellular matrix characteristics. *Neoplasia*, 15(3):249–IN7.

Durrett, R. and Levin, S. (1994). The importance of being discrete (and spatial). *Theor. Popul. Biol.*, 46(3):363–394.

Egea, J. A., Balsa-Canto, E., García, M.-S. G., and Banga, J. R. (2009). Dynamic optimization of nonlinear processes with an enhanced scatter search method. *Ind. Eng. Chem. Res.*, 48(9):4388–4401.

Egea, J. A., Martí, R., and Banga, J. R. (2010). An evolutionary method for complex-process optimization. *Comput. Oper. Res.*, 37(2):315–324.

Egeblad, M. and Werb, Z. (2002). New functions for the matrix metalloproteinases in cancer progression. *Nat. Rev. Cancer*, 2(3):161–174.

Elsevier B.V. (2006). Most cited cell articles. `https://www.journals.elsevier.com/cell/most-cited-articles`. Accessed: 15-12-2016.

Enderling, H., Anderson, A. R. A., Chaplain, M. A. J., Beheshti, A., Hlatky, L., and Hahnfeldt, P. (2009). Paradoxical dependencies of tumor dormancy and progression on basic cell kinetics. *Cancer Res.*, 69(22):8814–8821.

Enderling, H. and Chaplain, M. A. J. (2014). Mathematical modeling of tumor growth and treatment. *Curr. Pharm. Des.*, 20(30):4934–4940.

Ferlay, J., Soerjomataram, I., Dikshit, R., Eser, S., Mathers, C., Rebelo, M., Parkin, D. M., Forman, D., and Bray, F. (2015). Cancer incidence and mortality worldwide: sources, methods and major patterns in GLOBOCAN 2012. *Int. J. Cancer*, 136(5):E359–E386.

Fidler, I. J. (2003). The pathogenesis of cancer metastasis: the 'seed and soil' hypothesis revisited. *Nat. Rev. Cancer*, 3(6):453–458.

Fletcher, A. G., Osterfield, M., Baker, R. E., and Shvartsman, S. Y. (2014). Vertex models of epithelial morphogenesis. *Biophys. J.*, 106(11):2291–2304.

Folkman, J. (1990). What is the evidence that tumors are angiogenesis dependent? *J. Natl. Cancer Inst.*, 82(1):4–7.

Folkman, J. and Klagsbrun, M. (1987). Angiogenic factors. *Science*, 235(4787):442–447.

Francart, M.-E., Lambert, J., Vanwynsberghe, A. M., Thompson, E. W., Bourcy, M., Polette, M., and Gilles, C. (2018). Epithelial–mesenchymal plasticity and circulating tumor cells: Travel companions to metastases. *Dev. Dyn.*, 247(3):432–450.

Franssen, L. C. (2018). Using mathematics to outsmart cancer. *Mathematics Today*, 54(4):135–137.

Franssen, L. C. and Chaplain, M. A. J. (2019). A mathematical multi-organ model for bidirectional epithelial-mesenchymal transitions in the metastatic spread of cancer. *bioRxiv*.

Franssen, L. C., Lorenzi, T., Burgess, A. E. F., and Chaplain, M. A. J. (2019). A mathematical framework for modelling the metastatic spread of cancer. *Bull. Math. Biol.*, 81:1965.

Frei, C., Hillen, T., and Rhodes, A. (2019). A stochastic model for cancer metastasis: branching stochastic process with settlement. *Math. Med. Biol.*

Friedl, P., Locker, J., Sahai, E., and Segall, J. E. (2012). Classifying collective cancer cell invasion. *Nat. Cell Biol.*, 14(8):777–783.

Friedl, P. and Wolf, K. (2003). Tumour-cell invasion and migration: diversity and escape mechanisms. *Nat. Rev. Cancer*, 3(5):362–374.

Fujinaga, T., Kumamaru, W., Sugiura, T., Kobayashi, Y., Ohyama, Y., Ikari, T., Onimaru, M., Akimoto, N., Jogo, R., and Mori, Y. (2014). Biological characterization and analysis of metastasis-related genes in cell lines derived from the primary lesion and lymph node metastasis of a squamous cell carcinoma arising in the mandibular gingiva. *Int. J. Oncol.*, 44(5):1614–1624.

Fusenig, N. E., Breitkreutz, D., Dzarlieva, R. T., Boukamp, P., Bohnert, A., and Tilgen, W. (1983). Growth and differentiation characteristics of transformed keratinocytes from mouse and human skin in vitro and in vivo. *J. Investig. Dermatol.*, 81.

Gadea, G., Sanz-Moreno, V., Self, A., Godi, A., and Marshall, C. J. (2008). DOCK10-mediated Cdc42 activation is necessary for amoeboid invasion of melanoma cells. *Curr. Biol.*, 18(19):1456–1465.

Gaggioli, C., Hooper, S., Hidalgo-Carcedo, C., Grosse, R., Marshall, J. F., Harrington, K., and Sahai, E. (2007). Fibroblast-led collective invasion of carcinoma cells with differing roles for RhoGTPases in leading and following cells. *Nat. Cell Biol.*, 9(12):1392.

Gatenby, R. A. (1991). Population ecology issues in tumor growth. *Cancer Res.*, 51(10):2542–2547.

Gatenby, R. A. (1995a). Models of tumor-host interaction as competing populations: implications for tumor biology and treatment. *J. Theor. Biol.*, 176(4):447–455.

Gatenby, R. A. (1995b). The potential role of transformation-induced metabolic changes in tumor-host interaction. *Cancer Res.*, 55(18):4151–4156.

Gatenby, R. A. (1996). Application of competition theory to tumour growth: implications for tumour biology and treatment. *Eur. J. Cancer*, 32(4):722–726.

Gatenby, R. A. and Gawlinski, E. T. (1996). A reaction-diffusion model of cancer invasion. *Cancer Res.*, 56(24):5745–5753.

Gatenby, R. A., Gawlinski, E. T., Gmitro, A. F., Kaylor, B., and Gillies, R. J. (2006). Acid-mediated tumor invasion: a multidisciplinary study. *Cancer Res.*, 66(10):5216–5223.

Gerisch, A. and Chaplain, M. A. J. (2008). Mathematical modelling of cancer cell invasion of tissue: local and non-local models and the effect of adhesion. *J. Theor. Biol.*, 250(4):684–704.

Giese, A., Loo, M. A., Tran, N., Haskett, D., Coons, S. W., and Berens, M. E. (1996). Dichotomy of astrocytoma migration and proliferation. *Int. J. Cancer*, 67(2):275–282.

Gilmore, A. (2005). Anoikis.

Gingold, R. A. and Monaghan, J. J. (1977). Smoothed particle hydrodynamics: theory and application to non-spherical stars. *Mon. Notices Royal Astron. Soc.*, 181(3):375–389.

Glover, F. W. and Kochenberger, G. A. (2006). *Handbook of metaheuristics*, volume 57. Springer Science & Business Media.

Godlewski, J., Nowicki, M. O., Bronisz, A., Nuovo, G., Palatini, J., De Lay, M., Van Brocklyn, J., Ostrowski, M. C., Chiocca, E. A., and Lawler, S. E. (2010). MicroRNA-451 regulates LKB1/AMPK signaling and allows adaptation to metabolic stress in glioma cells. *Mol. Cell*, 37(5):620–632.

Graner, F. and Glazier, J. A. (1992). Simulation of biological cell sorting using a two-dimensional extended Potts model. *Phys. Rev. Lett.*, 69(13):2013.

Greco, F. A. (2014). Cancer of unknown primary site: still an entity, a biological mystery and a metastatic model. *Nat. Rev. Cancer*, 14(1):3.

Greenspan, H. (1972). Models for the growth of a solid tumor by diffusion. *Stud. Appl. Math.*, 51(4):317–340.

Greenspan, H. (1976). On the growth and stability of cell cultures and solid tumors. *J. Theor. Biol.*, 56(1):229–242.

Gunasinghe, N. D., Wells, A., Thompson, E. W., and Hugo, H. J. (2012). Mesenchymal–epithelial transition (MET) as a mechanism for metastatic colonisation in breast cancer. *Cancer Metastasis Rev.*, 31(3-4):469–478.

Guo, W., Keckesova, Z., Donaher, J. L., Shibue, T., Tischler, V., Reinhardt, F., Itzkovitz, S., Noske, A., Zürrer-Härdi, U., Bell, G., and Tam, W. (2012). Slug and Sox9 cooperatively determine the mammary stem cell state. *Cell*, 148(5):1015–1028.

Gupta, G. P. and Massagué, J. (2006). Cancer metastasis: Building a framework. *Cell*, 127(4):679–695.

Haeno, H., Iwasa, Y., and Michor, F. (2007). The evolution of two mutations during clonal expansion. *Genetics*, 177(4):2209–2221.

Haeno, H. and Michor, F. (2010). The evolution of tumor metastases during clonal expansion. *J. Theor. Biol.*, 263(1):30–44.

Hahnfeldt, P., Panigrahy, D., Folkman, J., and Hlatky, L. (1999). Tumor development under angiogenic signaling: a dynamical theory of tumor growth, treatment response, and postvascular dormancy. *Cancer Res.*, 59(19):4770–4775.

Hallou, A., Jennings, J., and Kabla, A. J. (2017). Tumour heterogeneity promotes collective invasion and cancer metastatic dissemination. *Royal Soc. Open Sci.*, 4(8):161007.

Hanahan, D. and Weinberg, R. A. (2000). The hallmarks of cancer. *Cell*, 100(1):57–70.

Hanahan, D. and Weinberg, R. A. (2011). Hallmarks of cancer: the next generation. *Cell*, 144(5):646–674.

Handler, J., Cullis, J., Avanzi, A., Vucic, E. A., and Bar-Sagi, D. (2018). Pre-neoplastic pancreas cells enter a partially mesenchymal state following transient TGF-β exposure. *Oncogene*, 37(31):4334–4342.

Hanin, L., Rose, J., and Zaider, M. (2006). A stochastic model for the sizes of detectable metastases. *J. Theor. Biol.*, 243(3):407–417.

Harlow, F. H. (1962). The particle-in-cell method for numerical solution of problems in fluid dynamics. Technical report, Los Alamos Scientific Lab., N. Mex.

Harper, K. L., Sosa, M. S., Entenberg, D., Hosseini, H., Cheung, J. F., Nobre, R., Avivar-Valderas, A., Nagi, C., Girnius, N., Davis, R. J., Farias, E. F., Condeelis, J., Klein, C. A., and Aguirre-Ghiso, J. A. (2016). Mechanism of early dissemination and metastasis in Her2+ mammary cancer. *Nature*, 540(7634):588–592.

Hartung, N., Mollard, S., Barbolosi, D., Benabdallah, A., Chapuisat, G., Henry, G., Giacometti, S., Iliadis, A., Ciccolini, J., Faivre, C., and F, H. (2014). Mathematical modeling of tumor growth and metastatic spreading: validation in tumor-bearing mice. *Cancer Res.*, 74(22):6397–6407.

Hatzikirou, H., Böttger, K., and Deutsch, A. (2015). Model-based comparison of cell density-dependent cell migration strategies. *Math. Model. Nat. Phenom.*, 10(1):94–107.

Hatzikirou, H., Brusch, L., Schaller, C., Simon, M., and Deutsch, A. (2010). Prediction of traveling front behavior in a lattice-gas cellular automaton model for tumor invasion. *Comput. Math. Appl.*, 59(7):2326–2339.

Hatzikirou, H. and Deutsch, A. (2008). Cellular automata as microscopic models of cell migration in heterogeneous environments. *Curr. Top. Dev. Biol.*, 81:401–434.

Hellmann, N., Kolbe, N., and Sfakianakis, N. (2016). A mathematical insight in the epithelial-mesenchymal-like transition in cancer cells and its effect in the invasion of the extracellular matrix. *B. Braz. Math. Soc.*, 47(1):397–412.

Hill, A. (1928). The diffusion of oxygen and lactic acid through tissues. *P. Roy. Soc. Lond. B Bio.*, 104(728):39–96.

Huang, R. Y., Wong, M., Tan, T., Kuay, K., Ng, A., Chung, V., Chu, Y., Matsumura, N., Lai, H., Lee, Y., and Sim, W. (2013). An EMT spectrum defines an anoikis-resistant and spheroidogenic intermediate mesenchymal state that is sensitive to E-cadherin restoration by a src-kinase inhibitor, saracatinib (AZD0530). *Cell Death Dis.*, 4(11):e915.

Hughes, L., Malone, C., Chumsri, S., Burger, A. M., and McDonnell, S. (2008). Characterisation of breast cancer cell lines and establishment of a novel isogenic subclone to study migration, invasion and tumourigenicity. *Clin. Exp. Metastasis*, 25(5):549–557.

Hummert, S., Bohl, K., Basanta, D., Deutsch, A., Werner, S., Theißen, G., Schroeter, A., and Schuster, S. (2014). Evolutionary game theory: cells as players. *Mol. Biosyst.*, 10(12):3044–3065.

Hüsemann, Y., Geigl, J. B., Schubert, F., Musiani, P., Meyer, M., Burghart, E., Forni, G., Eils, R., Fehm, T., Riethmüller, G., and Klein, C. A. (2008). Systemic spread is an early step in breast cancer. *Cancer Cell*, 13(1):58–68.

ICRP (2009). Adult reference computational phantoms. *Ann. ICRP*, 110(39(2)).

Imai, T., Horiuchi, A., Wang, C., Oka, K., Ohira, S., Nikaido, T., and Konishi, I. (2003). Hypoxia attenuates the expression of E-cadherin via up-regulation of SNAIL in ovarian carcinoma cells. *Am. J. Pathol.*, 163(4):1437–1447.

Institute, N. C. (2017). SEER Training Modules: Cancer classification. `https://training.seer.cancer.gov/disease/categories/classification.html`. Accessed: 07-02-2017.

Itoh, Y. (2015). Membrane-type matrix metalloproteinases: their functions and regulations. *Matrix Biol.*, 44:207–223.

Iwasa, Y., Nowak, M. A., and Michor, F. (2006). Evolution of resistance during clonal expansion. *Genetics*, 172(4):2557–2566.

Iwata, K., Kawasaki, K., and Shigesada, N. (2000). A dynamical model for the growth and size distribution of multiple metastatic tumors. *J. Theor. Biol.*, 203(2):177–186.

Jackson, B. C., Nebert, D. W., and Vasiliou, V. (2010). Update of human and mouse matrix metalloproteinase families. *Hum. Genomics*, 4(3):194.

Japanese Collection of Research Bioresources Cell Bank (2015). Cell Number: JCRB0623 Cell Name: HSC-3. `https://cellbank.nibiohn.go.jp/~cellbank/en/search_res_det.cgi?ID=468`. Accessed: 02-05-2019.

Jie, X.-X., Zhang, X.-Y., and Xu, C.-J. (2017). Epithelial-to-mesenchymal transition, circulating tumor cells and cancer metastasis: Mechanisms and clinical applications. *Oncotarget*, 8(46):81558.

Jolly, M. K., Mani, S. A., and Levine, H. (2018). Hybrid epithelial/mesenchymal phenotype(s): The 'fittest' for metastasis? *Biochim. Biophys. Acta, Rev. Cancer*.

Jolly, M. K., Tripathi, S. C., Somarelli, J. A., Hanash, S. M., and Levine, H. (2017). Epithelial/mesenchymal plasticity: how have quantitative mathematical models helped improve our understanding? *Mol. Oncol.*, 11(7):739–754.

Kabla, A. J. (2012). Collective cell migration: leadership, invasion and segregation. *J. Royal Soc. Interface*, page rsif20120448.

Kalluri, R. and Weinberg, R. A. (2009). The basics of epithelial-mesenchymal transition. *J. Clin. Invest.*, 119(6):1420–1428.

Kansal, A., Torquato, S., Harsh Iv, G., Chiocca, E., and Deisboeck, T. (2000). Cellular automaton of idealized brain tumor growth dynamics. *Biosystems*, 55(1):119–127.

Karagiannis, E. D. and Popel, A. S. (2004). A theoretical model of type I collagen proteolysis by matrix metalloproteinase (MMP) 2 and membrane type 1 MMP in the presence of tissue inhibitor of metalloproteinase 2. *J. Biol. Chem.*, 279(37):39105–39114.

Karagiannis, G. S., Pastoriza, J. M., Wang, Y., Harney, A. S., Entenberg, D., Pignatelli, J., Sharma, V. P., Xue, E. A., Cheng, E., D'Alfonso, T. M., Jones, J. G., Anampa, J., Rohan, T. E., Sparano, J. A., Condeelis, J. S., and Oktay, M. H. (2017). Neoadjuvant chemotherapy induces breast cancer metastasis through a TMEM-mediated mechanism. *Sci. Transl. Med.*, 9(397):eaan0026.

Karmarkar, N. (1984). A new polynomial-time algorithm for linear programming. *Combinatorica*, 4:373–395.

Kaznatcheev, A., Scott, J. G., and Basanta, D. (2015). Edge effects in game-theoretic dynamics of spatially structured tumours. *J. Royal Soc. Interface*, 12(108):20150154.

Kennedy, C. and Carpenter, M. (2003). Additive Runge-Kutta schemes for convection-diffusion-reaction equations. *Appl. Numer. Math.*, 1(44):139–181.

Kenny, P. A., Lee, G. Y., and Bissell, M. J. (2007). Targeting the tumor microenvironment. *Front. Biosci.*, 12:3468.

Khoshyomn, S., Lew, S., DeMattia, J., Singer, E. B., and Penar, P. L. (1999). Brain tumor invasion rate measured in vitro does not correlate with Ki-67 expression. *J. Neuro-Oncol.*, 45(2):111–116.

Kim, Y. and Othmer, H. G. (2013). A hybrid model of tumor–stromal interactions in breast cancer. *Bull. Math. Bio.*, 75(8):1304–1350.

Kitanidis, P. K. (1994). Particle-tracking equations for the solution of the advection-dispersion equation with variable coefficients. *Water Resour. Res.*, 30(11):3225–3227.

Kleiner, D. E. and Stetler-Stevenson, W. G. (1999). Matrix metalloproteinases and metastasis. *Cancer Chemother. Pharmacol.*, 43(1):S42–S51.

Kloeden, P. E. and Platen, E. (2013). *Numerical solution of stochastic differential equations*, volume 23. Springer Science & Business Media.

Knutson, J. D. (2011). *A survey of the use of cellular automata and cellular automata-like models for simulating a population of biological cells*. PhD thesis, Iowa State University.

Kolbe, N., Kat'uchová, J., Sfakianakis, N., Hellmann, N., and Lukáčová-Medvid'ová, M. (2016). A study on time discretization and adaptive mesh refinement methods for the simulation of cancer invasion: The urokinase model. *Appl. Math. Comput.*, 273:353–376.

Koontongkaew, S. (2013). The tumor microenvironment contribution to development, growth, invasion and metastasis of head and neck squamous cell carcinomas. *J. Cancer*, 4(1):66.

Krebs, A. M., Mitschke, J., Losada, M. L., Schmalhofer, O., Boerries, M., Busch, H., Boettcher, M., Mougiakakos, D., Reichardt, W., Bronsert, P., and Brunton, V. (2017). The EMT-activator Zeb1 is a key factor for cell plasticity and promotes metastasis in pancreatic cancer. *Nat. Cell Biol.*, 19(5):518.

Kröger, C., Afeyan, A., Mraz, J., Eaton, E. N., Reinhardt, F., Khodor, Y. L., Thiru, P., Bierie, B., Ye, X., Burge, C. B., and Weinberg, R. (2019). Acquisition of a hybrid E/M state is essential for tumorigenicity of basal breast cancer cells. *Proc. Natl. Acad. Sci.*, page 201812876.

Krylov, A. (1931). On the numerical solution of the equation by which in technical questions frequencies of small oscillations of material systems are determined. *Otdel. mat. i estest. nauk.*, VII(4):491–539.

Kuhn Laboratory (2017). Breast Cancer Progression Models. `http://kuhn.usc.edu/breast_cancer/`. Accessed: 22-05-2019.

Lambert, A. W., Pattabiraman, D. R., and Weinberg, R. A. (2017). Emerging biological principles of metastasis. *Cell*, 168(4):670–691.

Le Guillou, L., Dard, N., Glisse, J., Maro, B., Louvet-Vallée, S., and Laforge, B. (2009). A 3D mechanical model of the early mammalian embryo. *J. Biol. Phys. Chem.*, 9:11.

Liotta, L. A., Delisi, C., Saidel, G., and Kleinerman, J. (1977). Micrometastases formation: a probabilistic model. *Cancer Lett.*, 3:203–208.

Liotta, L. A., Saidel, G. M., and Kleinerman, J. (1976). Stochastic model of metastases formation. *Biometrics*, pages 535–550.

Loo, J. M., Scherl, A., Nguyen, A., Man, F. Y., Weinberg, E., Zeng, Z., Saltz, L., Paty, P. B., and Tavazoie, S. F. (2015). Extracellular metabolic energetics can promote cancer progression. *Cell*, 160(3):393–406.

Lorenzi, T., Venkataraman, C., Lorz, A., and Chaplain, M. A. J. (2018). The role of spatial variations of abiotic factors in mediating intratumour phenotypic heterogeneity. *J. Theor. Biol.*, 451:101–110.

Lorusso, G. and Rüegg, C. (2008). The tumor microenvironment and its contribution to tumor evolution toward metastasis. *Histochem. Cell Biol.*, 130(6):1091–1103.

Lorz, A., Lorenzi, T., Clairambault, J., Escargueil, A., and Perthame, B. (2015). Modeling the effects of space structure and combination therapies on phenotypic heterogeneity and drug resistance in solid tumors. *Bull. Math. Biol.*, 77(1):1–22.

Lovisa, S., LeBleu, V. S., Tampe, B., Sugimoto, H., Vadnagara, K., Carstens, J. L., Wu, C.-C., Hagos, Y., Burckhardt, B. C., Pentcheva-Hoang, T., and Nischal, H. (2015). Epithelial-to-mesenchymal transition induces cell cycle arrest and parenchymal damage in renal fibrosis. *Nat. Med.*, 21(9):998.

Luzzi, K. J., MacDonald, I. C., Schmidt, E. E., Kerkvliet, N., Morris, V. L., Chambers, A. F., and Groom, A. C. (1998). Multistep nature of metastatic inefficiency: dormancy of solitary cells after successful extravasation and limited survival of early micrometastases. *Am. J. Pathol.*, 153(3):865–873.

Mackenzie, I. C. (2004). Growth of malignant oral epithelial stem cells after seeding into organotypical cultures of normal mucosa. *J. Oral Pathol. Med.*, 33(2):71–78.

Makridakis, C., Mitsoudis, D., and Rosakis, P. (2013). On atomistic-to-continuum couplings without ghost forces in three dimensions. *Appl. Math. Res. Express*, 2014(1):87–113.

Mansury, Y., Diggory, M., and Deisboeck, T. S. (2006). Evolutionary game theory in an agent-based brain tumor model: exploring the 'genotype–phenotype' link. *J. Theor. Biol.*, 238(1):146–156.

Margarit, D. H. and Romanelli, L. (2016). A mathematical model of absorbing Markov chains to understand the routes of metastasis. *Biomath.*, 5(1):1607281.

Martin, G. R. and Jain, R. K. (1994). Noninvasive measurement of interstitial pH profiles in normal and neoplastic tissue using fluorescence ratio imaging microscopy. *Cancer Res.*, 54(21):5670–5674.

Massey, S. C., Rockne, R. C., Hawkins-Daarud, A., Gallaher, J., Anderson, A. R., Canoll, P., and Swanson, K. R. (2018). Simulating PDGF-driven glioma growth and invasion in an anatomically accurate brain domain. *Bull. Math. Biol.*, 80(5):1292–1309.

McAllister, S. S. and Weinberg, R. A. (2014). The tumour-induced systemic environment as a critical regulator of cancer progression and metastasis. *Nat. Cell Biol.*, 16(8):717–727.

McDougall, S. R., Watson, M. G., Devlin, A. H., Mitchell, C. A., and Chaplain, M. A. J. (2012). A hybrid discrete-continuum mathematical model of pattern prediction in the developing retinal vasculature. *Bull. Math. Biol.*, 74(10):2272–2314.

McGuire, M. and Beerman, K. A. (2012). *Nutritional sciences: from fundamentals to food*. Cengage Learning.

Meng, S., Tripathy, D., Frenkel, E. P., Shete, S., Naftalis, E. Z., Huth, J. F., Beitsch, P. D., Leitch, M., Hoover, S., Euhus, D., Haley, B., Morrison, L., Fleming, T. P., Herlyn, D., Terstappen, L. W., Fehm, T., Tucker, T. F., Lane, N., Wang, J., and Uhr,

J. W. (2004). Circulating tumor cells in patients with breast cancer dormancy. *Clin. Cancer Res.*, 10(24):8152–8162.

Metzcar, J., Wang, Y., Heiland, R., and Macklin, P. (2019). A review of cell-based computational modeling in cancer biology. *JCO Clin. Cancer Inform.*, 2:1–13.

Micalizzi, D. S., Farabaugh, S. M., and Ford, H. L. (2010). Epithelial–mesenchymal transition in cancer: Parallels between normal development and tumor progression. *J. Mammary Gland Biol. Neoplasia*, 15(2):117–134.

Michor, F. and Iwasa, Y. (2006). Dynamics of metastasis suppressor gene inactivation. *J. Theor. Biol.*, 241(3):676–689.

Michor, F., Nowak, M. A., and Iwasa, Y. (2006). Stochastic dynamics of metastasis formation. *J. Theor. Biol.*, 240(4):521–530.

Milo, R., Jorgensen, P., Moran, U., Weber, G., and Springer, M. (2009). Bionumbers—the database of key numbers in molecular and cell biology. *Nucleic Acids Res.*, 38(suppl_1):D750–D753. Accessed: 22-10-2017.

Mook, O. R., Frederiks, W. M., and Van Noorden, C. J. (2004). The role of gelatinases in colorectal cancer progression and metastasis. *Biochim. Biophys. Acta Rev. Cancer*, 1705(2):69–89.

Moran, S., Martínez-Cardús, A., Sayols, S., Musulén, E., Balañá, C., Estival-Gonzalez, A., Moutinho, C., Heyn, H., Diaz-Lagares, A., de Moura, M. C., and Stella, G. M. (2016). Epigenetic profiling to classify cancer of unknown primary: a multicentre, retrospective analysis. *Lancet Oncol.*, 17(10):1386–1395.

Moreira, J. and Deutsch, A. (2002). Cellular automaton models of tumor development: a critical review. *Adv. Complex Syst.*, 5(02n03):247–267.

Myerson, R. B. (2013). *Game theory*. Harvard University Press.

National Cancer Institute (2017). NCI dictionary of cancer terms. `https://www.cancer.gov/publications/dictionaries/cancer-terms?cdrid=45301`. Accessed: 06-02-2017.

NCI (2015). Cell lines in the *in vitro* screen. Accessed: 15-07-2019.

Newton, P. K., Mason, J., Bethel, K., Bazhenova, L., Nieva, J., Norton, L., and Kuhn, P. (2013). Spreaders and sponges define metastasis in lung cancer: a Markov chain Monte Carlo mathematical model. *Cancer Res.*, 73(9):2760–2769.

Newton, P. K., Mason, J., Bethel, K., Bazhenova, L. A., Nieva, J., and Kuhn, P. (2012). A stochastic Markov chain model to describe lung cancer growth and metastasis. *PLoS One*, 7(4):e34637.

Newton, P. K., Mason, J., Venkatappa, N., Jochelson, M. S., Hurt, B., Nieva, J., Comen, E., Norton, L., and Kuhn, P. (2015). Spatiotemporal progression of metastatic breast cancer: a Markov chain model highlighting the role of early metastatic sites. *NPJ Breast Cancer*, 1:15018.

Nguyen, D. X., Bos, P. D., and Massagué, J. (2009). Metastasis: from dissemination to organ-specific colonization. *Nat. Rev. Cancer*, 9(4).

Noël, A. (2012). New and paradoxical roles of matrix metalloproteinases in the tumor microenvironment. *Front. Pharmacol.*, 3:140.

Nowak, M. A., Bonhoeffer, S., and May, R. M. (1994). More spatial games. *Int. J. Bifurc. Chaos*, 4(01):33–56.

Nowak, M. A. and May, R. M. (1992). Evolutionary games and spatial chaos. *Nature*, 359(6398):826.

Nowak, M. A. and May, R. M. (1993). The spatial dilemmas of evolution. *Int. J. Bifurc. Chaos*, 3(01):35–78.

Nurmenniemi, S., Sinikumpu, T., Alahuhta, I., Salo, S., Sutinen, M., Santala, M., Risteli, J., Nyberg, P., and Salo, T. (2009). A novel organotypic model mimics the tumor microenvironment. *Am. J. Pathol.*, 175(3):1281–1291.

Nyström, M. L., Thomas, G. J., Stone, M., Mackenzie, I. C., Hart, I. R., and Marshall, J. F. (2005). Development of a quantitative method to analyse tumour cell invasion in organotypic culture. *J. Pathol.*, 205(4):468–475.

Obenauf, A. C. and Massagué, J. (2015). Surviving at a distance: organ-specific metastasis. *Trends Cancer*, 1(1):76–91.

Ocaña, O. H., Córcoles, R., Fabra, Á., Moreno-Bueno, G., Acloque, H., Vega, S., Barrallo-Gimeno, A., Cano, A., and Nieto, M. A. (2012). Metastatic colonization requires the repression of the epithelial-mesenchymal transition inducer Prrx1. *Cancer cell*, 22(6):709–724.

Paget, S. (1889). The distribution of secondary growths in cancer of the breast. *Lancet*, 133(3421):571–573.

Pantel, K. and Speicher, M. (2016). The biology of circulating tumor cells. *Oncogene*, 35(10):1216.

Park, K., Jang, J., Irimia, D., Sturgis, J., Lee, J., Robinson, J. P., Toner, M., and Bashir, R. (2008). 'Living cantilever arrays' for characterization of mass of single live cells in fluids. *Lab Chip*, 8(7):1034–1041.

Pastushenko, I. and Blanpain, C. (2018). EMT transition states during tumor progression and metastasis. *Trends Cell Biol.*, 29(3):212–226.

Patel, A. A., Gawlinski, E. T., Lemieux, S. K., and Gatenby, R. A. (2001). A cellular automaton model of early tumor growth and invasion: the effects of native tissue vascularity and increased anaerobic tumor metabolism. *J. Theor. Biol.*, 213(3):315–331.

Peng, L., Trucu, D., Lin, P., Thompson, A., and Chaplain, M. A. J. (2017). A multiscale mathematical model of tumour invasive growth. *Bull. Math. Biol.*, 79(3):389–429.

Perumpanani, A. J., Sherratt, J. A., Norbury, J., and Byrne, H. M. (1996). Biological inferences from a mathematical model for malignant invasion. *Invas. Metast.*, 16:209–221.

Petrova, V., Annicchiarico-Petruzzelli, M., Melino, G., and Amelio, I. (2018). The hypoxic tumour microenvironment. *Oncogenesis*, 7(1):10.

Pietras, K. and Östman, A. (2010). Hallmarks of cancer: interactions with the tumor stroma. *Exp. Cell Res.*, 316(8):1324–1331.

Ploetz, C., Zycband, E. I., and Birk, D. E. (1991). Collagen fibril assembly and deposition in the developing dermis: segmental deposition in extracellular compartments. *J. Struct. Biol.*, 106(1):73–81.

Podsypanina, K., Du, Y.-C. N., Jechlinger, M., Beverly, L. J., Hambardzumyan, D., and Varmus, H. (2008). Seeding and propagation of untransformed mouse mammary cells in the lung. *Science*, 321(5897):1841–1844.

Poincloux, R., Lizárraga, F., and Chavrier, P. (2009). Matrix invasion by tumour cells: a focus on MT1-MMP trafficking to invadopodia. *J. Cell. Sci.*, 122(17):3015–3024.

Popławski, N. J., Agero, U., Gens, J. S., Swat, M., Glazier, J. A., and Anderson, A. R. A. (2009). Front instabilities and invasiveness of simulated avascular tumors. *Bull. Math. Biol.*, 71(5):1189–1227.

Powathil, G. G., Adamson, D. J. A., and Chaplain, M. A. J. (2013). Towards predicting the response of a solid tumour to chemotherapy and radiotherapy treatments: clinical insights from a computational model. *PLoS Comput. Biol.*, 9(7):e1003120.

Powathil, G. G., Gordon, K. E., Hill, L. A., and Chaplain, M. A. J. (2012). Modelling the effects of cell-cycle heterogeneity on the response of a solid tumour to chemotherapy: biological insights from a hybrid multiscale cellular automaton model. *J. Theor. Biol.*, 308:1–19.

Puck, T. T., Marcus, P. I., and Cieciura, S. J. (1956). Clonal growth of mammalian cells in vitro: Growth characteristics of colonies from single hela cells with and without a "feeder" layer. *J. Exp. Med.*, 103(2):273–284.

Puram, S. V., Tirosh, I., Parikh, A. S., Patel, A. P., Yizhak, K., Gillespie, S., Rodman, C., Luo, C. L., Mroz, E. A., Emerick, K. S., and Deschler, D. (2017). Single-cell transcriptomic analysis of primary and metastatic tumor ecosystems in head and neck cancer. *Cell*, 171(7):1611–1624.

Radisky, E. S. and Radisky, D. C. (2010). Matrix metalloproteinase-induced epithelial-mesenchymal transition in breast cancer. *J Mammary Gland Biol Neoplasia*, 15(2):201–212.

Ramaswamy, S., Ross, K. N., Lander, E. S., and Golub, T. R. (2003). A molecular signature of metastasis in primary solid tumors. *Nature Genet.*, 33(1):49.

Ramis-Conde, I., Chaplain, M. A. J., and Anderson, A. R. A. (2008a). Mathematical modelling of cancer cell invasion of tissue. *Math. Comput. Model.*, 47(5):533–545.

Ramis-Conde, I., Drasdo, D., Anderson, A. R. A., and Chaplain, M. A. J. (2008b). Modeling the influence of the E-cadherin-β-catenin pathway in cancer cell invasion: a multiscale approach. *Biophys. J.*, 95(1):155–165.

Rejniak, K. A. (2007). An immersed boundary framework for modelling the growth of individual cells: an application to the early tumour development. *J. Theor. Biol.*, 247(1):186–204.

Rejniak, K. A. and Anderson, A. R. A. (2011). Hybrid models of tumor growth. *Wiley Interdiscip. Rev. Syst. Biol. Med.*, 3(1):115–125.

Rhim, A. D., Mirek, E. T., Aiello, N. M., Maitra, A., Bailey, J. M., McAllister, F., Reichert, M., Beatty, G. L., Rustgi, A. K., Vonderheide, R. H., Leach, S. D., and Stanger, B. Z. (2012). EMT and dissemination precede pancreatic tumor formation. *Cell*, 148(1):349–361.

Rhodes, A. and Hillen, T. (2019). A mathematical model for the immune-mediated theory of metastasis. *bioRxiv: 565531* [Preprint]. Accessed: 25-08-2019.

Ribba, B., Boetsch, C., Nayak, T., Grimm, H. P., Charo, J., Evers, S., Klein, C., Tessier, J., Charoin, J. E., Phipps, A., and Pisa, P. (2018). Prediction of the optimal dosing regimen using a mathematical model of tumor uptake for immunocytokine-based cancer immunotherapy. *Clin. Cancer Res.*, 24(14):3325–3333.

Rissanen, J. P., Fagerlund, K. M., Tuomela, J. M., Suominen, M. I., Halleen, J. M., and Salo, T. A. (2013). Abstract 3842: Culturing cancer cells on myoma tissue: Development of a novel fully human organotypic 3D invasion model applicable as a preclinical tool for cancer drug development. *Cancer Res.*, 73:5272–5272.

Rivera, C. and Venegas, B. (2014). Histological and molecular aspects of oral squamous cell carcinoma. *Oncol. Lett.*, 8(1):7–11.

Ross, J. S., Wang, K., Gay, L., Otto, G. A., White, E., Iwanik, K., Palmer, G., Yelensky, R., Lipson, D. M., Chmielecki, J., Erlich, R. L., Rankin, A. N., Ali, S. M., Elvin, J. A., Morosini, D., Miller, V. A., and Stephens, P. J. (2015). Comprehensive genomic profiling of carcinoma of unknown primary site: new routes to targeted therapies. *JAMA Oncol.*, 1(1):40–49.

Ruscetti, M., Quach, B., Dadashian, E. L., Mulholland, D. J., and Wu, H. (2015). Tracking and functional characterization of epithelial–mesenchymal transition and mesenchymal tumor cells during prostate cancer metastasis. *Cancer Res.*, 75(13):2749–2759.

Sabeh, F., Shimizu-Hirota, R., and Weiss, S. J. (2009). Protease-dependent versus-independent cancer cell invasion programs: Three-dimensional amoeboid movement revisited. *J. Cell Biol.*, 185(1):11–19.

Saidel, G. M., Liotta, L. A., and Kleinerman, J. (1976). System dynamics of a metastatic process from an implanted tumor. *J. Theor. Biol.*, 56(2):417–434.

Schiff, J. L. (2011). *Cellular automata: a discrete view of the world*, volume 45. John Wiley & Sons.

Scianna, M., Preziosi, L., and Wolf, K. (2013). A cellular Potts model simulating cell migration on and in matrix environments. *Math. Biosci. Eng.*, 10(1):235–261.

Scott, J. G., Basanta, D., Anderson, A. R. A., and Gerlee, P. (2013a). A mathematical model of tumour self-seeding reveals secondary metastatic deposits as drivers of primary tumour growth. *J. R. Soc. Interface*, 10(82):20130011.

Scott, J. G., Gerlee, P., Basanta, D., Fletcher, A. G., Maini, P. K., and Anderson, A. R. A. (2013b). Mathematical modeling of the metastatic process. In *Experimental Metastasis: Modeling and Analysis*, pages 189–208. Springer.

Sekimura, T., Zhu, M., Cook, J., Maini, P. K., and Murray, J. D. (1999). Pattern formation of scale cells in lepidoptera by differential origin-dependent cell adhesion. *Bull. Math. Bio.*, 61(5):807–828.

Sethi, N. and Kang, Y. (2011). Notch signalling in cancer progression and bone metastasis. *Br. J. Cancer*, 105(12):1805.

Sfakianakis, N., Kolbe, N., Hellmann, N., and Lukáčová-Medvid'ová, M. (2017). A multiscale approach to the migration of cancer stem cells: Mathematical modelling and simulations. *Bull. Math. Biol.*, 79(1):209–235.

Sfakianakis, N., Madzvamuse, A., and Chaplain, M. A. J. (2018a). A hybrid multiscale model for cancer invasion of the extracellular matrix. *arXiv:1805.10541* [Preprint]. Accessed: 25-08-2019.

Sfakianakis, N., Peurichard, D., Brunk, A., and Schmeiser, C. (2018b). Modelling cell-cell collision and adhesion with the filament based lamellipodium model. *arXiv:1809.07852* [Preprint]. Accessed: 25-08-2019.

Shahriyari, L. (2016). A new hypothesis: some metastases are the result of inflammatory processes by adapted cells, especially adapted immune cells at sites of inflammation. *F1000Res.*, 5.

Sherratt, J. A., Gourley, S. A., Armstrong, N. J., and Painter, K. J. (2009). Boundedness of solutions of a non-local reaction–diffusion model for adhesion in cell aggregation and cancer invasion. *Eur. J. Appl. Math.*, 20(01):123–144.

Starr, C., Evers, C., and Starr, L. (2010). *Biology: concepts and applications without physiology*. Cengage Learning.

Steeg, P. S. (2004). Perspectives on classic articles: metastasis suppressor genes. *J. Natl. Cancer Inst.*, 96(6):E4.

Stéphanou, A., McDougall, S. R., Anderson, A. R. A., and Chaplain, M. A. J. (2006). Mathematical modelling of the influence of blood rheological properties upon adaptative tumour-induced angiogenesis. *Math. Comput. Model.*, 44(1-2):96–123.

Stokes, C., Rupnick, M., Williams, S., and Lauffenburger, D. (1990). Chemotaxis of human microvessel endothelial cells in response to acidic fibroblast growth factor. *Lab. Invest.*, 63(5):657–668.

Stratonovich, R. (1966). A new representation for stochastic integrals and equations. *SIAM J. Control*, 4(2):362–371.

Strilic, B., Yang, L., Albarrán-Juárez, J., Wachsmuth, L., Han, K., Müller, U. C., Pasparakis, M., and Offermanns, S. (2016). Tumour-cell-induced endothelial cell necroptosis via death receptor 6 promotes metastasis. *Nature*, 536(7615):215–218.

Świerniak, A. and Krześlak, M. (2016). Cancer heterogeneity and multilayer spatial evolutionary games. *Biol. Direct*, 11(1):53.

Szabó, A. and Merks, R. M. (2013). Cellular potts modeling of tumor growth, tumor invasion, and tumor evolution. *Front. Oncol.*, 3:87.

Talmadge, J. E. and Fidler, I. J. (2010). AACR centennial series: the biology of cancer metastasis: historical perspective. *Cancer Res.*, 70(14):5649–5669.

Tamaki, M., McDonald, W., Amberger, V. R., Moore, E., and Del Maestro, R. F. (1997). Implantation of C6 astrocytoma spheroid into collagen type I gels: invasive, proliferative, and enzymatic characterizations. *J. Neurosurg.*, 87(4):602–609.

Thiery, J. P. and Lim, C. T. (2013). Tumor dissemination: an EMT affair. *Cancer cell*, 23(3):272–273.

Toffoli, T. and Margolus, N. (1987). *Cellular automata machines: a new environment for modeling*. MIT press.

Tomlinson, I. P. M. and Bodmer, W. F. (1997). Modelling the consequences of interactions between tumour cells. *Br. J. Cancer*, 75(2):157.

Tompson, A. F. B. and Dougherty, D. E. (1992). Particle-grid methods for reacting flows in porous media with application to fisher's equation. *Appl. Math. Model.*, 16(7):374–383.

Trucu, D., Lin, P., Chaplain, M. A. J., and Wang, Y. (2013). A multiscale moving boundary model arising in cancer invasion. *Multiscale Model. Simul.*, 11(1):309–335.

Tsai, J. H., Donaher, J. L., Murphy, D. A., Chau, S., and Yang, J. (2012). Spatiotemporal regulation of epithelial-mesenchymal transition is essential for squamous cell carcinoma metastasis. *Cancer cell*, 22(6):725–736.

Tsuji, T., Ibaragi, S., and Hu, G.-F. (2009). Epithelial-mesenchymal transition and cell cooperativity in metastasis. *Cancer Res.*, 69(18):7135–7139.

Turajlic, S. and Swanton, C. (2016). Metastasis as an evolutionary process. *Science*, 352(6282):169–175.

Turner, S. and Sherratt, J. A. (2002). Intercellular adhesion and cancer invasion: a discrete simulation using the extended Potts model. *J. Theor. Biol.*, 216(1):85–100.

Urs, L., Stevens, L., and Kahwash, S. B. (2008). Leukemia presenting as solid tumors: report of four pediatric cases and review of the literature. *Pediatr. Devel. Pathol.*, 11(5):370–376.

Vajtai, R. (2013). *Springer handbook of nanomaterials*. Springer Science & Business Media.

Valastyan, S. and Weinberg, R. A. (2011). Tumor metastasis: molecular insights and evolving paradigms. *Cell*, 147(2):275–292.

Valiente, M., Obenauf, A. C., Jin, X., Chen, Q., Zhang, X. H.-F., Lee, D. J., Chaft, J. E., Kris, M. G., Huse, J. T., Brogi, E., and Massagué, J. (2014). Serpins promote cancer cell survival and vascular co-option in brain metastasis. *Cell*, 156(5):1002–1016.

van der Vorst, H. (1992). Bi-CGSTAB: A fast and smoothly converging variant of Bi-CG for the solution of nonsymmetric linear systems. *SIAM J. Sci. Comput.*, 13(2):631–644.

van Hasselt, J. C. and van der Graaf, P. H. (2015). Towards integrative systems pharmacology models in oncology drug development. *Drug Discov. Today Technol.*, 15:1–8.

Vega, S., Morales, A. V., Ocaña, O. H., Valdés, F., Fabregat, I., and Nieto, M. A. (2004). Snail blocks the cell cycle and confers resistance to cell death. *Genes Dev.*, 18(10):1131–1143.

Von Neumann, J. and Burks, A. W. (1966). Theory of self-reproducing automata. *IEEE Trans. Neural Netw.*, 5(1):3–14.

Von Neumann, J. and Morgenstern, O. (2007). *Theory of games and economic behavior*. Princeton University Press.

Wang, X., Yu, M., Zhao, K., He, M., Ge, W., Sun, Y., Wang, Y., Sun, H., and Hu, Y. (2016). Upregulation of Mir-205 under hypoxia promotes epithelial-mesenchymal transition by targeting ASPP2. *Cell Death Dis.*, 7(12):e2517.

Weilbaecher, K. N., Guise, T. A., and McCauley, L. K. (2011). Cancer to bone: a fatal attraction. *Nat. Rev. Cancer*, 11(6):411.

Weinberg, R. (2013). *The biology of cancer*. Garland Science.

Wolf, K., Mazo, I., Leung, H., Engelke, K., Von Andrian, U. H., Deryugina, E. I., Strongin, A. Y., Bröcker, E.-B., and Friedl, P. (2003a). Compensation mechanism in tumor cell migration. *J. Cell Biol.*, 160(2):267–277.

Wolf, K., Müller, R., Borgmann, S., Bröcker, E.-B., and Friedl, P. (2003b). Amoeboid shape change and contact guidance: T-lymphocyte crawling through fibrillar collagen is independent of matrix remodeling by MMPs and other proteases. *Blood*, 102(9):3262–3269.

Wolf, K., Wu, Y. I., Liu, Y., Geiger, J., Tam, E., Overall, C., Stack, M. S., and Friedl, P. (2007). Multi-step pericellular proteolysis controls the transition from individual to collective cancer cell invasion. *Nat. Cell. Biol.*, 9(8):893–904.

Wolf-Gladrow, D. A. (2004). *Lattice-gas cellular automata and lattice Boltzmann models: an introduction*. Springer.

Wong, S. Y. and Hynes, R. O. (2006). Lymphatic or hematogenous dissemination: how does a metastatic tumor cell decide? *Cell cycle*, 5(8):812–817.

Wurzel, M., Schaller, C., Simon, M., and Deutsch, A. (2005). Cancer cell invasion of brain tissue: guided by a prepattern? *Comput. Math. Methods Med.*, 6(1):21–31.

Wyllie, A., Rose, K., Morris, R., Steel, C., Foster, E., and Spandidos, D. (1987). Rodent fibroblast tumours expressing human myc and ras genes: growth, metastasis and endogenous oncogene expression. *Br. J. Cancer*, 56(3):251.

Xu, J.-L. and Prorok, P. C. (1998). Estimating a distribution function of the tumor size at metastasis. *Biometrics*, pages 859–864.

Yang, M.-H., Wu, M.-Z., Chiou, S.-H., Chen, P.-M., Chang, S.-Y., Liu, C.-J., Teng, S.-C., and Wu, K.-J. (2008). Direct regulation of TWIST by HIF-1α promotes metastasis. *Nat. Cell Biol.*, 10(3):295.

Ye, X., Tam, W. L., Shibue, T., Kaygusuz, Y., Reinhardt, F., Eaton, E. N., and Weinberg, R. A. (2015). Distinct EMT programs control normal mammary stem cells and tumour-initiating cells. *Nature*, 525(7568):256.

You, L., Brown, J. S., Thuijsman, F., Cunningham, J. J., Gatenby, R. A., Zhang, J., and Staňková, K. (2017). Spatial vs. non-spatial eco-evolutionary dynamics in a tumor growth model. *J. Theor. Biol.*, 435:78–97.

Yu, M., Bardia, A., Wittner, B. S., Stott, S. L., Smas, M. E., Ting, D. T., Isakoff, S. J., Ciciliano, J. C., Wells, M. N., Shah, A. M., , and Concannon, K. F. (2013). Circulating breast tumor cells exhibit dynamic changes in epithelial and mesenchymal composition. *Science*, 339(6119):580–584.

Zeisberg, E. M., Potenta, S., Xie, L., Zeisberg, M., and Kalluri, R. (2007). Discovery of endothelial to mesenchymal transition as a source for carcinoma-associated fibroblasts. *Cancer Res.*, 67(21):10123–10128.

Zhang, G. (2015). *Computational Bioengineering*. CRC Press.

Zhang, J., Cunningham, J. J., Brown, J. S., and Gatenby, R. A. (2017). Integrating evolutionary dynamics into treatment of metastatic castrate-resistant prostate cancer. *Nat. Commun.*, 8(1):1816.

Zhang, L., Wang, Z., Sagotsky, J. A., and Deisboeck, T. S. (2009). Multiscale agent-based cancer modeling. *J. Math. Biol.*, 58(4-5):545–559.

Appendices

Appendix A

Discretisation of the continuum model underlying the metastasis framework in Chapters 4 and 5

We discretise each of the equations (4.1.1), (4.1.2), (4.1.9) and (4.1.10) using an FTCS scheme. Thus, we approximate the time-derivative on the left hand side by a forward difference scheme of first order and the right hand side by the centred second order difference scheme.

For clarity of notation, when discretising equations (4.1.1) and (4.1.2), we denote $k = \mathsf{E}, \mathsf{M}$ to represent the coefficients corresponding the epithelial and mesenchymal cancer cells, respectively, and further drop the index k to when describing the cancer cell type, hence denoting $c_k = c$. This yields

$$\begin{aligned}\frac{c_{i,j}^{n+1} - c_{i,j}^{n}}{\Delta t} = D_k &\left(\frac{c_{i+1,j}^{n} - 2c_{i,j}^{n} + c_{i-1,j}^{n}}{(\Delta x)^2} + \frac{c_{i,j+1}^{n} - 2c_{i,j}^{n} + c_{i,j-1}^{n}}{(\Delta y)^2} \right) \\ &- \Phi_k \Bigg[\frac{(c_{i+1,j}^{n} - c_{i-1,j}^{n})(w_{i+1,j}^{n} - w_{i-1,j}^{n})}{4(\Delta x)^2} + \frac{w_{i+1,j}^{n} - w c_{i,j}^{n} + w_{i-1,j}^{n}}{(\Delta x)^2} \\ &\quad + \frac{(c_{i,j+1}^{n} - c_{i,j-1}^{n})(w_{i,j+1}^{n} - w_{i,j-1}^{n})}{4(\Delta y)^2} + \frac{w_{i,j+1}^{n} - 2w_{i,j}^{n} + w_{i,j-1}^{n}}{(\Delta y)^2} \Bigg].\end{aligned}$$

By continuing with the notation $c = c_k$, $k = \mathsf{E}, \mathsf{M}$ and solving for $c_{i,j}^{n+1}$, the number of cancer cells of epithelial and of mesenchymal phenotype, respectively, at grid point (x_i, y_j) at time t_{n+1},

$$c_{i,j}^{n+1} = \mathcal{P}_0 c_{i-1,j}^{n} + \mathcal{P}_1 c_{i+1,j}^{n} + \mathcal{P}_2 c_{i,j+1}^{n} + \mathcal{P}_3 c_{i,j-1}^{n} + \mathcal{P}_4 c_{i,j}^{n},$$

where

$$\begin{aligned}
\mathcal{P}_0 : \mathcal{P}^n_{i-1,j} &:= \frac{\Delta t}{(\Delta x)^2}\left[D_k - \frac{\Phi_k}{4}\left(w^n_{i+1,j} - w^n_{i-1,j}\right)\right],\\
\mathcal{P}_1 : \mathcal{P}^n_{i+1,j} &:= \frac{\Delta t}{(\Delta x)^2}\left[D_k + \frac{\Phi_k}{4}\left(w^n_{i+1,j} - w^n_{i-1,j}\right)\right],\\
\mathcal{P}_2 : \mathcal{P}^n_{i,j+1} &:= \frac{\Delta t}{(\Delta y)^2}\left[D_k + \frac{\Phi_k}{4}\left(w^n_{i,j+1} - w^n_{i,j-1}\right)\right],\\
\mathcal{P}_3 : \mathcal{P}^n_{i,j-1} &:= \frac{\Delta t}{(\Delta y)^2}\left[D_k - \frac{\Phi_k}{4}\left(w^n_{i,j+1} - w^n_{i,j-1}\right)\right],\\
\mathcal{P}_4 : \mathcal{P}^n_{i,j} &:= 1 - \frac{\Delta t}{(\Delta x)^2}\left[2D_k - \Phi_k\left(w^n_{i+1,j} - 2w^n_{i,j} + w^n_{i-1,j}\right)\right]\\
&\quad - \frac{\Delta t}{(\Delta y)^2}\left[2D_k - \Phi_k\left(w^n_{i,j+1} - 2w^n_{i,j} + w^n_{i,j-1}\right)\right].
\end{aligned}$$

If we substitute $\Delta x = \Delta y$, the five equations above simplify to equations (4.1.4), i.e.

$$\begin{aligned}
\mathcal{P}_0 : \mathcal{P}^n_{i-1,j} &:= \frac{\Delta t}{(\Delta x)^2}\left[D_k - \frac{\Phi_k}{4}\left(w^n_{i+1,j} - w^n_{i-1,j}\right)\right],\\
\mathcal{P}_1 : \mathcal{P}^n_{i+1,j} &:= \frac{\Delta t}{(\Delta x)^2}\left[D_k + \frac{\Phi_k}{4}\left(w^n_{i+1,j} - w^n_{i-1,j}\right)\right],\\
\mathcal{P}_2 : \mathcal{P}^n_{i,j+1} &:= \frac{\Delta t}{(\Delta x)^2}\left[D_k + \frac{\Phi_k}{4}\left(w^n_{i,j+1} - w^n_{i,j-1}\right)\right],\\
\mathcal{P}_3 : \mathcal{P}^n_{i,j-1} &:= \frac{\Delta t}{(\Delta x)^2}\left[D_k - \frac{\Phi_k}{4}\left(w^n_{i,j+1} - w^n_{i,j-1}\right)\right],\\
\mathcal{P}_4 : \mathcal{P}^n_{i,j} &:= 1 - \frac{\Delta t}{(\Delta x)^2}\left[4D_k - \Phi_k\left(w^n_{i+1,j} + w^n_{i-1,j} + w^n_{i,j+1} + w^n_{i,j-1} - 4w^n_{i,j}\right)\right].
\end{aligned}$$

Note that the discretisation time step Δt and space steps Δx and Δy were chosen to represent the physical properties of cancer cell size and remain fixed in corresponding equations. However, the abiotic time step Δt_a and the abiotic space steps Δx_a and Δy_a used in the discretisation of the equations describing the MMP-2 concentration and ECM density can be chosen freely for a more accurate discretisation of the PDEs in (4.1.9) and (4.1.10), as long as Δt, Δx and Δy are integer multiples of Δt_a, Δx_a and Δy_a, respectively. Consequently, when discretising equation (4.1.9), we obtain

$$\frac{m^{n+1}_{i,j} - m^n_{i,j}}{\Delta t_a} = D_m\left(\frac{m^n_{i+1,j} - 2m^n_{i,j} + m^n_{i-1,j}}{(\Delta x_a)^2} + \frac{m^n_{i,j+1} - 2m^n_{i,j} + m^n_{i,j-1}}{(\Delta y_a)^2}\right) + \Theta c_{\mathsf{M}}{}^n_{i,j} - \Lambda m^n_{i,j}.$$

Solving for $m^{n+1}_{i,j}$, the MMP-2 concentration at grid point (x_i, y_j) at time t_{n+1}, and substituting $\Delta x = \Delta y$, we find

$$m^{n+1}_{i,j} = \Delta t_a\left[D_m\left(\frac{m^n_{i+1,j} + m^n_{i-1,j} + m^n_{i,j+1} + m^n_{i,j-1} - 4m^n_{i,j}}{(\Delta x_a)^2}\right) + \Theta c_{\mathsf{M}}{}^n_{i,j} - \Lambda m^n_{i,j}\right] + m^n_{i,j}$$

and hence

$$m_{i,j}^{n+1} = D_m \frac{\Delta t_a}{(\Delta x_a)^2} \left(m_{i+1,j}^n + m_{i-1,j}^n + m_{i,j+1}^n + m_{i,j-1}^n \right) + m_{i,j}^n \left(1 - 4D_m \frac{\Delta t_a}{(\Delta x_a)^2} - \Delta t_a \Lambda \right) + \Delta t_a \Theta c_{\mathsf{M}}{}_{i,j}^{n}. \tag{A.0.1}$$

Finally, from the FTCS discretisation of equation (4.1.10), we obtain

$$\frac{w_{i,j}^{n+1} - w_{i,j}^n}{\Delta t_a} = - \left(\Gamma_1 c_{\mathsf{M}}{}_{i,j}^{n} + \Gamma_2 m_{i,j}^n \right) w_{i,j}^n.$$

Solving for $w_{i,j}^{n+1}$, the number of cancer cells at grid point (x_i, y_j) at time t_{n+1}, yields

$$w_{i,j}^{n+1} = w_{i,j}^n \left[1 - \Delta t_a \left(\Gamma_1 c_{\mathsf{M}}{}_{i,j}^{n} + \Gamma_2 m_{i,j}^n \right) \right]. \tag{A.0.2}$$

Appendix B

Pseudo-code for the metastasis models in Chapters 4 and 5

Here, we provide pseudo-code that provides insight into the computational implementation of the mathematical multi-organ model of metastatic spread. All of the pseudo-code applies to the model introduced in Chapter 5. For the model in Chapter 4, the underlined parts are omitted. Also, note that only some level of detail is provided to avoid repetition of the model outlines given in Sections 4.1 and 5.1. The reader is referred there for further detail e.g. on the entry conditions of the cells of various phenotypes to each of the vessel types or the types of mutations that occur on the various grids. The pseudo-code then reads as follows:

1. Plant seeds for random number generator
2. Create primary and secondary grids with their initial ECM density, vessels, and restriction zones for the initial cancer cell placement
3. Create the initial batch of cancer cells one after the other on the primary grid by storing them in a vector with their attributes (coordinates, grid, alive or dead, cell phenotype, age)
4. Main loop
   - 4.1. Print grids
   - 4.2. Simulate primary grid, cancer cell by cancer cell (in order of their creation)
     - 4.2.1. Increase cell age
     - 4.2.2. Process cells on vessel grid points:
       - *If vessel entry condition fulfilled:* add cell(s) to vessel vector, tag jointly entering cells as a cluster and remove them from the grid
       - *else:* do not alter cell position
     - 4.2.3. Cells on non-vessel grid points proliferate <u>while potentially undergoing EMT, as explained graphically in the left column of Figure 5.2</u>
     - 4.2.4. Erase dead cells
   - 4.3. Process cancer cells in vessel in order of their entry time

4.3.1. Decrease time to remain in vessel for each cell in vessel

4.3.2. Process potential cluster disaggregation for cells that have spent half of the total time in the vasculature

4.3.3. For cells that have spent sufficient time in the vasculature, determine if they die or survive according to the specific death probabilities associated with cells in clusters versus single cells of the various phenotypes

- *if cell dead:* remove from simulation
- *else:* remove from vessel and determine grid and vessel to place the cell or cell cluster on
  - *if vessel grid point not filled to carrying capacity Q:* place cell(s) on vessel grid point
  - *else if vessel grid point filled to carrying capacity Q but neighbour grid points provide space:* place on random grid point neighbouring vessel grid point
  - *else:* remove cell from simulation

4.4. Simulate cancer cells on secondary grids cell by cell (in order of their arrival at or creation on the respective secondary grid)

4.4.1. Increase cell age

4.4.2. Cells on all grid points proliferate—while potentially undergoing MET as shown in the right column of Figure 5.2—, remain dormant, or die

4.4.3. Erase dead cells

4.5. Update the ECM density by degrading it according to the MDE concentration on each grid point (grid point by grid point, starting top left to bottom left and then moving through the grid points left to right, column by column)

Appendix C

Numerical method for the ARD model in Chapter 6

We use a second order *Implicit-Explicit Runge-Kutta* (IMEX-RK) *Finite Volume* (FV) numerical method that was previously developed in Kolbe et al. (2016); Sfakianakis et al. (2017), where we refer to for more details. Here we provide a basic description of the method.

For ease of presentation, we consider the generic ARD system to be of the form

$$\mathbf{w}_t = A(\mathbf{w}) + R(\mathbf{w}) + D(\mathbf{w}), \tag{C.0.1}$$

where $\mathbf{w}$ represents the solution vector, and A, R, and D the *advection*, *reaction*, and *diffusion* operators respectively.

We denote by $\mathbf{w}_h(t)$ the corresponding semi-discrete numerical approximation—indexed here by the maximal spatial grid diameter h—that satisfies the system of ODEs

$$\partial_t \mathbf{w}_h = \mathcal{A}(\mathbf{w}_h) + \mathcal{R}(\mathbf{w}_h) + \mathcal{D}(\mathbf{w}_h), \tag{C.0.2}$$

where the numerical operators $\mathcal{A}$, $\mathcal{R}$, and $\mathcal{D}$ are *discrete approximations* of the operators A, R, and D in (C.0.1) respectively.

Our method of choice for solving (C.0.2) is an IMEX-RK method based on an explicit and implicit *splitting* of the form

$$\partial_t \mathbf{w}_h = \mathcal{E}(\mathbf{w}_h) + \mathcal{I}(\mathbf{w}_h). \tag{C.0.3}$$

The actual splitting depends on the particular problem at hand but in a typical case, the advection terms $\mathcal{A}$ are treated explicitly in time, the diffusion terms $\mathcal{D}$ implicitly, and the reaction terms $\mathcal{R}$ partly explicitly and partly implicitly.

More precisely, we employ a diagonally implicit RK method for the implicit part, and an explicit RK for the explicit part

$$\begin{cases} \mathbf{W}_i^* = \mathbf{w}_h^n + \tau_n \sum_{j=1}^{i-2} \bar{a}_{i,j} \mathbf{E}_j + \tau_n \bar{a}_{i,i-1} \mathbf{E}_{i-1}, & i = 1 \dots s, \\ \mathbf{W}_i = \mathbf{W}_i^* + \tau_n \sum_{j=1}^{i-1} a_{i,j} \mathbf{I}_j + \tau_n a_{i,i} \mathbf{I}_i, & i = 1 \dots s, \\ \mathbf{w}_h^{n+1} = \mathbf{w}_h^n + \tau_n \sum_{i=1}^{s} \bar{b}_i \mathbf{E}_i + \tau_n \sum_{i=1}^{s} b_i \mathbf{I}_i. \end{cases} \tag{C.0.4}$$

Table C.1: ***Butcher tableaux for the explicit (upper) and the implicit (lower) parts of the third-order IMEX scheme in equation*** (C.0.4)***.*** *See Kennedy and Carpenter (2003) for further information.*

0				
$\frac{1767732205903}{2027836641118}$	$\frac{1767732205903}{2027836641118}$			
$\frac{3}{5}$	$\frac{5535828885825}{10492691773637}$	$\frac{788022342437}{10882634858940}$		
1	$\frac{6485989280629}{16251701735622}$	$-\frac{4246266847089}{9704473918619}$	$\frac{10755448449292}{10357097424841}$	
	$\frac{1471266399579}{7840856788654}$	$-\frac{4482444167858}{7529755066697}$	$\frac{11266239266428}{11593286722821}$	$\frac{1767732205903}{4055673282236}$
0	0			
$\frac{1767732205903}{2027836641118}$	$\frac{1767732205903}{4055673282236}$	$\frac{1767732205903}{4055673282236}$		
$\frac{3}{5}$	$\frac{2746238789719}{10658868560708}$	$-\frac{640167445237}{6845629431997}$	$\frac{1767732205903}{4055673282236}$	
1	$\frac{1471266399579}{7840856788654}$	$-\frac{4482444167858}{7529755066697}$	$\frac{11266239266428}{11593286722821}$	$\frac{1767732205903}{4055673282236}$
	$\frac{1471266399579}{7840856788654}$	$-\frac{4482444167858}{7529755066697}$	$\frac{11266239266428}{11593286722821}$	$\frac{1767732205903}{4055673282236}$

Here $s = 4$ are the stages of the IMEX method, $\mathbf{E}_i = \mathcal{E}(\mathbf{W}_i)$, $I_i = \mathcal{I}(\mathbf{W}_i)$, $i = 1 \dots s$, $\{\bar{b}, \bar{A}\}$, $\{b, A\}$ are respectively the coefficients for the explicit and the implicit part of the scheme given by the Butcher Tableau in Table C.1, *cf.* Kennedy and Carpenter (2003). We solve the linear systems in (C.0.4) using the *iterative biconjugate gradient stabilised Krylov subspace* method (Krylov, 1931; van der Vorst, 1992).